Finite and Spectral Element Methods for Modeling Far-Field Underwater Explosion Effects on Ships

Bradley Klenow

Dissertation submitted to the Faculty of
Virginia Polytechnic Institute and State University
in partial fulfillment of the requirements for the degree of

Doctor of Philosophy

in

Aerospace Engineering

Dr. Alan J. Brown, Chairman
Dr. Romesh C. Batra
Dr. Owen F. Hughes
Dr. Rakesh K. Kapania

April 8, 2009
Blacksburg, Virginia

Keywords: underwater explosion, cavitation, finite element method, spectral element method

Finite and Spectral Element Methods for Modeling Far-Field Underwater Explosion Effects on Ships

Bradley Klenow

ABSTRACT

The far-field underwater explosion (UNDEX) problem is a complicated problem dominated by two phenomena: the shock wave traveling through the fluid and the cavitation in the fluid. Both of these phenomena have a significant effect on the loading of ship structures subjected to UNDEX.

An approach to numerically modeling these effects in the fluid and coupling to a structural model is using cavitating acoustic finite elements (CAFE) and more recently cavitating acoustic spectral elements (CASE). The use of spectral elements in CASE has shown to offer the greater accuracy and reduced computational expense when compared to traditional finite elements. However, spectral elements also increase spurious oscillations in both the fluid and structural response.

This dissertation investigates the application of CAFE, CASE, and a possible improvement to CAFE in the form of a finite element flux-corrected transport algorithm, to the far-field UNDEX problem by solving a set of simplified UNDEX problems. Specifically we examine the effect of increased oscillations on structural response and the effect of errors in cavitation capture on the structural response which have not been thoroughly explored in previous work.

The main contributions of this work are a demonstration of the problem dependency of increased oscillations in the structural response when applying the CASE methodology, the demonstration of how the sensitivity of errors in the structural response changes with changes in the structural model, a detailed explanation of how error in cavitation capture influences the structural response, and a demonstration of the need to accurately capture the shape and magnitude of cavitation regions in the fluid in order to obtain accurate structural response results.

DEDICATION

To Laura

ACKNOWLEDGEMENTS

First and foremost I would like to thank my advisor Dr. Alan Brown for giving me the opportunity to pursue this project. I would also like to express my gratitude for his guidance and support during my stay at Virginia Tech, especially during the final few months of this project. I would also like to thank the members of my committee, Dr. Romesh Batra, Dr. Owen Hughes, and Dr. Rakesh Kapania for their valuable input into this work. I am grateful to have had the support of both Dr. Jinwon Park and Ashley Nisewonger both in our class work and our many discussions on research in underwater explosions.

Personally I would like to thank my parents and family for all their support and encouragement throughout my graduate career. I would also like to thank all of my friends, especially my CSES friends at Virginia Tech, for making my stay in Blacksburg so enjoyable. Lastly, I am most grateful to have the love and support of my wife Laura, without whom this achievement would not have been possible.

TABLE OF CONTENTS

LIST OF FIGURES

LIST OF TABLES

CHAPTER 1 INTRODUCTION

1.1 Motivation and Background

The U.S. Navy defines survivability as, the capacity of the total ship system to avoid and withstand damage and maintain and/or recover mission integrity [1]. Mathematically, ship survivability can be expressed as a relation between the probabilities of three events occurring when a threat, defined as weapons and scenarios that have the ability to compromise the mission capacity of a ship, is encountered.

First is susceptibility, which is defined as the probability of a threat succeeding. This variable accounts for the ability of a threat to hit the ship, and also the ship's ability to avoid the threat. Second is the probability of kill or loss of mission capacity given a hit, called vulnerability. Third is the probability of recovering mission capacity given a specific kill or loss, called recovery.

Of particular interest in the study of naval ship survivability is the vulnerability of a ship to the threat of an underwater explosion and how to incorporate vulnerability into the design of a naval ship. Currently the U.S. Navy uses a set of guidelines and standards in conjunction with shock trial tests to determine the survivability characteristics of a ship.

Shock trial tests (e.g. see Figs 1.1 and 1.2) are performed by detonating explosive charges at various locations around the ship and recording the ship response. While shock trials give valuable information on ship response to specific UNDEX threat scenarios, there are several factors that limit the usefulness of the shock trial in the design process of a ship. First, shock trials are extremely expensive and require extensive planning [2].

Secondly, cost limitations allow only the lead ship in a new class or a ship that deviates considerably from other ships in the same class to undergo shock trials [2]. Thus, shock trials are post-design tests and can not be used early in design phase of a ship. Other limitations are the safety/environmental issues associated with shock trials. There is a safety risk to the crew of the ship, an environmental risk to marine life, and a risk of damaging the ship beyond repair or even sinking it.

Figure 1.1 USS Mobile Bay shock trial

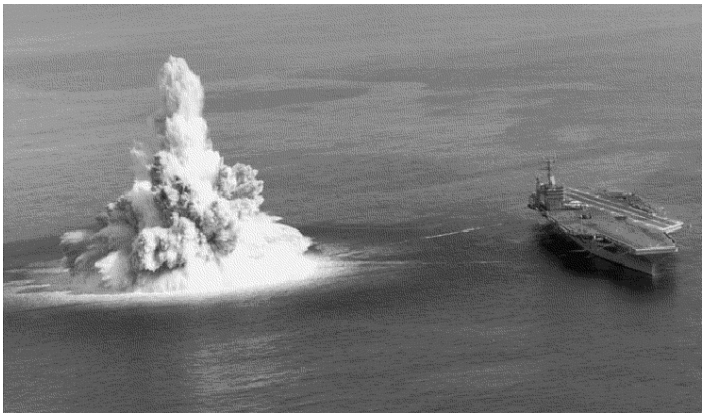

Figure 1.2 Aircraft carrier shock trial

Because of these safety/environmental issues shock trials are limited in the size/type of explosions that can be tested. Therefore shock trials only test risk-free UNDEX threat scenarios for the ship, they cannot be used to determine the survivability limits of a ship in a true combat situation [2].

For these reasons the U.S. Navy has recently set a goal of a 20% reduction in survivability test and evaluation. To meet this goal the Program Executive Office Ships (PEO Ships) has initiated a research program to develop alternative full scale ship shock trials, part of which is dedicated to advanced modeling and simulation methods [3] However, modeling full scale ship shock trials is a difficult task. The underwater explosion (UNDEX) and subsequent ship interaction is a unique problem governed by complex physics [4]. Therefore there is a clear need for the development of advanced numerical models of UNDEX scenarios that accurately approximate the explosion and structural response physics. Such models would not only reduce the cost of survivability

testing but also allow designers to conduct virtual ship shock trials to test the survivability of alternative designs for a new ship, selecting the best design from the model results while still in the design phase.

1.2 Underwater Explosions

1.2.1 Phenomena

The general underwater explosion problem begins with an explosive charge located at a depth below the free surface. The surrounding water is assumed to behave as a compressible fluid that is incapable of supporting significant tension.

The general sequence of events of an underwater explosion begins with the chemical reaction of the explosive material in the charge. This chemical reaction takes place in two parts: the initial chemical reaction and the detonation process. Initially, the explosive material is an unstable chemical substance in a gas, solid, or liquid state [5].

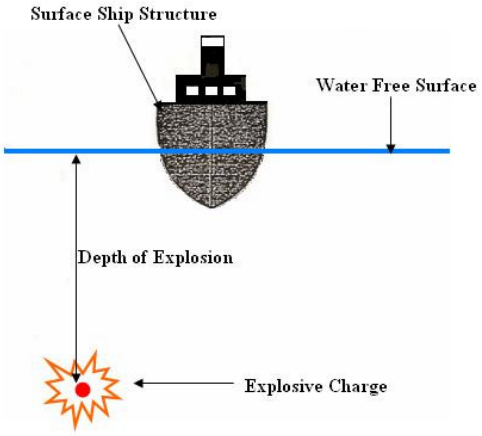

Figure 1.3 General description of an underwater explosion problem

As the explosive material reacts and releases energy it is transformed into a more stable state. The product of the initial reaction, shown in Fig. 1.4a is a hot gas at a very high pressure [7]. If the pressure created by the initial chemical reaction is large enough, a thermo-mechanical shock wave, referred to as the "detonation wave", is created and the detonation process begins. As illustrated in Fig. 1.4b, the detonation wave propagates at supersonic speed through the explosive material still in its original state causing new explosive reactions in the un-reacted material that result in additional gaseous products.

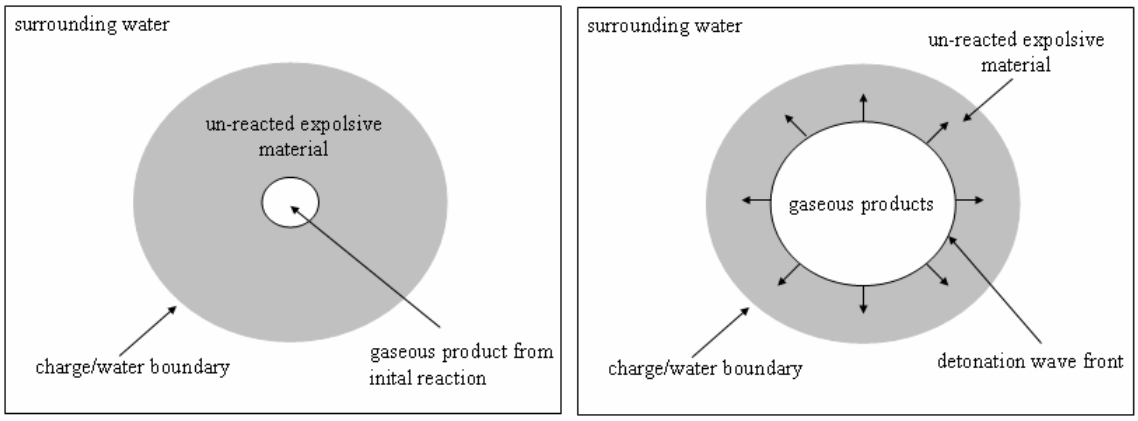

Figure 1.4 An UNDEX during the initial reaction (a) and the detonation process (b)

When the detonation wave reaches the charge/water boundary all explosive material has been converted to gas. These gaseous products now make up a very dense, superheated, and spherical gas bubble, shown in Fig. 1.5.

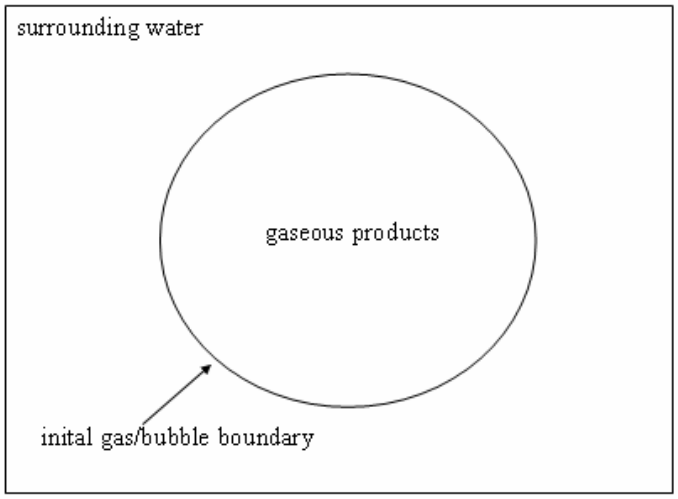

Figure 1.5 An UNDEX at instant the detonation process is complete

The immense pressure inside the initial gas bubble is initially relieved by the generation of a large compressive pressure wave which propagates outwards as a spherical shock wave. The shock wave front is characterized by a nearly discontinuous rise in pressure followed by a brief (a few milliseconds) exponential decay [7]. The maximum pressure reached of the shock wave for a given time and location is referred to as the peak pressure. Initially, the shock wave travels at supersonic speed, but decays to

the speed of sound in water as the wave moves further from the charge origin [6]. In addition to losing speed, the peak pressure reduces and the time decay of the shock wave increases.

As the shock wave propagates it approaches three physical boundaries: the rigid bottom boundary (seafloor), the free surface, and the fluid-structure interface. At the bottom the shock wave is reflected as a compression wave much smaller in magnitude than the original shock wave [6,7]. If the explosion occurs in shallow water, the reflected wave from the bottom can combine with the incident shock wave and the free surface reflected wave to change the pressure field of the surrounding water significantly. However, in most ship shock trials, the explosion occurs in deep water such that the wave reflected from the bottom does not interact with the primary shock wave.

The fluid-structure interface consists of the ship hull wet surface and the water immediately surrounding it. The initial pressure loading gives the hull an acceleration, which for surfaces ships always contains an upward component regardless of the explosion origin [6]. The hull acceleration continues until it begins to move faster than the surrounding water. When this point is reached the fluid load on the structure disappears and the water at the hull is exposed to tension [6]. Because water cannot sustain tension a cavitation region develops at the interface between the hull and water [8]. This cavitation region is termed “local” or “hull” cavitation. At the onset of local cavitation the hull has reached its maximum velocity, called the “kickoff” velocity, due to the shock wave loading [8].

After reaching the kickoff velocity the hull velocity begins to decay and eventually change its direction of motion. The influence of hydrostatic pressure and the motion of the hull eventually cause the local cavitation region to close. When the cavitation region closes a compressive pressure pulse, called a closure pulse, impacts the hull, causing a secondary loading [9]. The form of the re-loading pressure on the hull is similar to the shock wave induced pressure, although the loads imposed on the hull from re-loading are not as large [6].

At the free surface, the incident shock wave is reflected, as shown in Fig. 1.6, back into the water as a tensile wave. Due to the large impedance mismatch between water

and air, the pressure of the reflected wave is almost exactly the negative of the peak pressure of the shock wave at the free surface.

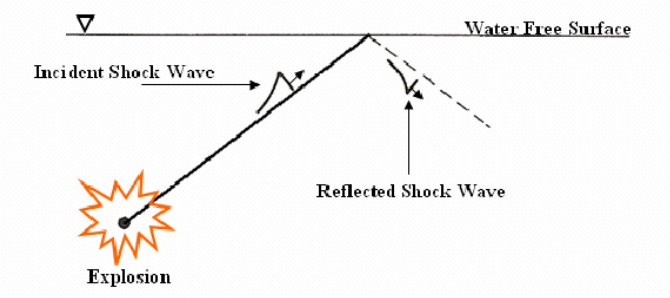

Figure 1.6 Reflection of an incident shock wave at free surface

Because water cannot sustain tension, the reflected wave reduces the pressure around the water surface below zero and cavitation occurs [8]. This cavitation region is termed the bulk cavitation region. This region remains cavitated until the pressure in the region returns to a value above the vapor pressure of water. The size of the bulk cavitation region is dependent on the location of the explosion origin and the size of explosive [8]. The bulk cavitation region is symmetric about the vertical axis of the explosion origin and is bounded by an upper and lower boundary [8]. The upper cavitation boundary is dependent on the atmospheric, hydrostatic, incident shock wave, and reflected wave pressures [8]. As the peak pressure of the reflected wave decays, it eventually reaches the minimum value required to cause cavitation. At this point, the lower cavitation boundary is formed. This boundary represents the line beyond which the peak pressure of the reflected wave is no longer large enough to reduce the absolute pressure in the water to the point where cavitation occurs. After a certain amount of time passes the bulk cavitation region begins to close. As it closes the water above the upper cavitation boundary crashes down on the water below the lower cavitation boundary. As in local cavitation, this causes a compressive wave, called the cavitation pulse, to radiate from the region. Depending on the ship's proximity to the point of closure of the cavitation region, the impact of the cavitation pulse on the hull can cause pressure loads more damaging than the loads created by the initial shock wave impact [6]. Bulk cavitation phenomena dominate the cavitation response of surface ships and do not typically affect

undersea vessels. Instead, local cavitation phenomena dominate the cavitation response of undersea vessels.

The combination of the initial shock loading and the cavitation reloading comprise the early time excitation and response of a ship to an underwater explosion. The following paragraphs describe the explosion phenomena that make up the late time response of the ship structure.

Recall that at the conclusion of the detonation process what remains is a very dense, superheated, and spherical gas bubble. While the release of the shock wave significantly lowers the pressure inside this gas bubble, it is still in excess of the hydrostatic pressure of the surrounding water [7]. The gas internal to the bubble seeks to return to the hydrostatic pressure of the surrounding water to restore equilibrium by expanding. The expansion of the gas creates a large flow of water away from the bubble. Once hydrostatic equilibrium is reached, the expansion of the gas bubble continues due to the inertia of the outwardly flowing water surrounding the bubble. As the inertia driven expansion continues the pressure of the gaseous products falls below hydrostatic pressure [5]. The inertia expansion continues until the pressure differential between the hydrostatic pressure and the internal gas bubble pressure becomes large enough to cause the outward flow of water to stop [6]. At this instant the internal gas bubble pressure is at its minimum and the diameter is at its largest. Next the bubble begins to contract. As it does this, the internal gas bubble pressure increases and the diameter of the bubble reduces. The bubble continues to contract until the compressibility of the gaseous products stop the contraction and force the bubble to expand again [6]. The process of expansion and contraction repeats throughout the duration of the gas bubble, making it an oscillating system. With each consecutive period, the time it takes the bubble to go through a single expansion/contraction cycle decreases. The maximum size of the bubble also decreases while the minimum size increases [7]. This behavior is a result of energy loss during the oscillation process.

The oscillation of the gas bubble causes new pressure waves called secondary or bubble pulses, to be radiated outward from the bubble. The manner in which the bubble pulses are created is similar to the manner in which the shock wave is created. Bubble

pulses are emitted when the pressure internal to the bubble is greatest which occurs at the bubble minimums [6,7]. All bubble pulses propagate at the speed of sound in water [10].

Unlike the shock wave, the bubble pulse waveform is not a discontinuous rise in pressure followed by an exponential decay. Assuming the gas bubble remains stationary at the origin of the explosion (valid for very deep water explosions), the general shape of a bubble pulse is a gradual rise to the peak pressure that is concave in form followed by a concave shaped decay [7]. For a migrating gas bubble, the pressure of the bubble pulses is significantly reduced and the waveform becomes more triangular [7]. The peak pressure of the first bubble pulse is between 10% and 20% of the peak of the shock and the magnitude of the peak pressure lowers for each subsequent bubble pulse [6,7]. Because the bubble pulses are so much weaker than the shock wave only the first bubble pulse is significant in most UNDEX scenarios. Though this is the strongest bubble pulse it does not always create a damaging load on the ship hull.

Bubble migration is created by the buoyancy of the gaseous products internal to the bubble and is heavily influenced by the oscillation of the bubble. At larger gas bubble sizes the inertia of the outward flowing water balances out a majority of the buoyancy force causing the bubble to rise minimally. When the gas bubble is close to or at minimum size the inertia of the outwardly flowing water is greatly reduced. This allows the buoyancy force of the gaseous products to have a greater effect on the net upward force acting on the gas bubble accounting for the much higher rate of ascent of the bubble at its smallest sizes.

As the bubble migrates towards the free surface and the ship hull, it experiences an attraction force to the ship and a repulsion force from the free surface [7,10]. If the bubble migrates such that it is close to the hull at the time it reaches the free surface then two types of loading can occur.

The first type of gas bubble loading is created by the outwardly flowing water around the bubble contacting the hull of the ship. Pressures on the hull in this case are quite high and the duration of the loading period is much longer than the loading period of the shock wave. These loads are capable of creating significant damage to the hull in localized areas, in some cases greater than the shock wave induced damage to the hull.

The second type of gas bubble loading occurs when the bubble actually collapses onto the hull of the ship. This occurs as the bubble contracts in contact with the hull, creating a pressure differential that results in both the collapsing bubble and a high-speed water jet [6]. The impact of the water jet can be sufficiently forceful to puncture the hull. In other cases the water jet causes an initial pressure loading like that of the shock wave and gives the hull a secondary kickoff velocity.

The ship response created by the bubble pulse and gas bubble loading make up the late time response of the ship. In circumstances where the water jet impacts the hull it is estimated that 60% of the total damage may result from the late time response and only 40% from the early time (shock wave impact) response [10].

1.2.2 Types of UNDEX

As detailed in the previous section there are two distinct phases to an UNDEX loading of a structure, the shock loading (early time) and the bubble loading (late time). Each type of loading has a distinct effect on the structure, thus for a given UNDEX scenario we can make some assumptions about which UNDEX phenomena are important to the structural response. Making these assumptions allows two types of underwater explosion scenarios to be defined. In the first type of UNDEX, the explosive charge detonates close to the ship hull. This is called a near-field underwater explosion. In near-field explosions both the shock and the gas bubble interact with the structure due to the proximity of the charge to the structure. If the charge is large enough, large scale plastic deformations and even rupture occur in the structure [12].

In the second type of UNDEX, the charge is detonated further away from the ship hull. This is called a far-field underwater explosion. Far-field underwater explosions may be further divided into two sub-categories based on how the gas bubble is treated. In type 1 far-field explosions the incident shock wave interacts with the structure but the location of the explosion is such that the gas bubble does not influence the ship response [4]. In type 2 far-field explosions both the incident shock wave and bubble pulses affect the ship loading but the gas bubble itself does not interact with the structure [4]. For the purposes of this work we consider only type 1 far-field underwater explosions in cases where the structural response remains elastic.

1.3 Literature Survey

1.3.1 Similitude

The first UNDEX modeling methods were the similitude relations developed primarily in the 1940s [7,13,14,15]. The method of similitude offers a quick and simple way to calculate approximate characteristics of an underwater explosion. Similitude relations yield information on properties such as pressure, impulse, and energy associated with each of the three major events of an underwater explosion [7]: 1) the shock wave, 2) the gas bubble, and 3) the secondary pressure pulses.

The similitude equations use experimentally-determined constants and a set of generic equations in three variables, the charge weight, explosion depth, and a point of interest in the explosive field to estimate shock and bubble characteristics. The method assumes that if the variables of two separate explosions are different by some ratio, the characteristics of the explosions are the same at two corresponding points of interest scaled by the same ratio. This is referred to by Cole [7] as the "principle of similarity".

The three most common relations are presented below in eqs. 1.1, 1.2, 1.3 and give the peak pressure, P_{peak}, time constant, τ, and pressure-time history, $p(t)$, for the shock wave [7,16]. Each equation has a set of constants [16] (see Table 1.1) associated with it that are determined by fitting the equation to experimental data. Note the constants are derived using a specific unit system (here constants given in [16] for S.I. units are used).

$$P_{peak} = K\left(\frac{W^{1/3}}{R}\right)^{\alpha} \tag{1.1}$$

$$\tau = W^{1/3} K\left(\frac{W^{1/3}}{R}\right)^{\alpha} \tag{1.2}$$

$$p(t) = P_{peak} e^{-t/\tau} \tag{1.3}$$

Table 1.1 S.I. constants used in eqs 1.1 and 1.2

Equation	K	α
Peak Pressure (1.1)	52.4	1.13
Time Constant (1.2)	0.084	-0.23

Equation 1.1 is known as the peak pressure approximation. It has been experimentally verified for numerous UNDEX cases and is accepted a reasonable approximation of the peak pressure of the shock wave [17].

Similitude methods have also been used as a basis to create more advanced models of pressure and velocity fields produced by underwater explosions. For example in [18] and [19], similitude like relations are used to describe the pressure and velocity field during the shock wave phase of the explosion while the fields produced for the gas bubble phase are derived from a translating acoustic source. Similitude equations like the peak approximation can also be used to determine input loads and initial conditions in numerical models.

1.3.2 Boundary Element Method Applied to UNDEX: DAA/USA

One approach to modeling fluid-structure interaction for far-field UNDEX problems is to use the boundary element method (BEM). Of particular interest in UNDEX problems is the Doubly Asymptotic Approximation (DAA) BEM used in the Underwater Shock Analysis program (USA). The significant advantage of the DAA method is that the governing equations of the fluid-structure interaction are expressed in terms of the wet surface variables only. Therefore the fluid surrounding the structure does not need to be modeled allowing for much faster computation times [20,21]. Such treatment also eliminates the difficulties associated with numerically capturing the propagation of the shock wave, as it simply applies the shock to the wet surface of the structure. However, when cavitation effects are included in the model the region of fluid surrounding the structure must be modeled and coupled to the structural model [8,22].

In 1992 Fox [23] modeled a submerged cylindrical shell subjected to a far-field UNDEX. This model was classified as far-field type 1 because the initial charge location was such that the gas bubble vented to the surface before interacting with the cylinder. The cylindrical shell was modeled without a surrounding fluid and because of the depth

cavitation was not accounted for in the analysis. The results of the USA model were compared to experimental data of the same UNDEX problem to show that the USA model compared well qualitatively with the experimental results. Beiter [24] and Wood [8] modeled "ship-like" box structures on the surface subjected to far-field UNDEX. Both made comparisons using a model in which cavitation was not included in the analysis (USA analysis) and a model in which cavitation was included in the analysis (LS-DYNA/USA analysis). Both found cavitation to have a significant effect on the structural response and concluded cavitation effects should be included in far-field UNDEX analysis.

1.3.3 Finite Element Method Applied to UNDEX: CAFE

Because of the need to include cavitation effects, the most common numerical method used to model far-field UNDEX is the finite element method (FEM). A typical FEM model of a far-field UNDEX illustrated in Fig. 1.7 consists of three parts, the structural domain, the fluid domain, and the fluid boundary.

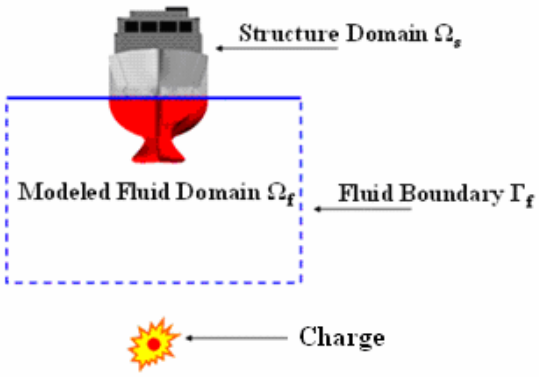

Figure 1.7 Schematic of a typical far-field UNDEX numerical model that includes cavitation effects

For far-field UNDEX FEM, the fluid region can be treated as an acoustic fluid. An acoustic fluid is defined as a fluid in which disturbances in the fluid propagate rapidly and are geometrically linear, even if the constitutive behavior of the fluid is non-linear [25]. Acoustic treatment of the fluid is valid in the far-field problem, because when the explosive charge is removed from the structure the fluid motion caused by the shock wave and formation of cavitation are small [26]. Recall from Sec. 1.2.2, UNDEX

phenomena that cause large fluid and structural motions such as the gas bubble and hull rupture are not considered in the far-field problem. Furthermore, both the shock and cavitation loading occur on the order of micro-seconds. Thus the far-field problem is of short duration with small structural and fluid displacements, which satisfies conditions for acoustic treatment given in [27].

The governing equation of an acoustic fluid can be formulated as a vector formulation or a scalar formulation. Due to the large size of a typical ship shock trial fluid model, a scalar formulation is preferred for far-field UNDEX models. A scalar formulation reduces the number of unknowns at a node in the fluid from three to one [25], thus saving computational costs in large fluid models.

There are four common choices of dependent variables for the scalar formulation of an acoustic fluid. Formulations exist for pressure [27,28,32], density [31], velocity potential [29], and displacement potential [22,26,27,30].

Newton [30,33] developed a FE cavitation model using the displacement potential formulation of the acoustic wave equation. His cavitation model was based on the Bleich-Sandler [34] model. This cavitation model tracks volumetric strain in the acoustic fluid, defining a linear relation between volumetric strain and pressure in the un-cavitated fluid and treating the cavitated fluid as a homogenous single phase region of constant total pressure.

This type of cavitation model is a one-fluid, cut-off cavitation model [35,36]. In a one-fluid model a single governing equation is used to model two separate phases of the fluid. The advantage of a one-fluid model is computational savings over a two-fluid model which requires multiple fluid equations to be solved [36]. Cut-off refers to the treatment of the cavitated fluid as a region of constant total pressure once the cavitation condition is reached in the fluid model. The disadvantage of cut-off treatment is that the phase transition between water and vapor is not considered. However, in large scale problems cut-off models have performed almost identically to cavitation models that include phase transition [12,35,36].

Newton's cavitation model was used by Zienkiewicz, Paul, and Hinton [37] to study cavitation effects on dam loading. Felippa and DeRuntz [22,25] latter used Newton's work in the development of the Cavitating Fluid Analysis (CFA) code. The CFA code,

used an explicit central difference time integration scheme for the fluid, an implicit time integration scheme for the structure, and coupled the fluid boundary to the boundary element code USA to act as a non-reflecting boundary. Sprauge and Geers [38] termed this approach Cavitating Acoustic Finite Elements (CAFE), and this nomenclature is adopted throughout this work. CAFE has been used in many far-field UNDEX modeling applications [2,8,23,24,40,41] and has also been implemented in the commercial FEM code LS-DYNA [26,39]. The most significant LS-DYNA/USA UNDEX model was done by Shin. In [2] Shin modeled a ship shock trial performed on the USS Winston S. Churchill (DDG 81) using LS-DYNA/USA. A ship shock trial was also modeled in [42], using the acoustic pressure formulation in ABAQUS. ABAQUS has also been used to examine UNDEX effects on a missile boat rudder in [43].

There are several aspects of the CAFE approach that limit its effectiveness, especially for large scale problems. These deficiencies are outlined below but were originally detailed by Sprague and Geers in [26] and [44]. The first deficiency in the CAFE approach is the use of linear elements in the fluid mesh, which cause CAFE fluid meshes to be highly dispersive [26,44]. This makes the CAFE approach susceptible to requiring very fine meshes for accurate solutions [38]. The application of such meshes is often not feasible for full ship far-field UNDEX models.

Another deficiency of the CAFE approach in [22,25] is that one-to-one or conformal nodal coupling is required along the fluid structure interface. The conformal coupling requirement makes it extremely difficult to couple a complex structure to the fluid. A good demonstration of this is found in the multi-layered mesh creation in [2]. In addition to the geometric difficulties, conformal coupling requires that any mesh refinement in the fluid must also be carried out for the structural elements on the fluid-structure interface [26]. For methods that treat both the fluid and the structure explicitly this causes a decrease in the critical time step of the model because of the difference in material sound speed for solids and water [26].

1.3.4 Spectral Element Method Applied to UNDEX: CASE

To overcome the highly dispersive nature of the CAFE approach Sprague and Geers [26,44,45] employed higher order spectral elements (SE) to discretize the governing

CAFE equations. They called this approach Cavitating Acoustic Spectral Elements (CASE).

Spectral elements are a combination of spectral methods and FEM. Spectral elements use high order basis functions derived from orthogonal polynomials to reduce interpolation error at the element nodes. These high order spectral basis functions are generally less dispersive than low order basis functions [46] and can exhibit exponential convergence for problems with smooth solutions [26,45]. Thus, the application of SE into CAFE improves the super refinement issues, resulting in a savings in required degrees of freedom to accurately solve a problem [26,44,45].

Sprague and Geers also incorporated a scattered field fluid model and a non-conformal coupling algorithm to couple the fluid to the structure. The scattered field fluid model uses field separation to divide the fluid into a known incident field (the incident shock wave) and an unknown scattered field (the reflected shock and cavitation region). The scattered field model of the governing equations are discretized and solved numerically to obtain the unknown scattered field while the incident field is known for all time. This is in contrast to a total field model of the governing equations in which both the incident and scattered fields are unknowns and must be solved for numerically. The advantage of the scattered field model is that an incident wave can be propagated through the mesh without being distorted by the numerical scheme [26,44].

The implementation of a non-conformal coupling algorithm removes the conformal coupling requirement along the fluid-structure interface [26]. This simplifies the coupling of complex structural geometries to the fluid and also allows the fluid mesh to be refined separately from the structural mesh [26].

1.3.5 Disadvantages of CAFE/CASE

Despite the advantages of CASE there are deficiencies that limit its effectiveness in certain problems. Higher-order spectral elements require smaller critical time steps for explicit time integration [44] than traditional linear finite elements. Thus, when compared to a CAFE model with the same number of total degrees of freedom a higher-order CASE model is more computationally expensive.

Potentially, the most significant disadvantage of the CASE approach is its tendency to increase spurious oscillations [44,46]. This is especially true in problems with steep

gradients and/or discontinuities [26,45,47,48], such as far-field UNDEX problems. In far-field UNDEX problems spurious oscillations can arise from the propagating incident shock wave and also the formation/closure of the cavitation region. Spurious oscillations due to cavitation formation in the CAFE approach were initially discussed by Newton [33]. Newton observed isolated regions of cavitated fluid within the pressurized fluid. He termed this phenomena "frothing". Frothing occurs in the pressurized fluid that exists between the upper cavitation boundary and the structure/free surface. Frothing that occurs in this region interacts with the structure and is responsible for non-physical oscillations or "ringing" in the structural response [22]. To combat frothing Newton applied artificial damping to the governing fluid equations. A similar form of this damping is used in both the CAFE [22] and CASE [26,44,45] equations. While artificial damping reduces the amount of frothing in the fluid it adds non-physical energy loss to propagating waves in the fluid and smears the front of both the incident shock wave and the cavitation boundaries. It is generally assumed that the consequences of adding artificial damping to the fluid model and dispersion effects in general are mitigated because the correct impulse of propagating waves is maintained and impulse drives the structural response [11]. This assumption is based on analysis of Taylor plate theory [7,8] which shows the structural motion is proportional to the impulse of the fluid load when cavitation is neglected [7]. While this assumption is true for shock loading [7] and loading due to cavitation closure pulses, it has not been fully investigated for the cavitation loading of the structure. Section 1.2.1 explained that when the fluid surrounding the structure is cavitated the response of the structure is driven by the absence of significant loading from the fluid rather than the impulse of an incident wave. Cavitation is a phenomenon that has a highly localized spatial component due to the formation of both upper and lower cavitation region boundaries [26,44]. Furthermore, in an acoustic treatment of the fluid the cavitation model is based solely on the magnitude of volumetric strain at a given point in time and space. Thus both minimizing dispersion [44] and capturing the magnitude (i.e. the volumetric strain in the cavitation region) of the cavitation region may be vital in modeling the inception, growth, and collapse of cavitation and its effect on the structural response.

1.3.6 Flux-Corrected Transport

Given the disadvantages of CASE one objective of the literature review was to assess the possibility of an alternative method of addressing the highly dispersive nature of the CAFE while maintaining the acoustic fluid assumptions. A method that accomplishes this is flux-corrected transport.

Flux-corrected transport was developed by Boris and Book [49,50,51] to provide smooth finite difference solutions to one-dimensional shock problems in compressible fluids. In general a flux-corrected transport algorithm consists of a transported diffusion stage and an anti-diffusion stage [57]. The transported diffusion stage advances the solution in time and diffuses the solution to remove dispersive ripples behind the wave front by applying the diffusive fluxes. The diffusion stage is comparable to adding artificial viscosity or (in CAFE/CASE) artificial damping to spread a sharp gradient over several elements. The anti-diffusion stage seeks to correct the dispersion errors introduced in diffusing the solution by adding anti-diffusive fluxes back into the solution. By correcting or limiting the anti-diffusive fluxes they can be added without allowing any existing oscillations to grow or causing any new oscillations [49]. Flux limiting is a crucial part of the FCT method.

Zalesak [52,53] extended flux limitation to a general multi-dimensional form by using the combination of a high and low order numerical scheme. The low order scheme, like the diffusion stage of the original algorithm, diffuses the solution in regions of discontinuity. The high order scheme gives a more accurate solution in smooth regions of the solution. Similar FCT algorithms have been developed or extended to finite elements [54,55] and spectral elements [47,56].

Of particular interest to far-field UNDEX problems is the FE-FCT method presented by Xiao [57] for the study of shock propagation in elastic solid materials. Xiao's method uses an explicit FE formulation on structured meshes with the FCT algorithm based on the original Boris and Book algorithm [49]. The algorithm in [57] does not require the combination of a high and a low order scheme. Thus it is appealing for application to far-field UNDEX problems because, like CAFE/CASE, it is explicit in nature and because of the reduced computational expense when compared to more complex FE-FCT algorithms [57].

1.4 Objective

Given the advantages and disadvantages of finite and spectral elements the primary goal of this work is to determine which method or alternative is better suited to far-field UNDEX modeling. The literature review indicates that the increased spurious oscillations in spectral elements have not been fully investigated for far-field UNDEX problems. Furthermore, the potential need to accurately resolve both the shape and magnitude of cavitation regions in the fluid has not been fully explored. To address these issues and accomplish the primary goal we investigate CAFE, CASE, and a potential improvement to CAFE in the form of a finite element flux-corrected transport (FE-FCT) algorithm. The FE-FCT algorithm potentially offers an improvement to the dispersion properties of linear elements without the increased spurious oscillations and higher computational cost associated with spectral elements but has not been previously applied to the UNDEX problem. Each method is compared first in its ability to capture a step exponential wave in an acoustic fluid and then in its ability to capture cavitation in far-field UNDEX problems. Through this comparison we determine the severity of increased spurious oscillations in CASE models, the effect of artificial damping on wave and cavitation capture in the fluid, the need to accurately resolve both the shape and the magnitude of cavitation regions in the fluid, and ultimately which method is best suited for far-field UNDEX modeling. This assessment has not previously been performed.

1.5 Outline

Chapter 1 gives an introduction to underwater explosion phenomena, a definition of near and far field underwater explosions, and a review of numerical methods used to model far-field underwater explosions. It was concluded that acoustic treatment of the fluid in far-field underwater explosion models allows both the incident shock and cavitation region in the fluid to be treated with reduced computational expense. The review of the state of the art in far-field underwater explosion modeling revealed the need to better understand the importance of dispersion error in accurate resolution of cavitation regions in the fluid and the impact of increased oscillations when applying spectral elements (CASE) to far-field underwater explosion problems. Chapter 2 gives the details of the governing equations used in the dissertation and introduces the concept of field

separation. Chapter 3 begins with an introduction to the spectral element method and then gives the discretized form of the CASE governing equations. Boundary conditions, artificial damping, and non-conformal fluid-structure coupling as applied to CASE are also described in Chapter 3. Chapter 4 introduces the finite element flux-corrected transport algorithm used in this dissertation. The discretized form of the governing equations used in the FE-FCT algorithm and the boundary conditions are also given in Chapter 4. Chapter 4 concludes with a discussion on applying the FE-FCT algorithm to cavitating acoustic fluid problems. Chapter 5 compares finite elements (CAFE), spectral elements (CASE), and the FE-FCT algorithms first in their ability to capture a step exponential wave and then in their ability to capture cavitation in two 1D benchmark problems. A comparison to a non-acoustic fluid solution is also made for the two 1D benchmark problems. Chapter 6 compares finite (CAFE) and spectral (CASE) elements over a variety of mass-spring oscillator problems on a 2D mesh in order to determine the severity of oscillations and the importance of accurate cavitation capture. From these results conclusions are drawn as to the applicability and accuracy of finite (CAFE) and spectral (CASE) elements to general far-field underwater explosion models. Lastly Chapter 7 summarizes the findings of the dissertation and offers possibilities for future work.

CHAPTER 2 GOVERNING EQUATIONS

In the previous chapter we discussed the application of cavitating acoustic fluid models to far-field UNDEX problems using CAFE and CASE. In this chapter we present a derivation of the governing CAFE/CASE equations for both total field and scattered field fluid models. The governing equations for the pressure formulation for a cavitating acoustic fluid are also presented for both total field and scattered field fluid models.

2.1 The Acoustic Wave Equation

Recall from Section 1.3.3 that the far-field UNDEX problem is of short duration and with small structural and fluid displacements, which allow for the acoustic treatment of the fluid. To derive the governing equations for an acoustic fluid we first assume the fluid can be modeled as a Navier-Stokes fluid. The motion of the fluid is governed by the Euler momentum equation and the continuity equation. We define the total displacement, $\vec{\xi}$, of a fluid particle as [22]

$$\vec{\xi}\left(\vec{X},t\right)=\vec{x}\left(\vec{X},t\right)+\vec{x}_{eq}\left(\vec{X}\right), \tag{2.1}$$

where $\vec{x}$ is the dynamic displacement of a fluid particle, $\vec{x}_{eq}$ is the equilibrium displacement of a fluid particle, $\vec{X}$ is the global Cartesian coordinate vector, and t is time.

An acoustic fluid is compressible, however we make the assumption that fluctuations between the density, ρ, and the reference density, ρ_o, remain small. This allows the continuity equation with the fluid particle displacement measured relative to the equilibrium displacement

$$\frac{\partial\rho}{\partial t}+\nabla\cdot\left(\rho\frac{\partial\vec{x}}{\partial t}\right)=0, \tag{2.2}$$

to be linearized and written in terms of total condensation [26,58], $S=\dfrac{\rho}{\rho_o}-1$,

$$\frac{\partial S}{\partial t} + \nabla \cdot \left(\frac{\partial \vec{x}}{\partial t} \right) = 0 ,$$

(2.3)

for $|S| << 1$. Using $|S| << 1$ and neglecting viscous effects and convective acceleration terms simplifies the Euler momentum equation for the acoustic fluid to

$$\rho_o \frac{\partial^2 \vec{x}}{\partial t^2} = \rho_o \vec{f} - \nabla p^t ,$$

(2.4)

where p^t is the total fluid pressure, $\vec{f}\left(\vec{X}\right)$ is the body force field, and again we have measured the fluid particle displacement relative to the equilibrium displacement [22]. Equations 2.3 and 2.4 form the basis of both the displacement potential formulation, used in CAFE/CASE, and the pressure formulation. In the following sections we show how each formulation is derived via eqs. 2.3 and 2.4.

2.2 Displacement Potential Formulation for Cavitation Problems

2.2.1 Total Field Model

The term total field refers to the combination of the equilibrium field, incident field, and scattered field. The equilibrium field is a static field which represents static equilibrium in the fluid. The combined incident and scattered fields are the dynamic fields which represent the deviation of the fluid from equilibrium [26]. For a far-field UNDEX problem the equilibrium field is given by the hydrostatic state of the fluid [22], the incident field is the state of the fluid caused by the propagation of the incident shock wave, and the scattered field is caused by the shock waves interaction with the structure, free surface, and non-reflecting boundary [26]. In a total field model of the fluid the dependent variables consist of the unknown incident and scattered fields, while the equilibrium field is known.

The total field model governing equations for the displacement potential form of the cavitating acoustic wave equation were derived in [22] and [26]. Here we present an overview of those derivations. Assuming an irrotational flow field, the dynamic displacement potential of the fluid is defined as

$$-\nabla\Psi = \vec{x} = \vec{\xi} - \vec{x}_{eq},$$

(2.5)

Taking the first time derivative of eq. 2.5 and inserting into the linearized continuity equation, eq. 2.3, gives

$$\frac{\partial S}{\partial t} - \nabla^2 \frac{\partial \Psi}{\partial t} = 0 .$$

(2.6)

Equation 2.6 can be integrated in time once to yield the strain-displacement relation for CAFE and CASE

$$S - \nabla^2 \Psi = S_{eq}\left(\vec{X}\right),$$

(2.7)

where the term, S_{eq}, represents the equilibrium condensation in the fluid [26]. Note from eqs. 2.5 and 2.7 we see the dynamic condensation, S_{dyn},

$$S_{dyn} = S - S_{eq} = -\nabla \cdot \left(\vec{x}\right),$$

(2.8)

is a measure of volumetric strain or dilation in the fluid [32].

The second governing equation relates the fluid pressure to the dynamic displacement potential in order to allow incorporation of an equation of state to model cavitation [33]. To accomplish this, the first time derivative of the dynamic displacement potential in eq. 2.5, replaces the dynamic fluid particle displacement in eq. 2.4 giving

$$-\rho_o \frac{\partial^2 \nabla\Psi}{\partial t^2} = \rho_o \vec{f} - \nabla p^t .$$

(2.9)

For the static equilibrium problem eq. 2.4 gives [22]

$$\rho_o \vec{f} = \nabla p^H ,$$

(2.10)

where p^H is the hydrostatic pressure in the fluid. Inserting eq. 2.10 into eq. 2.9 gives

$$-\rho_o \frac{\partial^2 \nabla \Psi}{\partial t^2} = \nabla\left(p^H - p^t\right),$$

(2.11)

which can be integrated spatially to yield

$$\rho_o \frac{\partial^2 \Psi}{\partial t^2} = p^t - p^H - g(t),$$

(2.12)

where $g(t)$ is a constant of integration. As in [26], we define the equilibrium pressure, p_{eq}, as $p_{eq} = p^H + g(t)$. This allows eq. 2.12 to be written as

$$\rho_o \frac{\partial^2 \Psi}{\partial t^2} = p\,,$$

(2.13)

where p ($p = p^t - p_{eq}$) is the dynamic pressure.

To relate eqs. 2.7 and 2.13 we define a relation between p^t and S. This is done through the equation of state for a cavitating acoustic fluid [26]

$$p^t = p^{cav} + \begin{cases} \rho_o c^2 S, & \text{if } S > 0 \\ 0, & \text{otherwise} \end{cases},$$

(2.14)

where p^{cav} is the vapor pressure of the fluid and c is the speed of sound in the fluid. Physically the equation of state (eq. 2.9) represents a linear relation between pressure and volumetric strain in the un-cavitated fluid and a homogenous region of zero total pressure in the cavitated fluid [22,26,37]. For the dynamic pressure in eq. 2.13 the equation of state becomes

$$p = p^{cav} - p_{eq} + \begin{cases} \rho_o c^2 S, & \text{if } S > 0 \\ 0, & \text{otherwise} \end{cases}.$$

(2.15)

Note that in practice p^{cav} is small compared to the hydrostatic pressure, thus its effect on the formation of cavitation in the fluid is negligible [22,26].

To simplify the governing equations (eqs. 2.7 and 2.13) both Felippa and DeRuntz [22] and Sprague and Geers [26] define the densified dynamic displacement potential

$$\psi = \rho_o \Psi \,,$$

(2.16)

and densified dynamic condensation

$$s = \rho_o \left(S - S_{eq} \right) = -\rho_o \nabla \cdot \left(\vec{x} \right).$$

(2.17)

Replacing the dynamic displacement potential and dynamic condensation in eqs. 2.7, 2.13, and 2.15 with the densified variables yields the final system of the CAFE/CASE governing equations [22,26]

$$s = \nabla^2 \psi \,,$$

$$\frac{\partial^2 \psi}{\partial t^2} = \begin{cases} c^2 s, & if\ s > \left(p^{cav} - p_{eq} \right) / c^2 \\ p^{cav} - p_{eq}, & otherwise \end{cases}.$$

(2.18)

2.2.2 Scattered Field Model

In the scattered field model of the fluid both the incident field and equilibrium fields are known for all time [26]. Thus, the dependent variables consist only of the unknown scattered field. For UNDEX problems the incident field can be represented by a simple step exponential shock wave using the peak approximation from Section 1.3.1 [26,44] or a more complex wave form such as the one presented in [18,19]. Adopting the scattered field model allows the wave in either incident field model to be propagated through the incident field without error [44]. Following [26,44], the system of CAFE/CASE governing equations for the unknown scattered field variables become

$$s_{sc} = \nabla^2 \psi_{sc} \,,$$

$$\frac{\partial^2 \psi_{sc}}{\partial t^2} = \begin{cases} c^2 s_{sc}, & if\ s_{sc} > \left[p^{cav} - \left(p_{eq} + p_{inc} \right) \right] / c^2 \\ p^{cav} - \left(p_{eq} + p_{inc} \right), & otherwise \end{cases},$$

(2.19)

where the subscript *sc* signifies a scattered field variable and the subscript *inc* signifies a know incident field variable. After solution of eq. 2.14, the dynamic field variables in eq. 2.13 may be recovered via the following relations [26]

$$\psi = \psi_{inc} + \psi_{sc},$$

$$s = s_{inc} + s_{sc},$$

$$p = p_{inc} + p_{sc}.$$

(2.20)

2.3 Pressure Formulation for Cavitation Problems

2.3.1 Total Field Model

As in the displacement potential formulation, in the total field model for the pressure formulation of the fluid the dependent variables consist of the unknown incident and scattered fields, while the equilibrium field is known. The pressure formulation of the fluid is derived by first using the static equilibrium problem in eq. 2.10 to express eq. 2.4 in terms of dynamic pressure

$$\rho_o \frac{\partial^2 \vec{x}}{\partial t^2} = -\nabla p.$$

(2.21)

Taking the second time derivative of eq. 2.8 and equating it to the divergence of eq. 2.21 yields the relation

$$\rho_o \frac{\partial^2 S_{dyn}}{\partial t^2} = \nabla^2 p.$$

(2.22)

In [56] Nimmagadda and Cipolla derived a cavitation model for eq. 2.22. This cavitation model coupled with the pressure formulation are used in the commercial finite element code ABAQUS [32,59]. Both [32] and [59] define a dynamic "pseudo pressure" that replaces the use of condensation in eq. 2.16. The dynamic pseudo pressure is defined as

$$p_e = -\rho_o c^2 \left(\nabla \cdot \vec{x}\right),$$

(2.23)

and represents the mass dilation in the fluid scaled by the square of the fluid sound speed [37,32]. From eqs. 2.8 and 2.16 we see the relation between pseudo pressure and dynamic densified condensation is simply, $s=p_e/c^2$. Thus replacing S_{dyn} in eq. 2.22 with the dynamic pseudo pressure gives

$$\frac{1}{c^2}\frac{\partial^2 p_e}{\partial t^2} = \nabla^2 p\,,$$

(2.24)

the governing equation for the pressure formulation for a cavitating acoustic fluid. The relationship between dynamic pressure and pseudo pressure is given by the same cavitation model as that used in the CAFE/CASE equations. The equation of state for p in eq. 2.24 is given by the same cavitation model used in eq. 2.18 transformed to relate dynamic pressure to the dynamic pseudo pressure. This modified equation of state is given in eq. 2.25.

$$p = \begin{cases} p_e\,, & \text{if } p_e > p^{cav} - p^H \\ p^{cav} - p^H\,, & \text{otherwise} \end{cases}.$$

(2.25)

Thus the final system of governing equations for the pressure formulation of a cavitating acoustic fluid is given by eqs. 2.24 and 2.25.

2.3.2 Scattered Field Model

Adopting the scattered field model outlined in Section 2.2.2 to the pressure formulation, given in eqs. 2.24 and 2.25, yields the following system of governing equations for the unknown pressure formulation scattered field variables

$$\frac{1}{c^2}\frac{\partial^2 p_{e-sc}}{\partial t^2} = \nabla^2 p_{sc}\,,$$

$$p_{sc} = \begin{cases} p_{e-sc}\,, & \text{if } p_{e-sc} > p^{cav} - \left(p^H + p_{inc}\right) \\ p^{cav} - \left(p^H + p_{inc}\right), & \text{otherwise} \end{cases}.$$

(2.26)

Recall that p_{inc} represents the dynamic pressure in the known incident field and that the dynamic field variables are determined by

$$p_e = p_{e-inc} + p_{e-sc},$$
$$p = p_{inc} + p_{sc}. \tag{2.27}$$

CHAPTER 3 FINITE/SPECTRAL ELEMENT MODELING

In the previous chapter we derived the governing equations for CAFE and CASE fluid models. In this chapter we give a more thorough introduction to the spectral element method and detail the discretization of the CAFE/CASE governing equations in both space and time. We also discuss the application of boundary conditions and the implementation of non-conformal fluid-structure coupling.

3.1 The Spectral Element Method

As described in Section 1.3.4 the spectral element method (SEM) is a combination of the finite element method (FEM) and traditional spectral methods. To illustrate the difference between SEM, FEM, and traditional spectral methods consider the spatial discretization of a 1D domain.

In FEM the spatial domain is discretized by dividing the domain into n_{el} non-overlapping elements. If these elements use linear interpolation, (e.g. the elements used in CAFE) this results in two interpolation nodes per element located at the geometric end points of the element. Improving the accuracy of the FE solution with linear elements requires the addition of elements in a process called h-refinement [60]. The accuracy of the FE solution can also be increased by increasing the order of the polynomial interpolation over each element. If N is the order of the element interpolation polynomial, this results in an individual element having two internodes at the geometric end points of the element and N-1 interior nodes. Improving the accuracy of the FE solution through use of higher order polynomials is called p-refinement [60].

Traditional spectral methods discretize the spatial domain by using high order orthogonal polynomials without sub-division into elements. For a polynomial of order N this results in N+1 interpolation nodes which are located at the roots of the orthogonal polynomial [61,62]. This choice of interpolation node locations allows for the highest possible accuracy for a given polynomial order [60,62]. Unlike FEM which can use both h and p-refinement to increase accuracy, traditional spectral methods can only use p-refinement. The term spectral refers to the fact that for a given polynomial the numerical error will decrease faster than any power of $1/N$ [60].

In SEM the spatial domain is discretized by dividing the domain into n_{el} elements to retain the geometric flexibility of FEM [62,63]. Like high order finite elements, SEM uses high order interpolation polynomials over the elements. The difference between SEM and high order finite elements is the choice of element interpolation nodes. Like traditional spectral methods, to reduce interpolation error over an element SEM takes the element interpolation nodes as the roots of orthogonal polynomials [44]. High order finite elements typically use evenly spaced element interpolation nodes [60].

To demonstrate the difference between interpolation with evenly spaced nodes and nodes defined by the roots of orthogonal polynomials we use Lagrange interpolation to approximate two example functions over the interval [-1,1] [60]. For the interpolation nodes defined by the roots of orthogonal polynomials, we use a Lobatto interpolation node distribution. The Lobatto interpolation nodes are defined by [60] the roots of the N-1 order Lobatto polynomial and the endpoints of the [-1,1] interval as given in eq. 3.1.

$$(1-x^2)L_{O_{N-1}}(x)=0\,. \tag{3.1}$$

Figures 3.1a and 3.1b show, respectively, the N=4 and N=8 interpolating polynomials for the function

$$f(x)=\frac{1}{1+5x^2}\,. \tag{3.2}$$

using evenly spaced interpolation nodes and the Lobatto node distribution. As a measure of accuracy the L_2 error norm defined by eq. 3.3 is given in parenthesis in the legend for each nodal distribution in Fig. 3.1.

$$\mathrm{L}_2=\frac{\sqrt{\int_{-1}^{1}\left[f(x)-P(x)\right]^2\,dx}}{\sqrt{\int_{-1}^{1}\left[f(x)\right]^2\,dx}}, \tag{3.3}$$

Note in eq. 3.3 $P(x)$ is the interpolating polynomial of *f(x)*. Comparison of the L_2 norms in Fig. 3.1 shows for both the *N*=4 and *N*=8 interpolating polynomial the Lobatto nodal base gives superior results. Furthermore, oscillations near the end points of the domain, the Runge effect [60], occur for the evenly spaced interpolation nodes. Comparing Fig. 3.1a to 3.1b, these oscillations grow larger as the order of the interpolating polynomial is increased. Note that even with the presence of oscillations, the error norm is still decreased by increasing the polynomial order on the Lobatto grid. However, this is not always the case for interpolation with evenly spaced nodes.

Figure 3.2 shows the interpolating polynomials for the function

$$f(x) = \frac{1}{1+25x^2}, \tag{3.4}$$

using the same evenly spaced and Lobatto interpolation node distributions as in the previous example. In this example the Runge effect oscillations for the evenly spaced node distribution are more severe, especially for the *N*=8 polynomial.

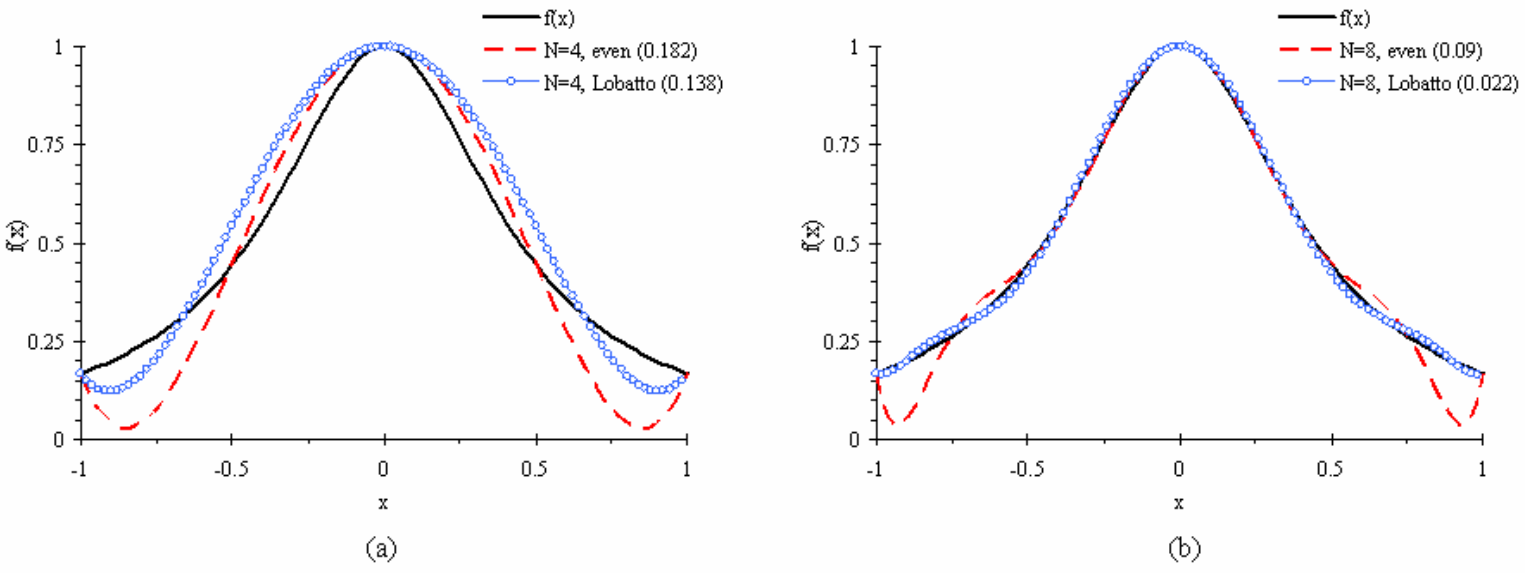

Figure 3.1 Polynomial interpolation of the function $f(x) = \frac{1}{1+5x^2}$ using an evenly spaced and Lobatto node distribution

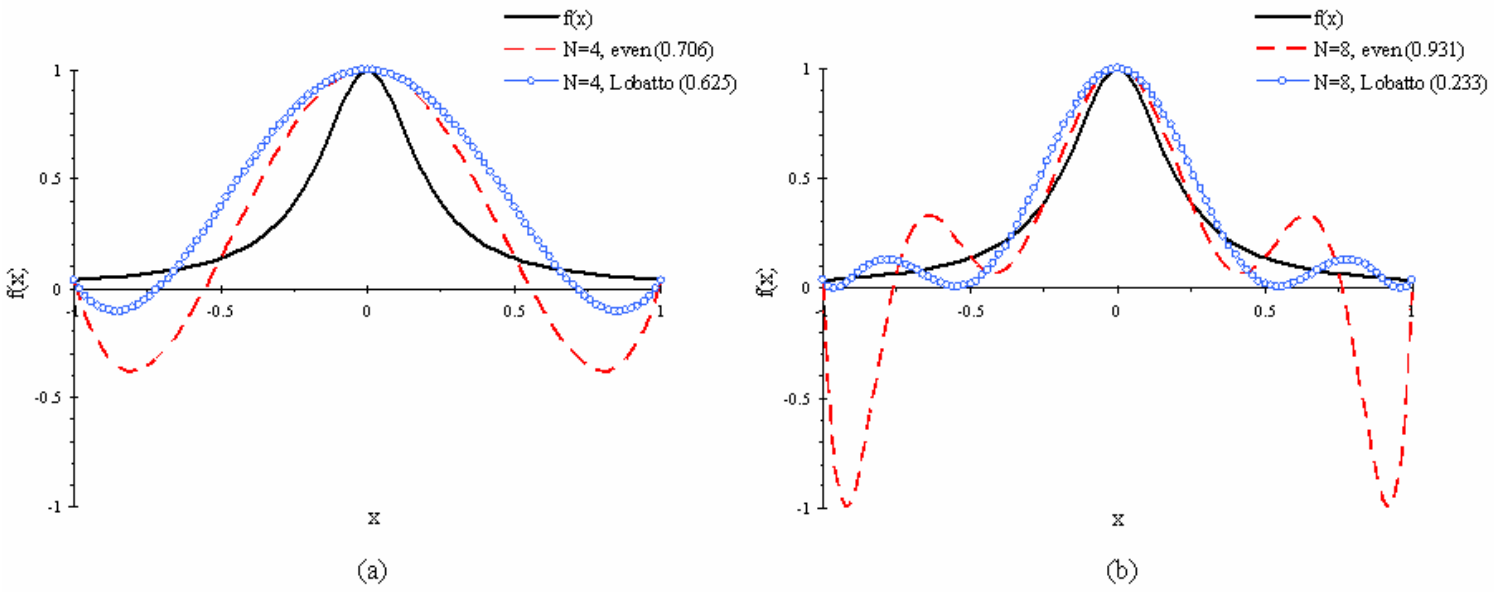

Figure 3.2 Polynomial interpolation of the function $f(x) = \frac{1}{1+25x^2}$ using an evenly spaced and Lobatto node distribution

Looking at the error norms we see increasing the polynomial order from four to eight for the evenly spaced node distribution results in a 0.225 increase in the L_2 error norm. In contrast, increasing the polynomial order from four to eight using the Lobatto node distribution results in a 0.392 reduction in the L_2 error norm.

In application to acoustic wave propagation problems, the interpolation properties of high order spectral elements result in a decrease in the number of nodes per wavelength required to correctly propagate the impulse of a wave [61,64]. Furthermore, when compared to linear finite elements, spectral elements offer a decrease in numerical dispersion error [63]. For acoustic wave propagation, both Lobatto [46,61,64,65] and Chebyshev [46,63,64] nodal bases have been studied, with Lobatto nodal bases being preferred for explicit schemes, such as CASE [26,44,46,61,65].

The main caveat in the application of spectral elements to wave propagation problems is the tendency to increase oscillations along the wave form [26,46]. There are two main sources of increased oscillation in spectral element methods. The first is the appearance of spurious modes, which are investigated for both Chebyshev and Lobatto nodal bases in [46]. The conclusion of [46] was that the decreased numerical dispersion

error overcomes the contribution of spurious modes to the total error of the solution. The second source of increased oscillation in the application of spectral elements to wave propagation problems is the Gibbs phenomenon error introduced by interpolation of discontinuities on interior element nodes [47]. This source of increased oscillations is of particular interest in far-field UNDEX problems which must treat sharp gradients resulting from the incident shock wave and cavitation region boundaries. A demonstration of oscillations due to Gibbs phenomenon is given in Fig.3.3, where the Heavisde function H(x) is interpolated over the interval [-1,1] using the Lobatto nodal base (eq. 3.1). Clearly as the polynomial order is increased more oscillations occur in the interpolating functions. However, examination of the L_2 error norms provided in the legend of Fig. 3.3 show that even with the increase in oscillation, increasing the polynomial order still reduces the error of the interpolation in the L_2 norm.

In Chapters 5 and 6 we determine if this finding holds when spectral elements are applied to far-field UNDEX problems by examining error norms for the propagation of a step exponential wave and fluid-structure interaction problems with cavitation.

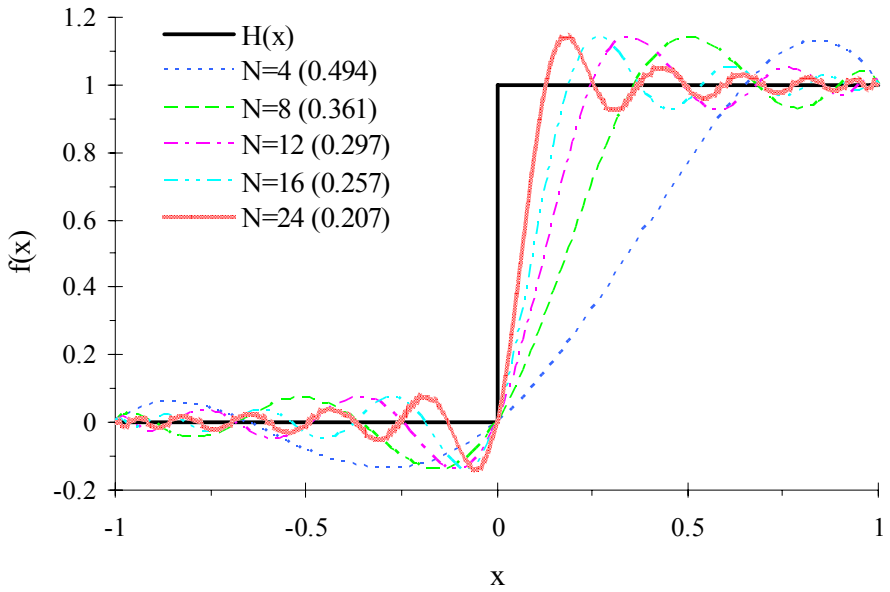

Figure 3.3 Polynomial interpolation of the Heaviside function using a Lobatto node distribution

3.2 CASE Discretization

3.2.1 Total Field Model

In this section we present the discretization of the CASE governing equations using the spectral element method described in the previous section. Recall from Chapter 2 the system of CASE governing equations for the total field fluid model [22,26]

$$s = \nabla^2 \psi ,$$

$$\frac{\partial^2 \psi}{\partial t^2} = \begin{cases} c^2 s, & if\ s > \left(p^{cav} - p_{eq}\right)/c^2 \\ p^{cav} - p_{eq}, & otherwise \end{cases} . \tag{3.5}$$

Following [26,44,45] eq. 3.5 is solved numerically by first applying the standard Galerkin approach [e.g. see 66] to the CASE strain-displacement equation (the first relation in eq. 3.5). Pre-multiplying the strain-displacement equation by test function $\boldsymbol{\varphi}$ and integrating over the fluid domain Ω_f gives

$$\int_{\Omega_f} \left[s\boldsymbol{\varphi} - \nabla^2 \psi \boldsymbol{\varphi} \right] d\Omega = 0 . \tag{3.6}$$

Applying Green's first identity to eq. 3.6 yields the weak form of the strain-displacement equation

$$\int_{\Omega_f} s\boldsymbol{\varphi}\, d\Omega + \int_{\Omega_f} \nabla \psi \cdot \nabla \boldsymbol{\varphi}\, d\Omega = \int_{\Gamma_f} \boldsymbol{\varphi} \nabla \psi \cdot \vec{n}\, d\Gamma , \tag{3.7}$$

where Γ_f denotes the fluid boundary in domain and $\vec{n}$ is the outward pointing normal vector on Γ_f. We approximate the solution to eq. 3.7 as in [26] by dividing the domain into n_{nel} non-overlapping hexagonal elements using a sub-parametric discretization. In the sub-parametric discretization, standard linear basis functions are used for the element geometry and higher order spectral basis functions are used to approximate the dependent variables in eq. 3.7. Thus, densified condensation and displacement potential can be written over an element as [26]

$$s(\xi,\eta,\zeta,t) = \boldsymbol{\varphi}^T \mathbf{s}(t) = \sum_{i,j,k=1}^{N+1} \phi_i(\xi)\phi_j(\eta)\phi_k(\zeta) s_{ijk}(t),$$

(3.8)

$$\psi(\xi,\eta,\zeta,t) = \boldsymbol{\varphi}^T \boldsymbol{\psi}(t) = \sum_{i,j,k=1}^{N+1} \phi_i(\xi)\phi_j(\eta)\phi_k(\zeta) \psi_{ijk}(t),$$

(3.9)

where $\boldsymbol{\varphi}$ is a column vector of the 1D spectral basis functions $\phi_i(\xi)\phi_j(\eta)\phi_k(\zeta)$ of order *N*, **s** and $\boldsymbol{\psi}$ are column vectors of the time dependent nodal values $s_{ijk}(t)$ and $\psi_{ijk}(t)$, and ζ, η, ξ are the local element coordinates (ξ, η, ζ ∈ [-1,1]).

For CASE, Sprague and Geers [26] use a Gauss-Lobatto-Legendre (GLL) element node distribution given by the roots of

$$(1-\xi^2) L'_N(\xi) = 0,$$

(3.10)

where L'_N is the first derivative of the *N*-th degree Legendre polynomial with respect to the argument. Note due to the relation [60]

$$Lo_N(\xi) = L'_{N+1}(\xi),$$

(3.11)

between Lobatto and Legendre polynomials, the GLL node base is equivalent to the Lobatto base (eq. 3.1) used in Section 3.1.

The spectral basis functions in eqs. 3.8 and 3.9 are found using Lagrange interpolation via the relation

$$\phi_i(\xi) = -\frac{(\xi^2-1)L'_N(\xi)}{N(N+1)L_N(\xi_i)(\xi-\xi_i)} \quad i = 1,2,\ldots N+1 \ ,$$

(3.12)

where ξ_i is the *i*-th GLL node and $\phi_i(\xi_j) = \delta_{ij}$ [26,60]. The local derivatives of the spectral basis functions are evaluated at the GLL nodes using the relation given by [65]

$$\left.\frac{\partial \phi_i}{\partial \xi}\right|_{\xi=\xi_i} = \begin{cases} \dfrac{L_N(\xi_j)}{L_N(\xi_i)}\dfrac{1}{\xi_j - \xi_i}, & i \neq j \\ -\dfrac{(N+1)N}{4}, & i = j = 1 \\ \dfrac{(N+1)N}{4}, & i = j = N \\ 0, & otherwise \end{cases}, \quad \begin{matrix} i = 1,2,\ldots N+1 \\ j = 1,2,\ldots N+1 \end{matrix},$$

(3.13)

Substitution of the discretization scheme given in eqs. 3.8 and 3.9 into the weak form of the CASE strain-displacement equation gives the matrix equation [26]

$$\mathbf{Qs} + \mathbf{H}\boldsymbol{\psi} = \mathbf{b},$$

where

$$\mathbf{Q} = \int_{\Omega_f} \boldsymbol{\varphi}\boldsymbol{\varphi}^T \, d\Omega, \quad \mathbf{H} = \int_{\Omega_f} \nabla\boldsymbol{\varphi} \cdot \nabla\boldsymbol{\varphi}^T \, d\Omega, \quad \mathbf{b} = \int_{\Gamma_f} \boldsymbol{\varphi} \nabla\psi \cdot \vec{n} \, d\Gamma,$$

(3.14)

where **Q** is the global capacitance matrix, **H**, is the global reactance matrix, and **b** is the global fluid force vector. The integrals in eq. 3.14 are evaluated using the spectral basis functions given in eqs. 3.10 and 3.13 with GLL integration quadrature [26]. This treatment makes the element nodes and quadrature points coincident, which automatically lumps the capacitance matrix, **Q**. Note that, as originally done in CAFE [22], and latter for CASE [26,44,45], the global reactance matrix, **H**, is not explicitly calculated and stored. Instead, the product $\mathbf{H}\boldsymbol{\psi}$ is evaluated element-by-element.

The equation of state in the CASE system of governing equations, eq. 3.5 is evaluated in a node-by-node fashion for the discretized system. Thus at node *i* the equation of state becomes [26,44]

$$\ddot{\boldsymbol{\psi}}\big|_i = \begin{cases} c^2 \mathbf{s}\big|_i, & if \quad \mathbf{s}\big|_i > \left(p^{cav} - p_{eq}\big|_i\right)/c^2 \\ p^{cav} - p_{eq}\big|_i, & otherwise \end{cases} \quad i = 1,2,\ldots n_{node},$$

(3.15)

where we use $\big|_i$ to denote evaluation of a variable at node *i*, n_{node} is the total number of nodes.

3.2.2 Scattered Field Model

In Chapter 2, we gave the CAFE/CASE system of governing equations for the scattered field model as [26,44]

$$s_{sc} = \nabla^2 \psi_{sc},$$

$$\frac{\partial^2 \psi_{sc}}{\partial t^2} = \begin{cases} c^2 s_{sc}, & if\ s_{sc} > \left[p^{cav} - \left(p^H + p_{inc}\right)\right]/c^2 \\ p^{cav} - \left(p^H + p_{inc}\right), & otherwise \end{cases}. \tag{3.16}$$

Equation 3.16 is solved numerically using the same discretization procedure as that used for the total field model. The resulting matrix equation is [26,44]

$$\mathbf{Q}\mathbf{s}_{sc} + \mathbf{H}\boldsymbol{\psi}_{sc} = \mathbf{b},$$

where

$$\mathbf{Q} = \int_{\Omega_f} \boldsymbol{\varphi}\boldsymbol{\varphi}^T \, d\Omega, \quad \mathbf{H} = \int_{\Omega_f} \nabla\boldsymbol{\varphi} \cdot \nabla\boldsymbol{\varphi}^T \, d\Omega, \quad \mathbf{b} = \int_{\Gamma_f} \boldsymbol{\varphi} \nabla \psi_{sc} \cdot \vec{n} \, d\Gamma, \tag{3.17}$$

where integrals in 3.17 and the product $\mathbf{H}\boldsymbol{\psi}_{sc}$ are evaluated as in the total field model. The scattered field model equation of state for the discretized system becomes [26,44]

$$\ddot{\boldsymbol{\psi}}_{sc}\big|_i = \begin{cases} c^2 \mathbf{s}_{sc}\big|_i, & if \quad \mathbf{s}_{sc}\big|_i > \left[p^{cav} - \left(p_{eq}\big|_i + p_{inc}\big|_i\right)\right]/c^2 \\ p^{cav} - \left(p_{eq}\big|_i + p_{inc}\big|_i\right), & otherwise \end{cases} \qquad i = 1,2,\ldots n_{node}, \tag{3.18}$$

where $p_{inc}\big|_i$ is the known incident pressure evaluated at node *i*.

3.3 Boundary Conditions

For far-field UNDEX, there are three types of boundaries that are applied to eqs. 3.14 and 3.17: known pressure, fluid-structure interaction, and non-reflecting (NRB) boundaries. For fluid-structure interaction problems, that require a NRB we apply a scattered field fluid model in this work. Thus, the boundary conditions presented in this section are for the scattered field model only. Details on the application of fluid-structure

interaction conditions and NRBs for CAFE and CASE total field models are given in [22] and [26,67].

The CAFE/CASE essential boundary conditions are the known pressure boundaries, where p is known for all time. An example is the scattered field model fluid free surface boundary condition,

$$p_{sc} = -p_{inc}\,. \tag{3.19}$$

The fluid-structure interaction and non-reflecting boundary terms are natural boundary conditions governed by the fluid force vector, **b**, in eq. 3.17. The fluid force vector can be expressed as [22,26]

$$\mathbf{b} = \mathbf{b}^{s} + \mathbf{b}^{nrb}\,, \tag{3.20}$$

a combination of the force of the structure on the fluid, $\mathbf{b}^{s}$, and the force of the NRB on the fluid, $\mathbf{b}^{nrb}$. The force of the structure on the fluid is evaluated using the continuity of normal velocities/displacements along the fluid-structure interface. Following [22,26] we approximate the normal velocity/displacement continuity condition using the relation

$$\frac{\partial \psi_{sc}}{\partial n} = -\rho_o \vec{x}^{s}_{sc} \cdot \vec{n}^{s}\,, \tag{3.21}$$

where $\vec{x}^{s}_{sc}$ is the scattered displacement of the structure and $\vec{n}^{s}$ is the normal to the structure surface taken as positive into the fluid. The scattered displacement of the structure is found by subtracting the total structure displacement from the known incident displacement [26]. Using the relation $x^{s}_{sc} = \vec{x}^{s}_{sc} \cdot \vec{n}^{s}$ we substitute eq. 3.21 into the relation for the force vector in eq. 3.17 to obtain the force of the structure on the fluid [26]

$$\mathbf{b}^{s} = -\rho_o \int_{\Gamma_{fs}} \phi \mathbf{x}^{s}_{sc}\, d\Gamma \quad , \tag{3.22}$$

where $\mathbf{x}^{s}_{sc}$ is a column vector of scattered normal displacements on the fluid-structure boundary and Γ_{fs} is the surface that makes up the fluid-structure boundary.

On the NRB, eq. 3.21 becomes

$$\frac{\partial \psi_{sc}}{\partial n} = -\rho_o \vec{x}_{sc}^{nrb} \cdot \vec{n}^{nrb},$$

(3.23)

where, $\vec{x}_{sc}^{nrb}$, the scattered displacement of the NRB, and ,$\vec{n}^{nrb}$,is the NRB normal, taken as positive into the fluid. If we let, $x_{sc}^{nrb} = \vec{x}_{sc}^{nrb} \cdot \vec{n}^{nrb}$, then x_{sc}^{nrb} is determined by the non-reflecting boundary condition applied to, Γ_{nrb}, the surface that makes up the NRB [26]. For this work we apply the plane wave approximation (PWA) on the NRB surface but others such as the curved wave approximation [32,26] and the doubly asymptotic approximation [2,8,20,21,22,25] are applicable as well. In [68] it was determined use of the PWA instead of the more complex DAA gave very similar results and significant savings in computational time for the box barge UNDEX problem in [8]. Applying the PWA, x_{sc}^{nrb} is given by [22]

$$x_{sc}^{nrb} = \frac{1}{\rho_o c} p_{sc}^{*},$$

(3.24)

where the * superscript denotes temporal integration. Writing eq. 3.23 for nodes on the NRB in discrete form yields

$$\mathbf{x}_{sc}^{nrb} = \frac{1}{\rho_o c} \mathbf{p}_{sc}^{*},$$

(3.25)

where $\mathbf{x}_{sc}^{nrb}$ is a column vector of the scattered normal NRB displacements and $\mathbf{p}_{sc}$ is a column vector of scattered pressure [67]. Using eqs. 3.23 and 3.25, the force vector for the NRB, $\mathbf{b}^{nrb}$, becomes [67]

$$\mathbf{b}^{nrb} = -\rho_o \int_{\Gamma_{nrb}} \phi \phi^T \mathbf{x}_{sc}^{nrb} d\Gamma \quad .$$

(3.26)

3.4 Non-conformal Fluid-Structure Coupling

One of the improvements incorporated into CASE by Sprague and Geers [26,45] was the use of non-conformal fluid-structure coupling to remove the requirement for one to one nodal coupling. Such a coupling scheme allows the fluid to be refined independent of the structure which simplifies coupling the fluid to the structure and is less computationally expensive when the structure is solved explicitly. Following [26], the methodology to coupling the fluid to the structure begins with the creation of a structure mesh and a base fluid mesh. The structure mesh should be refined such that an accurate solution of the structural equations of motion is obtained. The base fluid must be coincident with the elements of the structural mesh along the fluid-structure boundary, Γ^e_{fs}, where the superscript, e, denotes an individual element. This is illustrated in Fig. 3.4 which shows the coupling of a single structural element to a single base fluid element. Note that the coupling of the base fluid mesh to the structure mesh represents one-to-one nodal coupling along the fluid-structure interface.

Figure 3.4 Coupling of the base structure mesh along the structure-fluid boundary, Γ^e_{sf}, to the base fluid mesh along the fluid-structure boundary, Γ^e_{fs}

Coupling of the structure mesh to the base fluid mesh defines a new surface, Γ^e_c, over each coupled fluid-structure element called the coupling membrane [69]. For each element in the base mesh, the coupling membrane defines the area of the fluid that is coupled to a given structural element. This is illustrated in Fig. 3.5, where there is a single structural element on Γ_{sf} but the fluid has been refined such that five fluid nodes lie on Γ_{fs}. Note the fluid mesh in Fig. 3.5a is refined using h-refinement and the fluid mesh in figure 3.5b is refined using p-refinement. Using the coupling membrane as a guide, information from the fluid nodes is used to determine the loading on the single structural element while information from the single structural element is used to determine the loading on the five fluid nodes coupled to the that structural element. For example, the

pressure from the fluid nodes can be integrated over the surface of the coupling membrane and applied to the structural nodes. Similarly, the displacement of the structure at any point on the coupling membrane may be found via interpolation and applied to the fluid nodes [26]. Following [26,67], in this work the coupling scheme is simplified by using the average structural displacement and fluid pressure over the coupling membrane to transfer loads between the fluid and structure.

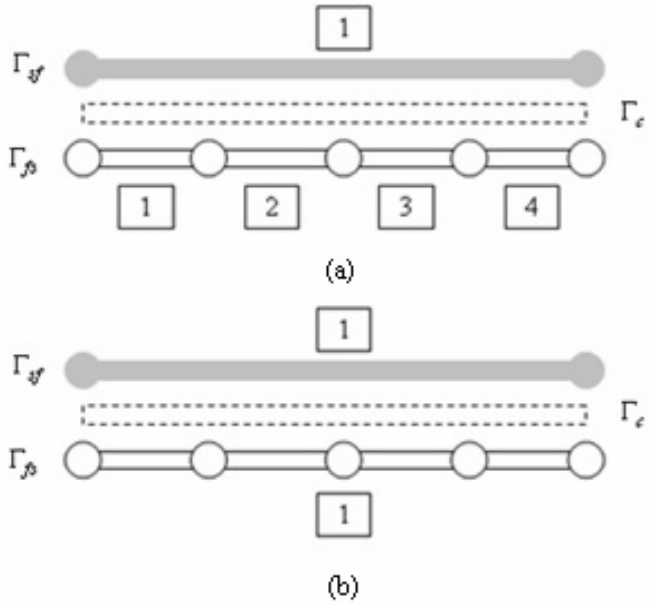

Figure 3.5 Coupling of the base structure mesh to a refined fluid mesh using h-refinement (a) and p-refinement (b)

3.4.1 Non-conformal Structure Loading

The FE equation for the motion of an un-damped elastic the structure can be expressed as

$$\mathbf{M}\ddot{\mathbf{x}}^s + \mathbf{K}\mathbf{x}^s = \mathbf{f}\,, \tag{3.27}$$

where **M** is the consistent mass matrix, **K** the stiffness matrix, and **f** the force vector. The force vector consists of three components that correspond to the global Cartesian coordinates [*X, Y, Z*]. Thus, from the continuity of interface traction the force the fluid exerts on the structure can be expressed as [27]

$$\mathbf{f}_i = \int_{\Gamma_{sf}} N\mathbf{p}\vec{n}^f \, d\Gamma \ ,$$

(3.28)

where N is a column vector of the structure shape functions, $\mathbf{p}$ is a column vector of the dynamic pressure at the fluid nodes on Γ_{sf}, i is the global Cartesian coordinate direction and $\vec{n}^f$ is a normal vector on Γ_{sf} taken as positive out of the fluid. The non-conformal coupling scheme outlined in the previous section uses the average dynamic pressure, $\overline{p}^e$, over Γ^e_{sf} to force the structure [26,67]. Thus, when the coupling scheme is applied to eq. 3.28, the force on the structure becomes [26]

$$\mathbf{f}_i^e = \gamma_i^e \int_{\Gamma^e_{sf}} N\overline{p}^e \, d\Gamma \quad i \in [X, Y, Z],$$

(3.29)

on an element level, where the index i is the global Cartesian coordinate direction, γ_i^e is the cosine of the angle between $\vec{n}^f$, and the i-th global coordinate direction.

3.4.2 Non-conformal Fluid Loading

Using the non-conformal coupling scheme, the element level fluid force vector for $\mathbf{b}^s$ becomes

$$\mathbf{b}^{s,e} = -\rho_o \int_{\Gamma^e_{fs}} \phi \overline{x}^{s,e}_{sc} \, d\Gamma \ ,$$

(3.30)

where the term $\overline{x}^{s,e}_{sc}$, represents the average scattered normal structural displacement calculated at the center of each structure element on Γ^e_{sf} [26].

3.5 Solution Methodology

3.5.1 Artificial Damping

In Section 1.3.5, the concept of frothing or the appearance of spurious oscillations, called frothing, due to cavitation formation was introduced. To reduce frothing both

CAFE and CASE employ artificial damping that increases with frequency. Artificial damping is added to the governing equations by adding the damping term [22],

$$\beta \Delta t\, c^2 \dot{s}\,, \tag{3.31}$$

to the relation $\ddot{\psi} = p$, such that it becomes

$$\ddot{\psi} = p + \beta \Delta t\, c^2 \dot{s}\,, \tag{3.32}$$

for the total field model and

$$\ddot{\psi}_{sc} = p_{sc} + \beta \Delta t\, c^2 \dot{s}_{sc}\,, \tag{3.33}$$

for the scattered field model. The amount of damping applied is determined by the dimensionless coefficient, $\beta \in [0,1]$. The damping coefficient, β, is a numerical parameter that is selected based on the sensitivity of the structure to frothing in the fluid. Typically (see Section 5.1.3) β is selected between 0.25 and 1.0 [22,26].

The beneficial effect of this damping parameter is the smoothing of dispersive ripples caused by the short-wavelength components of traveling waves and the suppression of frothing. The negative side effect is the smearing of sharp wave fronts, such as those present in the incident shock wave and cavitation boundaries, and the dissipation of wave magnitude. We investigate the severity of both of these effects in Chapters 5 and 6.

3.5.2 Temporal Discretization

The CAFE/CASE governing equations are integrated in time using a staggered explicit central difference scheme developed by Felippa and DeRuntz [22,25]. The structure equation of motion may be integrated using an implicit scheme as in [22] or an explicit scheme as in [26,45,67]. In this section, we present the general methodology for solution of the CAFE/CASE scattered field model governing equations when coupled to an explicitly solved structure. The procedure begins with the calculation of the equilibrium pressure vector $\mathbf{p}_{eq}$ (taken as the combination of hydrostatic pressure and atmospheric pressure [26]) and initial incident pressure vector $\mathbf{p}^0_{inc}$ for all fluid nodes. Then following [67] the time integration scheme proceeds as follows:

1) Solve for the structural displacement at time t^n using central difference time integration:

$$\mathbf{x}^{s,n} = \mathbf{x}^{s,n-1} + \Delta t \dot{\mathbf{x}}^{s,n-1} + \frac{\Delta t^2}{2} \ddot{\mathbf{x}}^{s,n-1},$$

$$\ddot{\mathbf{x}}^{s,n} = \widetilde{\mathbf{M}}^{-1}\left(-\mathbf{K}\mathbf{x}^{s,n} + \mathbf{f}^n\right),$$

$$\dot{\mathbf{x}}^{s,n} = \dot{\mathbf{x}}^{s,n-1} + \frac{\Delta t}{2}\left(\ddot{\mathbf{x}}^{s,n} + \ddot{\mathbf{x}}^{s,n-1}\right),$$

(3.34)

where from eqs. 3.28 and 3.29

$$\mathbf{f}_i^n = \gamma_i \int_{\Gamma_{sf}} N \overline{p}^n \, d\Gamma \, .$$

(3.35)

Note that for central time integration the structure mass matrix must be lumped, which is denoted in eq. 3.34 by $\widetilde{\mathbf{M}}$.

2) Predict the NRB displacement at time t^{n+1} using the PWA (eq. 3.25)

$$\Delta x_{sc-pred}^{nrb} = \frac{\Delta t}{\rho_o c} \mathbf{p}_{sc}^n,$$

$$\mathbf{x}_{sc\text{-}pred}^{nrb,n+1} = \mathbf{x}_{sc}^{nrb,n} + \Delta x_{sc-pred}^{nrb} \, .$$

(3.36)

Using eq. 3.36 and the structural displacement found in eq. 3.34 the fluid force vector at time t^{n+1} becomes

$$\mathbf{b}^{n+1} = -\rho_o \int_{\Gamma_{fs}} \phi \overline{x}_{sc}^{s,n} \, d\Gamma - \rho_o \int_{\Gamma_{nrb}} \phi \phi^T \mathbf{x}_{sc-pred}^{nrb,n+1} \, d\Gamma \quad .$$

(3.37)

3) Apply eq 3.37 and update the fluid equations at time t^{n+1}

$$\dot{\mathbf{s}}_{sc} = \frac{\left(\mathbf{s}_{sc}^n - \mathbf{s}_{sc}^{n-1}\right)}{\Delta t},$$

$$\dot{\boldsymbol{\psi}}_{\boldsymbol{sc}}^{\boldsymbol{n+1}} = \dot{\boldsymbol{\psi}}_{\boldsymbol{sc}}^{\boldsymbol{n}} + \Delta t\left(\mathbf{p}_{sc}^n + \beta \Delta t c^2 \dot{\mathbf{s}}_{sc}\right),$$

$$\boldsymbol{\psi}_{sc}^{n+1} = \boldsymbol{\psi}_{sc}^{n} + \Delta t \dot{\boldsymbol{\psi}}_{sc}^{n+1},$$
$$\mathbf{s}_{sc}^{n+1} = \mathbf{Q}^{-1}\left(-\mathbf{H}\boldsymbol{\psi}_{sc}^{n+1} + \mathbf{b}^{n+1}\right).$$

(3.38)

Apply equation of state to update $\mathbf{p}_{sc}^{n+1}$

$$\mathbf{p}_{sc}^{n+1}\Big|_i = \begin{cases} c^2 \mathbf{s}_{sc}^{n+1}\Big|_i, & \text{if } \mathbf{s}_{sc}^{n+1}\Big|_i > \left[p^{cav} - \left(\mathbf{p}_{eq}\Big|_i + \mathbf{p}_{inc}^{n+1}\Big|_i\right)\right]/c^2 \\ p^{cav} - \left(\mathbf{p}_{eq}\Big|_i + \mathbf{p}_{inc}^{n+1}\Big|_i\right), & \text{otherwise} \end{cases} \quad i = 1,2,\ldots n_{node}\ .$$

(3.39)

4) Correct the NRB displacement at time t^{n+1} using the updated scattered pressures on the NRB

$$\Delta \mathbf{p}_{sc}^{*} = \frac{\Delta t}{2}\left(\mathbf{p}_{sc}^{n+1} + \mathbf{p}_{sc}^{n}\right),$$
$$\mathbf{p}_{sc}^{*\,n+1} = \mathbf{p}_{sc}^{*\,n+1} + \Delta \mathbf{p}_{sc}^{*},$$
$$\mathbf{x}_{sc}^{nrb,\,n+1} = \mathbf{x}_{sc}^{nrb,\,n} + \frac{1}{\rho_o c}\Delta \mathbf{p}_{sc}^{*}.$$

(3.40)

Felippa and DeRuntz give a detailed stability analysis of the CAFE/CASE integration scheme presented above in [22]. The resulting critical time step is

$$\Delta t_{crit} = \frac{2}{c\sqrt{\lambda_{\max}\left(1 + 2\beta\right)}},$$

(3.41)

where $\lambda_{\max}$ is the maximum fluid mesh egienvalue that is determined using Gerschgorin's theorem as described in [26] for CASE or by estimation based on smallest element dimension as described in [25] for CAFE (note the method in [25] is based on the use of a lumped mass matrix).

CHAPTER 4 FLUX-CORRECTED TRANSPORT MODELING

4.1 Flux-Corrected Transport Algorithm

Given the errors associated with the application of spectral elements to problems with steep gradients one of the objectives of this work is to study a method that combines the less oscillatory nature of linear finite elements with the superior wave propagation properties of high order spectral elements. The literature review revealed one such method to be flux-corrected transport (FCT).

A general representation of the original FCT algorithm devised by Boris and Book [49] for finite difference methods and extended to FEM by Xiao [57] is given below. Following Xiao's routine, let Ξ be a function of time and space in one-dimension. The value of Ξ at time step $n+1$ and location x (represented by the index j) is written as

$$\Xi_j^{n+1} = f\left(\Xi_j^n, \Delta t, h_e\right), \tag{4.1}$$

a function of the value of Ξ_j at time step n, the time step Δt, and element length h_e. The FE-FCT algorithm consists of the following steps:

1. Compute transported solution by FE approximation of Ξ_j at time step $n+1$:

$$\widetilde{\Xi}_j^{n+1} = f\left(\Xi_j^n, \Delta t, h_e\right). \tag{4.2}$$

2. Compute the diffusive fluxes:

$$\Phi_j^D = \eta_D\left(\Xi_{j+1}^n - \Xi_j^n\right), \tag{4.3}$$

where η_D is the diffusion coefficient.

3. Compute the transported diffused solution:

$$\Xi_j^{TD} = \widetilde{\Xi}_j^{n+1} + \Phi_j^D - \Phi_{j-1}^D. \tag{4.4}$$

4. Compute the anti-diffusive fluxes:

$$\Phi_j^A = \eta_A\left(\widetilde{\Xi}_{j+1}^n - \widetilde{\Xi}_j^n\right),$$

(4.5)

where η_A is the anti-diffusion coefficient.

5. Limit/correct the anti-diffusive fluxes:

$$\Phi_j^C = \chi \cdot \max\left\{0, \min\left(\chi \cdot \Delta_{j-1}, \left|\Phi_j^A\right|, \chi \cdot \Delta_{j+1}\right)\right\},$$

(4.6)

where $\Delta_{j\pm1} = \pm\left(\Xi_{j\pm1}^{TD} - \Xi_j^{TD}\right)$ and $\chi = sign\left(\Phi_j^A\right)$

6. Apply the corrected anti-diffusive fluxes to the solution:

$$\Xi_j^{n+1} = \Xi_j^{TD} - \Phi_j^C + \Phi_{j-1}^C.$$

(4.7)

The key component of any FCT algorithm is the limiting of the anti-diffusive fluxes to determine the corrected flux, Φ^C. In Xiao's algorithm this is accomplished using the limiter given in eq. 4.6, which is referred to as a strong flux limiter [70]. To understand how the strong flux limiter determines the corrected fluxes consider the following scenarios for calculating the corrected flux at location *j* pictured in Fig. 4.1. Assuming $\chi > 0$, in situation (a) no minimum or maximum exists thus the corrected flux is non-zero and anti-diffusion is added to the solution at point *j*. In situations (b) and (c) there are a maximum and minimum, respectively, at location *j*. To prevent the growth of these maximum and minimum the corrected flux is set to zero and the corrected variable at point *j* is fully diffused [50]. Further explanations of strong flux limiting can be found in [50,70].

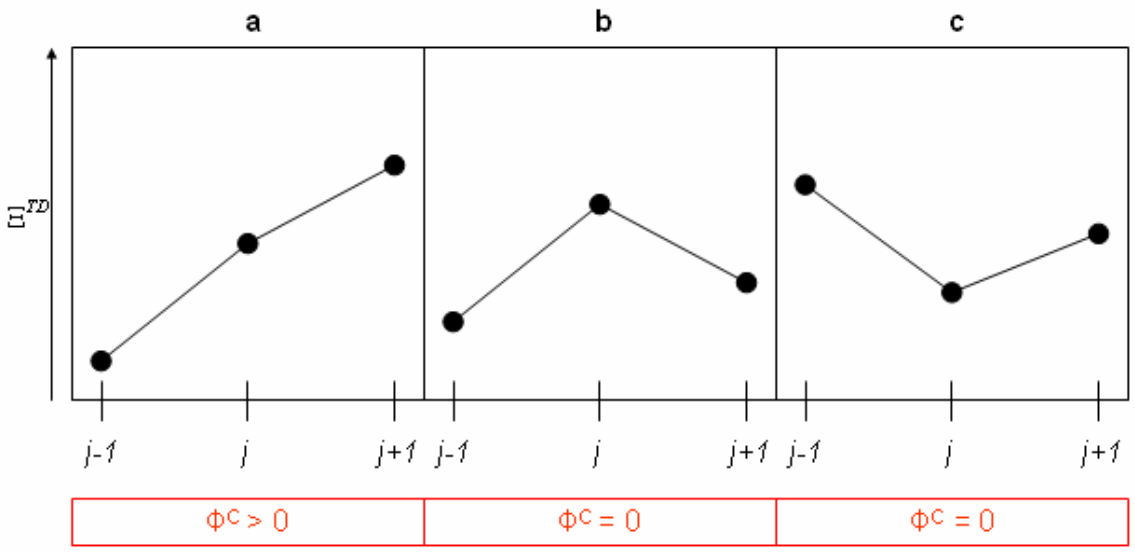

Figure 4.1 Example actions of a strong flux limiter

4.2 Discretization of the Pressure Formulation

4.2.1 Total Field Model

To implement Xiao's FE-FCT algorithm in a far-field UNDEX model, the pressure form of the acoustic wave equation is used. Recall from Chapter 2 that for a cavitating fluid the pressure form of the acoustic wave equation is expressed as

$$\frac{1}{c^2}\frac{\partial^2 p_e}{\partial t^2} = \nabla^2 p, \tag{4.8}$$

where p is given by

$$p = \begin{cases} p_e, & \text{if } p_e > p^{cav} - p^H \\ p^{cav} - p^H, & \text{otherwise} \end{cases}. \tag{4.9}$$

Equation 4.8 is solved numerically using the standard Galerkin approach. Pre-multiplying eq. 4.8 by test function $\boldsymbol{\varphi}$ and integrating over the fluid domain Ω_f gives

$$\int_{\Omega_f} \left[\frac{1}{c^2} \frac{\partial^2 p_e}{\partial t^2} \boldsymbol{\varphi} + \nabla^2 p \boldsymbol{\varphi} \right] d\Omega .$$

(4.10)

Applying Green's first identity to eq. 2.43 yields the weak form of eq. 4.8

$$\frac{1}{c^2} \int_{\Omega_f} \ddot{p}_e \boldsymbol{\varphi} d\Omega + \int_{\Omega_f} \nabla p \cdot \nabla \boldsymbol{\varphi} d\Omega = \int_{\Gamma_f} \boldsymbol{\varphi} \nabla p \cdot \vec{n} d\Gamma ,$$

(4.11)

where again, Γ_f denotes the fluid boundary in domain and $\vec{n}$ is the outward pointing normal vector on Γ_f. Note the dots above the p_e term in eq. 4.11 signify temporal differentiation. We approximate the solution to eq. 4.11 by dividing the domain into n_{nel} non-overlapping hexagonal elements using a parametric discretization. Piecewise linear basis functions are used for the pseudo pressure, dynamic pressure, and test function $\boldsymbol{\varphi}$ using. This gives the matrix equation

$$\mathbf{Q}_P \ddot{\mathbf{p}}_e + \mathbf{H}_P \mathbf{p} = \mathbf{b}_P ,$$

where

$$\mathbf{Q}_P = \frac{1}{c^2} \int_{\Omega_f} \boldsymbol{\varphi} \boldsymbol{\varphi}^T \, d\Omega , \quad \mathbf{H}_P = \int_{\Omega_f} \nabla \boldsymbol{\varphi} \cdot \nabla \boldsymbol{\varphi}^T \, d\Omega , \quad \mathbf{b}_P = \int_{\Gamma_f} \boldsymbol{\varphi} \nabla p \cdot \vec{n} \, d\Gamma ,$$

(4.12)

where $\mathbf{Q}_P$ is the capacitance matrix, $\mathbf{H}_P$ is the reactance matrix, and $\mathbf{b}_P$ is the fluid force vector. Note the subscript p in eq. 4.12 is used to differentiate between the matrices of the pressure formulation and the CAFE/CASE formulation. The integrals in eq. 4.12 are approximated using Gauss quadrature. As done in CAFE and CASE the product $\mathbf{H}_P \mathbf{p}$ is evaluated element-by-element to avoid storing the global $\mathbf{H}_P$ matrix.

The FE-FCT algorithm given by Xiao is explicit, which implies that the corrected variable be independent [57]. Therefore the capacitance matrix must be lumped and we do so using the row sum technique. The lumped capacitance matrix is denoted as $\widetilde{\mathbf{Q}}_P$.

The pressure formation equation of state, eq. 4.9, is evaluated node-by-node for the discretized system, giving the relation

$$\mathbf{p}\big|_i = \begin{cases} \mathbf{p}_e\big|_i, & if\ \mathbf{p}_e\big|_i > p^{cav} - p^H\big|_i \\ p^{cav} - p^H\big|_i, & otherwise \end{cases} \quad i = 1,2,\ldots n_{node} \ .$$

(4.13)

4.2.2 Scattered Field Model

Recall the system of governing equations for the scattered field model of the pressure formulation from Chapter 2

$$\frac{1}{c^2}\frac{\partial^2 p_{e-sc}}{\partial t^2} = \nabla^2 p_{sc} \ ,$$

$$p_{sc} = \begin{cases} p_{e-sc}, & if\ p_{e-sc} > p^{cav} - \left(p^H + p_{inc}\right) \\ p^{cav} - \left(p^H + p_{inc}\right), & otherwise \end{cases} .$$

(4.14)

Equation 4.14 is solved numerically using the same procedure as that used in the previous section for the total field model. This results in the scattered field model matrix equation

$$\mathbf{Q}_P \ddot{\mathbf{p}}_{e-sc} + \mathbf{H}_P \mathbf{p}_{sc} = \mathbf{b}_P \ ,$$

where

$$\mathbf{Q}_P = \frac{1}{c^2}\int_{\Omega_f} \boldsymbol{\varphi}\boldsymbol{\varphi}^T \, d\Omega \ , \quad \mathbf{H}_P = \int_{\Omega_f} \nabla\boldsymbol{\varphi} \cdot \nabla\boldsymbol{\varphi}^T \, d\Omega \ , \quad \mathbf{b}_P = \int_{\Gamma_f} \boldsymbol{\varphi} \nabla p_{sc} \cdot \vec{n} \, d\Gamma \ .$$

(4.15)

The integrals and the product $\mathbf{H}_P \mathbf{p}_{sc}$ are evaluated as in the total field model. The capacitance matrix, $\widetilde{\mathbf{Q}}_P$, is lumped using the row sum technique.

The scattered filed model equation of state for the discretized system is

$$\mathbf{p}_{sc}\big|_i = \begin{cases} \mathbf{p}_{e-sc}\big|_i, & if\ \mathbf{p}_{e-sc}\ \big|_i > p^{cav} - \left(p^H\big|_i + p_{inc}\big|_i\right) \\ p^{cav} - \left(p^H\big|_i + p_{inc}\big|_i\right), & otherwise \end{cases} \quad i = 1,2,\ldots n_{node} \ .$$

(4.16)

4.3 Pressure Formulation Boundary Conditions

Here we present the boundary conditions for the scattered field model of the pressure formulation used in the fluid-structure interaction problems in this work. The essential boundary conditions of eq. 4.15 are the same known pressure boundaries as in the scattered field model CAFE/CASE formulation.

The natural boundary conditions are again the fluid-structure interaction and non-reflecting boundary terms governed by the fluid force vector $\mathbf{b}_P$ in eq. 4.15. Following [27,32] the approximation of the continuity of normal velocity condition along the fluid-structure boundary gives the expression

$$\frac{\partial p_{sc}}{\partial n} = -\rho_o \ddot{x}^s_{sc}, \tag{4.17}$$

for the structure forcing term where $\ddot{x}^s_{sc} = \vec{\ddot{x}}^s_{sc} \cdot \vec{n}^s$ is the scattered normal acceleration of the structure. Using eq. 4.17 and the non-conformal coupling scheme from Section 3.4 gives the fluid forcing term as

$$\mathbf{b}^s_P = -\rho_o \int_{\Gamma_{fs}} \phi \bar{\ddot{x}}^s_{sc} \, d\Gamma \tag{4.18}$$

where $\bar{\ddot{x}}^s_{sc}$ is the average scattered normal structural acceleration calculated at the center of each structure element on Γ_{sf}.

The non-reflecting boundary forcing term is given as [27,32,71]

$$\frac{\partial p_{sc}}{\partial n} = -\frac{1}{c}\frac{\partial p_{e-sc}}{\partial t}, \tag{4.19}$$

which is the expression for the Sommerfeld radiation condition [72,73]. The Sommerfeld radiation condition is a local NRB [73,74]. It is exact for one-dimensional plane waves [74] but this accuracy is degraded for high frequency loading (e.g. a planar shock wave) at the boundary [75]. Substitution of eq. 4.19 into the fluid force term in eq. 4.15 yields the new matrix equation for the scattered field model

$$\mathbf{Q}_P \ddot{\mathbf{p}}_{e-sc} + \mathbf{D}_P \dot{\mathbf{p}}_{sc} + \mathbf{H}_P \mathbf{p}_{sc} = \mathbf{b}_P ,$$

where

$$\mathbf{Q}_P = \frac{1}{c^2} \int_{\Omega_f} \boldsymbol{\varphi}\boldsymbol{\varphi}^T \, d\Omega , \quad \mathbf{H}_P = \int_{\Omega_f} \nabla\boldsymbol{\varphi} \cdot \nabla\boldsymbol{\varphi}^T \, d\Omega , \quad \mathbf{D}_P = \int_{\Gamma_{nrb}} \boldsymbol{\varphi}\boldsymbol{\varphi}^T \, d\Gamma , \mathbf{b}_P = \int_{\Gamma_f} \boldsymbol{\varphi} \nabla p_{sc} \cdot \vec{n} \, d\Gamma .$$

(4.20)

The new matrix, $\mathbf{D}_P$, is a diagonal "damping" matrix which has non-zero entries only at NRB nodes [74].

4.4 Application of the FE-FCT Algorithm to the Acoustic Pressure Formulation

To solve the discretized form of the cavitating acoustic formulation given in eq. 4.20 an explicit time integration algorithm [71] is used in tandem with the FE-FCT algorithm presented in eqs. 4.2-4.7. The fluid is coupled to the structure using the non-conformal coupling scheme Section 3.4. The structure equation of motion and forcing term is identical to that used in the CAFE/CASE formulation.

In this section we present the routine for the solution of the pressure formulation using the scattered field model coupled to an explicitly solved structure. Note the following algorithm is for a 1D application on structured meshes. We begin with the calculation of the hydrostatic pressure vector $\mathbf{p}^{\mathrm{H}}$ and initial incident pressure vector $\mathbf{p}_{inc}^{0}$ for all fluid nodes. The solution procedure then proceeds as follows:

1) Solve the structure at time t^n using central difference time integration (see eqs. 3.34-3.35) to yield the fluid forcing term

$$\mathbf{b}_P^{n+1} = -\rho_o \int_{\Gamma_{fs}} \phi \bar{\bar{\ddot{x}}}_{sc}^{s,n} \, d\Gamma .$$

(4.21)

2) Apply eq. 4.21 and update the fluid equations at time t^{n+1} using the FE-FCT scheme outlined in Section 4.1

1. Compute the transported $\dot{\mathbf{p}}_{e-sc}$ via the scheme in [71]:

$$\tilde{\dot{\mathbf{p}}}_{e-sc}^{n+1/2} = \left[\Delta t\left(\mathbf{b}_P^{n+1} - \mathbf{H}_P \mathbf{p}_{sc}^{n}\right) + \left(\widetilde{\mathbf{Q}}_P - \frac{\Delta t}{2}\mathbf{D}_P \right) \dot{\mathbf{p}}_{e-sc}^{n-1/2} \right] \widetilde{\mathbf{Q}}_P^{-1}. \tag{4.22}$$

Note in eq. 4.22 that the evaluation of the NRB term is centered in time removing the need for the predictor-corrector evaluation used in the CAFE/CASE scheme.

2. Compute the diffusive fluxes:

$$\Phi_i^D = \eta_D\left(\dot{p}_{e-sc,i+1}^{n-1/2} - \dot{p}_{e-sc,i}^{n-1/2}\right). \tag{4.23}$$

3. Compute the transported diffused solution:

$$\dot{p}_{e-sc,i}^{TD} = \tilde{\dot{p}}_{e-sc,i}^{n+1/2} + \Phi_i^D - \Phi_{i-1}^D. \tag{4.24}$$

4. Compute the anti-diffusive fluxes:

$$\Phi_i^A = \eta_A\left(\tilde{\dot{p}}_{e-sc,i+1}^{n-1/2} - \tilde{\dot{p}}_{e-sc,i}^{n-1/2}\right). \tag{4.25}$$

5. Limit/correct the anti-diffusive fluxes:

$$\Phi_i^C = \chi \cdot \max\left\{0, \min\left(\chi \cdot \Delta_{i-1}, \left|\Phi_i^A\right|, \chi \cdot \Delta_{i+1}\right)\right\},$$

where $\Delta_{i\pm1} = \pm\left(\dot{p}_{e-sc,i\pm1}^{TD} - \dot{p}_{e-sc,i}^{TD}\right)$ and $\chi = sign\left(\Phi_i^A\right)$. (4.26)

6. Apply the corrected anti-diffusive fluxes to the solution:

$$\dot{p}_{e-sc,i}^{n+1/2} = \dot{p}_{e-sc,i}^{TD} - \Phi_i^C + \Phi_{i-1}^C. \tag{4.27}$$

7. Update the pseudo pressure

$$\mathbf{p}_{e-sc}^{n+1} = \mathbf{p}_{e-sc}^{n} + \Delta t \dot{\mathbf{p}}_{e-sc}^{n+1/2}.$$

(4.28)

8. Apply the equation of state to update $\mathbf{p}_{sc}^{n+1}$

$$\mathbf{p}_{sc}\big|_i = \begin{cases} \mathbf{p}_{e-sc}\big|_i, & \text{if } \mathbf{p}_{e-sc}\big|_i > p^{cav} - \left(\mathbf{p}^H\big|_i + \mathbf{p}_{inc}\big|_i\right) \\ p^{cav} - \left(\mathbf{p}^H\big|_i + \mathbf{p}_{inc}\big|_i\right), & \text{otherwise} \end{cases} \quad i = 1,2,\ldots n_{node}$$

(4.29)

In the above FE-FCT algorithm the diffusive, η_D, and anti-diffusive, η_A, coefficients are constants, chosen to suit a particular problem or algorithm. Book gave $\eta_D = \eta_A = 1/8$ [70] as the optimal choice, which was also used in [57]. For the anti-diffusion stage to fully correct errors introduced in the diffusion stage, $\eta_D = \eta_A$. Experiments in applying the above algorithm to cavitation problems have shown this last requirement to be problematic for cavitation problems. One of the deficiencies of the strong flux limiter (eq. 4.25) is its tendency to over correct the anti-diffusive fluxes in areas where sharp peaks occur on slopes. In these regions strong flux limitation tends to remove the peaks and replace it with a terraced region. For problems with cavitation this terraced region forms along the lower cavitation boundary and leads to large amplitude oscillations entering the pressurized fluid between the upper cavitation boundary and the structure.

A solution to this problem is to add residual diffusion [70] to the algorithm by taking, $\eta_D > \eta_A$. In taking this approach in applying the FE-FCT algorithm to cavitation problems a significant amount of residual diffusion must be added. However, the strong flux limiter applies diffusion where sharp peaks occur (see Fig 4.1). Thus, when a large amount of residual diffusion is used in cavitation problems the result is a significant loss in the magnitude of the pseudo pressure. To overcome the over diffusive nature of strong flux limiting for $\eta_D > \eta_A$, a one sided flux limiter [50], given by eq. 4.30, is adapted to Xiao's FE-FCT algorithm for cavitation problems.

$$\Phi_i^C = \chi \cdot \max\left\{0, \min\left(\left|\Phi_i^A\right|, \chi \cdot \Delta_{i+1}\right)\right\}.$$

(4.30)

Compared to strong flux limitation this one-sided flux limiter does not over-diffuse peaks. The consequence of this is that, with $\eta_D = \eta_A$, the one-sided flux limiter allows a greater number of oscillations overall. However, in Sec. 5.1.4 it is demonstrated that when the one-sided limiter is applied with $\eta_D > \eta_A$ the residual diffusion smoothes large peaks and the limiter is effective in smoothing some of the smaller remaining oscillations. When compared to CAFE/CASE which uses only artificial damping to smooth the solution the result is a small reduction in the amount of diffusion needed to smooth oscillations that result from the dispersion effects of linear finite elements.

CHAPTER 5 BENCHMARK PROBLEMS

In this chapter we apply the finite/spectral element method detailed in Chapter 3 and the FE-FCT algorithm given in Chapter 4 to both a wave propagation and fluid-structure interaction problem with cavitation. We investigate the advantages and disadvantages when applying spectral elements to both problems and also how the addition of artificial damping affects the solution to each problem. We also demonstrate that the FE-FCT algorithm can significantly improve the dispersion properties of finite elements but that its application to problems with cavitation can be problematic. Lastly, we compare the acoustic fluid models to a compressible flow model.

5.1 Shock Wave in a Fluid Bar

5.1.1 Setup

The first benchmark problem is used to assess the shock wave capturing ability of CAFE, CASE, and the proposed FE-FCT algorithm. The problem consists of a 1D horizontal bar of acoustic fluid, with length L=4.5m. The fluid has properties ρ_o=1025 kg/m^3 and c=1450m/s. The equilibrium pressure (i.e. hydrostatic and atmospheric pressure)in the fluid is neglected. At the x=0 end of the bar we apply a known pressure boundary given by a plane step exponential wave

$$p(0,t) = P_{peak} \exp\left[-\frac{t}{\tau}\right], \tag{5.1}$$

where P_{peak} is the peak pressure of the shock wave and τ is the decay constant. The peak pressure is taken as P_{peak} =16.12 MPa and the decay constant as τ =0.423 ms. Note that no cavitation occurs in this problem and that the x=L boundary is neglected as the simulation is terminated before the shock wave reaches this point on the fluid bar. For each case studied a comparison is made to the exact solution of the problem [44] using the L_2 error norm given in as

$$L_2 = \frac{\sqrt{\int_0^L \left[p_{exact}(x,t) - p_{computed}(x,t)\right]^2 dx}}{\sqrt{\int_0^L \left[p_{exact}(x,t)\right]^2 dx}},$$

(5.2)

where p_{exact} is the known solution at a given time t, and $p_{computed}$ is the calculated solution at time t.

5.1.2 Un-damped CAFE and CASE Results

First we compare a CAFE (N=1) solution with a N=4 and N=8 CASE solution without artificial damping applied to the fluid. The time step taken as $\Delta t = \Delta t_{crit}$ (see eq. 3.41). Figure 5.1a shows this comparison at t=2ms on a 121 degree of freedom (DOF) fluid mesh. The L_2 error norms for each result are provided in parenthesis in the legend. Note in Fig.5.1a, and all subsequent plots of the wave at t=2ms, the length of the fluid column is normalized as x/L and the pressure in the fluid is normalized as p/P_{peak}. The CAFE solution in Fig. 5.1a is the exact solution, a demonstration of the cancellation of errors introduced by the spatial and temporal discretization when the time step is taken as the critical limit in explicit schemes [66]. Both the N=4 and N=8 CASE solutions exhibit undershooting before the wave front but maintain the sharpness of wave front overall. After the front of the wave both CASE solutions show dispersive oscillations. The N=8 CASE solution shows smaller dispersive oscillations until x/L=0.20 at which point large oscillations appear in the domain. These oscillations are the cause of the larger error norm for the N=8 solution (L_2=0.1386) compared to the N=4 (L_2=0.1308). Figure 5.1b shows that as the mesh is refined both CASE solutions tend to improve, but the convergence of the N=4 solution is erratic.

In far-field UNDEX applications it is not feasible to use $\Delta t = \Delta t_{crit}$ due to the presence of the structure and non-reflecting boundary condition [18]. Thus in Fig.5.2 we show the effect of reducing the time step to half the critical limit ($\Delta t = (1/2)\Delta t_{crit}$). As expected from [60] the CAFE solution increases in error as the time step is reduced, going from L_2=0.0 to L_2=0.2234. At t=2ms on the 121 DOF fluid mesh the CAFE solution in Fig. 5.2a shows a significant smearing of the wave front and also shows an overshoot in the

magnitude of the wave. After the wave front there are large oscillations along the wave caused by dispersion error introduced by the finite element mesh.

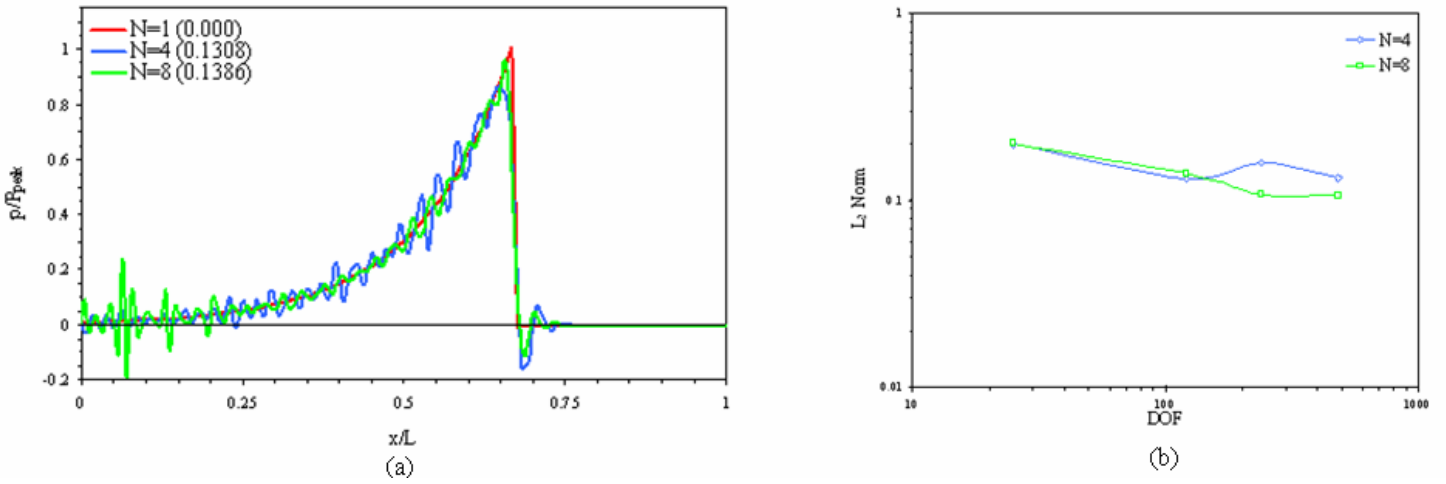

Figure 5.1 Results for propagation of step exponential wave with $\Delta t = \Delta t_{crit}$ shown at t = 2ms by (a) normalized pressure on a 121 DOF mesh and (b) L_2 norm as the mesh is refined

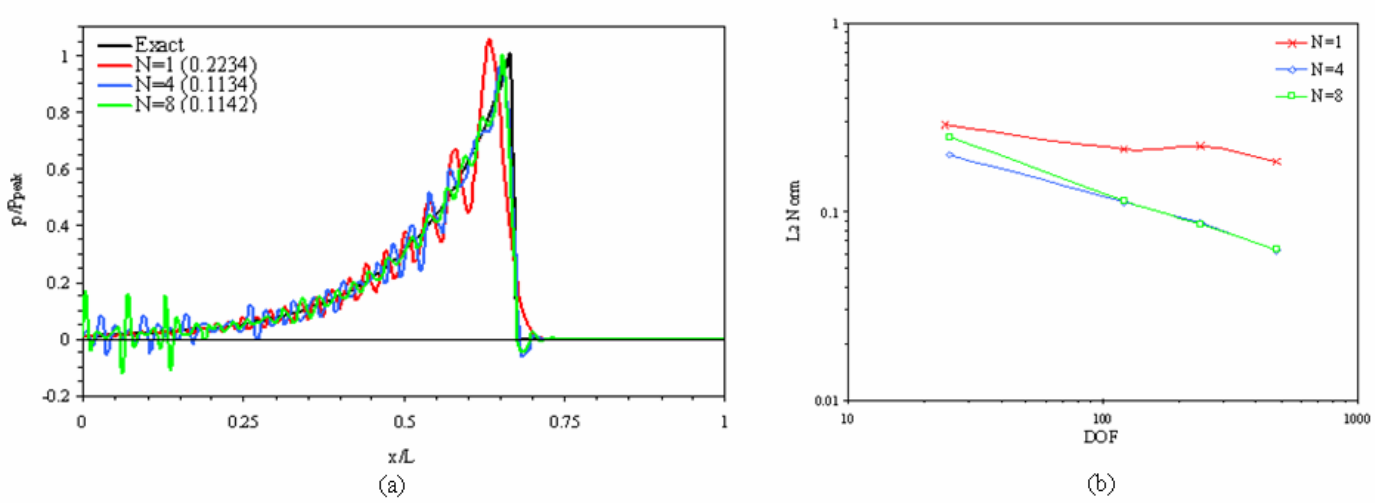

Figure 5.2 Results for propagation of step exponential wave with $\Delta t = (1/2)\Delta t_{crit}$ shown at t = 2ms by (a) normalized pressure on a 121 DOF mesh and (b) L_2 norm as the mesh is refined

Compared to the CAFE solution, both CASE solutions capture the wave front more accurately and do not exhibit any overshoot of the wave magnitude. The undershooting observed with $\Delta t = \Delta t_{crit}$ (Fig. 5.1a) is still present in Fig. 5.2a but is reduced with the smaller time step. Note that unlike the CAFE results, both the CASE results show a small reduction in L_2 norm as the time step is decreased. This was also

observed for the propagation of a half sine pulse in [63]. The N=4 CASE solution reduces some of the larger CAFE oscillations immediately following the wave front but overall increases oscillations behind the wave front when compared to the CAFE solution. When compared to both CAFE and N=4 CASE, the N=8 CASE solution shows a reduction in dispersive oscillations behind the wave front. However, as with $\Delta t = \Delta t_{crit}$, it exhibits large oscillations near the origin of the wave. These large oscillations cause the N=4 CASE solution to have a smaller L_2 norm for not only the 121 DOF mesh but for all meshes studied as seen in Fig. 5.2b

Comparing the L_2 norms of each of the methods as the mesh is refined in Fig. 5.2b both the N=4 and N=8 CASE give superior results, even with the large oscillations that are observed, when compared to CAFE especially for high degrees of mesh refinement. This result is in agreement with that found earlier by other investigators [46,47,76], i.e., although spectral elements can cause larger oscillations, when the error of the total solution is taken into account, spectral elements are superior because of the reduction in dispersion error. For application to far-field UNDEX problems however, increased oscillations are more of a concern because of the effects of modeling cavitation. As discussed in Chapter 3, artificial damping must be introduced to CAFE and CASE for cavitation problems. Thus in the next section we examine the effect of adding artificial damping on the propagation of the step exponential wave.

5.1.3 Damped CAFE and CASE Results

In UNDEX problems β=0.25 [26,22,45,67] and β=0.50 [2,8,22,38,44,68,77] are two values of the CAFE/CASE artificial damping parameter commonly used. Figures 5.3 and 5.4 give results of the step exponential wave propagation problem using β=0.25 and β=0.50, respectively, with $\Delta t = (1/2)\Delta t_{crit}$. In Fig.5.3a results show that on a 121 DOF with β=0.25 the wave front is distorted and the peak magnitude of the wave is reduced for both CAFE and CASE solutions. The N=4 and N=8 CASE solutions smear the wave front less than the CAFE solution, and also retain more of the peak magnitude of the wave. When compared to the un-damped solution with $\Delta t = (1/2)\Delta t_{crit}$ the introduction of artificial damping to the 121 DOF mesh increases the L_2 norm of each model's solution. Thus artificial damping causes a loss of accuracy for both CAFE and CASE solutions. Compared to CAFE both CASE solutions give superior results as the mesh is refined as

observed in Fig. 5.3b. The large difference in L_2 norm seen in the un-damped results (Fig.5.2b) is reduced by the addition of artificial damping.

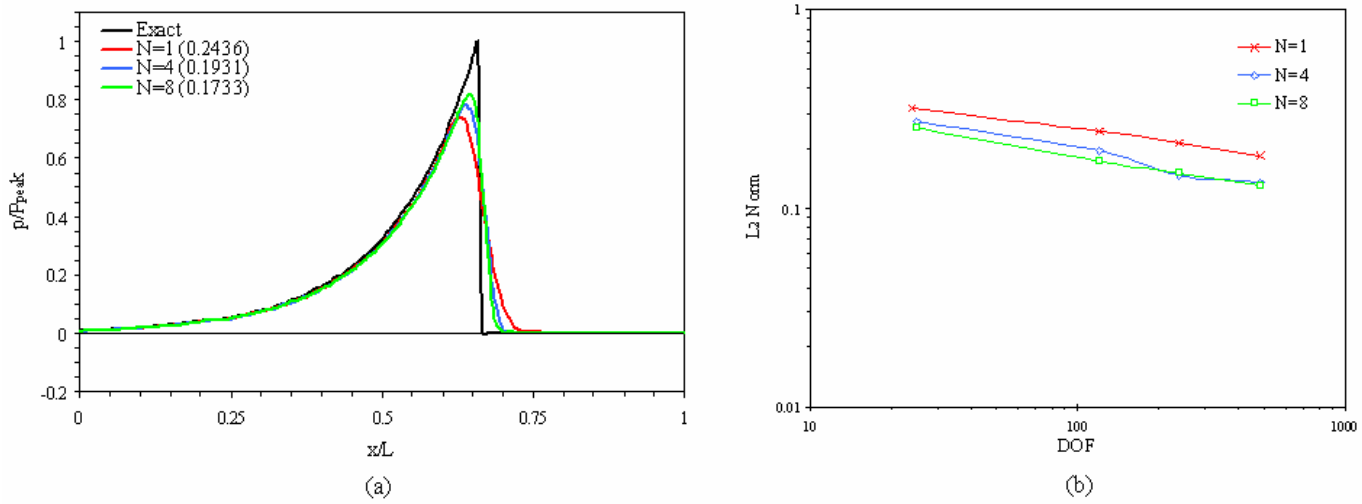

Figure 5.3 Results for propagation of step exponential wave with β=0.25 and $\Delta t = (1/2)\Delta t_{crit}$ shown at t = 2ms by (a) normalized pressure on a 121 DOF mesh and (b) L_2 norm as the mesh is refined

Figure 5.4a gives the CAFE and CASE results of the wave propagation problem at t=2 ms for a 121 DOF mesh with β=0.50 and $\Delta t = (1/2)\Delta t_{crit}$. Again for both CAFE and CASE the front of the wave is distorted and there is loss in peak magnitude of the wave.

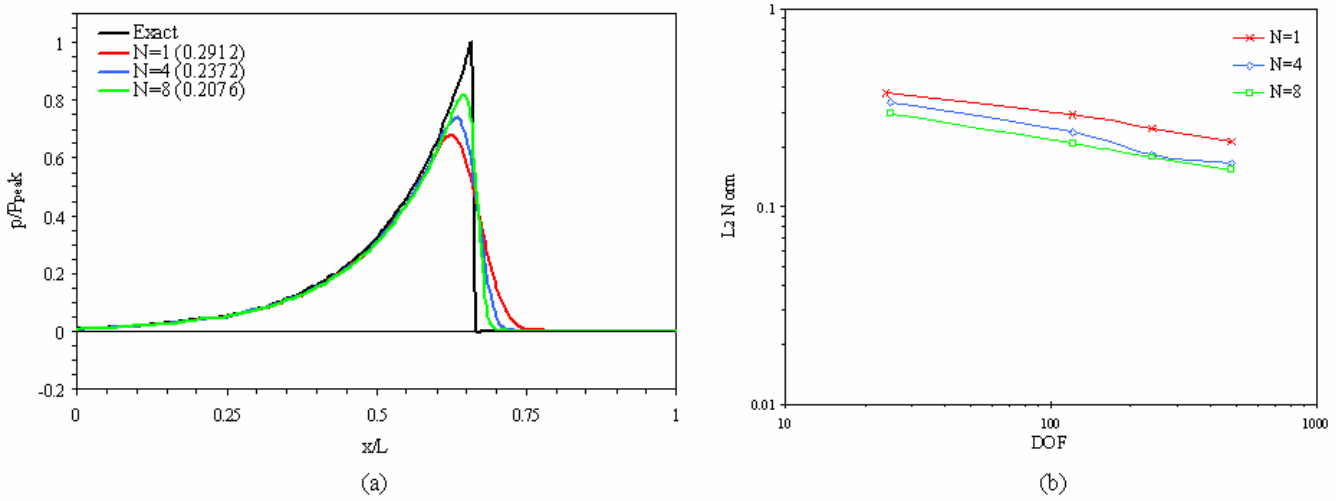

Figure 5.4 Results for propagation of step exponential wave with β=0.50 and $\Delta t = (1/2)\Delta t_{crit}$ shown at t = 2ms by (a) normalized pressure on a 121 DOF mesh and (b) L_2 norm as the mesh is refined

The N=8 CASE solution captures the peak magnitude and wave front better than the N=4 CASE and CAFE solution, and also yields the smallest error norm for the 121 DOF

mesh. Figure 5.4b shows that both the CASE solutions again give lower L_2 norms than the CAFE solution as the mesh is refined. However, the further increase in artificial damping leads to an overall increase of the error norm for both the CAFE and CASE solutions.

5.1.4 FE-FCT Results

The CAFE and CASE results in the previous sections have shown that there is a clear need to apply artificial damping to reduce the oscillations caused by the propagation of a step exponential wave. However, the addition of artificial damping causes a loss of accuracy for both the CAFE and CASE solutions when compared to the un-damped solutions. In this section, we apply the FE-FCT algorithm given in Chapter 4 to determine if it can increase the accuracy of the finite element solutions without increasing oscillations in the fluid. The FE-FCT algorithm is applied to the step exponential wave propagation problem using the strong flux limiter, with $\eta_D = \eta_A = 0.125$, and $\Delta t = (1/2)\Delta t_{crit}$. Note that for the FE-FCT algorithm, we take the experimentally determined $\Delta t_{crit} = 0.85 h_e/c$, where h_e is the length of an element [66]. For comparison to the FE-FCT solution, β is taken as 0.10 for the CAFE and CASE solutions. Reducing β to this amount gives similar results to those given by the FE-FCT algorithm in terms of peak magnitude in the captured wave.

Figure 5.5a compares results for FE-FCT, CAFE, and N=8 CASE on a 121 DOF fluid mesh. Both the FE-FCT and the N=8 CASE solutions capture the front of the wave better than the CAFE solution, although the CASE solution shows a slight undershoot at the wave front that is not seen in the FE-FCT result. The N=8 CASE solution also exhibits small oscillations along the wave form. These oscillations are not observed in the FE-FCT solution. Comparing L_2 norms as the mesh is refined in Fig. 5.5b, we see that the FE-FCT algorithm gives superior results. Furthermore, Fig. 5.6 shows the FE-FCT algorithm yields L_2 norms that are comparable with the L_2 norms obtained in the un-damped CASE solutions. This is a significant result because it proves that for the step exponential wave propagation problem, the dispersion properties of finite elements can be improved to match spectral element solutions without an increase in oscillations.

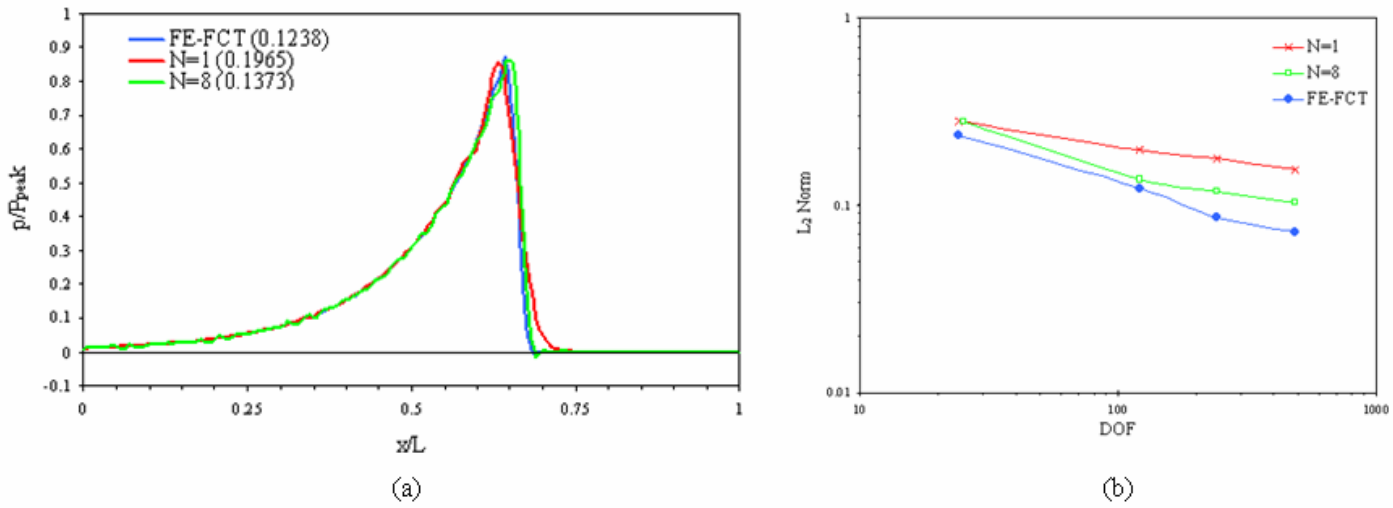

Figure 5.5 Propagation of step exponential wave using FE-FCT with $\eta_D = \eta_A = 0.125$ and $\Delta t = (1/2)\Delta t_{crit}$ compared to finite/spectral elements with $\beta = 0.10$ and $\Delta t = (1/2)\Delta t_{crit}$ shown at $t = 2$ms by (a) normalized pressure on a 121 DOF mesh and (b) L_2 norm as the mesh is refined

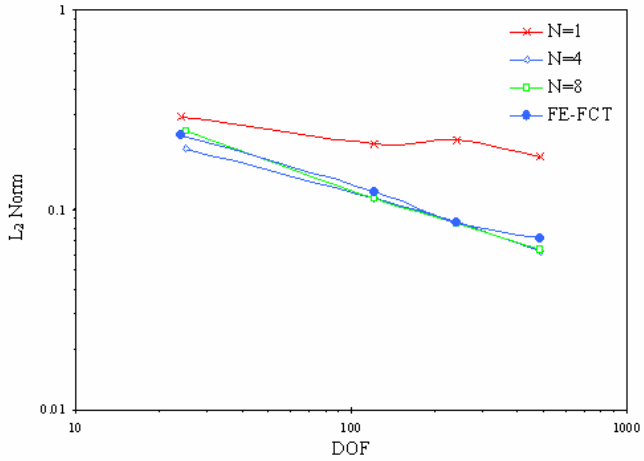

Figure 5.6 L_2 norm as the mesh is refined for FE-FCT with $\eta_D = \eta_A = 0.125$ and $\Delta t = (1/2)\Delta t_{crit}$ compared to finite/spectral elements with $\beta = 0.0$ and $\Delta t = (1/2)\Delta t_{crit}$

As discussed in Chapter 4, problems with cavitation require the addition of residual diffusion to the FE-FCT algorithm. This is necessary because cavitation oscillations are not well smoothed during the diffusion stage of the FE-FCT algorithm. When residual diffusion is added to the FE-FCT algorithm, a one-sided flux limiter is used instead of the strong flux limiter, which tends to over diffuse the solution. As seen in the previous section, as the amount of damping in a model is increased, the accuracy of the solution decreases. Thus, ideally we want to use the least amount of damping as necessary. When

compared to a CAFE solution, using residual diffusion in the FE-FCT algorithm with the one-sided flux limiter allows for a reduction in the amount of damping needed to smooth oscillations for coarse meshes. This is shown in Fig. 5.7, where on a 41 DOF CAFE solution with β=0.10 and $\Delta t = (1/2)\Delta t_{crit}$ is compared to a FE-FCT solution with the one-sided flux limiter, η_D= 0.125, η_A=0.09, and $\Delta t = (1/2)\Delta t_{crit}$ at t=2ms. Both the FE-FCT and CAFE solutions give the same peak magnitude of the wave, but the oscillations observed along the wave form in the CAFE solution are better smoothed in the FE-FCT solution.

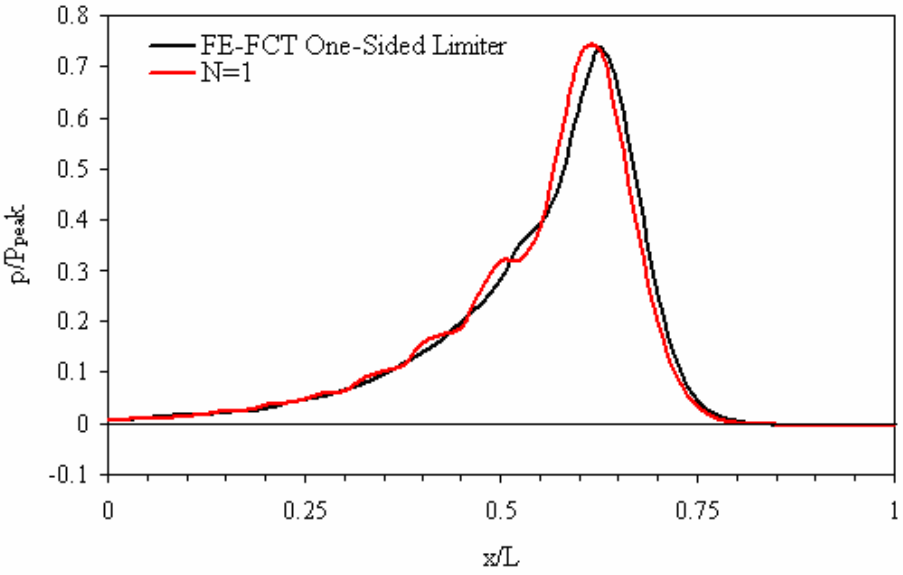

Figure 5.7 Step exponential wave at t= 2 ms using FE-FCT with one-sided limiter, η_D= 0.125, η_A=0.09, and $\Delta t = (1/2)\Delta t_{crit}$ compared to finite elements with β=0.10 and $\Delta t = (1/2)\Delta t_{crit}$ for a 41 DOF mesh

5.2 2 DOF Mass-Spring Oscillator

In the previous section, we saw that spectral elements allowed for more accurate wave propagation in an acoustic fluid at the cost of an increase in spurious oscillations. Artificial damping reduces these oscillations, but also smears the wave front and causes dissipation of the wave magnitude. By incorporating a FE-FCT algorithm with strong flux limitation, the dispersion properties of finite elements can be improved, making them competitive with the accuracy of spectral elements. We now apply finite elements (CAFE), spectral elements (CASE), and the FE-FCT algorithm to two example problems that involve fluid-structure interaction and cavitation to determine how each method

performs in problems with cavitation. We look at how oscillations and artificial damping affect the structural response in each problem. The need for residual diffusion when applying the FE-FCT algorithm to cavitation problems is demonstrated. And we also determine if reducing artificial damping and applying the FE-FCT algorithm with a one-sided limiter reduces oscillations in finite element solutions to cavitation problems as it did in the wave propagation problem. Additionally, a comparison between acoustic and compressible flow solutions is also made in an attempt to validate the acoustic fluid assumptions.

5.2.1 Setup

To evaluate CAFE, CASE, and the FE-FCT algorithm when applied to a far-field UNDEX problem with cavitation, a two degree of freedom mass-spring oscillator problem shown in Fig. 5.8 is solved in one-dimension. The problem consists of a structure with masses m_1 and m_2, and displacements $d_1(t)$ and $d_2(t)$, sitting on top of a column of fluid with depth L. The two masses are connected by a spring with spring constant k and are initially at rest.

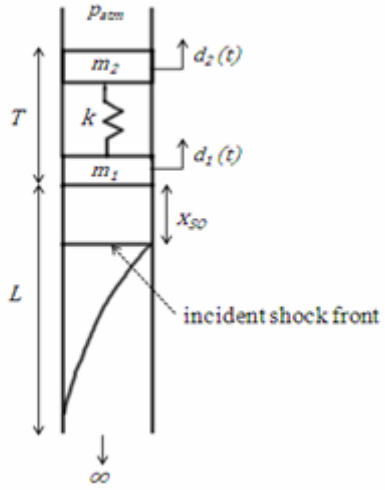

Figure 5.8 Schematic of the mass-spring oscillator UNDEX problem

This problem was originally solved by Sprague and Geers in [38] using CAFE. Since then, it has been used as a benchmark problem for CASE [26,44], the approach of Nimmagadda and Cipolla (ABAQUS approach) [78], and most recently with a compressible flow solver combined with the ghost fluid method [79]. Here, this problem

is solved for $m_1/m_2=5$ in using CAFE/CASE and the FE-FCT algorithm with both strong and one-sided limiting.

For both CAFE/CASE and FE-FCT we apply the scattered field model to the fluid domain. Thus, the known incident field (i.e. the shock wave) in this problem is given as

$$p_{inc}(x,t) = P_{peak} \exp\left[-\frac{t + \frac{x - x_{so}}{c}}{\tau} \right] H\left(t + \frac{x - x_{so}}{c} \right), \tag{5.3}$$

where $H(t)$ is the Heaviside function. At time t=0, the wave front of the incident shock wave, modeled as a plane step exponential wave, is located at x_{so}.

Following [44], the fluid has depth L=3.0 m and a cross sectional area of unity. We take the reference density ρ_o=1025 kg/m^3 and c=1500 m/s. The structure has a draft, T= 5.08 m, a total mass, m_1+m_2=5207 kg, and $k=(10\pi)^2 m_2$ N/m. The peak pressure is taken as P_{peak}=16.12 MPa, the decay constant is τ=0.423 ms, and x_{so}=0 m. The structure is modeled as two lumped mass elements connected by a single spring element and integrated in time with the central difference method. For all methods studied, the simulation is run to a termination time of 0.15 s and the time step is set at half the critical limit [38,44].

For both CAFE and CASE solutions, the damping parameter, β, is set to 0.50 [44]. As in the first example (Sec. 3.1) the diffusion and anti-diffusion coefficients, η_D= η_A=0.125, are used for the strong flux limiter. For the one-sided flux limiter the diffusion and anti-diffusion coefficients are chosen as, η_D= 0.125 and η_A=0.09, which is approximately equivalent to β~0.10. These coefficients are chosen as such to determine if reducing the amount of damping used with finite elements can improve the capture of cavitation.

5.2.2 Results

We begin by comparing CAFE and N=8 CASE to both FE-FCT algorithms using uniform meshes consisting of 41 DOF and 81 DOF. For each method m_1 responds to the incident wave with a sharp rise in velocity to the kick-off velocity of ~6.5m/s. After this

velocity is reached, the velocity begins to decay and take on a negative magnitude as the cavitation region in the fluid grows. At t=0.05s the cavitation closure pulse re-loads m_1 causing a second sharp rise in velocity. The upward motion of the mass system resulting from the closure pulse causes a small [26] secondary cavitation region to form. The closer pulse of the second cavitation region re-loads the structure at t=0.13s.

Figure 5.9a gives the m_1 velocity response using a 41 DOF mesh for each method. A closer view of the same velocity response during the first cavitation region is given in Fig. 5.9b. Figure 5.9b shows that m_1 has most oscillations between t=0.02s and t=0.05s, but the rest of the response is unaffected by oscillations in the fluid. Note that taking β=0.50 for spectral elements does not smooth oscillations in the structural response as it smoothed oscillations in the wave propagation problem, indicating that oscillations caused by cavitation in the fluid are more severe than those that result from wave propagation error. Comparing the solutions in Figs. 5.9a and 5.9b, the CAFE solution exhibits the least oscillations but like in the wave propagation problems does not agree well with the CASE solution. This is an indication that impulse does not drive the structural response during cavitation and that capturing the magnitude and shape of the cavitation region is important in obtaining structural responses to cavitation regions. The difference between CASE and CAFE is better observed in Fig. 5.9b, which shows the CAFE solution gives a lower velocity during the cavitation response and also gives a delayed arrival time of the cavitation closure pulse.

In Fig. 5.9a the FE-FCT algorithm with strong flux limiting suffers from large oscillations which significantly alter the response during the first cavitation region. These oscillations are a result of the strong flux limiter causing terracing as the lower cavitation boundary forms in the fluid. Figure 5.10 demonstrates the terracing effect by comparing dynamic densified condensation during the growth and collapse of the cavitation region in the fluid for CAFE, N=8 CASE, and FE-FCT. At t=0.015s, the upper boundary of cavitation region for the CAFE, N=8 CASE, and FE-FCT solution is located near the fluid structure interface (x=0m) and the lower cavitation boundary has extended approximately 1.7m into the fluid as indicated by the arrows in Fig. 5.10a. Figure 5.10a also shows the regions of terracing that have formed in the FE-FCT solution. As the cavitation region contracts, shown in Figs. 5.10b (t =0.03s) and 5.10c (t =0.04s), the

upper cavitation boundary moves deeper into the fluid and the lower cavitation boundary moves towards the fluid-structure interface. When the upper cavitation boundary encounters a terraced region, the terraced region enters the region of pressurized fluid between the fluid-structure interface and upper cavitation boundary as a large oscillation. This effect is demonstrated in Fig. 5.10c, where a large oscillation occurs immediately before the upper cavitation boundary which is located at a depth of 0.6 m. These large oscillations caused by terraced regions entering the pressurized fluid have magnitudes large enough to cause large non-physical pockets of cavitation in this pressurized fluid (an extreme example of frothing) and are responsible for the large oscillations observed in the structural response (Fig. 5.9). This result makes FE-FCT with strong flux limiting unsuitable for problems with cavitation but demonstrates the need for applying artificial damping or diffusion to cavitation problems.

Although the FE-FCT algorithm with strong flux limiting fails to improve cavitation capture, the FE-FCT algorithm with one-sided limiting solution agrees well with the N=8 CASE solution in Fig. 5.9. This confirms for problems with cavitation that reducing the amount of damping used with finite elements can produce solutions that are similar to spectral element solutions. The same effect was observed for the solution to the propagation of a step exponential wave. In addition to matching the N=8 CASE solution, Fig. 5.9b also shows that the FE-FCT with one-sided limiting gives a small reduction in the larger oscillations between t=0.02s and t=0.03s when compared to CASE. Returning again to the wave propagation problem in Section 5.1.4, FE-FCT with one-sided limiting reduced oscillations when compared to finite elements with an equivalent amount of damping (see Fig. 5.7). Thus, to test the effect of the one-sided limiter on oscillations in a problem with cavitation the FE-FCT one-sided limiter solution in Fig. 5.9 is compared to a 41 DOF CAFE solution with the damping factor reduced to, $\beta = 0.10$.

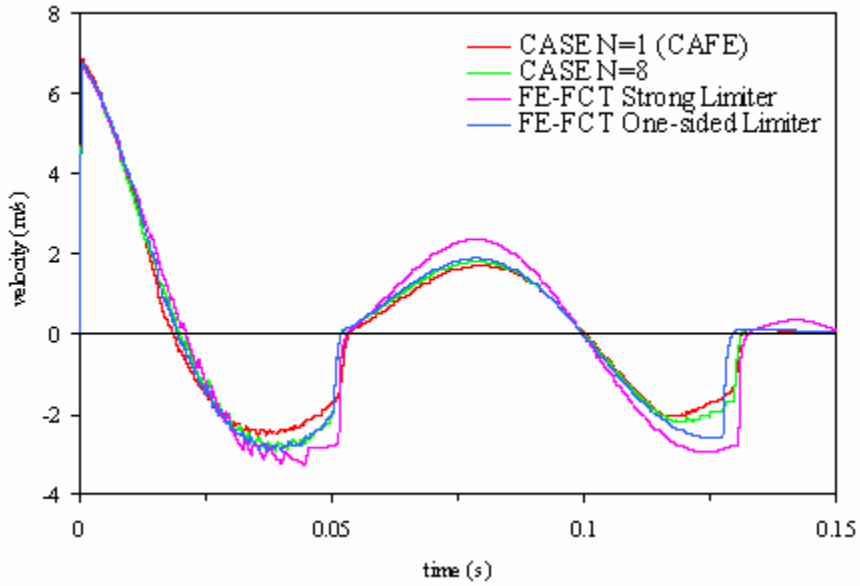

(a)

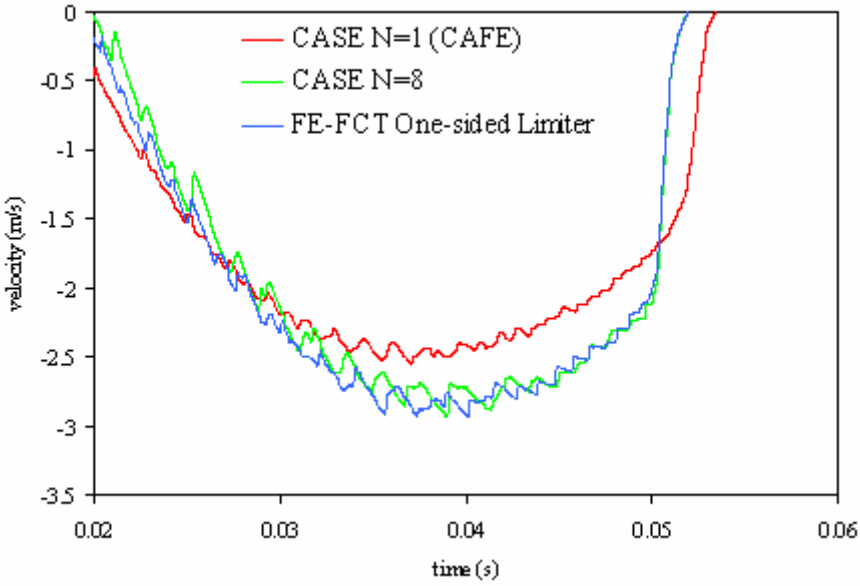

(b)

Figure 5.9 Results for the velocity of m_1 on two time scales using 41 DOF

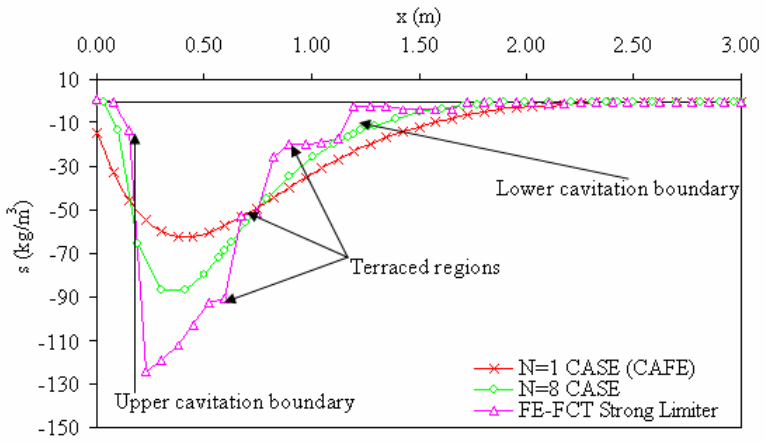

(a)

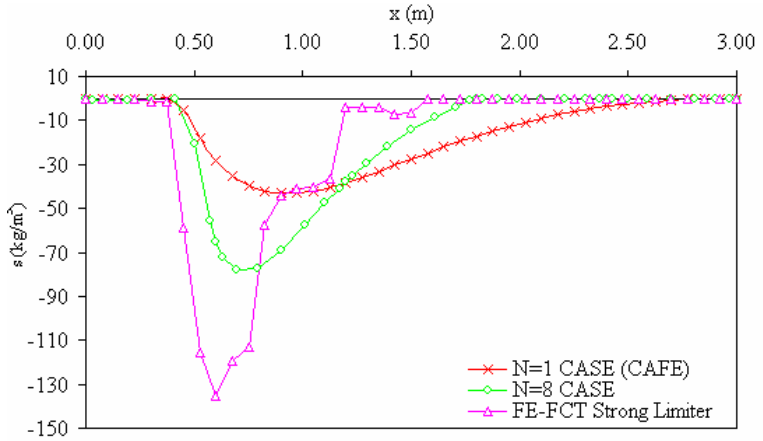

(b)

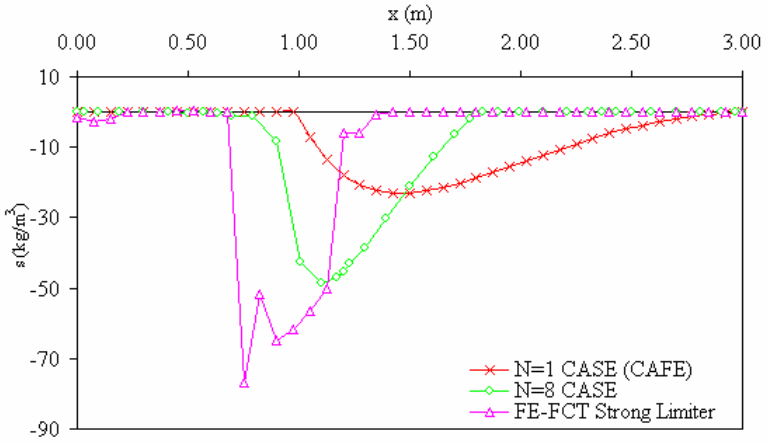

(c)

Figure 5.10 Dynamic densified condensation in the fluid column with 41 DOF for *N*=8 CASE and FE-FCT with strong flux limitation at times 0.015s (a), 0.03s (b), and 0.04s (c)

This comparison, shown in Fig. 5.11, reveals that the FE-FCT algorithm with one-sided limiting is successful in reducing some of the larger oscillations that occur in the CAFE solution between t=0.02s and t=0.035s. Figure 5.11 also shows CAFE gives a delayed arrival time of the cavitation closure pulse even with a reduced amount of damping.

Figure 5.12 gives m_1 velocity response results for each method after refining the mesh to 81 DOF. Fig. 5.12b gives the velocity response during the duration of the first cavitation region. The FE-FCT with strong flux limiting result is included in Fig. 5.12a to demonstrate that refinement of the mesh has little effect on the large oscillations that make FE-FCT with strong flux limiting unsuitable for cavitation problems. As in the 41 DOF results, Figs. 5.12a and 5.12b show the CAFE solution exhibits the least oscillations but gives a lower velocity during the cavitation response and gives a delayed arrival time of the cavitation closure pulse.

Fig. 5.12b shows the FE-FCT algorithm with one-sided limiting results again agree well with the N=8 CASE solutions and again reduce the larger N=8 CASE oscillations. However, when compared to CAFE with reduced damping the effect of the limiter on structural response oscillations is significantly reduced as the mesh is refined. This is shown in Fig. 5.13**,** where unlike the 41 DOF results there is negligible difference between oscillations in the FE-FCT with one-sided limiting and CAFE with β = 0.10 results.

In addition to the reduced effect of the limiter for 81 DOF, the FE-FCT results agree with the N=8 CASE results and the reduced damping CAFE results only until t= 0.05s at which point the cavitation closure pulse in FE-FCT results arrives earlier than in the N=8 CASE results. This also occurs for the closure time of the second cavitation region at t=0.125s in both the 41 DOF (Fig. 5.9) and 81 DOF (Fig. 5.12) results. Additionally, the velocity magnitudes reached during the second cavitation region are lower in the CASE/CAFE solutions when compared to the FE-FCT solutions. The reason for the difference lies in how the methods apply artificial damping to the fluid. Recall, the artificial damping in CASE/CAFE is added to the governing equation of the fluid but in FE-FCT it is applied through the diffusion equation to the corrected variable.

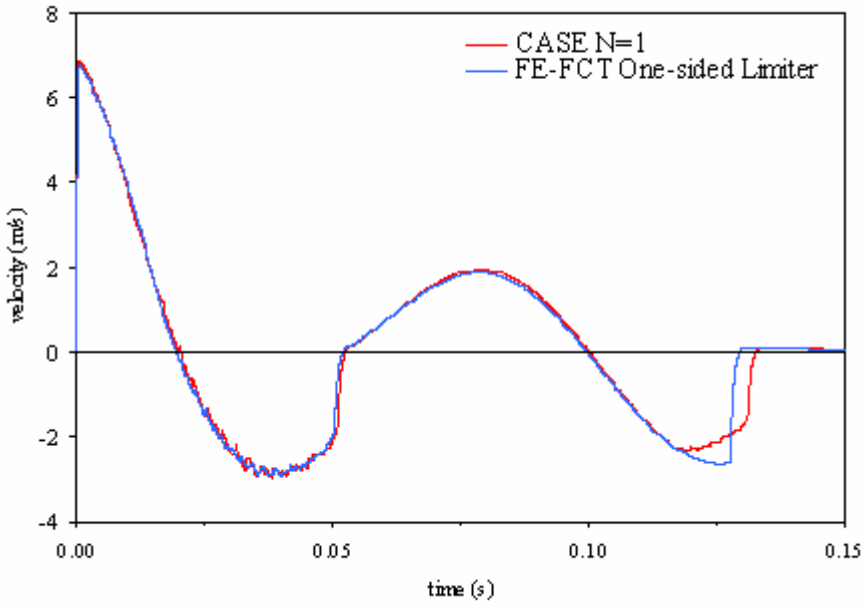

(a)

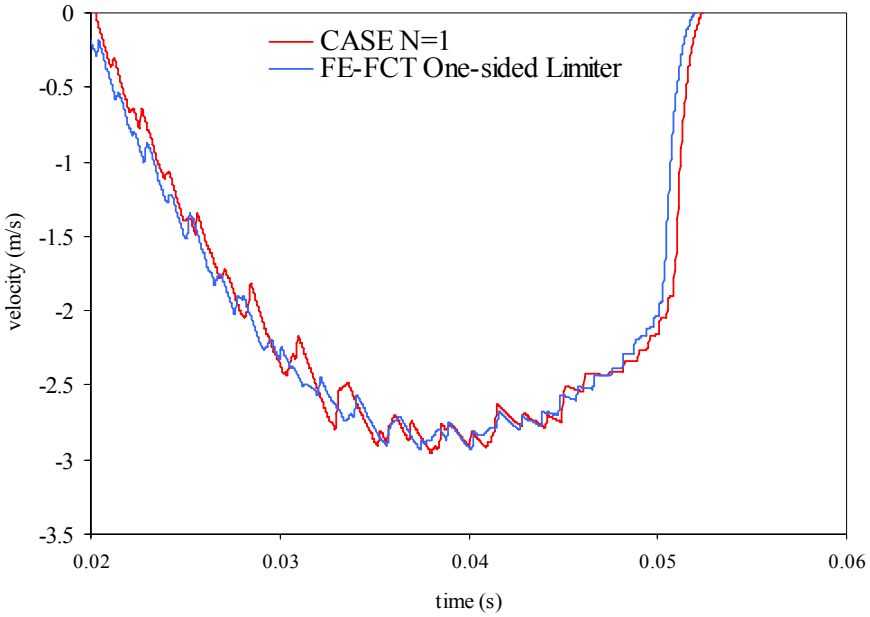

(b)

Figure 5.11. Results for the velocity of m_1 on two time scales using FE-FCT with one-sided limiter (η_D= 0.125 ,η_A=0.09) and CASE N=1 with β = 0.10 with 41 DOF

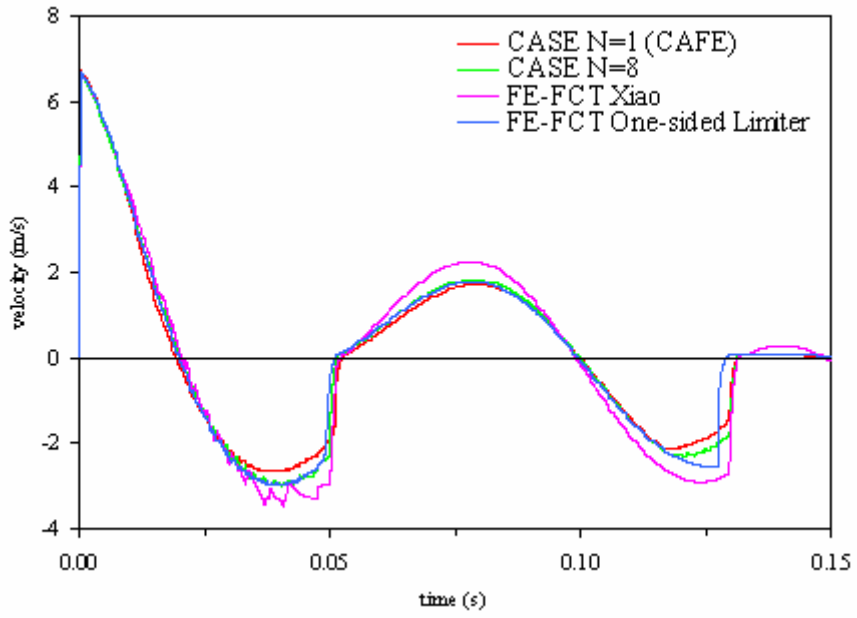

(a)

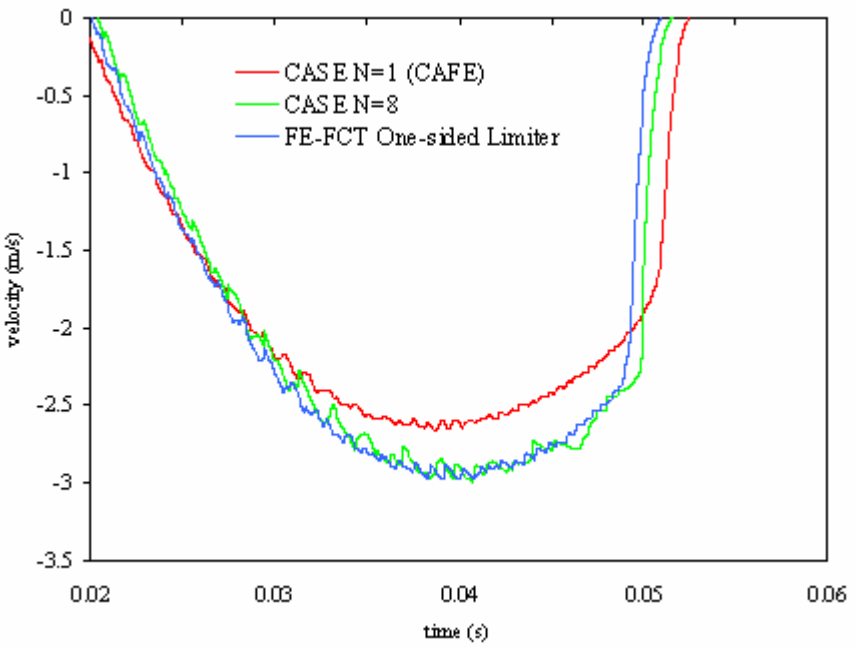

(b)

Figure 5.12 Results for the velocity of m_1 on two time scales using 81 DOF

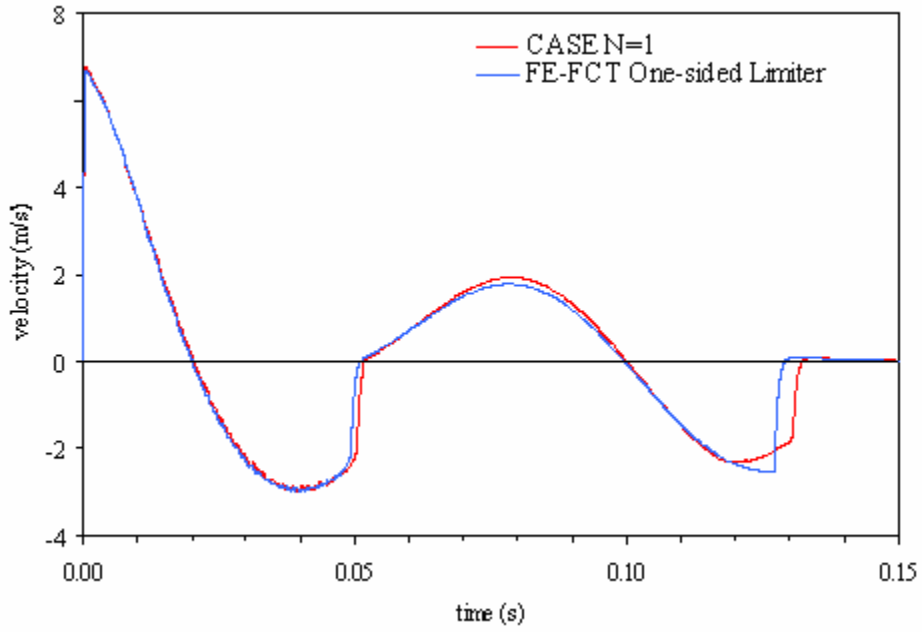

(a)

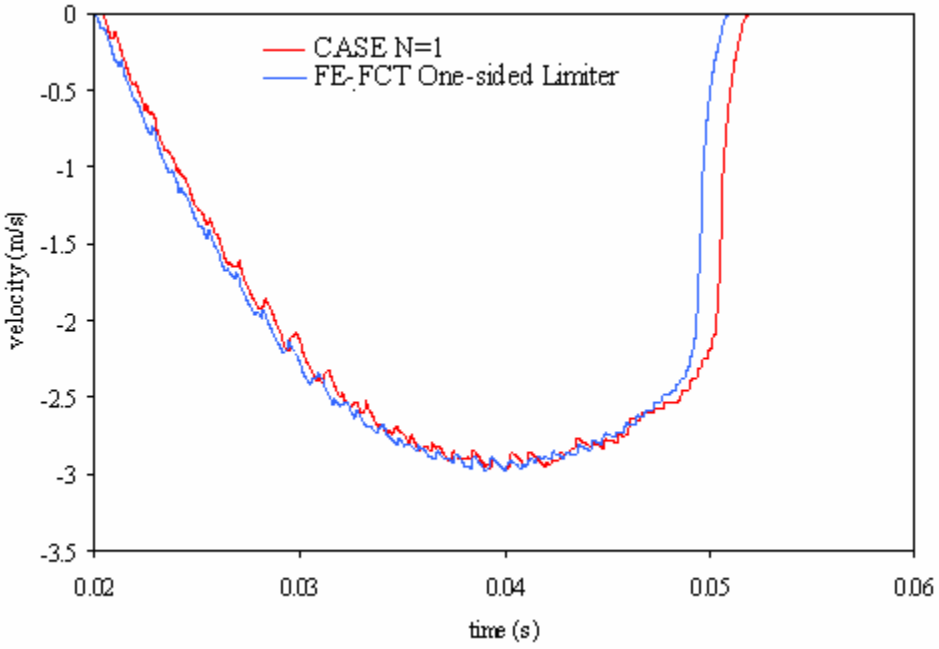

(b)

Figure 5.13 Results for the velocity of m_1 on two time scales using FE-FCT with one-sided limiter (η_D= 0.125 ,η_A=0.09) and CASE N=1 with β = 0.10 with 81 DOF

The results in Figs. 5.9 and 5.12 indicate that how artificial damping applied to the fluid affects the structural response. This is especially true for the smaller regions of cavitation occurring directly beneath the structure.

To further examine the differences between the velocity responses during the second cavitation region we compare results to two benchmark solutions. For the first benchmark solution we compare both N=8 CASE and FE-FCT using a highly refined mesh consisting of 1201 DOF. Next the N=8 CASE and FE-FCT solutions are compared to a second benchmark solution taken from [79]. The solution in [79] is obtained with an Eulerian compressible flow solver in combination with a one-fluid multiphase cavitation model [35,36] and the ghost fluid method (GFM) [12,79] to treat fluid-structure interaction. This model consists of 1201 DOF. For comparison to [79] the properties of the fluid and incident shock wave remain the same but the depth of the fluid mesh is extended to L = 10 m.

Figure 5.14 gives the comparison between the N=8 CASE and FE-FCT solutions with 1201 DOF. The FE-FCT results still exhibit an earlier closure time for both the first and second cavitation regions. However, when compared to the 41 and 81 DOF results the difference in the velocity magnitudes seen during the second cavitation region response, are significantly reduced for this degree of mesh refinement. This indicates that as the mesh is refined the difference between the CASE/CAFE and FE-FCT solutions diminishes because the effect of artificial damping on the fluid mesh is reduced.

Figure 5.15 compares the 1201 DOF N=8 CASE and FE-FCT solutions to the compressible flow solution. The response during the first cavitation region for the three solutions agrees in terms of velocity magnitudes reached. However, the compressible flow solution gives a delayed closure time of the first cavitation region and a much faster closure time for the second cavitation region. It is interesting to note in Fig. 5.15 that the difference in velocity response during the second cavitation region begins to occur at the same time, t=0.12s, for each method.

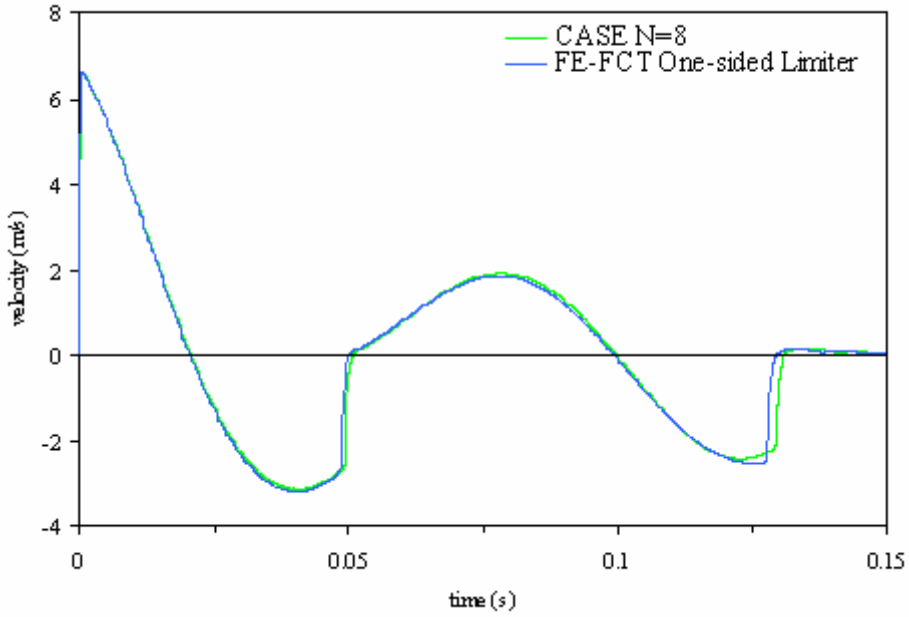

Figure 5.14 *N=8* CASE and FE-FCT with one-sided flux limiter results for the velocity of m_1 using 1201 DOF

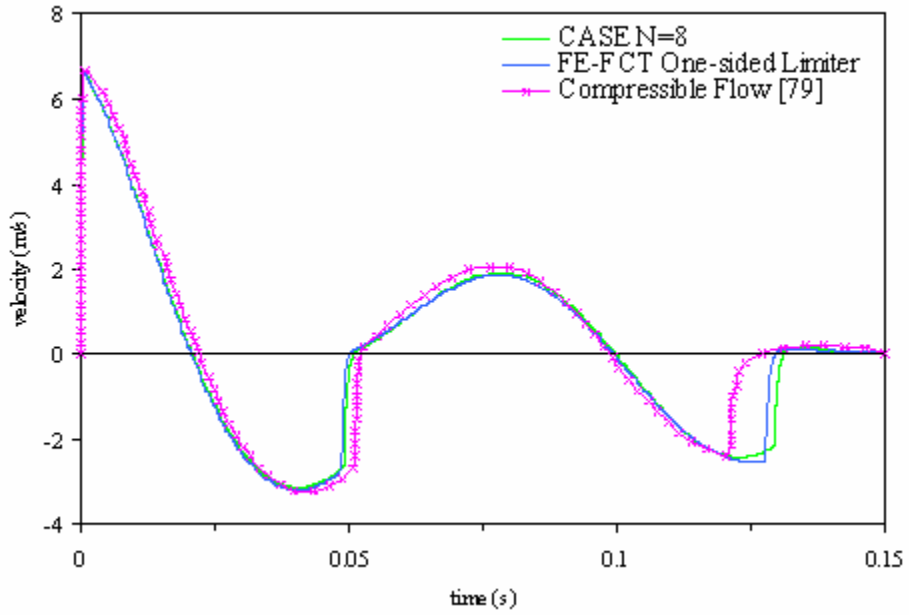

Figure 5.15 Comparison of *N=8* CASE, FE-FCT with one-sided flux limiter, and compressible flow [79] solutions of the velocity of m_1

In [79], Xie et al. suggest that the difference between the compressible flow solution and the acoustic (CASE and FE-FCT) solutions was due to the governing equations in the fluid , the use of a multiphase cavitation model, and the extension of the fluid depth to L=10m. Looking at Fig. 5.16, which compares a 1201 DOF N=8 CASE solution with L=3m to the N=8 CASE solution given in Fig. 5.14, we see the extension of the fluid mesh from L=3m to L=10m does not cause a significant change in the velocity response histories.

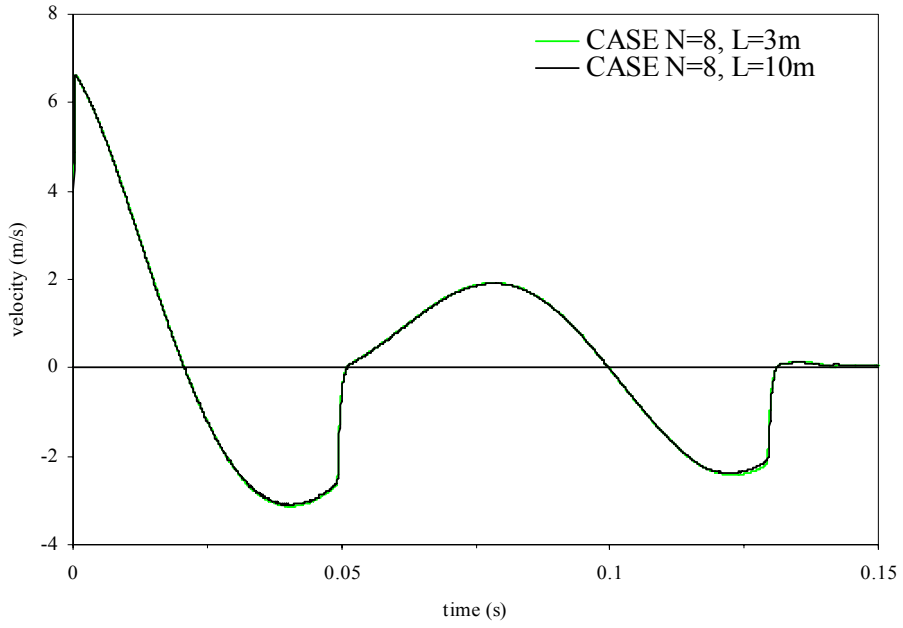

Figure 5.16 Comparison of N=8 CASE solution of the velocity of m_1 using L = 3m and L= 10m

Furthermore, comparisons of multiphase cavitation models and cutoff cavitation models (such as the ones used with CAFE/CASE and FE-FCT in this work) in [12,80] have shown both to give very similar results. Additionally, in [26] Sprague demonstrated assuming small fluid motions and neglecting of the convective velocity terms in the governing fluid equations did not significantly affect the velocity response history for this benchmark problem. The last explanation for the difference between the compressible flow solution and acoustic solutions in Fig. 5.15 is the use of the ghost fluid method to treat fluid-structure interaction.

CASE and FE-FCT results demonstrated earlier that the response of the structure to cavitation is sensitive to how artificial damping is applied to the fluid. It follows that the addition of the ghost fluid method to treat the fluid-structure interaction would also cause a change in the structural response, especially for small cavitation regions that are very local in space. Unfortunately, without an experimental or analytical solution to this benchmark problem no conclusions as to which method is correct can be drawn. However, a comparison of the acoustic and compressible flow models to a problem with an analytical solution is possible and is presented in the following section.

5.3 Bleich-Sandler

5.3.1 Setup

The Bleich-Sandler problem consists of a mass sitting at the free surface of a fluid column that is infinitely deep. The mass is subjected to loading from a step exponential wave, which causes cavitation in the fluid after reflection from the mass. A solution via the method of characteristics is given by Bleich-Sandler in [34]. Using the mass-spring structure given in Section 5.2.1, we set m_1 =144 kg, m_2=0, and k=0, which gives the draft of the mass as, T= 0.141 m. Following [22,38,41] the fluid depth is L=3.81 m and we take ρ_o=989 kg/m^3 and c=1450 m/s.

We use the scattered field model for both CAFE/CASE and FE-FCT. Thus the known incident field is found using eq. 5.3. We take x_{so}=0, peak pressure as P_{peak}=0.712 MPa and decay constant as τ=0.999 ms. As in the previous section, for CAFE/CASE solutions the damping parameter, β, is set to 0.50. For the one-sided flux limiter the diffusion and anti-diffusion coefficients are chosen as, η_D= 0.125 and η_A=0.09. For both CAFE/CASE and FE-FCT the simulation is run to a termination time of 0.012 s and the time step is set at half the critical limit.

5.3.2 Results

Figure 5.17a gives results for an N=8 CASE solution with 97 DOF, a CAFE solution with 101 DOF, and a FE-FCT solution with 101 DOF. All methods in Fig. 5.17a agree well with the exact solution, with CASE and FE-FCT capturing the velocity magnitudes between t=0.01s and t=0.012s better than CAFE. Also note that how artificial damping is

applied to the fluid does not cause a large change in response of the structure to cavitation as it did in the previous section.

Figure 5.17b shows the 97 DOF N=8 CASE solution and 101 DOF FE-FCT solutions compared to the compressible flow solution from [79]. Note the compressible flow solution from [79] extends L to 10 m and uses 801 DOF. The extension of the fluid depth in the Bleich-Sandler problem does not significantly affect the response as shown in [44]. Note the compressible flow mesh is more refined (in terms of element size) than the acoustic fluid meshes in Fig. 5.17. However the 97 DOF N=8 CASE mesh and the 101 DOF CAFE and FE-FCT meshes match the refinement level for L=3.81m that have given good approximations to the Bleich-Sandler problem solution in [22,38,41].

Comparing results in Fig. 5.17b shows for the Bleich-Sandler problem the differences between the acoustic and compressible flow solutions are minimal. In fact comparing Fig. 5.17a to Fig. 5.17b shows the compressible flow solution in [79] is almost identical to the CAFE solution.

In the previous section, we saw that the N=8 CASE solution increased oscillations in the structural response but only during a short period of the response. However, for the Bleich-Sandler problem Fig. 5.17a shows the CASE solution gives large oscillations that persist thought the entire response of the mass. Indicating the severity of increased oscillations when applying CASE is problem dependent. The FE-FCT solution reduces the oscillations, but as seen in the previous section reducing the damping factor in the CAFE solution gives almost identical results. This is shown in Fig. 5.18 where the 101 DOF FE-FCT solution is compared to a 101 DOF CAFE solution with β = 0.25. It is interesting to note that for the Bleich-Sandler problem reducing the damping causes the CAFE solution to match the N=8 CASE solution, where previously it caused a mismatch in the prediction of cavitation closure times.

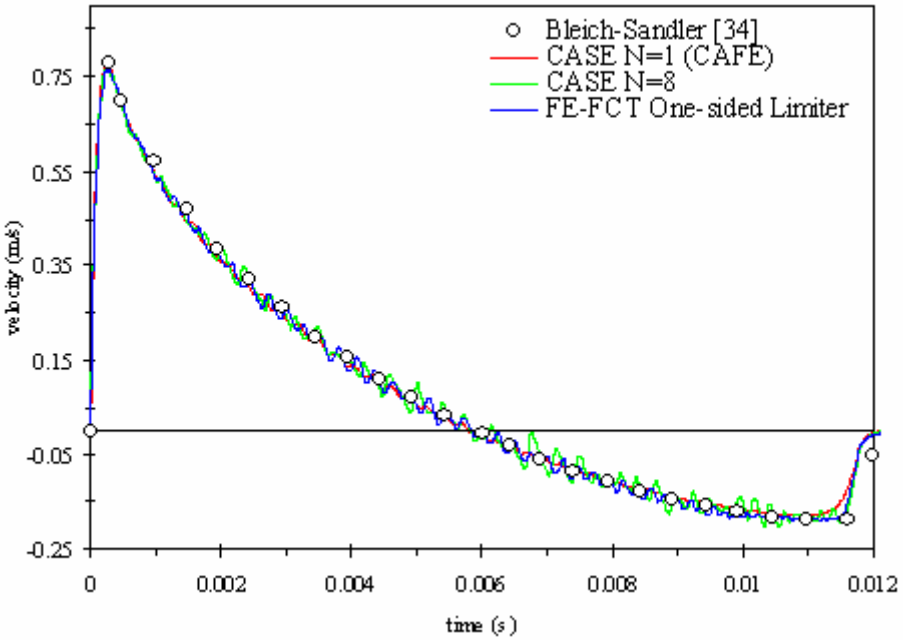

(a)

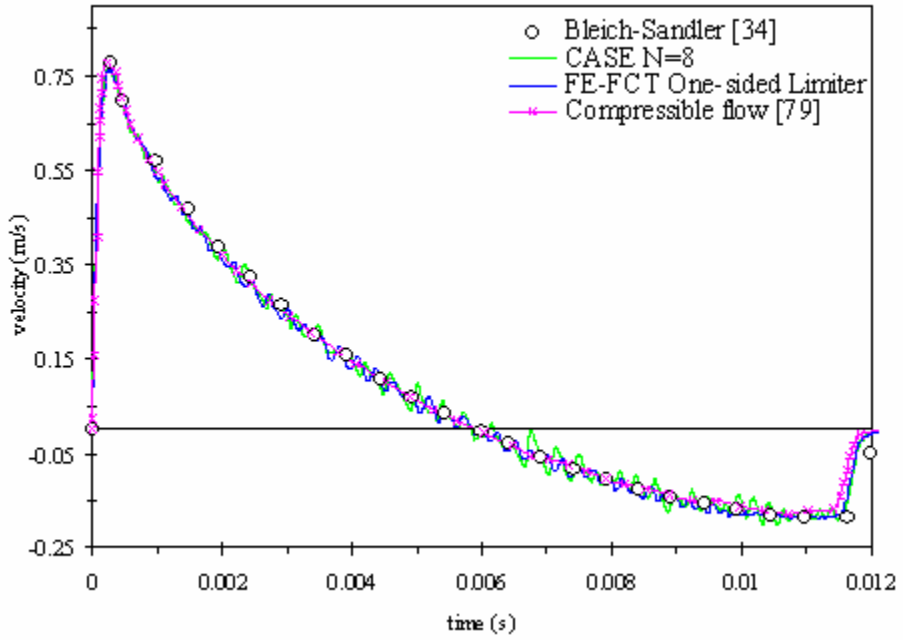

(b)

Figure 5.17 Bleich-Sandler problem results for the velocity of m_1 using CAFE, CASE, FE-FCT, and the compressible flow model in [79]

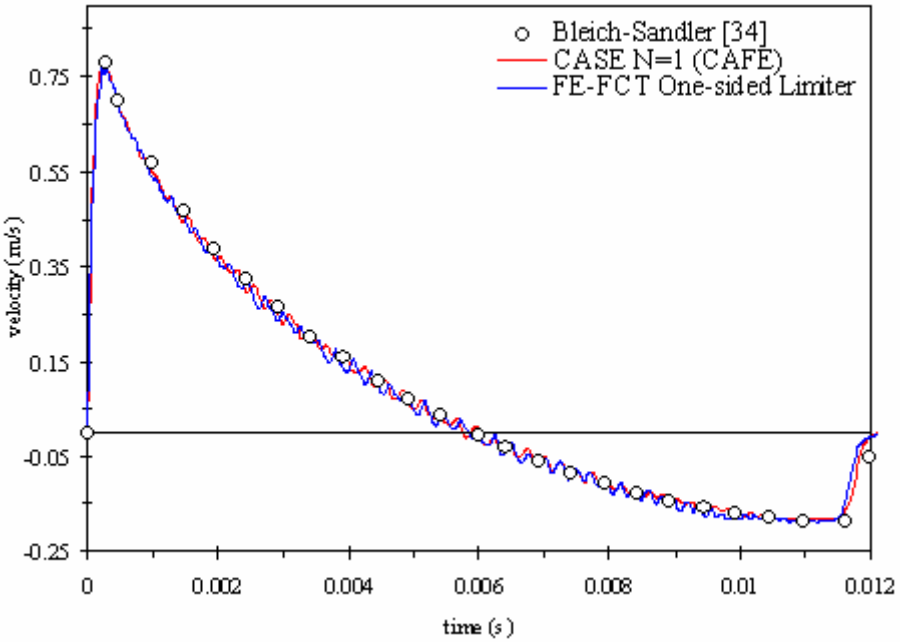

Figure 5.18 Bleich-Sandler problem results for the velocity of m_1 using CAFE (CASE N=1) with reduced damping (β = 0.25) and FE-FCT (η_D= 0.125, η_A=0.09)

5.4 Summary

In this chapter, we compared finite elements (CAFE), spectral elements (CASE), and an FE-FCT algorithm first in terms of its ability to capture a step exponential wave in an acoustic fluid and then in terms of its ability to capture cavitation in a fluid-structure interaction problem. In the wave propagation problem, we saw that spectral elements produce large oscillations in some regions of the solution but overall cause less dispersion of the wave and therefore give more accurate solutions. We demonstrated that oscillations that result from wave propagation in both finite and spectral element solutions can be effectively smoothed by applying artificial damping to the fluid but that this smoothing degrades the accuracy of the solution. We found that when the time step is taken as less than the critical limit incorporation of an FE-FCT algorithm with a strong flux limiter gave a smooth solution to the wave propagation problem and maintained the un-damped accuracy of the spectral element solutions.

When each method was applied to a fluid-structure interaction problem, we found the FE-FCT method with strong flux limitation failed to reduce oscillations in the structural

response, making the algorithm unsuitable for cavitation problems. Spectral element solutions had larger structural oscillations compared to finite element solutions, even with the application of artificial damping. These increased oscillations are problem dependent in terms of their impact on the structural response. A significant difference between finite and spectral element solutions was observed for the two degree-of-freedom mass-spring oscillator problem, indicating a connection between each method's ability to capture wave propagation and its ability to capture the cavitation response of a structure. By reducing the amount of damping used with finite elements the difference between finite element and spectral element solutions is reduced, especially in the Bleich-Sandler problem. When damping is reduced in the finite element model, the effect of oscillations on both wave propagation and the structural response can be reduced by incorporation of a one-sided flux limiter to the FE-FCT algorithm. However, the effect of the limiter is observed only for solutions obtained with low DOF meshes.

A comparison between both acoustic fluid and compressible flow models revealed that the structural response to cavitation is sensitive to how artificial damping and the ghost fluid method is applied to the fluid. This is especially true for the response to small secondary cavitation regions that occur in the fluid. However this difference in behavior is problem dependent as no such difference is observed in the solution to the Bleich-Sandler problem.

In the next chapter, we study the same two degree of freedom mass spring oscillator problem solved in Sec. 5.2 using different values of m_1 and m_2 to further asses the effect of increased oscillations using spectral elements, the effect of how damping is applied to the fluid, and also to determine what errors in the fluid model cause the differences observed between spectral and finite elements.

CHAPTER 6 ASSESSMENT

In the previous chapter, we found that CASE solutions differed significantly from CAFE solutions in wave propagation problems, but the difference was problem dependent for fluid-structure interaction problems with cavitation. Furthermore, it was observed that the severity of increased oscillations in the structural response are also problem dependent and that in some problems reducing the amount of damping used with CAFE can give results that match spectral element results. We also saw how an artificial damping, applied to the fluid model, can cause a discrepancy in the cavitation response of the structure.

This chapter further investigates the above findings by solving the same two degree of freedom mass spring oscillator Sec. 5.2 using different values of m_1 and m_2 with both finite and spectral elements on a two-dimensional grid. We demonstrate how oscillations affect the structural response over a range of problems, the need to accurately capture cavitation, and determine which method is best suited for far-field UNDEX modeling.

6.1 Problem Setup

In this chapter, we study the same two degree-of-freedom mass-spring oscillator structure used in Section 5.2. However, in this chapter we use a 2D mesh and vary the ratio, m_2/m_1 from 0 to 25. Again the problem, shown in Fig. 6.1 consists of a structure with masses m_1 and m_2, displacements $d_1(t)$ and $d_2(t)$, sitting on top of a column of fluid with depth L and width Δx. The masses are connected by a spring with spring constant k and are initially at rest.

In the y-direction the fluid has depth L=3.0 m, a width Δx=0.15 m in the x-direction, and an out of plane thickness of 1 m. Following [78], we take ρ_o=1025 kg/m^3 and c=1500 m/s. The structure has a draft, T= 5.08 m, a total mass, m_1+m_2=781.05 kg, and $k=(10\pi)^2 m_2$ N/m. Note the total mass of the structure is decreased from the 1D problem due to the addition of the fluid column width which reduces the volume of fluid displaced by the structure.

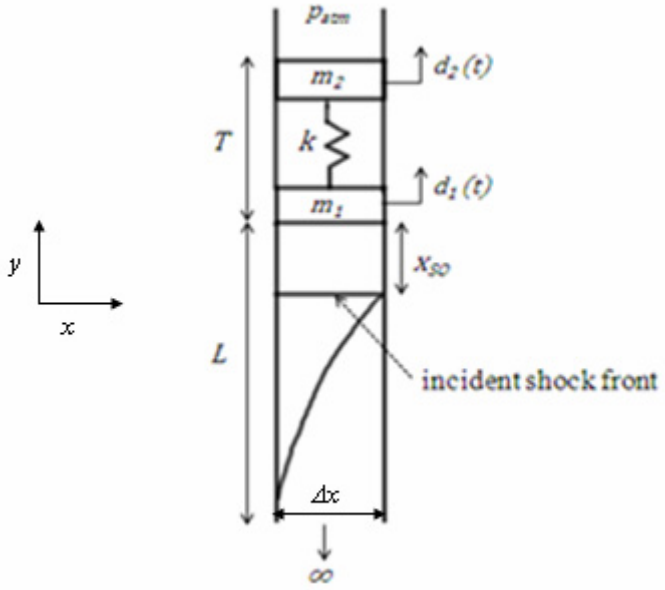

Figure 6.1 Schematic of the mass-spring oscillator UNDEX problem on a 2D grid

The peak pressure of the incident shock wave is again P_{peak}=16.12 MPa, the decay constant is τ=0.423 ms, and x_{so}=0 m. The known incident field for each ratio of m_2/m_1 considered is given as

$$p_{inc}\left(\vec{X},t\right)=P_{peak}\exp\left[-\frac{t+\frac{\vec{X}-x_{so}}{c}}{\tau}\right]H\left(t+\frac{\vec{X}-x_{so}}{c}\right), \tag{6.1}$$

where $H(t)$ is the Heaviside function and $\vec{X}$ represents the global (x,y) 2D Cartesian coordinate.

This series of problems was solved in 1D using CAFE [38] and on a 2D grid using the pressure formulation grid in [78]. We solve it in this chapter with both CASE and the pressure formulation of Chapter 4 using the scattered field fluid model, the plane wave approximation as the NRB, and the non-conformal coupling method in Chapter 3 to link the fluid and structure. Because it was found in Sections 5.2 and 5.3 that the FE-FCT algorithm was not applicable to fluid-structure interaction problems with cavitation, we use the term pressure formulation in this chapter to signify the use of the pressure

formation in Chapter 4 without the addition of the full flux-corrected transport algorithm. Artificial diffusion is still applied to the pressure formulation models in this chapter, by applying the diffusion stage (eqs. 4.22 and 4.23) of the FE-FCT algorithm in the direction of the propagating plane shock wave (i.e. the y-direction in Fig. 6.1). Thus the transported diffused solution in eq. 4.23 becomes the "corrected" solution in eq. 4.26. This process is paramount to taking η_A=0.0 in the FE-FCT algorithm. We note that the application of diffusion in this manner on a 2D grid causes a significant increase in computational time, which is not desirable for far-field UNDEX problems. However, we include the results in this chapter to study how the application of artificial damping/diffusion can affect the structural response.

For all methods we use a base fluid mesh of 1 element in the *x*-direction and 20 elements in the *y*-direction which results in a base fluid mesh of 20 square elements with sides of 0.15m. We refine this base mesh using h-refinement for the N=1 CASE models and pressure formulation models and p-refinement for the higher-order CASE models. As an example, taking N=4 on the base mesh gives 405 DOF. Thus for the N=1 CASE model and pressure formulation model, we use 4 elements in the *x*-direction and 80 elements in the *y*-direction to obtain the same 405 DOF level of refinement. A table of the polynomial order N used to refine the higher-order CASE models in this chapter and their corresponding total DOF is given in Table 6.1.

Table 6.1 Table of total fluid DOF and the corresponding order of CASE p-refinement of the 20 element base mesh used for results in Chapter 6

CASE Order	Total DOF
N=3	244
N=4	405
N=6	847
N=8	1449

The same lumped mass and spring structure model used in Sections 5.2 and 5.3 is used for the 2D model and is integrated in time with the central difference method. For all methods studied the simulation is run to a termination time of 0.16 s and the time step in the fluid is set at half the critical limit (see eq. 3.41).

To assess each method we compare the velocity response of m_1, the displacement response of m_1, and the history of dynamic densified condensation, s, in the fluid for both the CASE and pressure formulation results compared to a benchmark solution. An evaluation of CASE velocity response histories using a highly refined CAFE benchmark solution was made in [26,44,45]. In this chapter, the highly refined benchmark solution is found by solving each m_2/m_1 problem with a N=1 CASE 12002 DOF 2D fluid mesh with β=0.25 and the time step set to half the critical limit. We make a numerical assessment of a method's ability to reproduce the benchmark solution by comparing the L_2 error norm, which we define as:

$$L_2 = \frac{\sqrt{\int_0^{t_{term}} \left[f_{benchmark}(t) - f_{computed}(t) \right]^2 dt}}{\sqrt{\int_0^{t_{term}} \left[f_{benchmark}(t) \right]^2 dt}}, \tag{6.2}$$

where $f_{benchmark}$ is the benchmark solution and $f_{computed}$ is the computed solution. Note that the integrals in eq. 6.2 are approximated numerically, using composite trapezoidal integration as in [81].

6.2 m_2/m_1=0 Results and Discussion

6.2.1 β = 0.25 and η_D= 0.020

First we present results for the m_2/m_1=0 case. Figure 6.2a and 6.2b gives results for the velocity of m_1 using 405 DOF and 1449 DOF respectively. Both fluid meshes in Fig. 6.2 use β = 0.25 for CASE and η_D= 0.020 for the pressure formulation. In the benchmark solution, the mass, m_1, reaches a kick-off velocity of ~2 m/s at which point the velocity begins to decrease as cavitation begins. At t=0.13s there is a sharp rise in velocity which signifies the arrival of the cavitation closure pulse at m_1.

The results shown in Fig. 6.2 are in excellent agreement with the benchmark solution, with the only noticeable difference occurring at t=0.13s. Furthermore, Fig 6.2 shows that the velocity response does not exhibit any visible oscillations for any of the methods

used. Looking at the table of L_2 error norms in Table 6.2 we see that, although visually the solutions are very similar, for each level of mesh refinement the higher order CASE meshes give results closer to the benchmark solution than either the *N=1* CASE or the pressure formulation. Note the pressure formulation meshes give smaller error norms when compared to the *N=1* CASE results due to the choice of η_D.

Figure 6.3a and 6.3b gives results for the displacement of m_1 using 405 DOF and 1449 DOF respectively. Again, the results of both fluid meshes in Fig. 6.3 are in excellent agreement with the benchmark solution. The L_2 error norms for the displacement of m_1 are given in Table 6.3, which shows that the higher order CASE meshes give results closer to the benchmark solution. However, we note for each mesh the error norms for the displacement results are lower than those obtained for the velocity results. For example, the maximum error norm for the velocity results was, $L_2 \approx 0.05439$, for the 405 DOF *N=1* CASE mesh. For this same fluid mesh the error norm for the displacement results is reduced to $L_2 \approx 0.01743$.

Table 6.2 L_2 error norms for the velocity of m_1 (m_2/m_1=0 case) with $\beta = 0.25$ for CASE and $\eta_D = 0.020$ for the pressure formulation

Fluid DOF	CASE N=1	Pressure	CASE
244	0.05167	0.03355	0.02750
405	0.05493	0.04119	0.03328
847	0.05325	0.04275	0.03023
1449	0.04890	0.03972	0.01957

Table 6.3 L_2 error norms for the displacement of m_1 (m_2/m_1=0 case) with $\beta = 0.25$ for CASE and $\eta_D = 0.020$ for the pressure formulation

Fluid DOF	CASE N=1	Pressure	CASE
244	0.01578	0.01044	0.00993
405	0.01744	0.01248	0.01142
847	0.01786	0.01391	0.01057
1449	0.01683	0.01335	0.00695

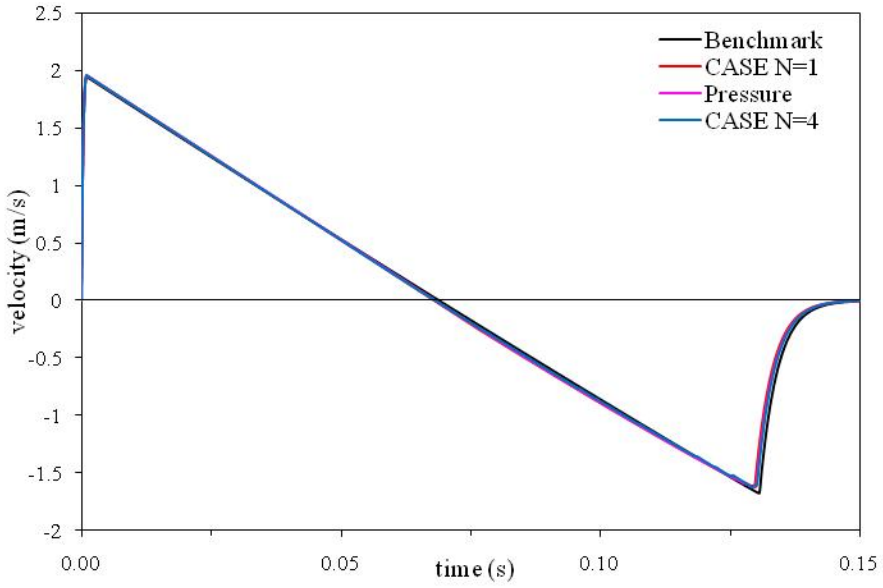

(a)

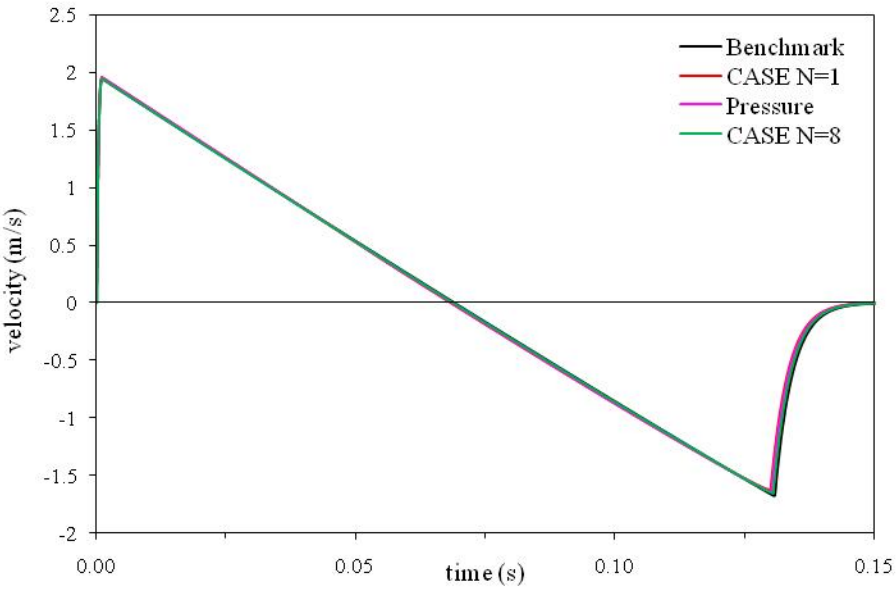

(b)

Figure 6.2 Velocity of m_1 for the m_2/m_1=0 case using 405 DOF (a) and 1449 DOF (b) with β = 0.25 for CASE and η_D= 0.020 for the pressure formulation

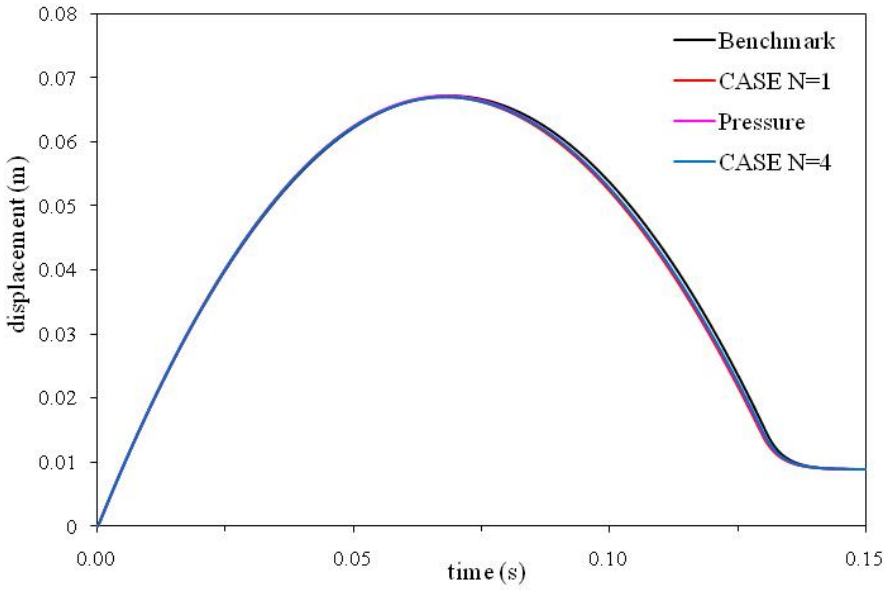

(a)

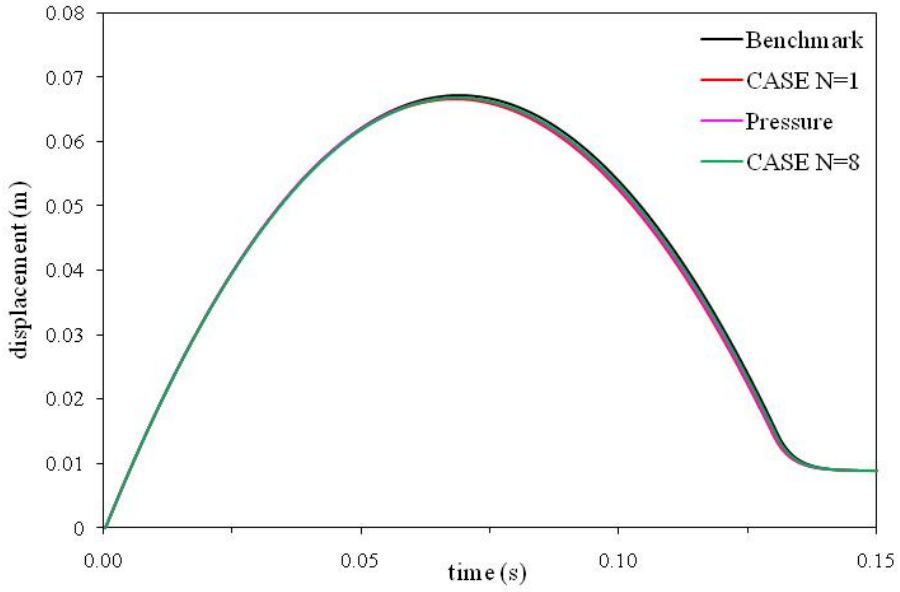

(b)

Figure 6.3 Displacement of m_1 for the m_2/m_1=0 case using 405 DOF (a) and 1449 DOF (b) with β = 0.25 for CASE and η_D= 0.020 for the pressure formulation

In the introduction to this chapter we noted the need to understand how well each method captures cavitation in the fluid and what affect this has on the structural response. To accomplish this, we compare plots of dynamic densified condensation, s, in the fluid at various times during the inception, growth, and collapse of the cavitation region. This is shown in Fig. 6.4 for the 405 DOF fluid meshes and Fig. 6.5 for the 1449 DOF fluid meshes. In both Figs. 6.4 and 6.5, s is plotted at t=0.002s, t=0.02s, t=0.04s, and t=0.10s. At t=0.002s, the scattered wave front has just arrived at the NRB. At t=0.02s the upper cavitation boundary in the benchmark solution is clearly visible as the sharp change in s at a depth of 0.06m and the lower cavitation boundary by the sharp positive jump at a depth of 1.125 m. At t=0.04s, the upper cavitation boundary in the benchmark solution has propagated deeper into the fluid and the lower cavitation boundary has moved closer to the fluid-structure interface as the cavitation region begins to contract. At t=0.10s both the upper and lower cavitation boundaries in the benchmark solution have again moved closer together as the cavitation region nears collapse.

Inspection of Figs. 6.4 and 6.5 show that at t=0.002s each of the methods give results that agree well with the benchmark solution, except near the fluid-structure interface (x=0m) and the NRB (x=3m). Note that at this time, both the higher-order CASE solutions exhibit oscillations not seen in the N=1 CASE and pressure formulation results. As time increases, both Figs. 6.4 and 6.5 show that each of the methods fails to capture both the magnitude and sharpness of the cavitation boundaries seen in the benchmark solution. As in the wave propagation problem in Chapter 5, the cavitation boundaries are smeared and there is a loss in the magnitude of dynamic densified condensation in the cavitation region.

Comparing the L_2 error norms, which are given in parenthesis in the legends of Figs. 6.4 and 6.5, we see that for each model the error in the fluid is much larger than the error in the structural response and grows with time. For example, in the N=1 CASE 405 DOF results the error norm goes from 0.0688 at t=0.002s to $L_2 \approx 0.7336$ at t=0.10s. For the 405 DOF models, the N=4 CASE results give better results than both the N=1 CASE and pressure formulation.

As the mesh is refined to 1449 DOF, the N=8 CASE model, in Fig. 6.5, captures both the shape and magnitude of the cavitation region better than the other meshes, clearly

giving superior results in the fluid. The N=8 CASE model reduces the error norm at t=0.10s from $L_2 \approx 0.6205$ in the N=4 CASE model to $L_2 \approx 0.3544$ in the N=8 CASE model. The refinement of both the N=1 CASE and pressure formulation, improve the solution for these models. Reducing the error norm at t=0.10s from $L_2 \approx 0.7336$ to $L_2 \approx 0.6383$, in the N=1 CASE model and from $L_2 \approx 0.7037$ to $L_2 \approx 0.5982$ in the pressure formulation mesh. However, even with refinement, all the methods show large amount of error in the fluid that is not seen in the velocity and displacement response of the structure.

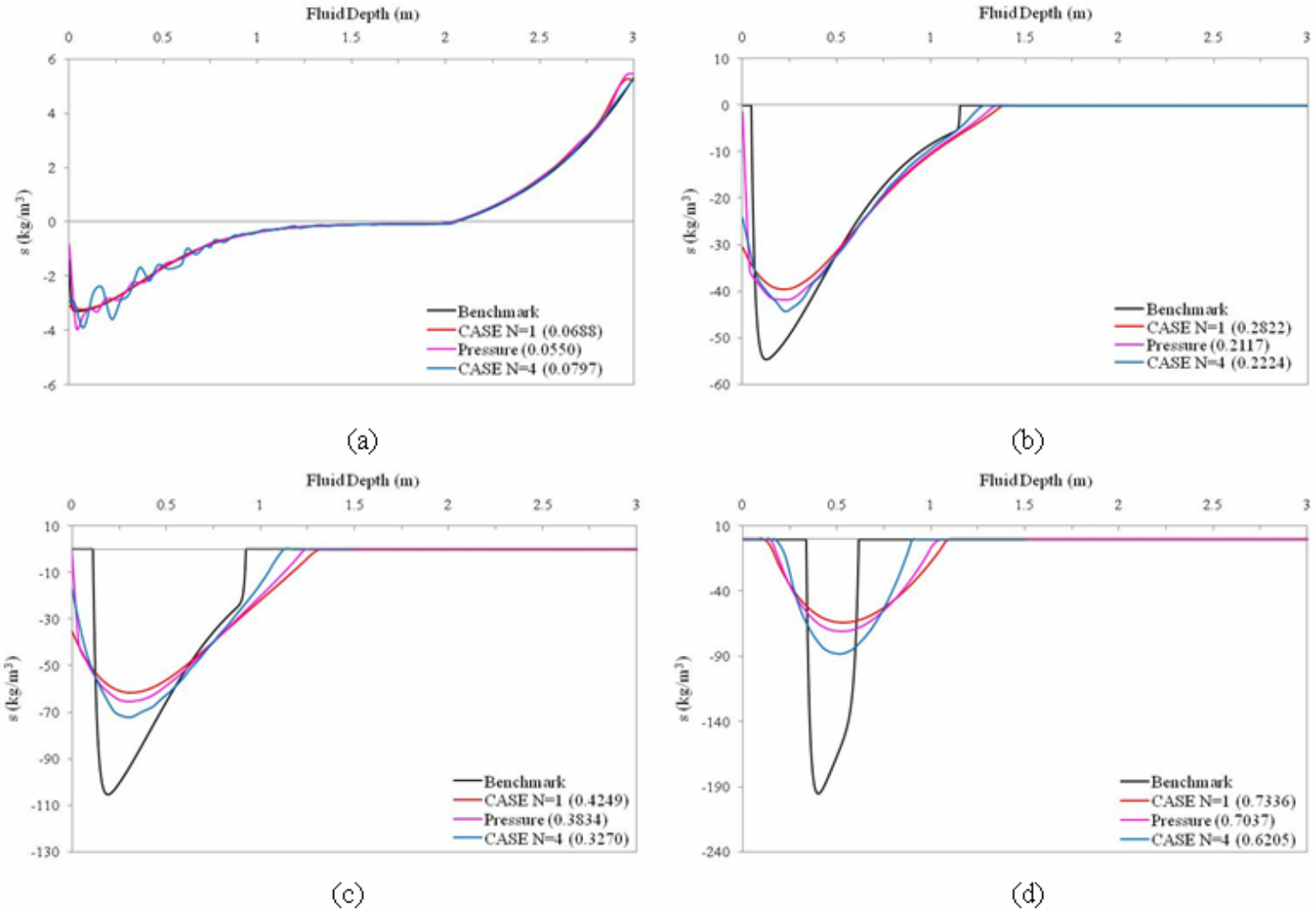

Figure 6.4 Dynamic densified condensation in the fluid at t=0.002 s (a), t=0.02 s (b), t=0.04 s (c), and t=0.10 s (d) for the m_2/m_1=0 case using 405 DOF with β = 0.25 for CASE and η_D= 0.020 for the pressure formulation

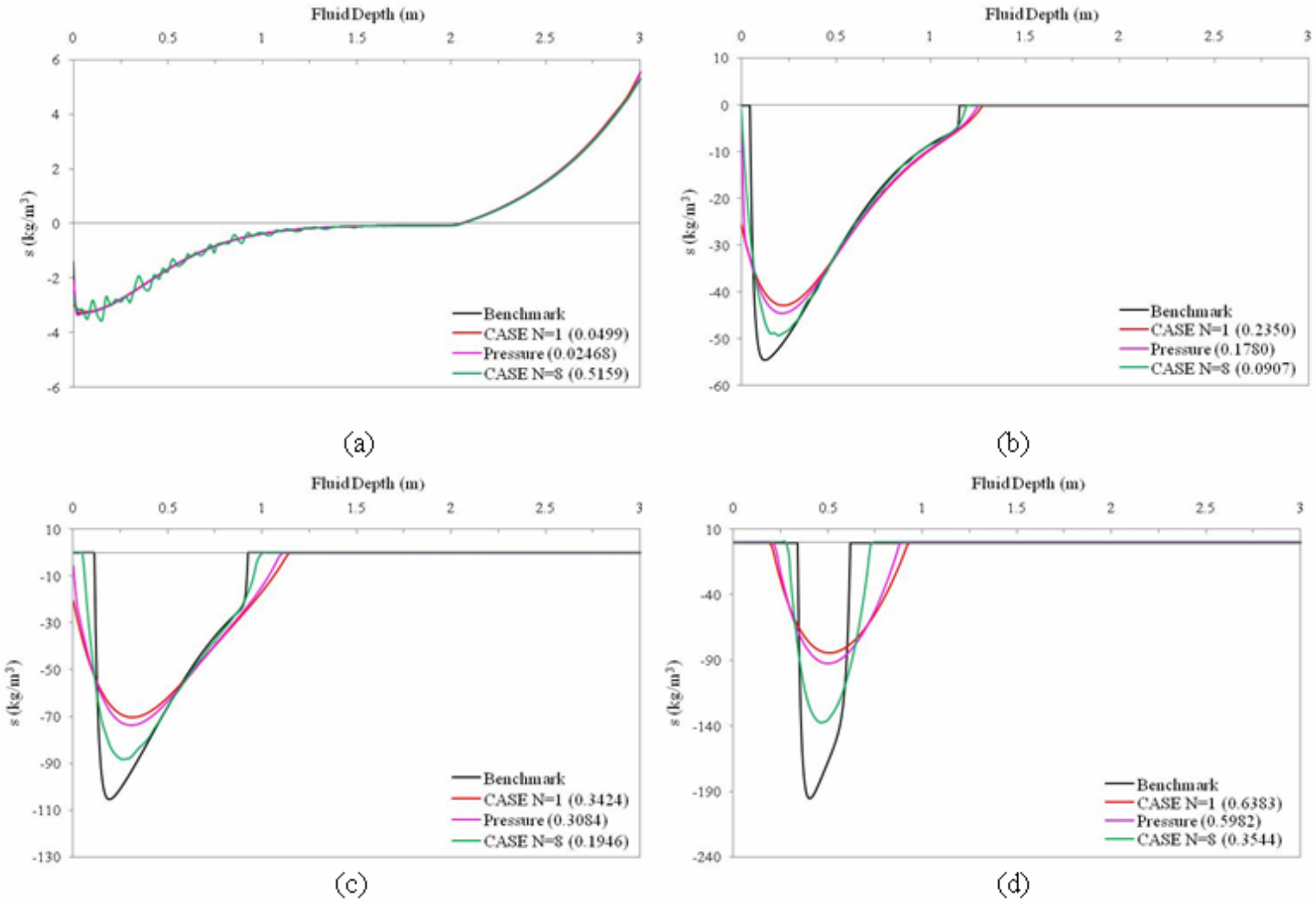

Figure 6.5 Dynamic densified condensation in the fluid at t=0.002 s (a), t=0.02 s (b), t=0.04 s (c), and t=0.10 s (d) for the m_2/m_1=0 case using 1449 DOF with β = 0.25 for CASE and η_D= 0.020 for the pressure formulation

The difference in error norms between the fluid and structural response indicate two phenomena. First, when we consider that no oscillations occur in the structural response and that the error norms for all models studied are reasonably low (e.g. the maximum L_2 in the velocity responses is 0.055), it indicates that the structure in the m_2/m_1=0 case is not as sensitive to the fluid as the problems studied previously in Chapter 5. Secondly, the large errors in the fluid are an indication that the cavitation model in both CASE and the pressure formulation do not allow any disturbances in the fluid below the cavitation region to interact with the structure. Thus when cavitation is present in the fluid the

capture of the propagation of the upper cavitation boundary is critical, as the structural response is driven by the fluid between the structure and upper cavitation boundary [38].

Looking again at Figs. 6.4 and 6.5 we see that as time increases the largest discrepancy between the benchmark, CASE, and pressure formulations occurs in the capture of the lower cavitation boundary. There is a smaller difference in the capture of the upper cavitation boundary, which is the boundary that contributes most to the response of the structure [38]. The results of each model in Figs. 6.4 and 6.5 show that at all times the upper cavitation boundary is predicted to be closer to the fluid-structure interface than in the benchmark solution. This is especially true at t=0.02s in Figs. 6.4b and 6.5b. Although not clearly visible in Fig. 6.2, this causes the velocity of m_1 to decay faster than in the benchmark solution, as the mass remains in an extended state of free fall [38].When coupled with the dissipation of dynamic densified condensation in the cavitation region, the faster velocity decay of m_1 causes the cavitation region to re-pressurize (i.e. close) faster. In the m_2/m_1=0 problem this results in the small differences in the arrival times of the cavitation closure pulse at t=0.13s in the velocity response (Fig. 6.2). Figs. 6.4 and 6.5 show that the higher-order CASE models capture the upper cavitation boundary and the magnitude of densified condensation better than both the N=1 CASE and pressure formulation methods. Thus, they give superior structural response results for a given level of mesh refinement.

6.2.2 β = 0.50 and η_D= 0.035

In this section we look at the effect of increasing the amount of artificial damping/diffusion in the fluid for the m_2/m_1=0 case. For all meshes in this section we use β = 0.50 for CASE and η_D= 0.035 for the pressure formulation. Figures 6.6a and 6.6b give results for the velocity of m_1 using 405 DOF and 1449 DOF respectively. In Fig. 6.6a a noticeable difference between the 405 DOF models and the benchmark solution is observed. In Fig. 6.6b, this difference is decreased for the 1499 DOF N=8 CASE model, which gives the result that is closest to the benchmark solution. This is confirmed numerically by comparing the L_2 error norms for the velocity response in Table 6.4. Note that with the increase in damping both the N=1 CASE and pressure formulation give better results than the higher-order CASE solution at 244 DOF, and the pressure formulation gives the best results at 405 DOF. The pressure formulation results are

attributed to the choice of η_D=0.035, which does not damp the fluid as much as the choice of β = 0.50 for the CASE models. As the mesh is refined further, Table 6.4 shows that the higher-order CASE models with 847 DOF and 1449 DOF give the more accurate results, as in the β = 0.25 results.

Overall the error norm for each level of mesh refinement in Table 6.3 shows an increase when compared to the results in the previous section when β = 0.25 and η_D= 0.020. For example, the error norm of the N=8 CASE mesh velocity response with β = 0.25 is increased from $L_2 \approx 0.0195$ to $L_2 \approx 0.0353$ by increasing β to 0.50. Similar increases are seen for the other models as well.

The results for the displacement of m_1 using 405 DOF and 1449 DOF are given in Figs. 6.7a and 6.7b respectively. As in the velocity results, the increase in artificial damping/diffusion causes a noticeable difference in the displacement of m_1 when compared to the benchmark solution for each of the meshes in Fig. 6.7. The L_2 error norms for the displacement in Table 6.4 show both the N=1 CASE and pressure formulation give better results than the higher-order CASE solution at 244 DOF, and the pressure formulation gives the best results even at 405 DOF. However, as the mesh is further refined, the higher-order CASE results become superior.

Table 6.4 L_2 error norms for the velocity of m_1 (m_2/m_1=0 case) with β = 0.50 for CASE and η_D= 0.035 for the pressure formulation

Fluid DOF	CASE N=1	Pressure	CASE
244	0.07434	0.04852	0.07780
405	0.07767	0.05728	0.06978
847	0.07635	0.06129	0.05041
1449	0.07212	0.05933	0.03534

Compared to the results with β = 0.25, increasing β to 0.50 causes an increase in the displacement response error norms for each of the models in Table 6.5. Using the previous example of the error norm of the N=8 CASE mesh, the displacement response L_2 error norm is increased from $L_2 \approx 0.00694$, with β = 0.25, to $L_2 \approx 0.0127$, with β = 0.50. Note that as in the previous section, the error norms found in the displacement results are less than those observed in the velocity response.

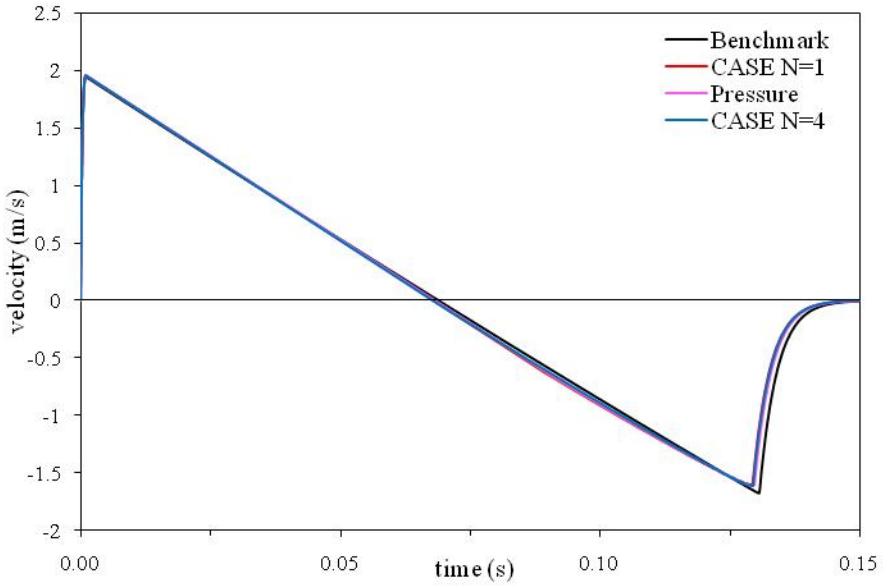

(a)

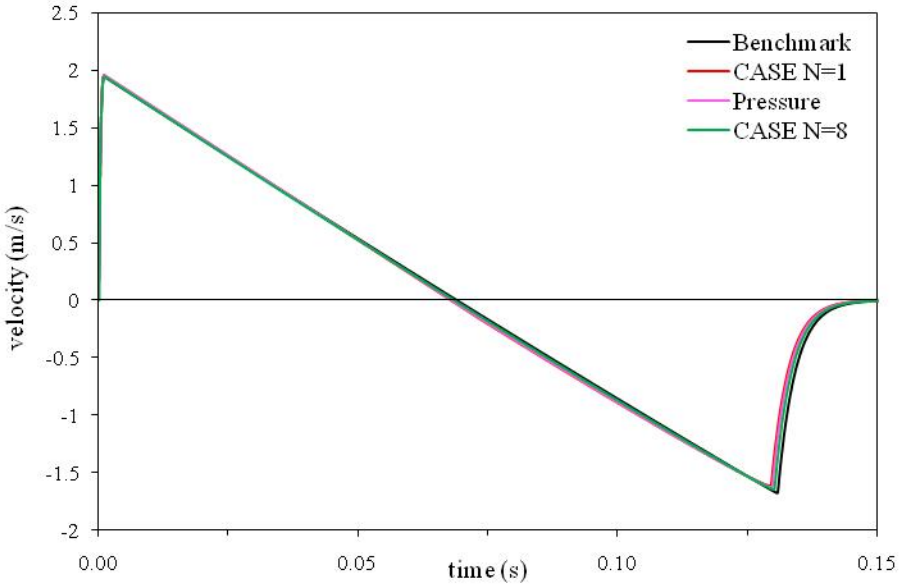

(b)

Figure 6.6 Velocity of m_1 for the m_2/m_1=0 case using 405 DOF (a) and 1449 DOF (b) with β = 0.50 for CASE and η_D= 0.035 for the pressure formulation

The velocity and displacement results show that increasing the amount of damping/diffusion in the fluid increases the error in the structural response when compared to the benchmark solution. Now we wish to determine the effect of increased damping/diffusion on cavitation capture in the fluid. To do this we again plot dynamic densified condensation in the fluid at t=0.002s, t=0.02s, t=0.04s, and t=0.10s. Figure 6.8 shows results for the 405 DOF fluid models and Fig.6.9 shows results for1449 DOF fluid models.

Table 6.5 L_2 error norms for the displacement of m_1 (m_2/m_1=0 case) with β = 0.50 for CASE and η_D= 0.035 for the pressure formulation

Fluid DOF	CASE N=1	Pressure	CASE
244	0.02189	0.01356	0.02551
405	0.02414	0.01669	0.02401
847	0.02519	0.01950	0.01802
1449	0.02455	0.01973	0.01270

In Chapter 5 (Section 5.1.2) we saw for the wave propagation problem that increasing the amount of artificial damping/diffusion in the fluid caused increased smearing of the wave front and an increase in the loss of peak magnitude of the wave. Results in both Figs. 6.8 and 6.9 shows that these same effects are observed in the capture of cavitation. Using the L_2 error norms given in the legend of each plot, we see that again for the 405 DOF model (Fig. 6.8) the N=4 CASE mesh gives superior results in the fluid at each time except t=0.002s and t=0.02s where, like in the structural response results, the pressure formulation gives better results. Again, this is attributed to the choice of η_D which damps the fluid motion less than β=0.50 does. Refining the mesh, Fig. 6.9 shows the N=8 CASE results, give a large improvement over both the N=1 CASE and pressure formulations at times of t=0.02s, t=0.04s, and t=0.10s in Fig. 6.9. Thus, as in the structural response results the higher-order CASE results are superior for higher degrees of mesh refinement. Note in Figs. 6.8a and 6.9a that the increase in artificial damping smoothes the oscillations in the N=4 and N=8 CASE solutions at t=0.002 s that were seen with β = 0.25 in Figs. 6.4a and 6.5a.

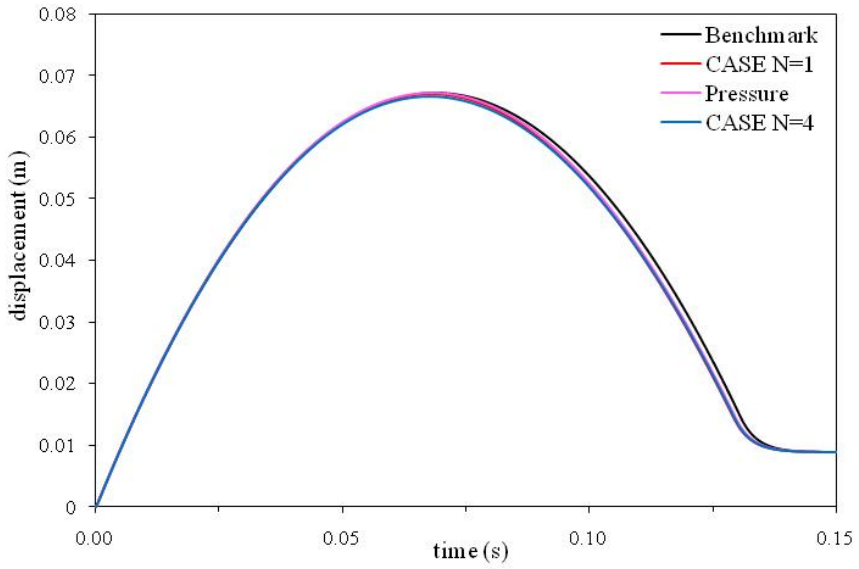

(a)

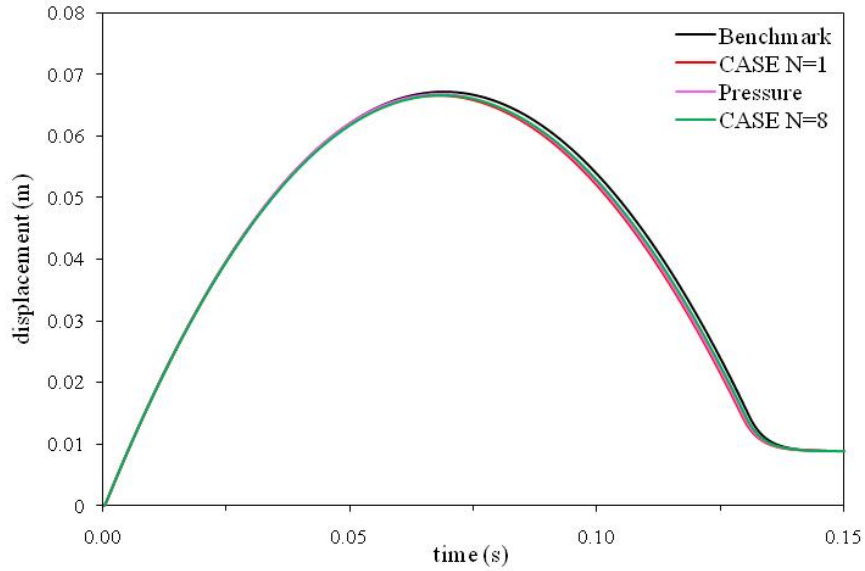

(b)

Figure 6.7 Displacement of m_1 for the m_2/m_1=0 case using 405 DOF (a) and 1449 DOF (b) with β = 0.50 for CASE and η_D= 0.035 for the pressure formulation

As in the structural response results, the net effect of increasing β in the fluid is an increase in the cavitation capture error. This is illustrated by comparing the dynamic densified condensation using the N=4 CASE mesh in Fig. 6.8 to the same mesh with β = 0.25 (Fig. 6.4). Initially there is a reduction in the L_2 error norm, from $L_2 \approx 0.0797$ to $L_2 \approx 0.0518$, that is attributed to the reduction in oscillations observed in the β = 0.25 results. As time increases however, the increase in error norm also increases. Going from $L_2 \approx 0.2224$ to $L_2 \approx 0.2618$ at t=0.02 s and from $L_2 \approx 0.6205$ to $L_2 \approx 0.7004$ at t=0.10 s. Similar increases in the error norms due to the increase in β are observed for the other models shown in Figs. 6.8 and 6.9.

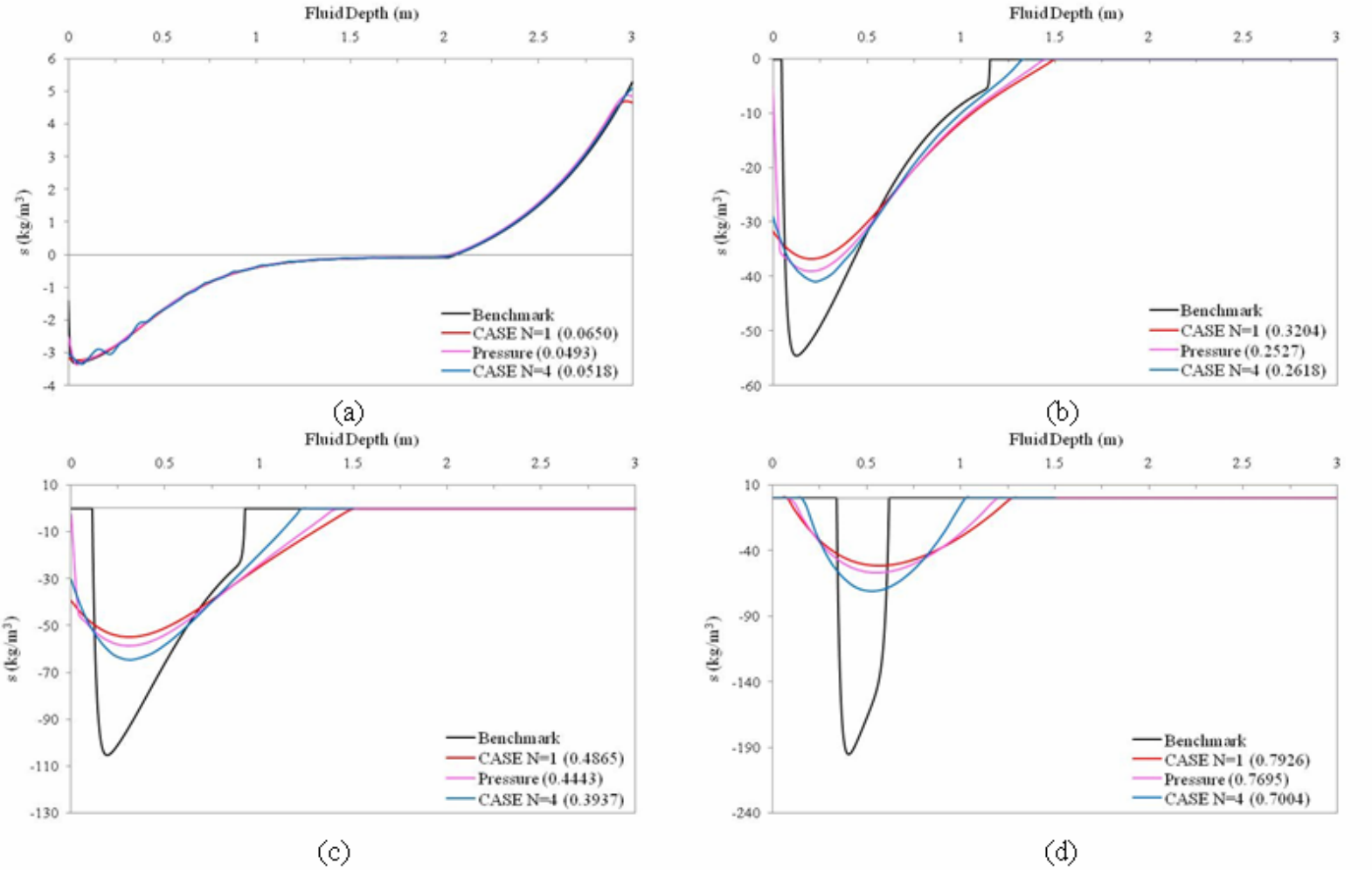

Figure 6.8 Dynamic densified condensation in the fluid at t=0.002 s (a), t=0.02 s (b), t=0.04 s (c), and t=0.10 s (d) for the m_2/m_1=0 case using 405 DOF with β = 0.50 for CASE and η_D= 0.035 for the pressure formulation

The effects of the error in cavitation capture on the structural response are more apparent for the increased damping/diffusion fluid models. Each model in Figs. 6.8 and 6.9 shows at all times the upper cavitation boundary is predicted to be closer to the fluid-structure interface than in the benchmark solution and there is a significant dissipation of densified condensation in the cavitation region.

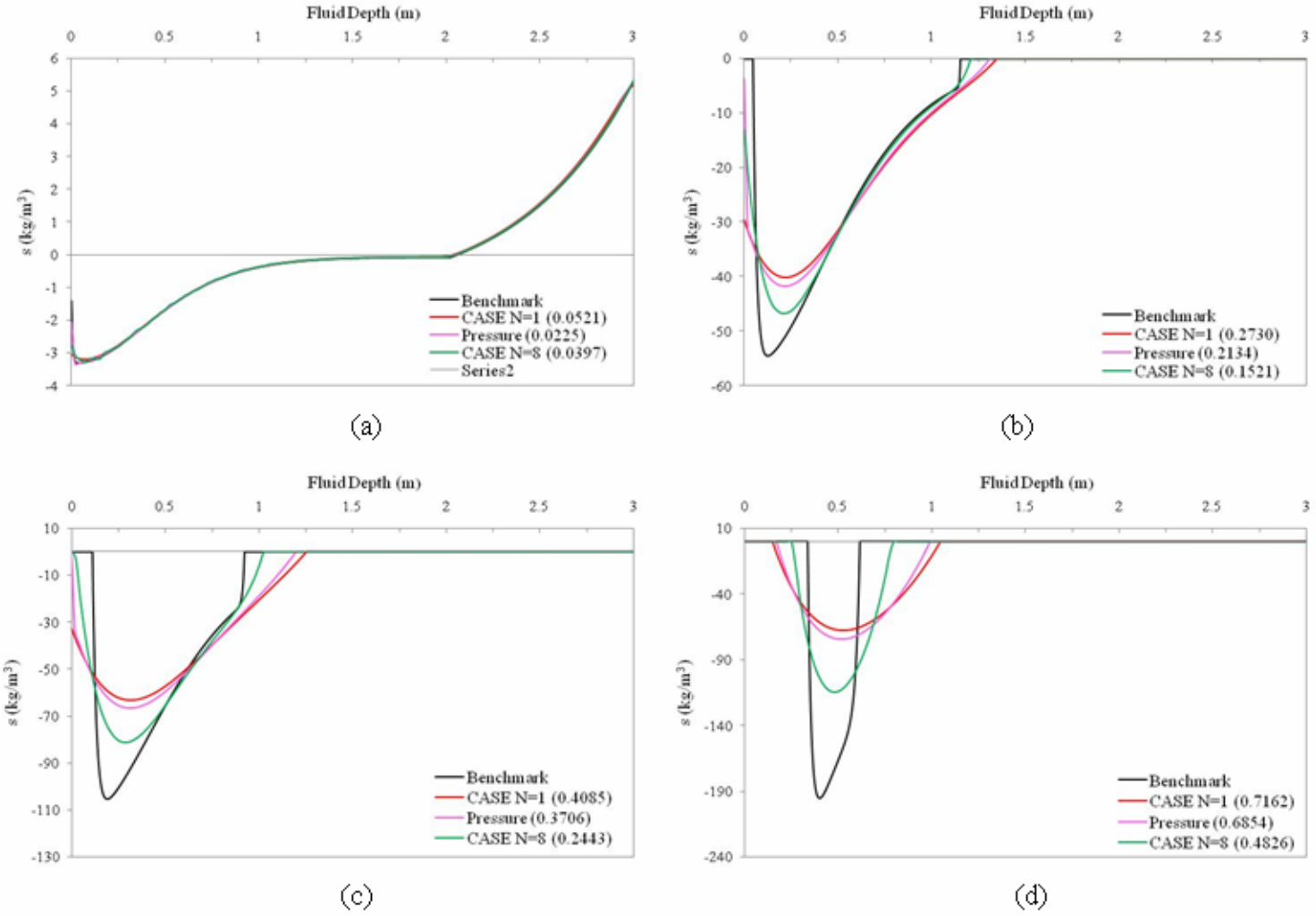

Figure 6.9 Dynamic densified condensation in the fluid at t=0.002 s (a), t=0.02 s (b), t=0.04 s (c), and t=0.10 s (d) for the m_2/m_1=0 case using 1449 DOF with β = 0.50 for CASE and η_D= 0.035 for the pressure formulation

As mentioned previously, this causes the cavitation region to re-pressurize faster. The faster re-pressurization of the fluid results in the faster arrival times of the cavitation closure pulse at t=0.13s in 405 DOF and 1449 DOF model velocity responses (Fig. 6.2).

This is most visible in the 405 DOF model results because the 405 DOF fluid models show a larger difference in the capture of the upper cavitation boundary and the magnitude of dynamic densified condensation when compared to the benchmark solution. Thus, the 405 DOF fluid models also give the larger difference in arrival time of the cavitation closure pulse in Fig. 6.2.

As in the previous section, the higher-order CASE models capture the upper cavitation boundary and the magnitude of dynamic densified condensation better than both the N=1 CASE and pressure formulation methods. Correspondingly, the higher-order CASE models capture the response of the structure closest to the benchmark model for the increased artificial damping/diffusion fluid models.

6.2.3 $\beta = 0.10$ and $\eta_D = 0.010$

In Chapter 5, we saw that for some problems it is possible to improve N=1 CASE results by simply reducing the amount of damping used. This was especially true in the Bleich-Sanlder results, where a reduction in damping gave results that closely matched the analytical solution and decreased oscillations when compared to an N=8 CASE solution. In this section, we look at the effect of decreasing the amount of artificial damping/diffusion in the fluid for the m_2/m_1=0 case.

Figures 6.10a and 6.10b gives results for the velocity and displacement of m_1, respectively, using 1449 DOF. Note that, in this section, all fluid meshes use β = 0.10 for CASE and η_D= 0.010 for the pressure formulation. For both the velocity and displacement of m_1 Fig 6.10 shows there is no visible difference between the benchmark solution and the N=1 CASE, pressure formulation, and N=8 CASE solutions. Looking at Tables 6.6 and 6.7 and comparing to the results in the previous two sections, each method shows that a reduction in the amount of artificial damping applied to the fluid mesh reduces both the velocity and displacement response L_2 error norm. For both velocity and displacement the higher-order CASE models give superior results for all levels of refinement.

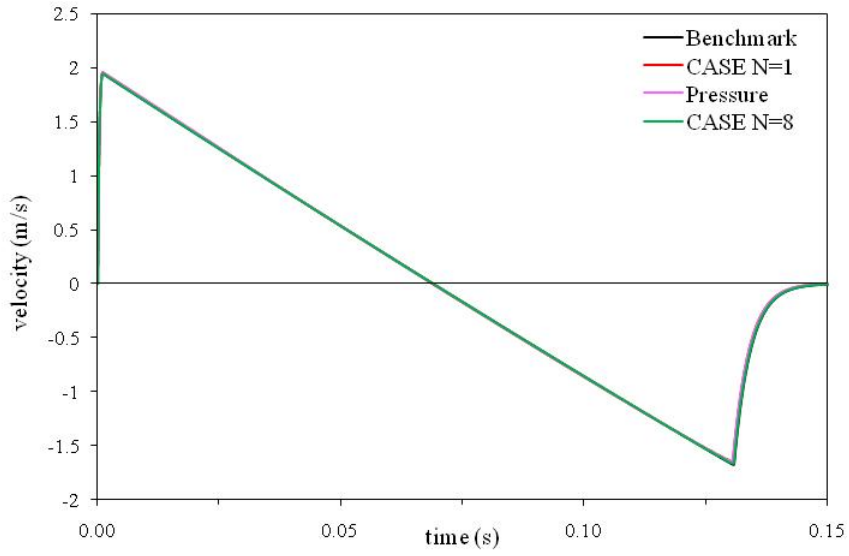

(a)

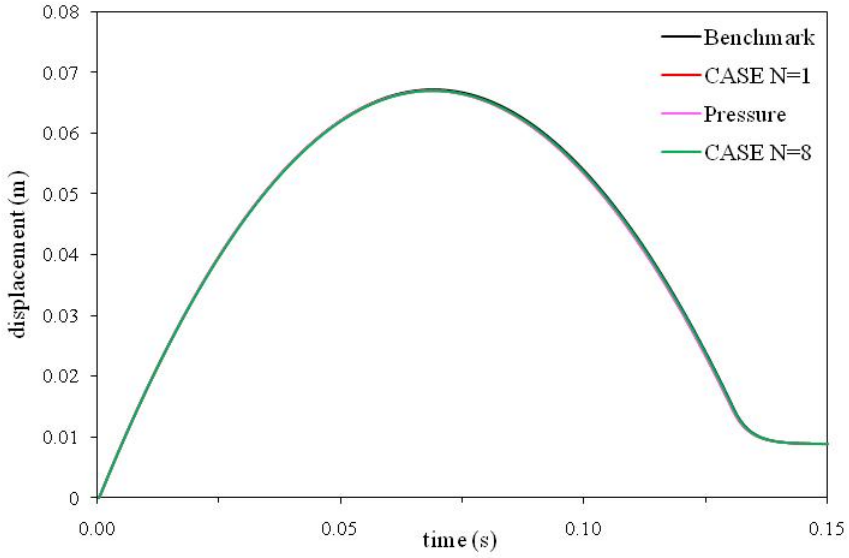

(b)

Figure 6.10 Velocity (a) and displacement (b) of m_1 for the m_2/m_1=0 case using 1449 DOF with β = 0.10 for CASE and η_D= 0.010 for the pressure formulation

Table 6.6 L_2 error norms for the velocity of m_1 (m_2/m_1=0 case) with β = 0.10 for CASE and η_D= 0.010 for the pressure formulation

Fluid DOF	CASE N=1	Pressure	CASE
244	0.01589	0.01316	0.01297
405	0.01886	0.01766	0.01343
847	0.01913	0.01912	0.00676
1449	0.01708	0.01719	0.00362

Table 6.7 L_2 error norms for the displacement of m_1 (m_2/m_1=0 case) with β = 0.10 for CASE and η_D= 0.010 for the pressure formulation

Fluid DOF	CASE N=1	Pressure	CASE
244	0.00693	0.00654	0.00486
405	0.00655	0.00600	0.00446
847	0.00640	0.00619	0.00230
1449	0.00576	0.00568	0.00118

Comparing the error norm for the 1449 DOF N=1 CASE fluid model with β = 0.10 (L_2≈0.01708), to the N=1 CASE models with β = 0.25, L_2≈0.01957, and β = 0.50, L_2≈0.00353, we confirm that lowering the amount of damping used with the N=1 CASE model can match the higher-order CASE solutions with larger amounts of damping. However, an inspection of Fig. 6.10a reveals, for the m_2/m_1=0, there is no benefit in reducing the amount of damping with the N=1 CASE mesh. This is because the same reduction in damping with the N=8 CASE mesh yields improved results (L_2≈0.003621) without any visible increase in oscillations in the velocity response.

Thus we conclude for the m_2/m_1=0 problem, higher-order CASE models will generally yield superior results without increasing oscillations when compared to both the N=1 CASE and the pressure formulation models for a given level of mesh refinement and a given amount of artificial damping.

6.3 m_2/m_1=1 Results and Discussion

6.3.1 β = 0.25 and η_D= 0.020

In this section, we present results for the m_2/m_1=1 case. Figures 6.11a and 6.11b gives results for the velocity of m_1 using 405 DOF and 1449 DOF respectively. Both fluid meshes in Fig. 6.11 use β = 0.25 for CASE and η_D= 0.020 for the pressure formulation. For the benchmark solution the mass, m_1, reaches a kick-off velocity of ~3.3m/s at which point the velocity begins to slope downwards as cavitation begins. The cavitation closure pulse re-loads m_1 at t=0.08 s causing a sharp increase in positive velocity. This second upward motion causes a second region of cavitation to form, whose closure pulse re-loads the structure at t=0.152s. The second closure pulse is not strong enough to cause a third cavitation region.

Figure 6.11a shows that there is a small difference between the N=4 CASE, N=1 CASE, and the pressure formulation solutions, when compared to the benchmark solution, between t=0.06s-0.085s and again at 0.152s. Note that the N=1 CASE and pressure formulation solutions are indistinguishable from each other at these times in Fig. 6.11a. The N=4 CASE solution has a small oscillation visible at 0.075s, but otherwise gives results closest to the benchmark solution. This is verified by looking at the L_2 error norms in Table 6.8. Note that as in the previous section, the pressure formulation meshes give smaller error norms when compared to the $N=1$ CASE results in Table 6.7 due to the choice of η_D.

As the mesh is refined to 1449 DOF in Fig. 6.11b, we see that the N=8 CASE solution agrees best with the benchmark solution, especially at 0.152 s, where there is a noticeable difference in the arrival of the second cavitation closure pulse when compared to the N=1 CASE and the pressure formulation solutions. Again, the N=1 CASE and the pressure formulation solutions are indistinguishable in Fig. 6.11b. Comparing the L_2 error norms (Table 6.8) of the N=8 CASE solution (L_2≈0.01808) to the N=1 CASE solution (L_2≈0.05604) and the pressure formulation solution (L_2≈0.04765) confirms the superiority of the N=8 CASE solution. In fact, the higher-order CASE solutions match the benchmark solution better than either the N=1 CASE or pressure formulation solutions for each level of mesh refinement in Table 6.8. Furthermore, the advantage of

the higher-order CASE solutions increases with mesh refinement as well. To illustrate this point, consider in Table 6.8 the error norm for the 244 DOF higher-order CASE mesh (N=3), L_2≈0.068221, is very close to the error norm of the 244 DOF pressure formulation mesh, L_2≈0.070137. When the mesh is refined to 1449 DOF, the difference between the higher-order CASE mesh (N=8), L_2≈0.01808, and the pressure formulation mesh, L_2≈0.04765, is much greater. This indicates the faster convergence of higher-order CASE models to the benchmark solution.

It is interesting to note that for each mesh in Table 6.8, the error norms are slightly increased when compared to the same meshes in the m_2/m_1=0 problem. For example, the 1449 DOF N=1 CASE solution goes from L_2≈0.0489 in the m_2/m_1=0 problem to L_2≈0.05604 in the m_2/m_1=1 problem. Likewise, the 1449 DOF N=8 CASE solution goes from L_2≈0.001957 in the m_2/m_1=0 problem to L_2≈0.01808 in the m_2/m_1=1 problem.

Table 6.8 L_2 error norms for the velocity of m_1 (m_2/m_1=1 case) with β = 0.25 for CASE and η_D= 0.020 for the pressure formulation

Fluid DOF	CASE N=1	Pressure	CASE
244	0.08593	0.07014	0.06822
405	0.07859	0.06593	0.05120
847	0.06578	0.05625	0.02983
1449	0.05604	0.04765	0.01808

The higher-order CASE solutions also give superior results for the displacement of m_1. This is shown in Fig. 6.12a and 6.12b, which show the displacement of m_1 for the 405 DOF and 1449 DOF meshes, and also in Table 6.8 which gives the L_2 error norm for each model used. There is a visible difference in the maximum displacements reached in response to the first and second cavitation regions between the 405 DOF solutions (which are all nearly the same in Fig. 6.12a) and the benchmark solution in Fig. 6.12a. This difference is reduced by refining the mesh to 1449 DOF in Fig. 6.12b. Clearly, form Fig. 6.12b and the error norm in Table 6.9, the N=8 CASE model (L_2≈0.006236) gives the best results. Note that, in Fig. 6.12b, the N=1 CASE and pressure formulation solutions are visually identical. Table 6.9 also shows that the higher-order CASE meshes give the best results for each level of mesh refinement and again give the fastest convergence to the benchmark solution as the mesh is refined.

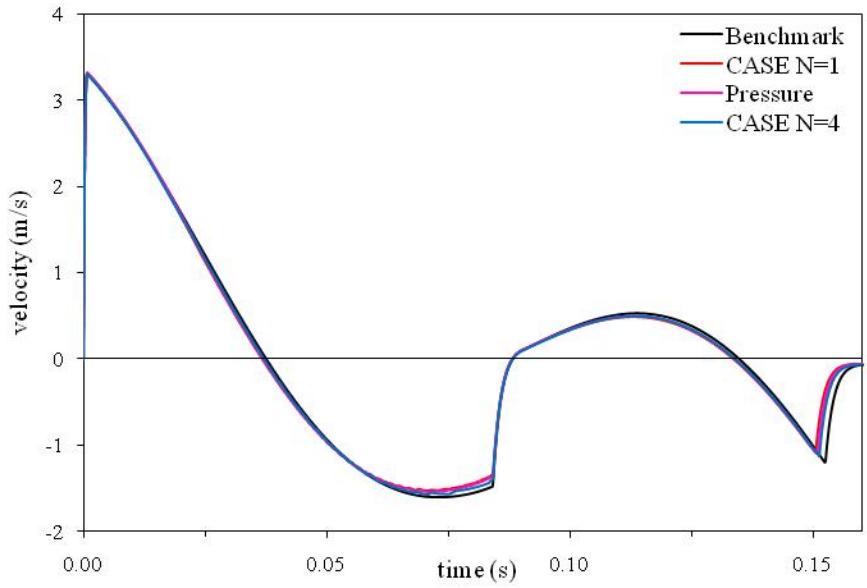

(a)

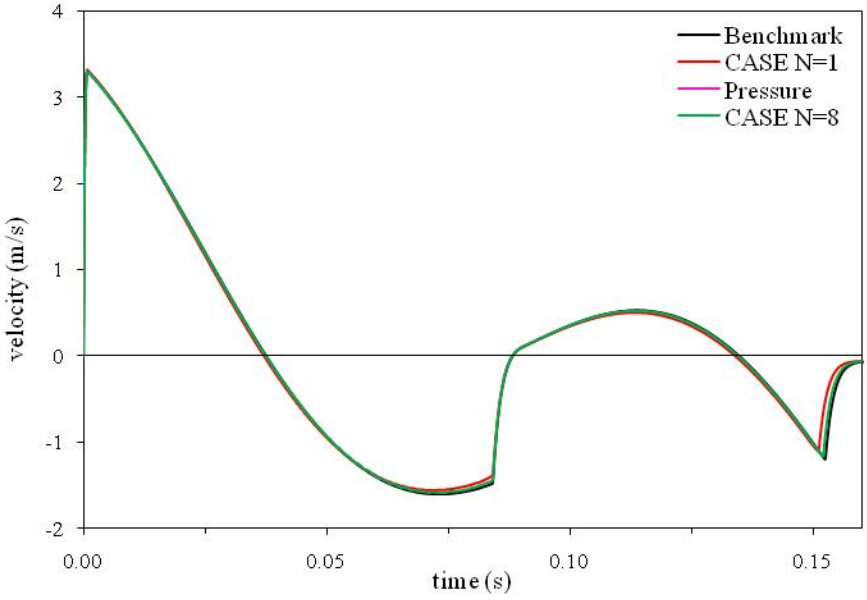

(b)

Figure 6.11 Velocity of m_1 for the m_2/m_1=1 case using 405 DOF (a) and 1449 DOF (b) with β = 0.25 for CASE and η_D= 0.020 for the pressure formulation

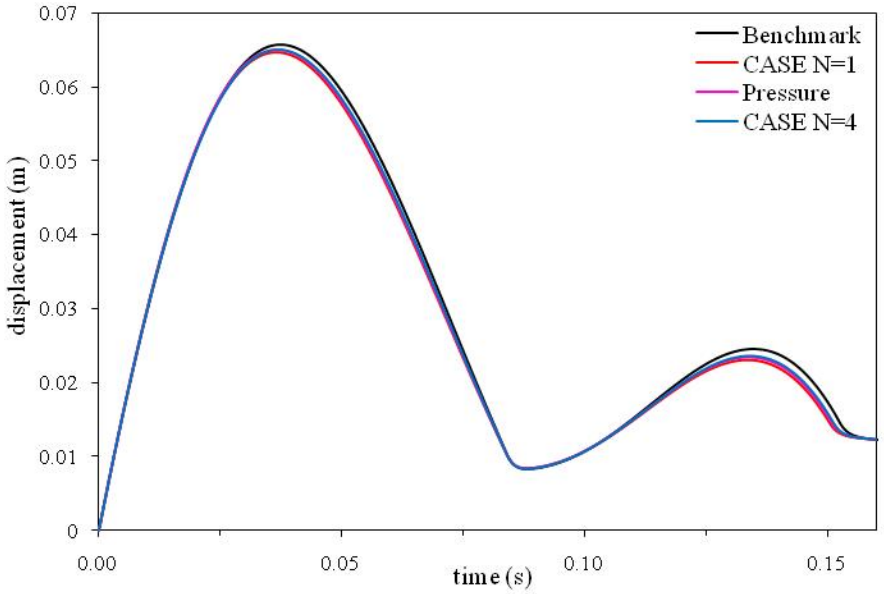

(a)

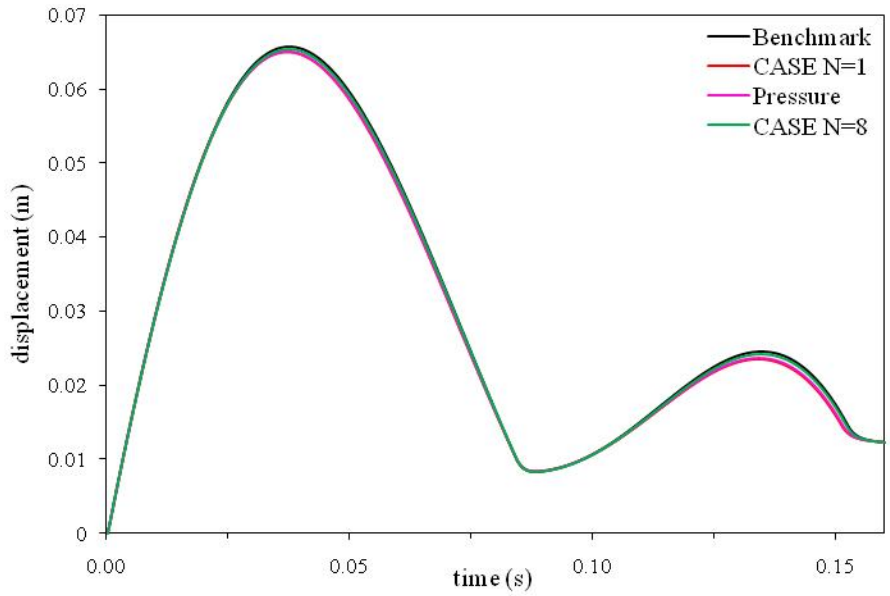

(b)

Figure 6.12 Displacement of m_1 for the m_2/m_1=1 case using 405 DOF (a) and 1449 DOF (b) with β = 0.25 for CASE and η_D= 0.020 for the pressure formulation

However, we note that for each mesh the error norms for the displacement response are lower than the error norms for the velocity response. This was also observed for the m_2/m_1=0 case in Section 6.2.

Table 6.9 L_2 error norms for the displacement of m_1 (m_2/m_1=1 case) with β = 0.25 for CASE and η_D= 0.020 for the pressure formulation

Fluid DOF	CASE N=1	Pressure	CASE
244	0.03185	0.02466	0.02517
405	0.02926	0.02363	0.01855
847	0.02428	0.02015	0.01047
1449	0.02045	0.01692	0.00624

To study the effect of cavitation capture on the structural response for the m_2/m_1=1 problem we again show plots of dynamic densified condensation in the fluid at various times during the duration of the first cavitation region. This is shown in Fig. 6.13 for the 405 DOF fluid meshes and Fig. 6.14 for the 1449 DOF fluid meshes. The L_2 error norms are provided in the legend of each plot. In both Figs. 6.13 and 6.14, s is plotted at t=0.002s, t=0.025s, t=0.05s, and t=0.075s. At t=0.002s the scattered wave front has just arrived at the NRB. At t=0.025s the upper cavitation boundary in the benchmark solution is clearly visible at a depth of 0.2m and the lower cavitation boundary at a depth of 1.25m. At t=0.05s the upper cavitation boundary in the benchmark solution has propagated deeper into the fluid moving to 0.4m and the lower cavitation boundary has moved to 1.1m as the cavitation region is now contracting. At t=0.075s both the upper and lower cavitation boundaries have moved closer together in the benchmark solution and are only separated by 0.125m as the cavitation region is close to collapsing.

Comparing the results for the 405 DOF mesh in Fig. 6.13, we see that, as in the m_2/m_1=0 case, the cavitation boundaries are smeared and there is a loss in the magnitude of dynamic densified condensation in the cavitation region. At t=0.002 s, the pressure formulation gives the best results and there are large oscillations visible in the N=4 CASE solution. For the three other times in Fig. 6.13, the N=4 CASE solution captures the magnitude and boundaries of the cavitation region the best, which is reflected by the smaller error norm. As time increases the solutions for each method get progressively

worse, illustrated by the error norm of the N=4 CASE solution going from L_2≈0.1668 at t=0.002 s to L_2≈0.9797 at t=0.075 s. Similar increases in error as time increased are also observed for the N=1 CASE and the pressure formulation models.

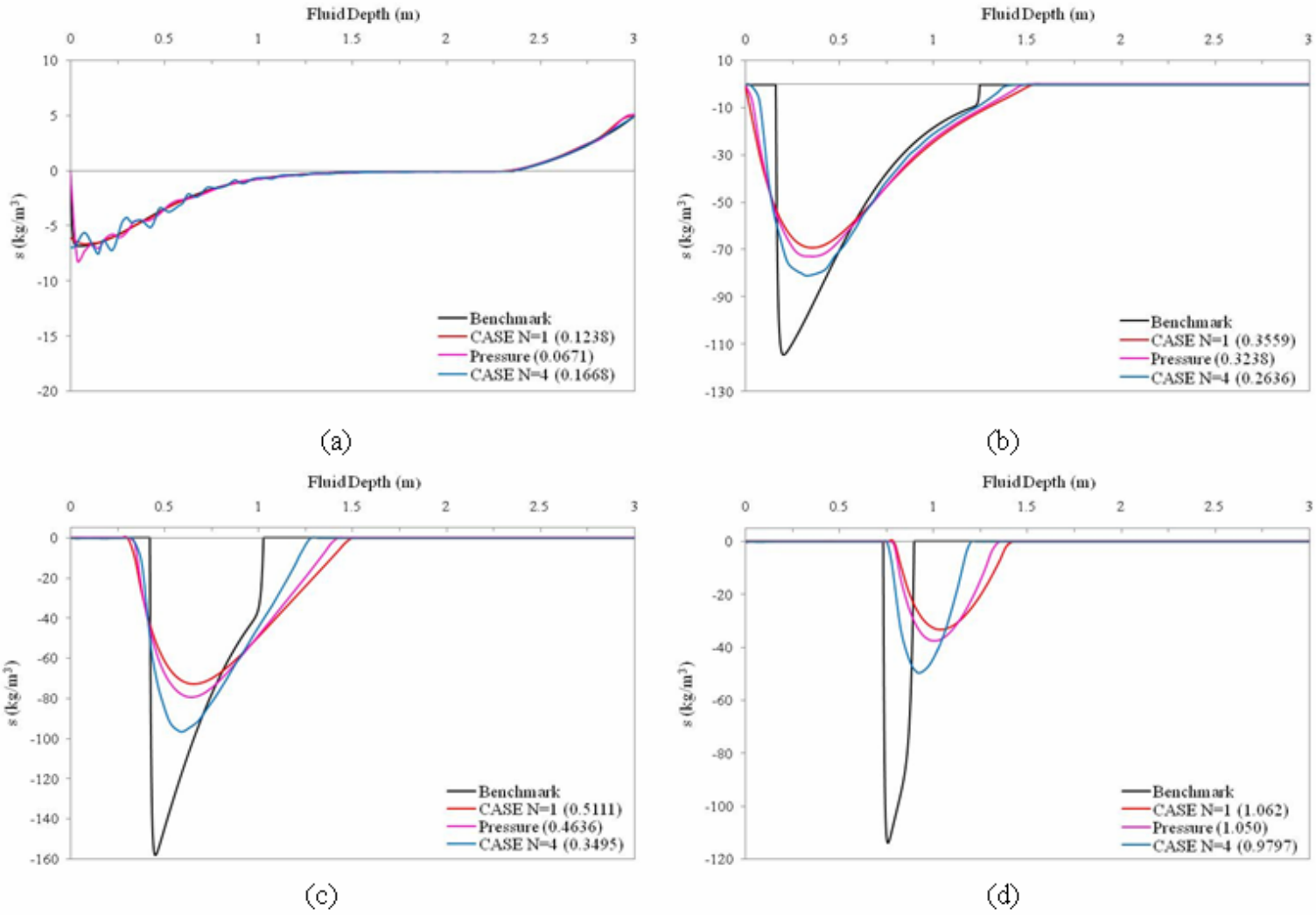

Figure 6.13 Dynamic densified condensation in the fluid at t=0.002 s (a), t=0.025 s (b), t=0.05 s (c), and t=0.075 s (d) for the m_2/m_1=1 case using 405 DOF with β = 0.25 for CASE and η_D= 0.020 for the pressure formulation

Refining the mesh to 1449 DOF improves the capture of the cavitation region at all times, especially for the N=8 CASE model which reduces the error norm at t=0.075s from L_2≈0.9797 in the N=4 solution to L_2≈0.68344. Note that even with the mesh refinement, the N=8 CASE solution still shows increased oscillations at t=0.002s. The mesh refinement for the N=1 CASE model results in a much smaller reduction in the L_2

norm, going from $L_2 \approx 1.062$ in the 405 DOF mesh to $L_2 \approx 0.9928$ in the 1449 DOF mesh. This reduction in the t=0.075 error norm is not enough to make the N=1 1449 DOF CASE results match the benchmark solution better than the N=4 405 DOF CASE results. This is a further example of the superior convergence rate of the order CASE models.

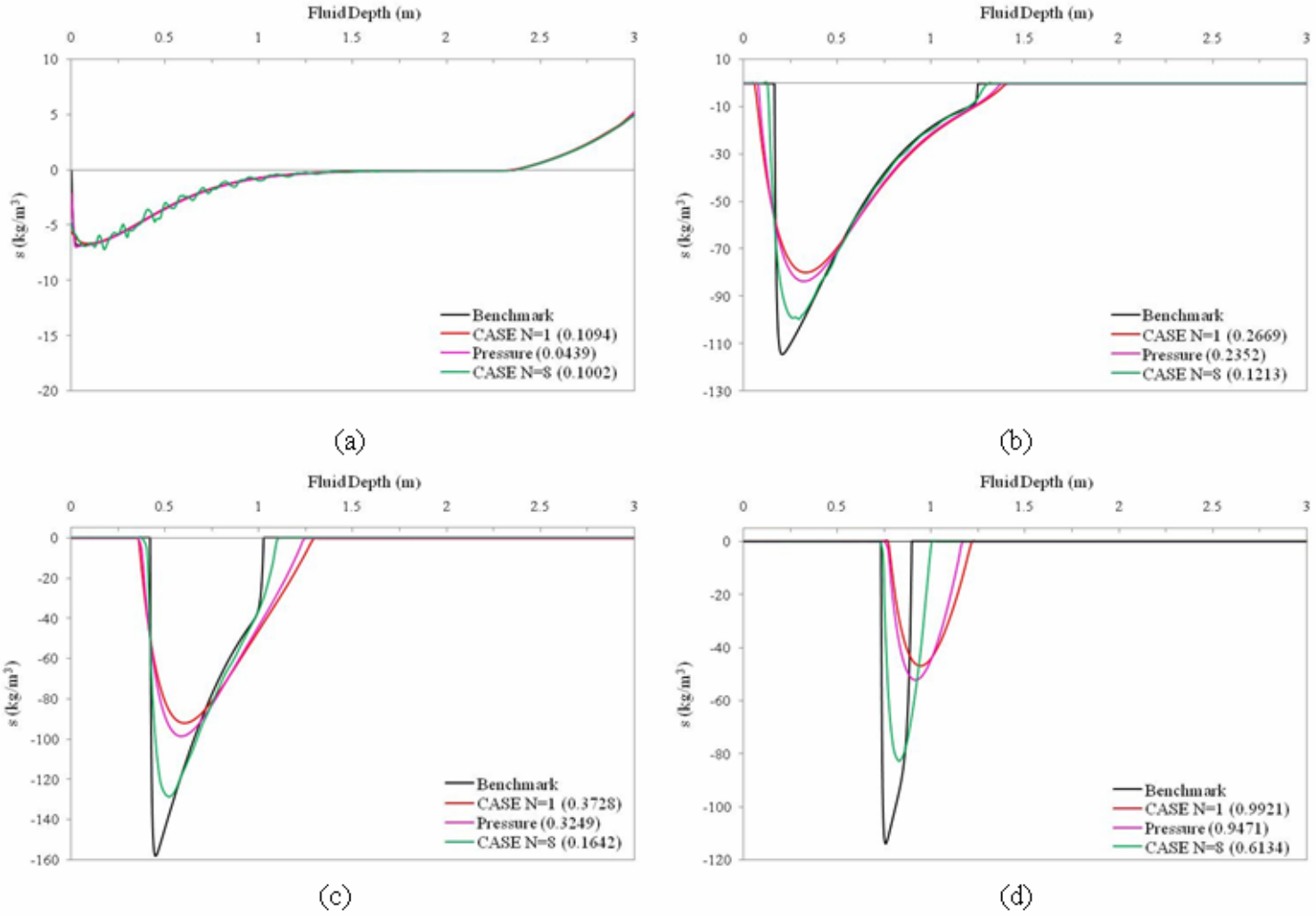

Figure 6.14 Dynamic densified condensation in the fluid at t=0.002 s (a), t=0.025 s (b), t=0.05 s (c), and t=0.075 s (d) for the m_2/m_1=1 case using 1449 DOF with β = 0.25 for CASE and η_D= 0.020 for the pressure formulation

As stated in Section 6.2.1 and [38], it is the capture of the upper cavitation boundary that is most important in obtaining an accurate structural response. To illustrate the effect of cavitation capture on the structure we consider the 405 DOF fluid models in Fig. 6.13. Initially, as Fig. 6.13b shows, each model predicts the upper cavitation boundary to be closer to the fluid-structure interface than the benchmark solution. Physically, as explained in Section 6.2.1, this results in a faster decay of the positive velocity magnitude

from the kick-off velocity to zero velocity. For the m_2/m_1=1 problem, the effect of this on the structure is best observed in the displacement response of m_1. Due to the faster decay of velocity predicted by the 405 DOF models, each of the 405 DOF models in Fig. 6.12a has a smaller maximum displacement than the benchmark solution. As the mesh is refined and the capture of the upper cavitation boundary improves (see Fig. 6.14b), so does the capture of the maximum displacement in Fig. 6.12b.

Once the maximum displacement of the mass is reached, the structural motion changes direction and the mass begins to compress the fluid. Hydrostatic pressure and the compressive motion of the mass cause the fluid between the fluid-structure interface and the upper cavitation boundary to re-pressurize, which ultimately drives the collapse of the cavitation region. Due to the faster decay of the positive velocity magnitude and the loss of dynamic densified condensation magnitude in the cavitation region, re-pressurization of the fluid occurs faster in the 405 DOF models than in the benchmark model. This is observed in Fig. 6.13d as the 405 DOF models pushing the upper cavitation boundary deeper into the fluid than in the benchmark solution. The larger mass associated with this additional re-pressurized fluid causes a decrease in the velocity magnitude during the structural response to the first cavitation region [38]. This is visible in Fig. 6.11a as the difference between the magnitudes of negative velocity reached during the response to the first cavitation region in the benchmark and 405 DOF fluid model solutions.

Refinement of the mesh to 1449 DOF improves the cavitation capture in Fig. 6.14, which results in the improvement of the structural response results with mesh refinement for all fluid models. However, for both the 405 DOF and the 1449 DOF fluid models in Figs. 6.13 and 6.14, the N=4 and N=8 CASE models predict the cavitation region closest to the benchmark model as time increases. Because of this both CASE models give the structural response results closest to the benchmark solution when compared to the N=1 CASE and pressure formulation solutions.

6.3.2 β = 0.50 and η_D= 0.035

In this section we look at the effect of increasing the amount of artificial damping/diffusion in the fluid for the m_2/m_1=1 case. For all models in this section, we use β = 0.50 for CASE and η_D= 0.035 for the pressure formulation. Figures 6.15a and

6.15b give results for the velocity of m_1 using 405 DOF and 1449 DOF respectively. In Fig. 6.15a all three methods show a significant difference in the velocity during the response to first and second cavitation regions. Visually, the N=4 CASE solution in Fig. 6.15a is closer to the benchmark solution than either the N=1 CASE or the pressure formulation solution (which are visually the same in Fig. 6.15a), especially in the arrival time of the second cavitation closer pulse. This is reflected in the L_2 error norm in Table 6.10 for the N=4 CASE solution. Compared to the results observed with $\beta = 0.25$ and η_D= 0.020, Fig. 6.15a shows an increase in the difference between the 405 DOF meshes and the benchmark solution during the response to the first and second cavitation regions. Consequently, there is an increase in L_2 error norm of 0.03561 for the N=1 CASE results, 0.03022 for the pressure formulation results, and 0.03741 for the N=4 CASE results.

In Fig. 6.15b, the difference between the 405 DOF models and the benchmark solution is decreased for the 1449 DOF N=1 CASE and pressure formulation models (which again are visually the same in Fig. 6.15b), with the N=8 CASE model clearly giving the result closest to the benchmark solution. This is numerically confirmed by the L_2 error norms for the 1449 DOF meshes in Table 6.10, which shows the N=8 CASE solution ($L_2 \approx 0.03459$) gives the lowest error norm of all models. Furthermore, Table 6.10 shows with $\beta = 0.50$ and η_D= 0.035 the higher-order CASE models give the more accurate velocity response results for a given level of refinement and also give faster convergence to the benchmark solution as the mesh is refined. We note however, for each mesh considered in Table 6.10, the increase in artificial damping/diffusion results in an increase in the L_2 error norm, as demonstrated above for the 405 DOF model results.

Table 6.10 L_2 error norms for the velocity of m_1 (m_2/m_1=1 case) with $\beta = 0.50$ for CASE and η_D= 0.035 for the pressure formulation

Fluid DOF	CASE N=1	Pressure	CASE
244	0.12220	0.10089	0.10278
405	0.11420	0.09615	0.08861
847	0.09949	0.08516	0.05262
1449	0.08766	0.07505	0.03459

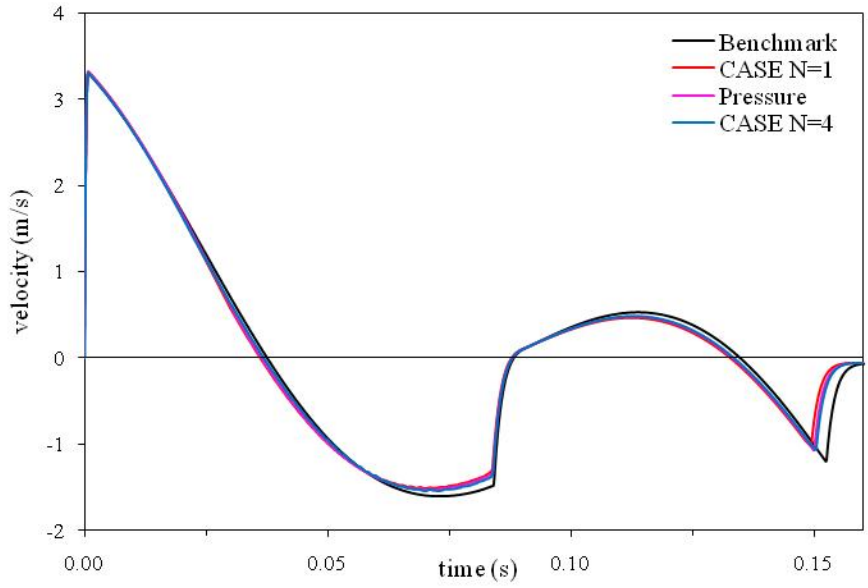

(a)

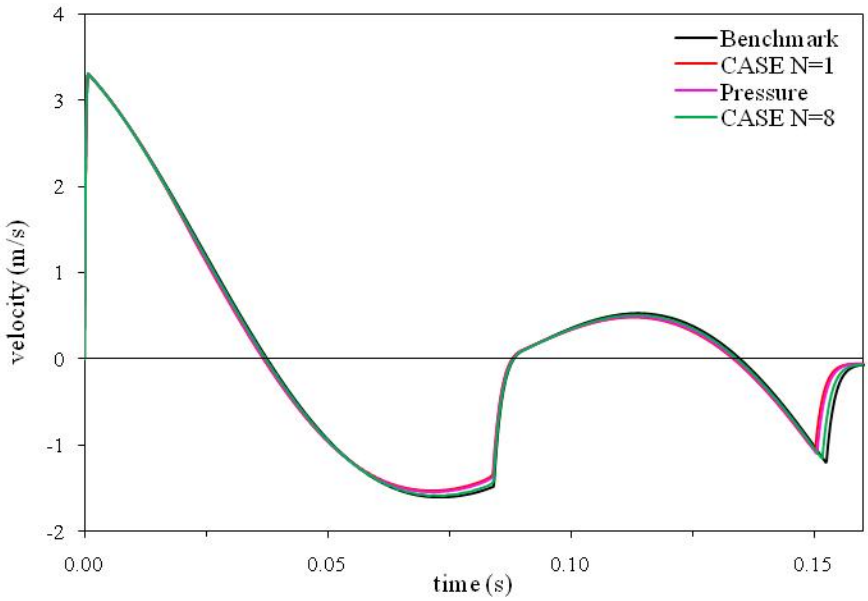

(b)

Figure 6.15 Velocity of m_1 for the m_2/m_1=1 case using 405 DOF (a) and 1449 DOF (b) with β = 0.50 for CASE and η_D= 0.035 for the pressure formulation

Figure 6.16 shows results for the displacement of m_1 using 405 DOF and 1449 DOF. Note, in both figures, the N=1 CASE and the pressure formulation solutions are nearly identical. As in the velocity results, the increase in artificial damping/diffusion causes a noticeable difference in the maximum displacements of m_1 reached during the response to the cavitation regions when compared to the benchmark solution. Looking at Fig. 6.16a, the N=4 CASE solution gives a small improvement over the N=1 CASE and the pressure formulation, which is confirmed in comparing the L_2 error norms in Table 6.11.

Note, as in the velocity results, Table 6.11 shows a general increase in the L_2 error norms for the displacement for each of the meshes when compared to the results with β = 0.25 and η_D= 0.020 in Table 6.9.

Table 6.11 L_2 error norms for the displacement of m_1 (m_2/m_1=1 case) with β = 0.50 for CASE and η_D= 0.035 for the pressure formulation

Fluid DOF	CASE N=1	Pressure	CASE
244	0.04983	0.03853	0.04123
405	0.04641	0.03702	0.03368
847	0.03970	0.03264	0.01953
1449	0.03444	0.02842	0.01247

The refinement of the mesh to 1449 DOF in Fig 6.16b gives results that are closer to the benchmark solution for each method, as evidenced by the reduction in L_2 error norms. As in the velocity response results the N=8 CASE solution gives the result closest to the benchmark solution, although the reduction in error norm when compared to the N=1 CASE and pressure formulation meshes is not as large as in the velocity results. Table 6.11 also shows the L_2 error norms for the displacement response are lower for each model than in the velocity response. This illustrates the findings in previous sections that the displacement response of the mass m_1 is not a sensitive to errors in the fluid mesh as the velocity response.

To determine the effect of increasing artificial damping/diffusion on the fluid, we plot dynamic densified condensation in the fluid during the duration of the first cavitation region at the times described in Section 6.3.1.

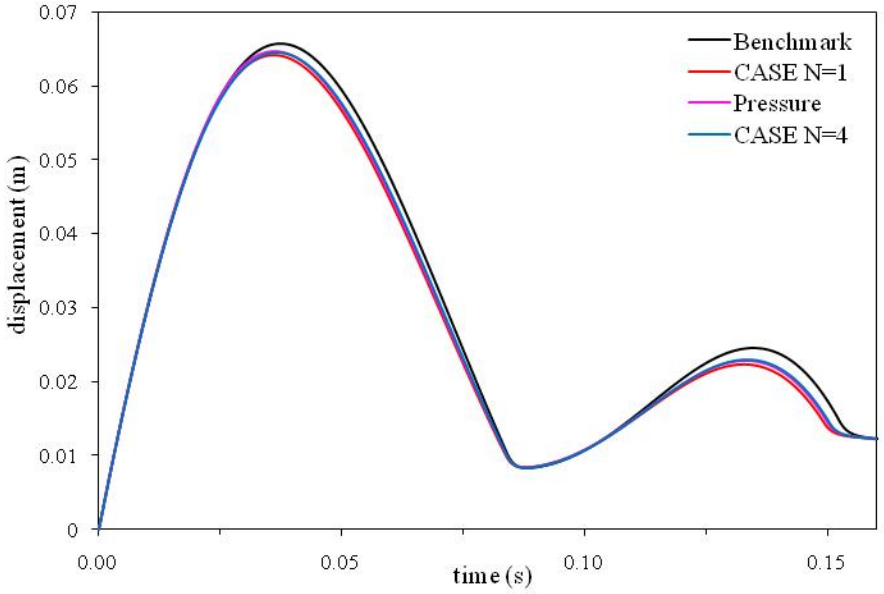

(a)

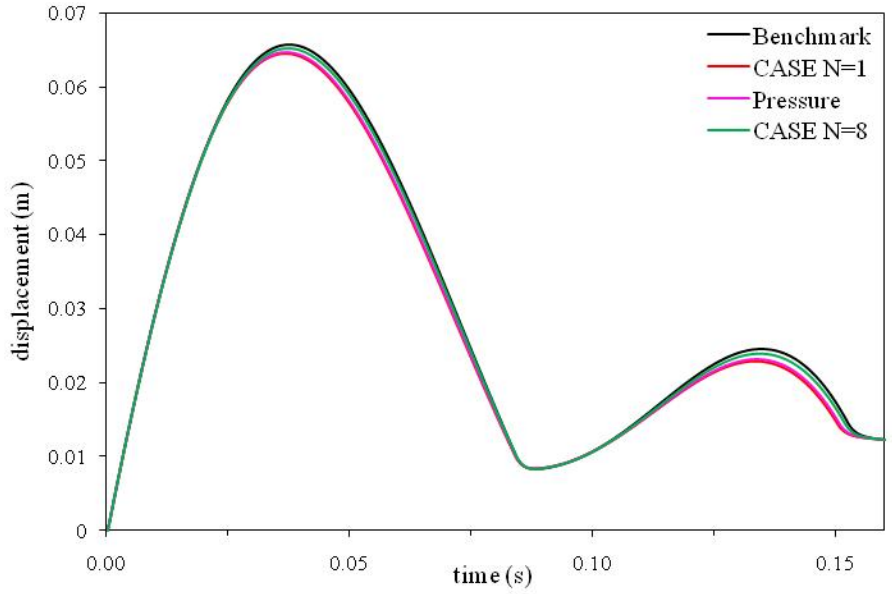

(b)

Figure 6.16 Displacement of m_1 for the m_2/m_1=1 case using 405 DOF (a) and 1449 DOF (b) with β = 0.50 for CASE and η_D= 0.035 for the pressure formulation

We show the dynamic densified condensation at t=0.002s, t=0.025s, t=0.05s, and t=0.075s in Fig. 6.17 for the 405 DOF fluid model and Fig. 6.18 for the 1449 DOF fluid models. Looking at the results for the 405 DOF mesh in Fig. 6.18 we see that, compared to the results with β = 0.25 and η_D= 0.020 , from t=0.025s to t=0.075s the cavitation boundaries are further smeared and there is an increased loss in the magnitude of the cavitation region. The error norms given in the legends of each plot further reflect this finding. For the largest observed error norms at t=0.07s, the N=4 CASE solution shows an increase from L_2≈0.9797 with β=0.25 to L_2≈0.1.087 with β=0.50. The N=1 CASE solution and pressure formulation solution also show a small increase in the L_2 error norm at this time. This increase in error was also observed when β and η_D were increased in the m_2/m_1=0 case.

Refinement of the mesh to 1449 DOF gives a reduction in the L_2 norm for each mesh with the N=8 CASE mesh giving the largest reductions and the best overall solution at each of the times considered. However, there is still an overall increase in error when compared to the β = 0.25 and η_D= 0.020 solutions due to the increase in artificial damping/diffusion. Note, at t=0.075s, the reduction in L_2 norm for the 1449 DOF N=1 CASE and pressure formulation mesh is minimal when compared to the 405 DOF mesh. This is further evidence of the superior convergence rates of higher-order CASE refinement.

In regards to the effect of cavitation capture on the structural response, the consequences of improperly capturing the upper cavitation region are much more apparent with the increase in damping. We illustrate this by comparing the location of the upper cavitation boundary at t=0.025s for the 405 DOF models in Fig. 6.17b to the location of the upper cavitation boundary at t=0.025 s for the 405 DOF models with β=0.25 in Fig. 6.13b, we see that the increase in damping has further dissipated the magnitude of the dynamic densified condensation in the cavitation region. Furthermore, the upper cavitation boundary is closer to the fluid-structure interface than in the β=0.25 models. The result of this error in cavitation capture is visible in the structural response as the smaller maximum displacements, do to an extended state of free fall, for the 405 DOF fluid models with β=0.50.

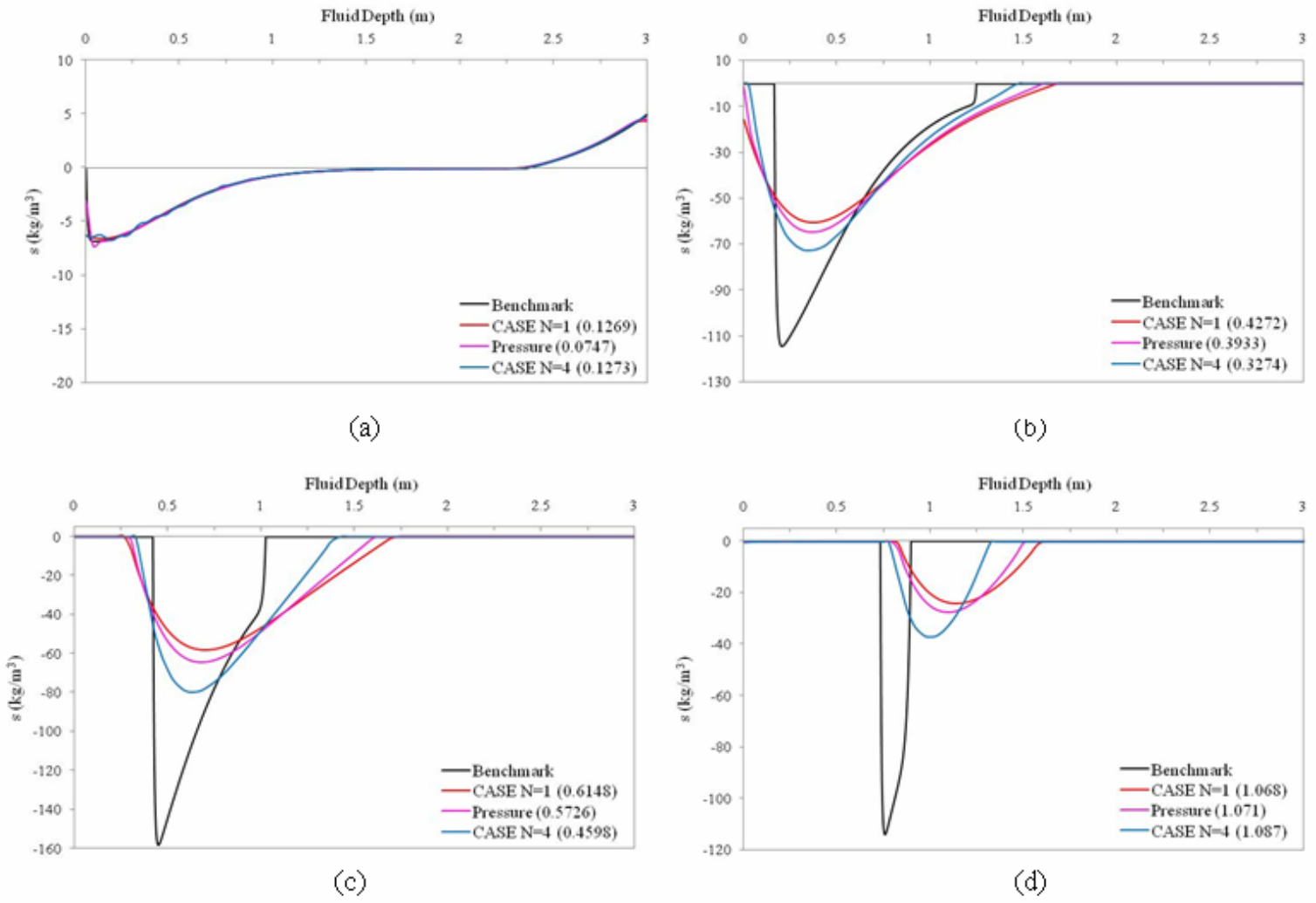

Figure 6.17 Dynamic densified condensation in the fluid at t=0.002 s (a), t=0.025 s (b), t=0.05 s (c), and t=0.075 s (d) for the m_2/m_1=1 case using 405 DOF with β = 0.50 for CASE and η_D= 0.035 for the pressure formulation

Similarly, comparison of the upper cavitation boundary at t=0.075s for the 405 DOF models in Fig. 6.17d to the location of the upper cavitation boundary at t=0.075 s for the 405 DOF models with β=0.25 in Fig. 6.13d, we see the increase in damping has again further dissipated the magnitude of dynamic densified condensation in the cavitation region and the upper cavitation boundary is located deeper in the fluid than in the β=0.25 models. The result of this is visible in the structural response as the increased difference between the magnitude of negative velocity reached during the response to the first cavitation regions of the 405 DOF models and benchmark solutions in Fig. 6.15a.

Refinement of the mesh to 1449 DOF improves the cavitation capture, which results in the improvement of the structural response results with mesh refinement for all fluid models. Comparing the fluid models in both Figs. 6.17 and 6.18 the N=4 and N=8 CASE models give the location of the upper cavitation boundary closest to the benchmark solution at all times. Because of this the higher-order CASE models correspondingly match the structural response of the benchmark solution the better than the N=1 CASE and pressure formulation models.

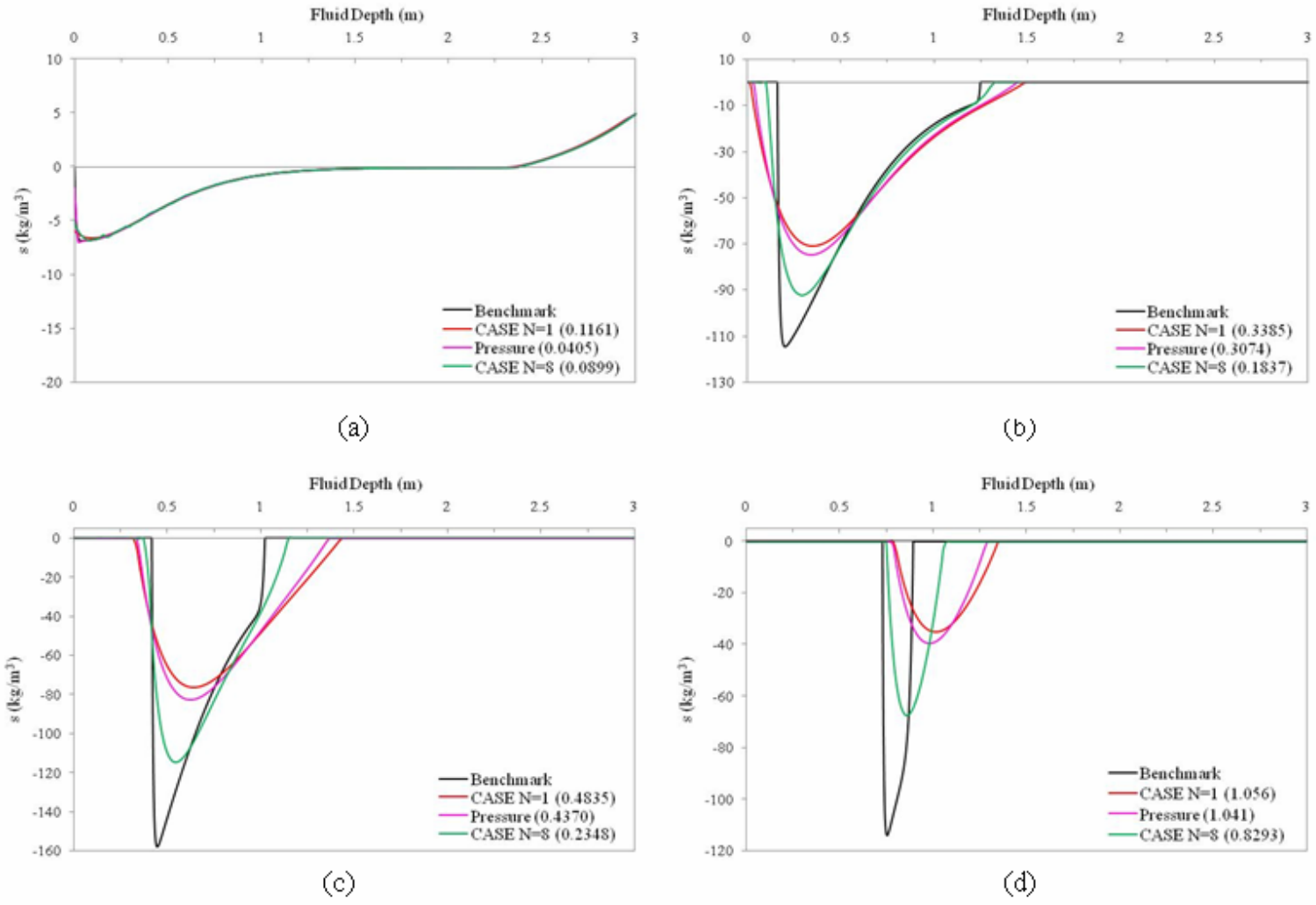

Figure 6.18 Dynamic densified condensation in the fluid at t=0.002 s (a), t=0.025 s (b), t=0.05 s (c), and t=0.075 s (d) for the m_2/m_1=1 case using 1449 DOF with β = 0.50 for CASE and η_D= 0.035 for the pressure formulation

6.3.3 $\beta = 0.10$ and $\eta_D = 0.010$

In this section, we determine the effect of reducing the amount of artificial damping/diffusion on the structural response. Section 6.2.3 showed that reducing the amount of artificial damping/diffusion in the fluid for the $m_2/m_1=0$ case allowed for more accurate $N=1$ CASE solutions, pressure formulation solutions, and higher-order CASE solutions and did not increase oscillations in the structural response for any of the methods.

Figure 6.19 shows the velocity response using 405 DOF and 1449 DOF with $\beta = 0.10$ for CASE and $\eta_D = 0.010$ for the pressure formulation. The 405 DOF results in Fig. 6.19a show some small ripples in the velocity response for each method between 0.06 s and 0.075 s. In this figure, each of the methods are visually identical to each other and all agree well with the benchmark solution. However, compared to the results with larger amounts of damping, there is a small increase in oscillations during the response to the first cavitation region. Refining the mesh to 1449 DOF in Fig. 6.19b, there is no visible difference between the benchmark solutions and the 1449 DOF solutions. Furthermore, the oscillations seen in the 405 DOF results are no longer visible, even for the $N=8$ CASE solution. Comparing the L_2 error norms for the velocity response in Table 6.12 we see that the higher-order CASE solutions give results closest to the benchmark solution for each level of mesh refinement and also show a larger reduction in error norm as the mesh is refined.

Table 6.12 L_2 error norms for the velocity of m_1 ($m_2/m_1=1$ case) with $\beta = 0.10$ for CASE and $\eta_D = 0.010$ for the pressure formulation

Fluid DOF	CASE N=1	Pressure	CASE
244	0.04367	0.03632	0.02876
405	0.03575	0.03130	0.01681
847	0.02648	0.02598	0.01124
1449	0.02117	0.02041	0.00658

The results for the displacement of m_1 are given in Fig. 6.20 for both the 405 DOF and 1449 DOF meshes. Note for each model, the results are indistinguishable from the benchmark solution and no oscillations are observed.

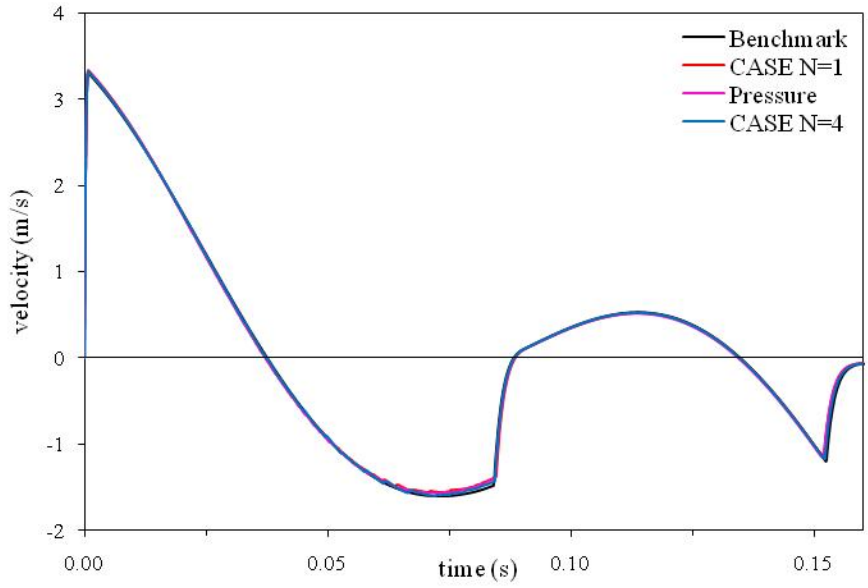

(a)

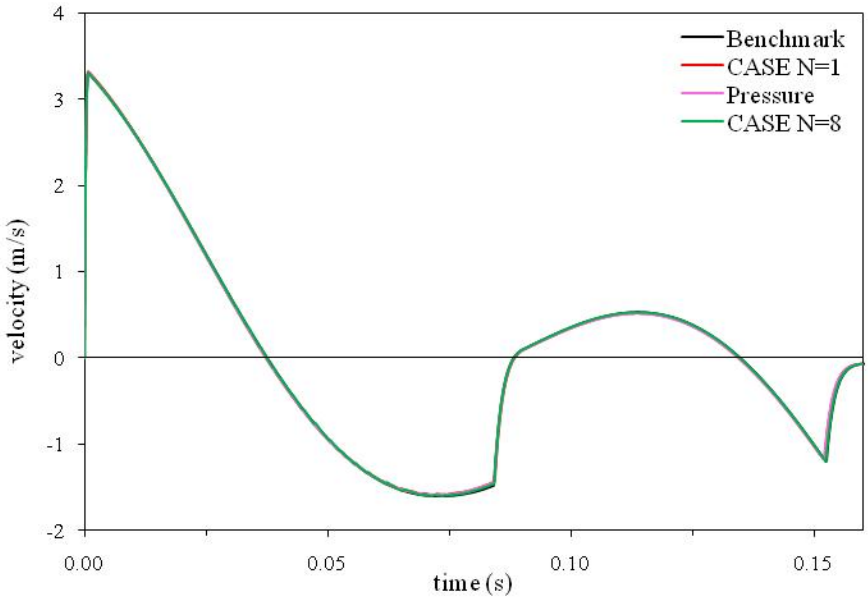

(b)

Figure 6.19 Velocity of m_1 for the m_2/m_1=1 case using 405 DOF (a) and 1449 DOF (b) with β = 0.10 for CASE and η_D= 0.010 for the pressure formulation

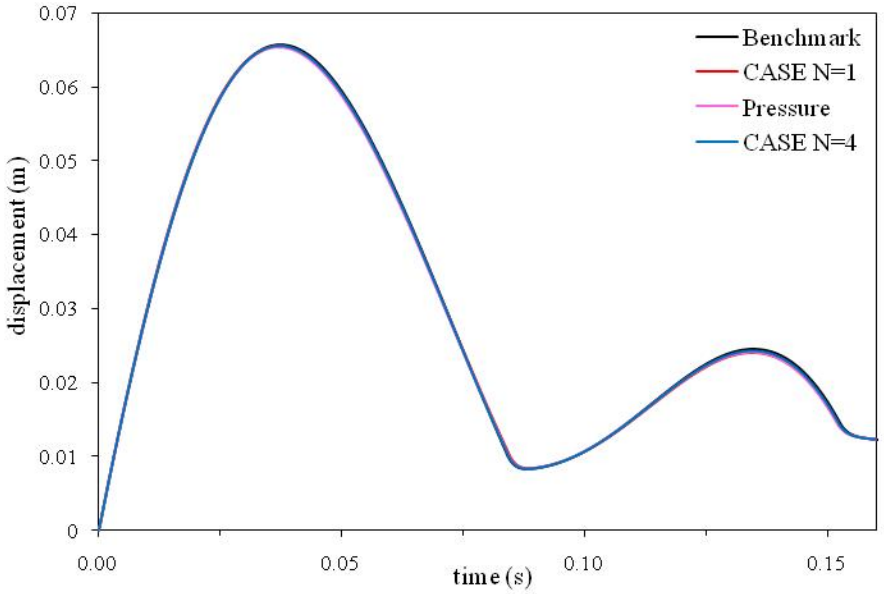

(a)

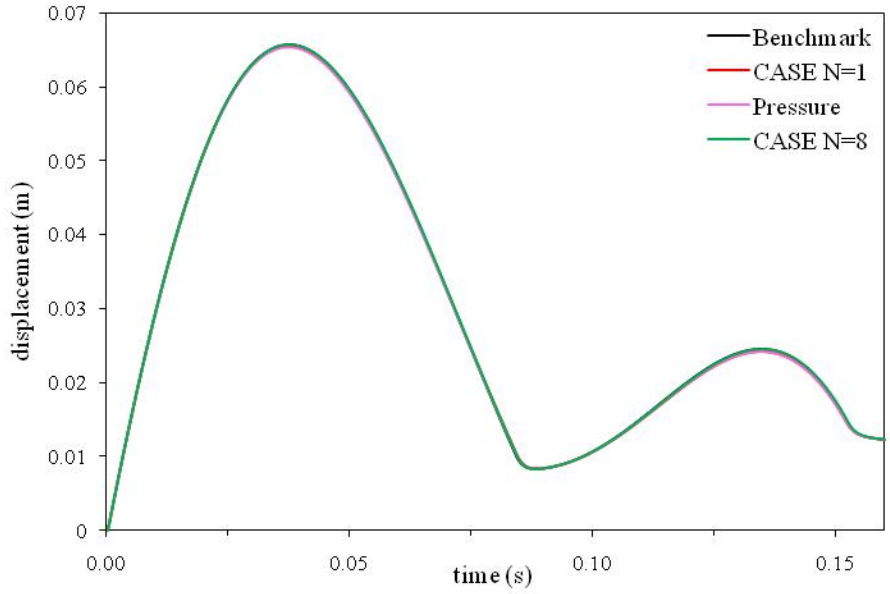

(b)

Figure 6.20 Displacement of m_1 for the m_2/m_1=1 case using 405 DOF (a) and 1449 DOF (b) with β = 0.10 for CASE and η_D= 0.010 for the pressure formulation

Comparison of the L_2 error norms in Table 6.13 shows that although there is little visible difference between the solutions, the higher-order CASE models give results closer to the benchmark solution for a given level of refinement. We note, however, that with $\beta = 0.10$ and $\eta_D = 0.010$ all meshes in Table 6.13 give very low L_2 error norms.

Table 6.13 L_2 error norms for the displacement of m_1 (m_2/m_1=1 case) with $\beta = 0.10$ for CASE and $\eta_D = 0.010$ for the pressure formulation

Fluid DOF	CASE N=1	Pressure	CASE
244	0.01011	0.00871	0.00610
405	0.00917	0.00829	0.00422
847	0.00736	0.00791	0.00230
1449	0.00600	0.00634	0.00106

The oscillations that appear in the velocity response of m_1 for low levels of refinement, especially with β=0.10, are not significant in this problem as they are very small, affect the response for a small fraction of the total time considered, and are removed as the mesh is refined. Because of this, we can take $\beta = 0.10$ with the higher-order CASE meshes to gain accuracy without a significant increase in oscillations. Thus, for the m_2/m_1=1 case reducing the amount of damping in N=1 CASE and pressure formulation meshes will not allow us to achieve results similar to the higher-order CASE results with a reduction in oscillations as it did in the Bleich-Sandler problem (Section 5.3). Therefore, as in the m_2/m_1=0 problem, we conclude for the m_2/m_1=1 problem the higher-order CASE meshes will yield superior results when compared to both N=1 CASE and the pressure formulation for a given level of mesh refinement and a given level of artificial damping.

6.4 m_2/m_1=5 Results and Discussion

6.4.1 $\beta = 0.25$ and $\eta_D = 0.020$

In this section, we present results for the m_2/m_1=5 case, which was solved with a 1D fluid model in Section 5.2. Figure 6.21a and 6.21b give results for the velocity of m_1 using 405 DOF and 1449 DOF respectively. Note, in this section, all models use $\beta = 0.25$ for CASE and $\eta_D = 0.020$ for the pressure formulation. The benchmark solution in Fig.

6.21 shows that the mass, m_1, reaches a kick-off velocity of ~6.5 m/s at which point the velocity begins to decay as cavitation begins. The cavitation closure pulse re-loads m_1 at t=0.05s causing a sharp increase in positive velocity. The upward motion of the mass system resulting from the closure pulse causes a secondary cavitation region to form. The closer pulse of the second cavitation region re-loads the structure at t=0.13s and its reflection causes a small third cavitation region to form and quickly collapse. This third cavitation region is visible in the velocity response of benchmark solution as a small dip in velocity at t=0.14s.

The results for the 405 DOF model in Fig 6.21a show the N=4 CASE solution to be closest to the benchmark solution. Each model in Fig. 6.21a gives a smaller velocity magnitude during the response to the first cavitation region and also shows a small delay in the arrival time of the first cavitation closure pulse. This delay is more pronounced in the N=1 CASE and pressure formulation solutions. Compared to the benchmark solution both CASE solutions also give smaller velocity magnitudes during the response to the second cavitation region, with the difference again being greater for the N=1 CASE model.

There is a significant increase in oscillations in the *N=4* CASE solution between t=0.025s–0.05s when compared to the *N=1* CASE and pressure formulation solutions. A small increase in oscillations is also observed during the response to the second cavitation region, from t=0.11s-0.13s. Despite this, comparing the L_2 error norms for the velocity response in Table 6.14 confirms that the N=4 CASE solution (L_2≈0.07299) gives the best approximation to the benchmark solution than either the N=1 CASE solution (L_2≈0.10492) or the pressure formulation solution (L_2≈0.10418). This shows that the increase in oscillations does not degrade the accuracy of the N=4 CASE solution to the point where the N=1 CASE solution or the pressure formulation give better results.

Table 6.14 L_2 error norms for the velocity of m_1 (m_2/m_1=5 case) with β = 0.25 for CASE and η_D= 0.020 for the pressure formulation

Fluid DOF	CASE N=1	Pressure	CASE
244	0.12073	0.11606	0.08721
405	0.10492	0.10412	0.07299
847	0.08527	0.08469	0.04894
1449	0.07316	0.07202	0.03483

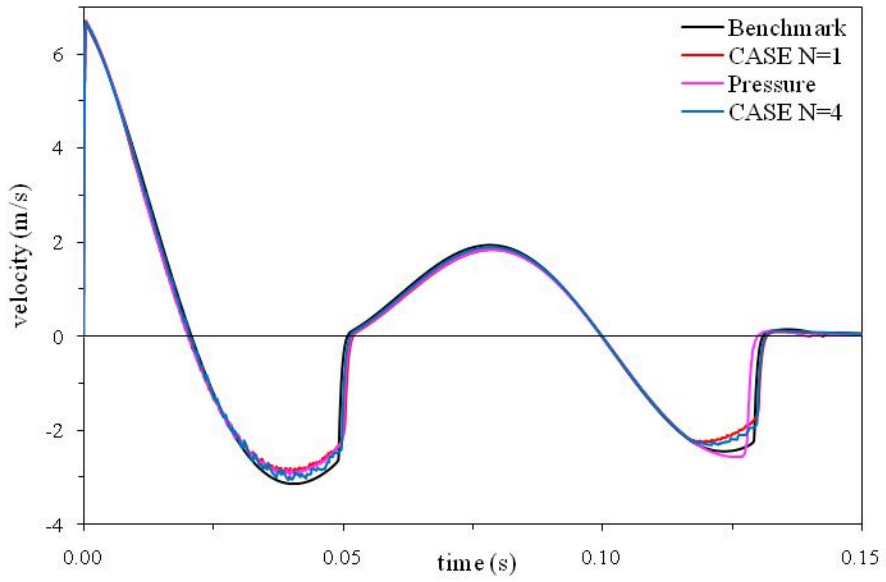

(a)

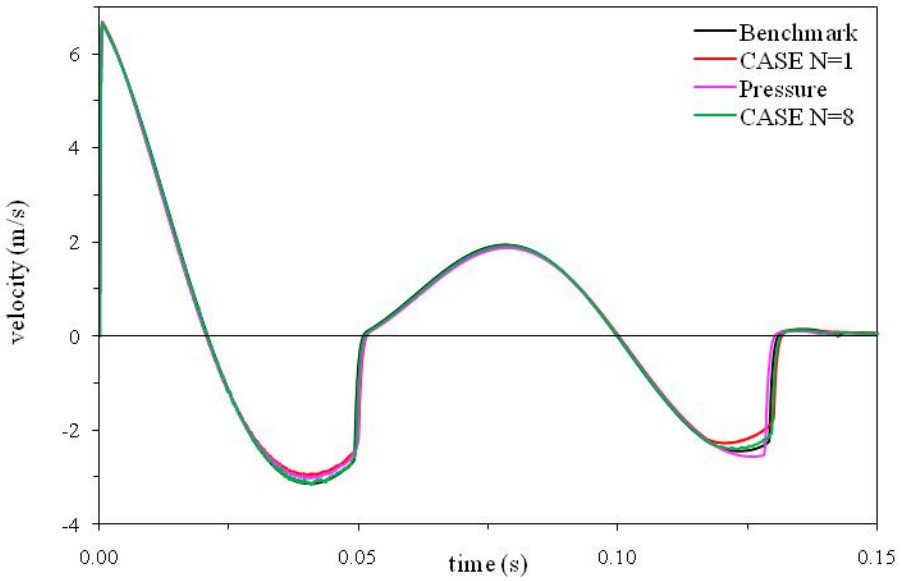

(b)

Figure 6.21 Velocity of m_1 for the m_2/m_1=5 case using 405 DOF (a) and 1449 DOF (b) with β = 0.25 for CASE and η_D= 0.020 for the pressure formulation

As we saw in Chapter 5, Fig. 6.21a shows that the *N=1* CASE solution and pressure formulation solution are almost identical during the response to the first cavitation region but give different responses to the second cavitation region. In the pressure formulation solution, the magnitude of the velocity response is larger during the second cavitation region and the cavitation closure pulse re-loads m_1 at an earlier time. It is interesting to note that in the two previous problems studied in this chapter, the pressure formulation solutions did not show any significant differences in the structural response when compared to the *N=1* CASE solutions. Comparing the L_2 norms in Table 6.14 we see that the differences in velocity response during the second cavitation region do not cause a large difference in error between the two solutions. This is attributed to the fact that the two solutions are almost identical throughout the majority of the response history.

As the fluid model is refined to 1449 DOF, Fig. 6.21b shows that the *N*=1 CASE and the pressure formulation solutions give smaller velocity magnitudes during the response to the first cavitation region. Although not as apparent as in the 405 DOF results, the *N*=1 CASE and pressure formulation solutions also give a delayed arrival time for the first cavitation closure pulse when compared to the benchmark solution. The *N*=1 CASE solution also gives smaller velocity magnitudes during the response to the second cavitation region. The *N*=8 CASE solution shows no visual difference compared to the benchmark solution during the response to the first cavitation region and only a small difference in the response to the second cavitation region. The L_2 error norms for the 1449 DOF models in Table 6.14 shows the *N*=8 CASE solution ($L_2 \approx 0.03483$) gives significant improvement over both the *N*=1 CASE ($L_2 \approx 0.07316$) and the pressure formulation ($L_2 \approx 0.07203$) solutions. In addition to the improved solution, the oscillations that were visible in the *N*=4 CASE solution have been reduced in the *N*=8 CASE solution. Although these oscillations remain larger than oscillations in the *N*=1 CASE and pressure formulation solutions with 1449 DOF, they are small in magnitude and only affect a small portion of the velocity response.

For the 1449 DOF model, we again find that the *N*=1 CASE solution and pressure formation solutions agree well until the response to the second cavitation region, where a noticeable difference in velocity magnitude and second cavitation closure time is visible. However, we found in Chapter 5 that the difference between the pressure formulation and

N=1 CASE solutions is reduced as the mesh is refined. This is most evident by comparing the arrival times of the second cavitation closure pulse for the pressure formulation solutions in Figs. 6.21a and 6.22b. Compared to the 405 DOF solution, the 1449 DOF the pressure formulation solution is much closer to that in the N=1 CASE and benchmark solutions. This is further reflected by the L_2 error norms in Table 6.14, which show that the refinement to the 1449 DOF model using the pressure formulation gives a reduction in error ($L_2 \approx 0.07202$) that is almost identical to that for the 1449 DOF N=1 CASE model ($L_2 \approx 0.07716$).

Figures 6.22a and 6.22b give results for the displacement of m_1 using 405 DOF and 1449 DOF, respectively. In both figures, the higher-order CASE model gives the solution closest to the benchmark solution with the N=8 CASE solution being almost indistinguishable from the benchmark solution in Fig. 6.22b. Note that no oscillations are observed in any of the solutions. The L_2 error norms for the displacement response are given in Table 6.15 and confirm that the higher-order CASE models give the closest approximation to the benchmark solution. As we saw in previous problems, the displacement response error norms for each model are significantly lower than the corresponding velocity response error norms.

Table 6.15 L_2 error norms for the displacement of m_1 (m_2/m_1=5 case) with β = 0.25 for CASE and η_D= 0.020 for the pressure formulation

Fluid DOF	CASE N=1	Pressure	CASE
244	0.04977	0.04196	0.03657
405	0.04434	0.04106	0.02381
847	0.03438	0.03251	0.01290
1449	0.02777	0.02629	0.00741

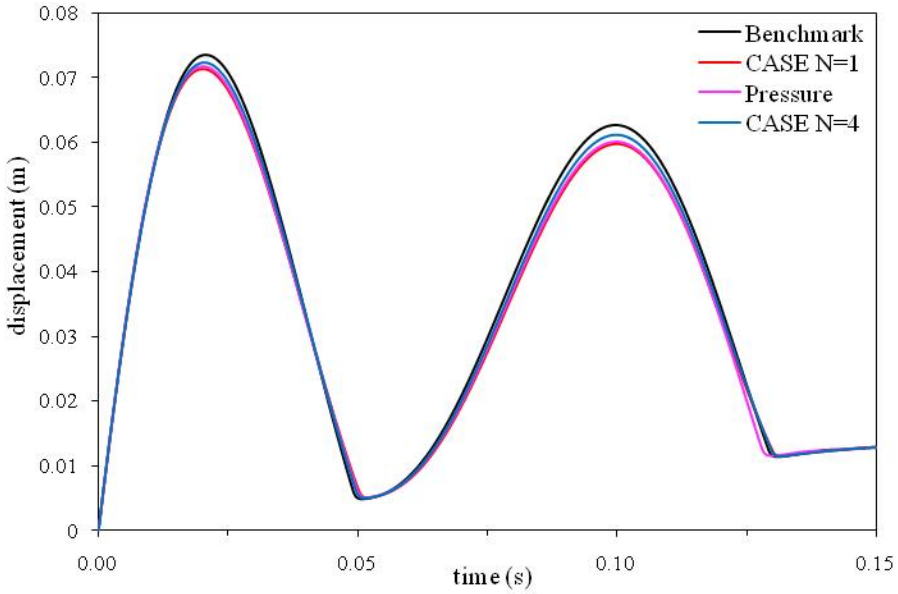

(a)

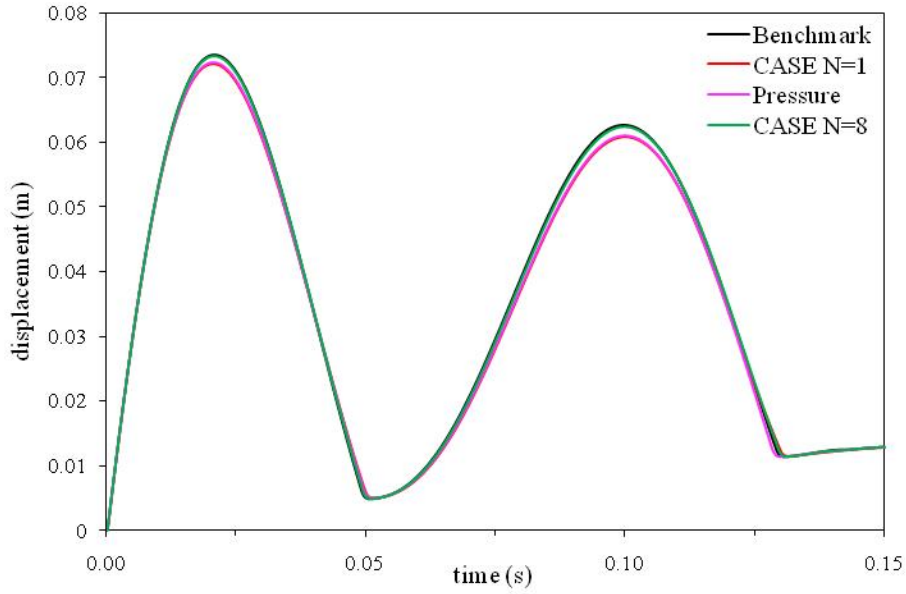

(b)

Figure 6.22 Displacement of m_1 for the m_2/m_1=5 case using 405 DOF (a) and 1449 DOF (b) with β = 0.25 for CASE and η_D= 0.020 for the pressure formulation

The difference observed between the N=1 CASE and pressure formulation solutions in the velocity response is also observed in the displacement response. In Fig. 6.22a, the pressure formulation solution diverges from the N=1 CASE solution at t=0.13s due to the early arrival of the cavitation closure pulse. This difference is decreased as the mesh is refined to 1449 DOF, as observed in Fig. 6.22b. Furthermore, comparing the L_2 error norms for each N=1 CASE and pressure formulation model in Table 6.15, we see the difference in response to the second cavitation region does not cause a large difference in error norm between the two models.

It is interesting to note that when both the velocity response results in Fig. 6.21 and displacement results in Fig. 6.22 are compared to the velocity and displacement response results generated with the same fluid models for the m_2/m_1=1 problem there is an increase in error. For example, the velocity response error norm for the 1449 DOF N=1 CASE result goes from $L_2 \approx 0.04890$ in the m_2/m_1=1 problem to $L_2 \approx 0.07716$ in the m_2/m_1=5 problem. The displacement response error norm for the same model goes from $L_2 \approx 0.01683$ in the m_2/m_1=1 problem to $L_2 \approx 0.02777$ in the m_2/m_1=5 problem. This illustrates the assertion in [38] that as m_1 becomes smaller (i.e. the ratio of m_2/m_1 is increased), the response of m_1 becomes more sensitive to the fluid model.

To study the effect of cavitation capture on the structural response for the m_2/m_1=5 problem we show the plots of dynamic densified condensation during the duration of the first cavitation region. These are shown in Fig. 6.23 for the 405 DOF fluid meshes and Fig. 6.24 for the 1449 DOF fluid meshes. In both Figs. 6.23 and 6.24, s is plotted at t=0.002s, t=0.015s, t=0.03s, and t=0.04s. At t=0.002s the scattered wave front has just arrived at the NRB. At t=0.015s, the upper cavitation boundary in the benchmark solution is located at a depth of 0.24m and the lower cavitation boundary at a depth of 1.625m. At t=0.03s the upper cavitation boundary in the benchmark solution has propagated to 0.5m and the lower cavitation boundary has contracted to 1.375m. At t=0.04s both the upper and lower cavitation boundaries have moved closer together in the benchmark solution and the cavitation region is close to collapsing.

Comparing the results for the 405 DOF fluid in Fig. 6.23, we see that, except at t=0.002s, the cavitation boundaries are not resolved well and there is a loss in the magnitude of dynamic densified condensation in the cavitation region. At t=0.002s, there

are oscillations present in all of the solutions, the largest clearly occurring in the N=4 CASE solution. As seen in previous sections, as time increases from t=0.002s each of the methods in Figs. 6.23b-d show an increase in error, as evidenced by the L_2 error norms given in the legends. For all times shown in Fig. 6.23, except t=0.002s, the N=4 CASE solution gives the result closest to the benchmark solution. This is especially true at t=0.04s where the L_2 error norm for the N=4 CASE model is $L_2 \approx 0.5008$, compared to $L_2 \approx 0.7798$ for the N=1 CASE solution and $L_2 \approx 0.7253$ for the pressure formulation solution.

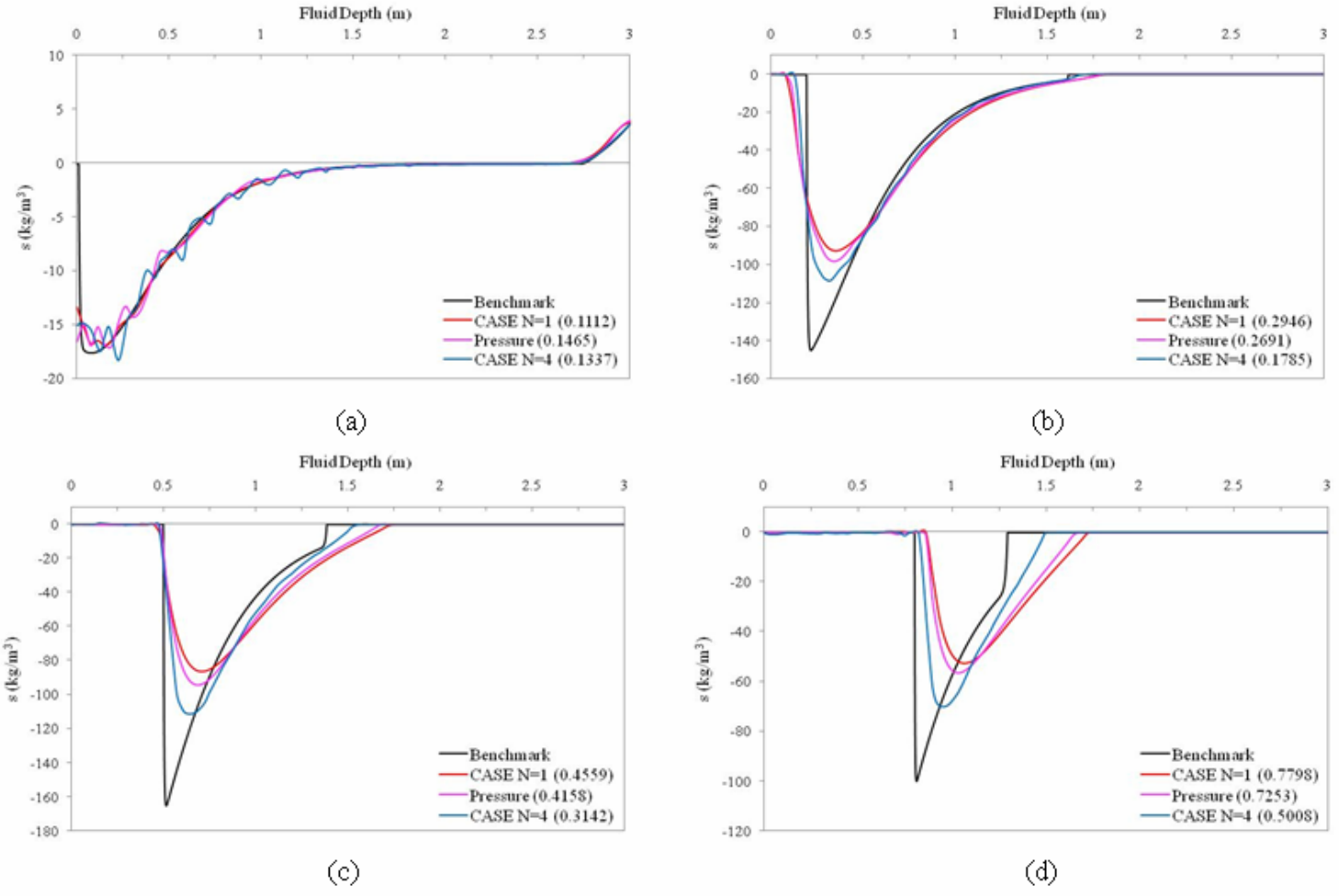

Figure 6.23 Dynamic densified condensation in the fluid at t=0.002 s (a), t=0.015 s (b), t=0.03 s (c), and t=0.04 s (d) for the m_2/m_1=5 case using 405 DOF with β = 0.25 for CASE and η_D= 0.020 for the pressure formulation

Refining the mesh to 1449 DOF improves the capture of cavitation for each model at the times observed in Fig. 6.24. Note, at t=0.002s, the oscillations observed in the 405 DOF are removed in both the N=1 CASE and pressure formulation results but are only reduced in the N=8 CASE result. As time progresses, Figs. 6.24b-d show that the N=8 CASE solution gives the best result, although the difference between the benchmark and each 1449 DOF solution grows with time for all methods. Due to the superior convergence rate observed for the higher-order CASE models, refinement of the CASE model produces a greater improvement in the capture of cavitation at each time in Figs. 6.24b-d.

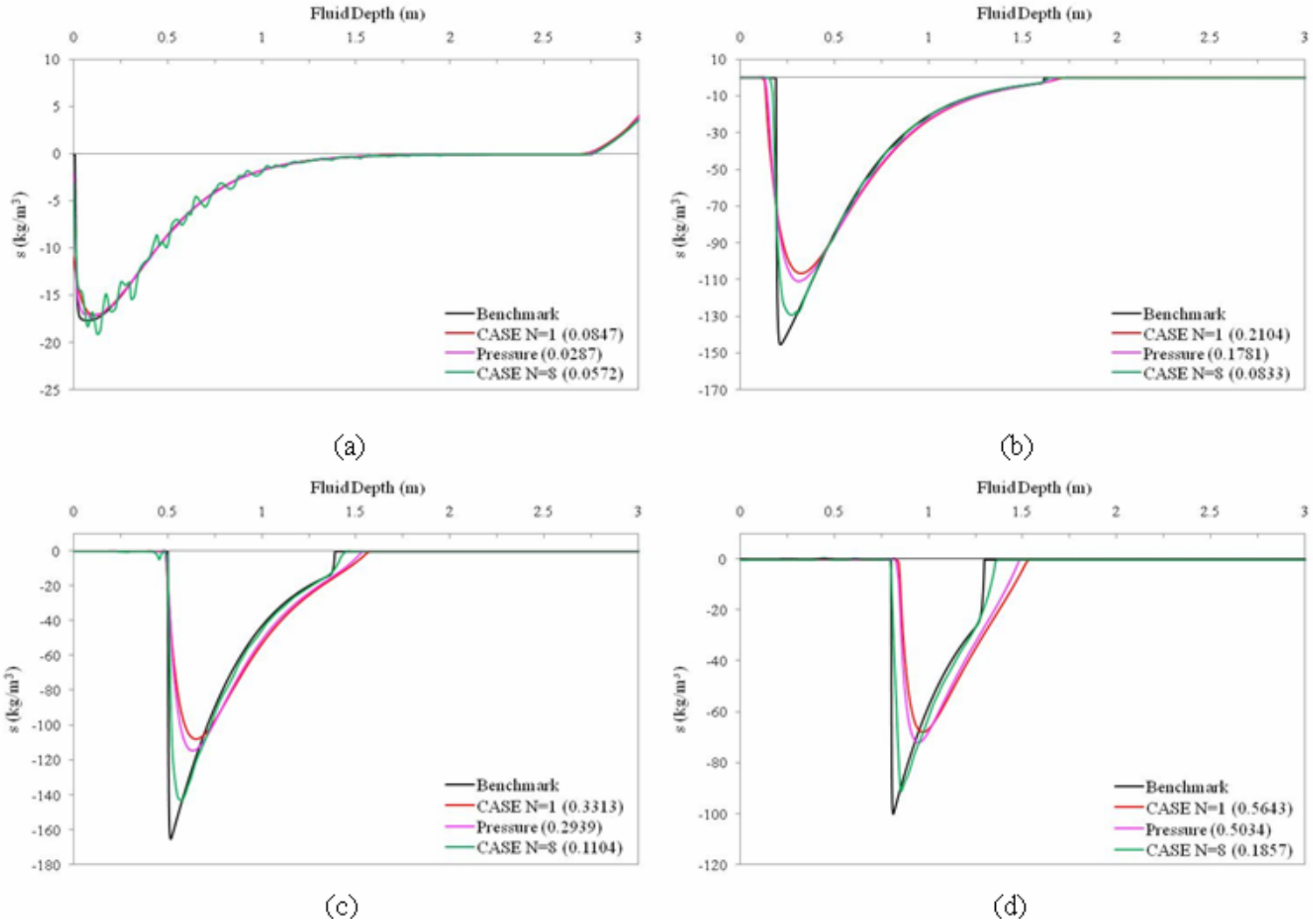

Figure 6.24 Dynamic densified condensation in the fluid at t=0.002 s (a), t=0.015 s (b), t=0.03 s (c), and t=0.04 s (d) for the m_2/m_1=5 case using 1449 DOF with β = 0.25 for CASE and η_D= 0.020 for the pressure formulation

In the previous sections, we noted that the error norms observed for cavitation capture in the fluid are much greater than those observed in the structural response. The results of the m_2/m_1=5 problem agree with this finding. We also observed in previous sections that the capture of the upper cavitation boundary and the magnitude of dynamic densified condensation in the cavitation region is most important to obtaining an accurate structural response.

As described in Section 6.3.1, early in the fluid response, the error of capturing the upper cavitation boundary closer to the fluid-structure interface, observed at t=0.015s in Figs. 6.23b and 6.24b, causes a decrease in the maximum displacement of m_1. The difference between the maximum displacement given by the 405 DOF and 1449 DOF fluid models and the benchmark model is visible in Fig 6.22. Because the N=4 and N=8 CASE models capture the upper cavitation boundary the best early in the fluid response, they correspondingly give the results closest to the benchmark solution for the maximum displacement of m_1 during the response to the first cavitation region in Fig. 6.22.

As time increases the dissipation in the magnitude of dynamic densified condensation in the cavitation region causes the effects of hydrostatic pressure and the motion of the structure to re-pressurize the fluid between the upper cavitation boundary and structure faster (see Section 6.3.1). The effect of this is observed at t=0.04s in Figs. 6.23d and 6.24d as the deeper location of upper cavitation in the 405 DOF and 1449 DOF solutions when compared to the benchmark solution. This error in cavitation capture causes a corresponding smaller magnitude of negative velocity, due to the larger mass of re-pressurized fluid [38], to be reached during the response to the first cavitation region when the 405 DOF and 1449 DOF solutions are compared to the benchmark solution in Fig. 6.21. Figs. 6.23d and 6.24d show, as time increases, both the N=4 and N=8 CASE models capture both the upper cavitation boundary and the magnitude of dynamic densified condensation closest to the benchmark solution. Thus, these higher-order CASE models also capture the magnitude of negative velocity closest to the benchmark solution during the structural response to the first cavitation region in Fig. 6.21.

Recall, in Fig. 6.21 we also found the N=1 CASE, N=4 CASE, and pressure formulation models gave a delayed arrival time of the first cavitation closure pulse for the m_2/m_1=5 problem. This difference in the structural response is also attributed to the error

in capture of the upper cavitation boundary and the loss of dynamic densified condensation magnitude in the cavitation region. As the upper cavitation boundary is pushed deeper into the fluid in the m_2/m_1=5 problem it causes the closure point of the cavitation region to occur deeper in the fluid. Thus, the closure pulse must travel further to reach the structure. This causes the delay in arrival time that, especially for the N=1 CASE and pressure formation models, is visible in the velocity response results.

Given these results, the study of cavitation capture in the fluid for the m_2/m_1=5 problem shows the N=4 and N=8 CASE models predict the evolution of the cavitation region and most importantly the upper cavitation boundary closest to the benchmark solution. Correspondingly, the N=4 and N=8 CASE models give the structure response solutions that compare best to the benchmark solution.

6.4.2 β = 0.50 and η_D= 0.035

In this section, we study the effect of increasing the amount of artificial diffusion/damping in the fluid models. This is an important effect to examine for the m_2/m_1=5 problem because it is the first problem studied in this chapter where oscillations were significantly increased in the higher-order CASE models. For all models in this section, we take β = 0.50 for CASE and η_D= 0.035 for the pressure formulation. Figures 6.25a and 6.25b gives results for the velocity of m_1 using 405 DOF and 1449 DOF respectively.

Compared to the results with β = 0.25 and η_D= 0.020 in Fig. 6.21a, the results for the 405 DOF fluid models in Fig. 6.25a show in each model the increase in artificial damping/diffusion has reduced oscillations occurring in the velocity response during t=0.025s-0.05s and again during t=0.11s-0.125s. This is especially true for N=4 CASE solution, which is also closest to the benchmark solution. This is confirmed by comparing the L_2 error norms for the velocity response given in Table 6.16. Note that each solution in Fig. 6.25a again gives a delayed arrival time for the first cavitation closer pulse.

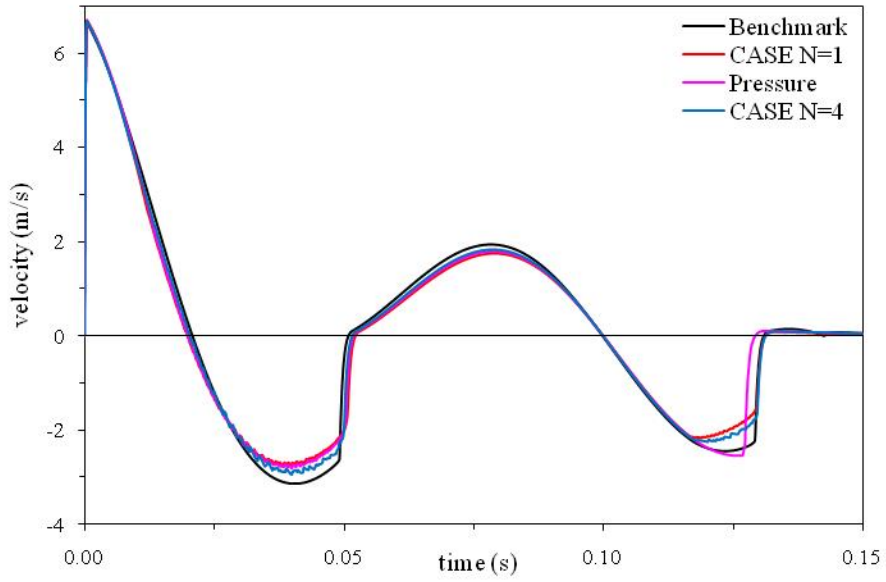

(a)

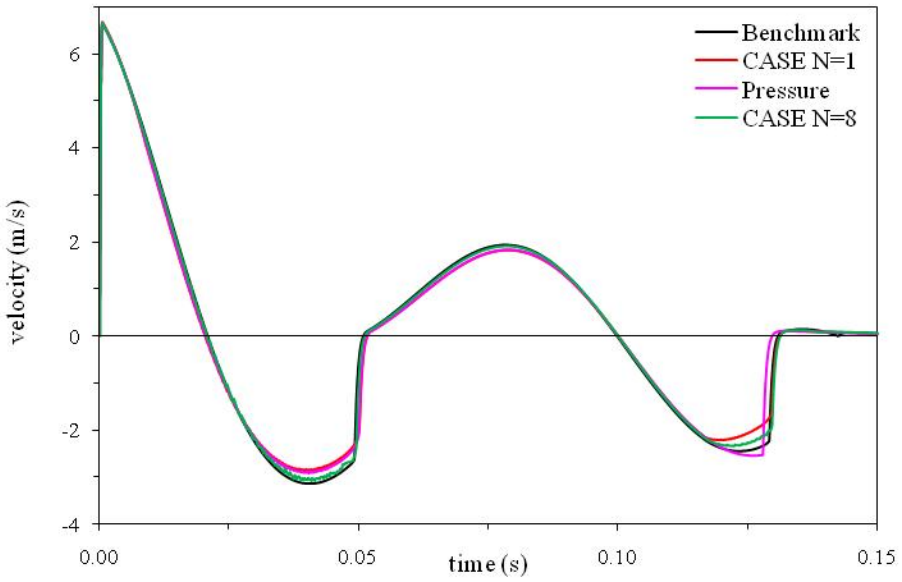

(b)

Figure 6.25 Velocity of m_1 for the m_2/m_1=5 case using 405 DOF (a) and 1449 DOF (b) with β = 0.50 for CASE and η_D= 0.035 for the pressure formulation

Table 6.16 L_2 error norms for the velocity of m_1 (m_2/m_1=5 case) with β = 0.50 for CASE and η_D= 0.035 for the pressure formulation

Fluid DOF	CASE N=1	Pressure	CASE
244	0.14595	0.15609	0.10999
405	0.12909	0.13950	0.08618
847	0.10542	0.11882	0.05921
1449	0.09194	0.10300	0.04281

When the error norms in Table 6.16 are compared to the velocity response error norms with β = 0.25 and η_D= 0.020 in Table 6.14 we find the increase in artificial damping/diffusion causes a much larger change in the N=1 CASE and pressure formulation result than it does the higher-order CASE result. To illustrate this, consider the increase in artificial damping causes an increase in the velocity response L_2 error norm of 0.02417 for N=1 CASE 405 DOF model. Comparatively the same increase in artificial damping causes an in crease of only 0.01319 in the velocity response L_2 error norm of the N=4 CASE 405 DOF model.

In Fig. 6.25a, we also observe that the pressure formulation solution differs from both CASE solutions during the response to the cavitation region. The increase in η_D causes an increase in this difference, as evidenced by the earlier arrival time of the closure pulse in the 405 DOF η_D=0.035 solution (Fig.6.25a) when compared to the solution with η_D=0.020 in Fig. 6.21a. However, from Table 6.16, the L_2 norm of the 405 DOF pressure formulation (L_2≈0.1395) is only slightly larger than the error norm of the N=1 CASE solution (L_2≈0.1291). This is attributed to the fact the two solutions agree well for the majority of the velocity response history.

Figure 6.25b shows the difference in the arrival time of the second cavitation region closure pulse between the CASE and pressure formulation solutions is again reduced with refinement of the mesh to 1449 DOF. This is evidenced by comparing the L_2 error norms in Table 6.16 as the models are refined. For each level of refinement the pressure formulation solution moves closer to the benchmark solution but still gives error norms that are slightly larger than the N=1 CASE error norms.

With 1449 DOF the N=8 CASE model clearly gives the best solution in Table 6.16, with L_2≈0.04280, compared to L_2≈0.09193 for the N=1 CASE model and L_2≈0.10300 for

the pressure formulation model. Again we note that the increase in artificial damping/diffusion affects the N=1 CASE and pressure formulation results more than it does the higher-order CASE result. Consider with 1449 DOF the increase in artificial damping causes an increase in the velocity response L_2 error norm of 0.01877 for N=1 model. The same increase in artificial damping causes increase of 0.00797 in the velocity response L_2 error norm of the N=8 CASE model. Both of these increases are less than those observed for the 405 DOF CASE models, thus the effect of increasing the artificial damping decreases as the mesh is refined.

Figure 6.25b shows both the N=1 CASE and pressure formulation model exhibit no visible oscillations and both give a delayed arrival time for the first cavitation closer pulse. For the N=8 CASE solution, there is a difference in the velocity magnitudes reached during the response first and second cavitation regions when compared to the benchmark solution, which cause the increase in the L_2 error norm when compared to the β=0.25 model. Furthermore, some small magnitude oscillations still remain in the N=8 CASE solution. However, as we found in the previous section, the small magnitude oscillations only affect the response for a short period thus are not considered to be detrimental to the accuracy of the solution.

Figures 6.26a and 6.26b give results for the displacement of m_1 using 405 DOF and 1449 DOF respectively. Note that no oscillations are observed in any of the displacement response solutions. In both figures, the higher-order CASE model gives the solution closest to the benchmark solution, especially in terms of maximum displacements during the response to the cavitation regions. For the pressure formulation solutions, the early arrival time of the second cavitation closure pulse causes a difference in the displacement of the mass visible at t=0.125 in Fig. 6.26. As in the velocity response results, this difference is decreased as the mesh is refined from 405 DOF to 1449 DOF.

The L_2 error norms for the displacement response given in Table 6.17, confirm that the higher-order CASE models give solutions closest to the benchmark solution for each level of mesh refinement used. Comparing the error norms in Table 6.17 to the $\beta = 0.25/\eta_D = 0.020$ fluid models we observe an increase due to the increase in artificial damping/diffusion for each level of mesh refinement.

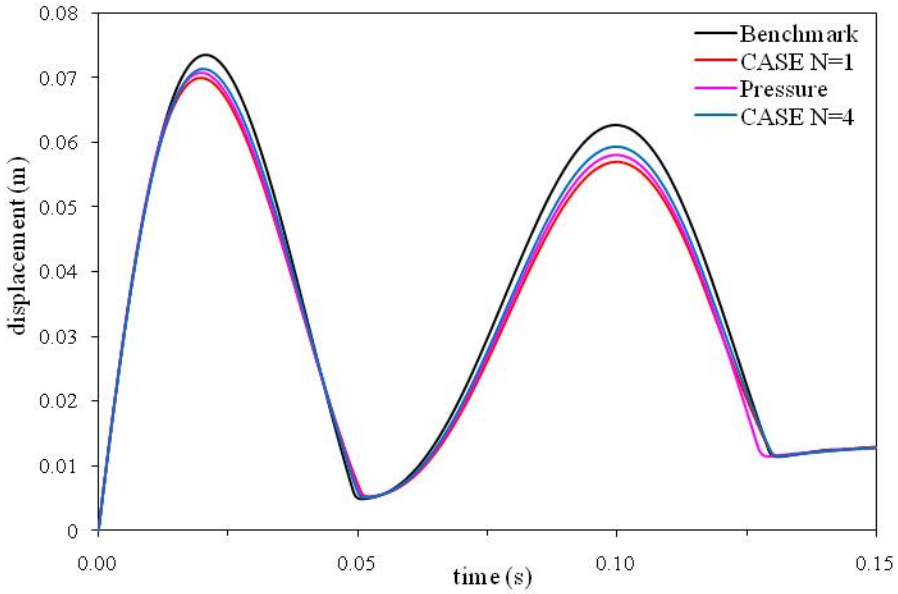

(a)

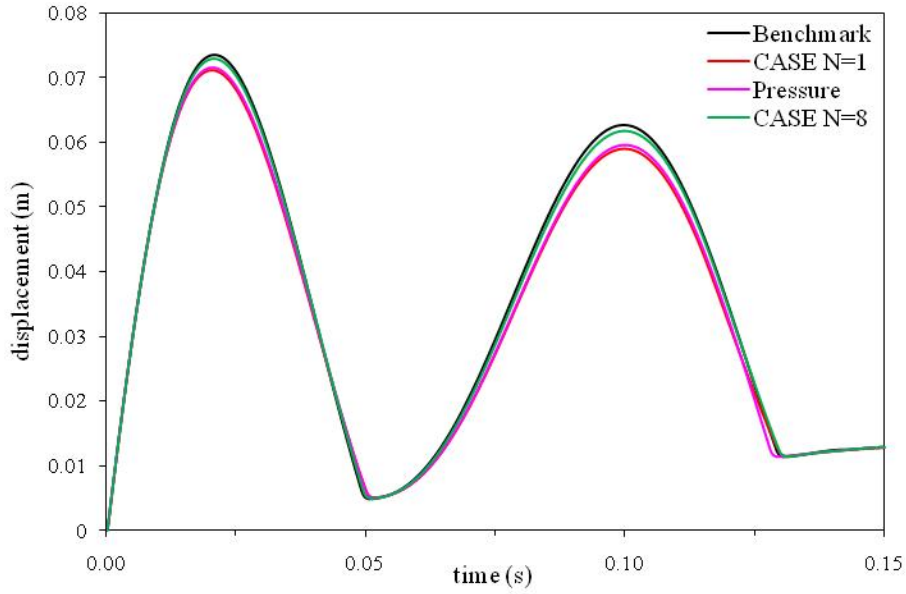

(b)

Figure 6.26 Displacement of m_1 for the m_2/m_1=5 case using 405 DOF (a) and 1449 DOF (b) with β = 0.50 for CASE and η_D= 0.035 for the pressure formulation

We also note that as we have found for each example in this chapter, the error norms for the displacement response solutions are less than those observed for the velocity response results.

Table 6.17 L_2 error norms for the displacement of m_1 (m_2/m_1=5 case) with β = 0.50 for CASE and η_D= 0.035 for the pressure formulation

Fluid DOF	CASE N=1	Pressure	CASE
244	0.09114	0.07620	0.06814
405	0.08036	0.06904	0.04790
847	0.06347	0.05647	0.02646
1449	0.05264	0.04668	0.01599

Figures 6.27 and 6.28 show the plots of dynamic densified condensation for the 405 DOF and 1449 DOF fluid models, respectively, during the development of the first cavitation region at t=0.002s, t=0.015s, t=0.03s, and t=0.04s. At t=0.002s for the 405 DOF fluid models in Fig. 6.27a we see the increase in artificial damping/diffusion smoothes the oscillations observed in Fig. 6.23a for the same 405 DOF fluid models with β = 0.25 and η_D= 0.020. With the exception of the t=0.002s result, where the pressure formulation gives the lowest error norm, Fig. 6.27 shows the N=4 CASE model give the solutions closest to the benchmark solution. However, Figs.6.27b-d also shows the increase in artificial damping/diffusion also increases the error in capture of the cavitation region when compared to the β = 0.25 and η_D= 0.020 solutions (Fig. 6.23). In the example of the N=4 CASE solution, the increase in artificial damping results in a 0.1835 increase in the L_2 error norm at t=0.04s.

Refinement of the mesh to 1449 DOF, shown in Fig.6.28, gives a decrease in L_2 error norm at each time considered. The N=8 CASE model gives the best solutions at each time in Fig. 6.28 except t=0.002s, where the pressure formulation gives the lowest error norm. Again we note that compared to the solutions with β = 0.25 and η_D= 0.020, the results in Fig. 6.28 show an overall increase in error due to the increase in artificial damping/diffusion.

In terms of capturing the upper cavitation boundary and the magnitude of dynamic densified condensation in the cavitation region both the N=4 and N=8 CASE models give

results closest to the benchmark solution. This is reflected by the superiority of the higher-order CASE models in the structural response results.

The effect of damping on the capture of the upper cavitation boundary is best illustrated by comparing, at t=0.015s and t=0.04s, the 405 DOF results with β = 0.25 and η_D= 0.020 in Figs. 6.23b and 6.23d to the 405 DOF β = 0.50 and η_D= 0.035 in Figs. 6.27b and 6.27d.

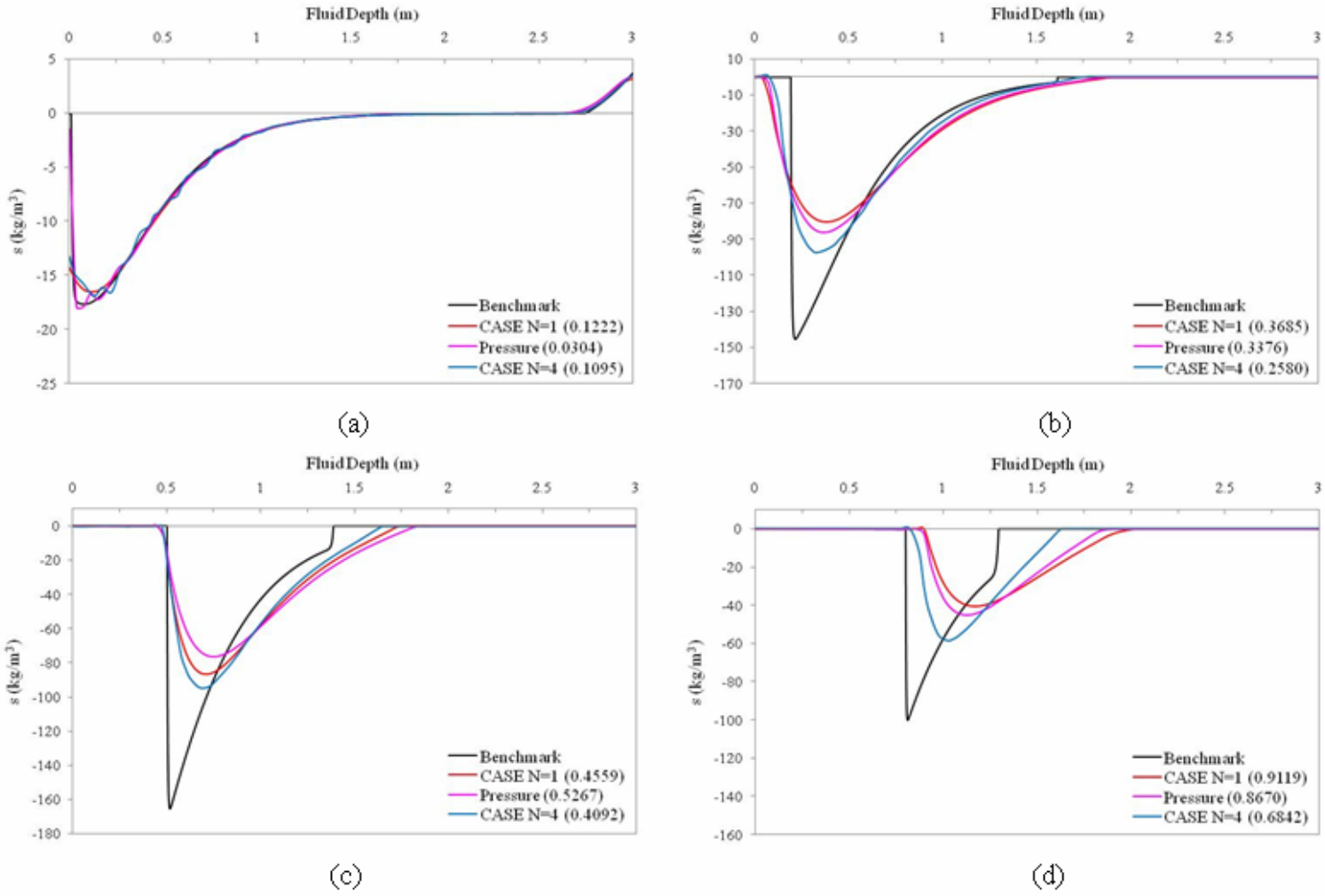

Figure 6.27 Dynamic densified condensation in the fluid at t=0.002 s (a), t=0.015 s (b), t=0.03 s (c), and t=0.04 s (d) for the m_2/m_1=5 case using 405 DOF with β = 0.50 for CASE and η_D= 0.035 for the pressure formulation

In this comparison we see that at t=0.015s the increased damping/diffusion has caused the upper cavitation boundary to be located closer to the fluid-structure interface. At t=0.04s, we see the increased damping/diffusion has caused further dissipation of the magnitude

of dynamic densified condensation in the cavitation region and has also caused the upper cavitation boundary to be propagated deeper into the fluid. Thus the structural response with 405 DOF and increased damping also show an increase in error when compared to the benchmark solution during the response to the first cavitation region.

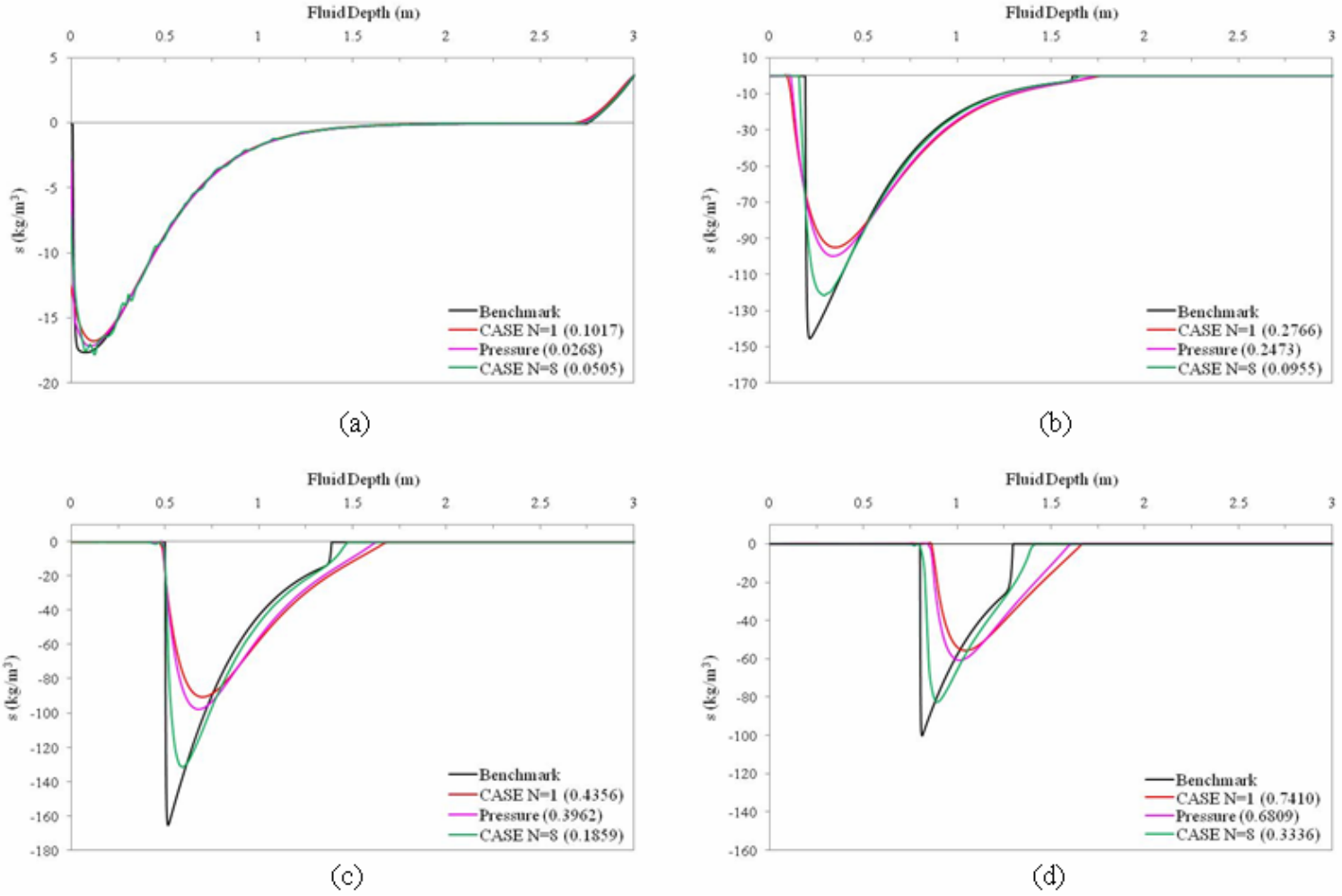

Figure 6.28 Dynamic densified condensation in the fluid at t=0.002 s (a), t=0.015 s (b), t=0.03 s (c), and t=0.04 s (d) for the m_2/m_1=5 case using 1449 DOF with β = 0.50 for CASE and η_D= 0.035 for the pressure formulation

Note that when we make the same comparison between the 1449 DOF models in Figs. 6.24 and 6.28 we observe the location of the upper cavitation boundary is not as affected by the increase in damping. This is especially true for the N=8 results which show almost no change in the location of the upper cavitation boundary. This is the reason that the increase in the velocity and displacement response error norms by going

from β = 0.25 and η_D= 0.020 to β = 0.50 and η_D= 0.035 for the 1449 DOF fluid models are less than those observed for the 405 DOF fluid models.

6.4.3 β = 0.10 and η_D= 0.010

For the 1D m_2/m_1=5 problem in Section 5.2 we examined the possibility of reducing the amount of damping used with N=1 models to obtain solutions that were similar to higher order CASE solutions. In this section we examine this possibility more thoroughly for the 2D problem.

First we present results for the velocity of m_1 in Fig. 6.29 using β = 0.10 and η_D= 0.020 with 405 DOF and 1449 DOF. Figure 6.29a shows that with the decrease in artificial damping/diffusion the N=1 and N=4 CASE models agree well with the benchmark solution, although again the solutions give a delayed arrival time of the first cavitation closer pulse. Figure 6.29a also shows there is a significant increase in oscillations during t=0.025s-0.05s and again during t=0.11s-0.125s. The increase in oscillations is most notable is the N=4 CASE solution. Despite the oscillations Table 6.18 confirms the N=4 405 DOF CASE model gives the best result.

Table 6.18 L_2 error norms for the velocity of m_1 (m_2/m_1=5 case) with β = 0.10 for CASE and η_D= 0.010 for the pressure formulation

Fluid DOF	CASE N=1	Pressure	CASE
244	0.11868	0.08720	0.06965
405	0.09404	0.06889	0.06321
847	0.07273	0.05243	0.04324
1449	0.05933	0.04577	0.02474

Figure 6.29a also shows that for the 405 DOF the pressure formulation solution initially agrees well with the N=1 CASE solution but again differs from both CASE solutions during the response to the second cavitation region. Unlike in the previous sections, the timing of the closure of the second cavitation region in the pressure formulation results is closest to the benchmark solution when compared to both CASE solutions which give a later closure time than the benchmark solution. This is attributed to the difference in amount of artificial damping/diffusion applied to the fluid by the choice of β = 0.10 and η_D= 0.010.

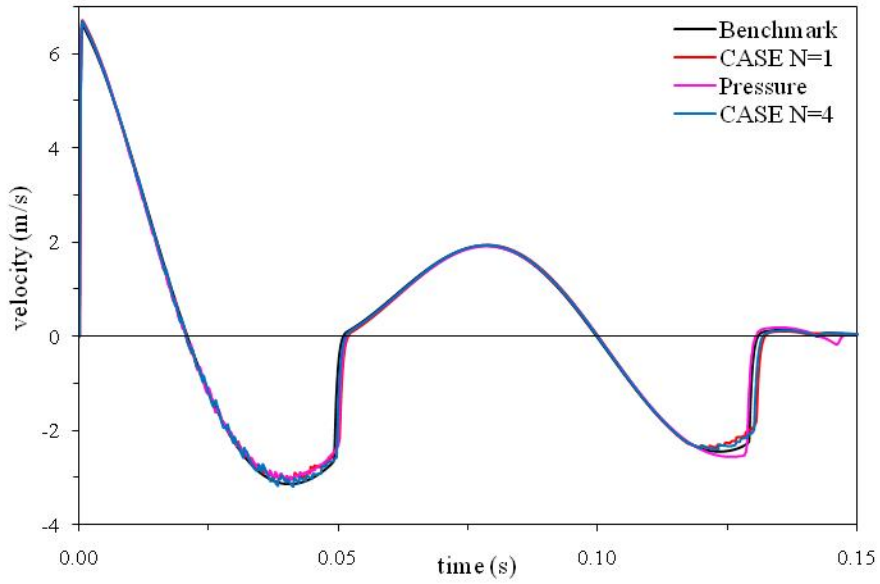

(a)

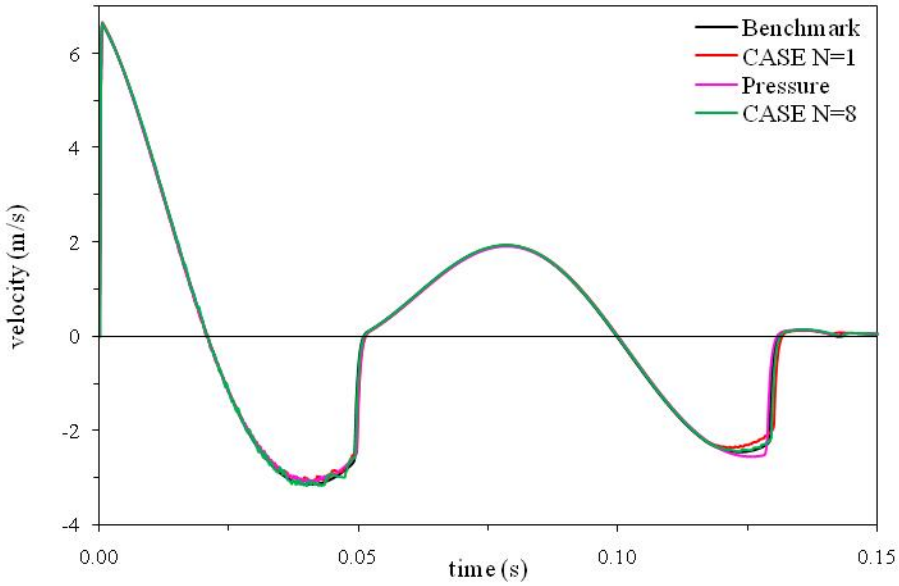

(b)

Figure 6.29 Velocity of m_1 for the m_2/m_1=5 case using 405 DOF (a) and 1449 DOF (b) with β = 0.10 for CASE and η_D= 0.010 for the pressure formulation

Another difference between the pressure formulation solution and CASE results is the appearance of a significant third cavitation region, evidenced by the dip in the velocity response at t=0.14s. While a third cavitation region does appear in the benchmark solution, it does not cause as large of a change in the velocity response of the structure. However, comparing the L_2 error norms for the velocity response in Table 6.18, we see the differences observed in the pressure formulation solution do not have a noticeable effect on the error norms when compared to the N=1 CASE model. This is attributed to the similarity of the solutions for the majority of the response history and in this reduced damping/diffusion case, to the fact that the closure of the second cavitation region in the pressure formulation solution is closest to the benchmark solution.

In Fig. 6.29b the refinement of the mesh reduces the oscillations in the solution and improves the solution for each model as shown by the L_2 error norms in Table 6.18. The only visible difference between the models in Fig. 6.29b occurs during the second cavitation region at t=0.11s. However, the L_2 norm in Table 6.18 show the N=8 CASE solution gives the result closest to the benchmark solution.

As in the 405 DOF results, we see that compared to the previous 1449 DOF cases with β = 0.25/η_D= 0.020 and β = 0.50/ η_D= 0.035, the solutions with β = 0.10/ η_D= 0.010 significantly increase the oscillations in the velocity response. However, the error norms are still reduced by the reduction in damping when compared to the cases with larger amounts of damping/artificial diffusion.

Results for the displacement of m_1 for the 405 DOF and 1449 DOF fluid models are given in Fig. 6.30. For both the 405 DOF (Fig. 6.30a) and the 1449 DOF (Fig. 6.30b) the results for each CASE model are almost indistinguishable from the benchmark solution. The pressure formulation results are also very close to the benchmark solution, except for the 405 DOF solution between t=0.125s-0.15s where there is a larger increase in maximum displacement visible. This is caused by the exaggerated response in the pressure formulation solution that causes the formation of the third cavitation region mentioned in the discussion of the velocity response results. Note for each model in Fig. 6.30 no oscillations are observed in the displacement response.

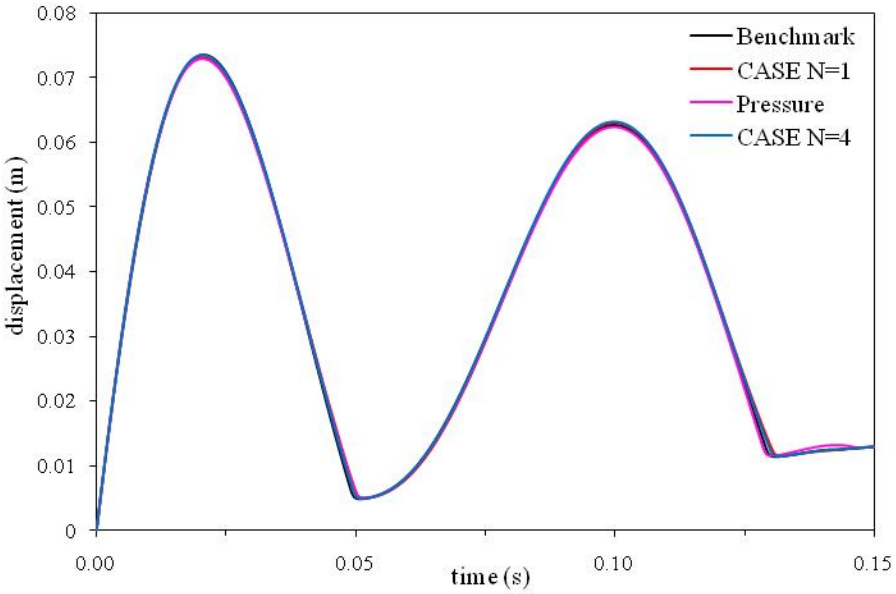

(a)

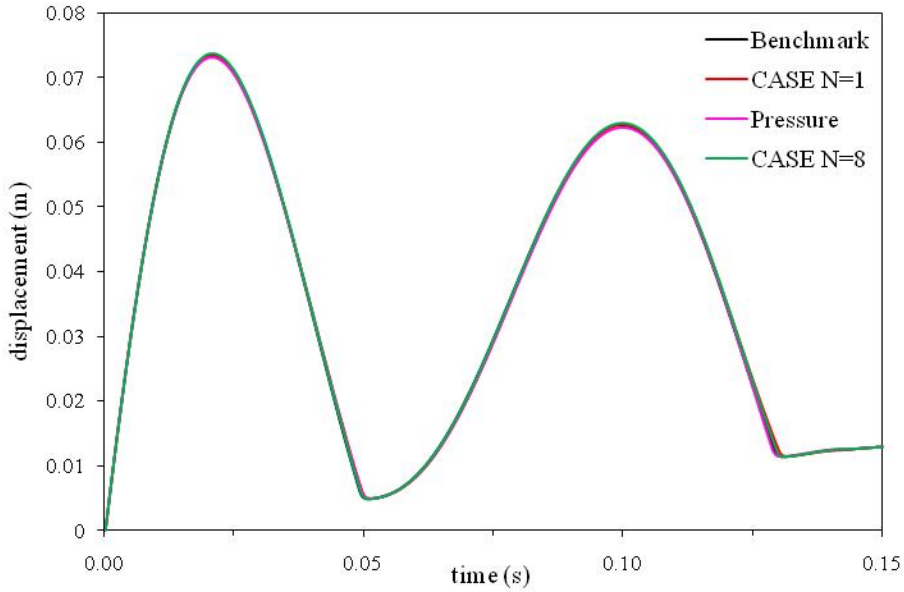

(b)

Figure 6.30 Displacement of m_1 for the m_2/m_1=5 case using 405 DOF (a) and 1449 DOF (b) with β = 0.10 for CASE and η_D= 0.010 for the pressure formulation

Comparison of the L_2 error norms for the displacement results shows that as in the velocity response, for a given level of refinement the higher-order CASE model gives the solution closest to the benchmark solution.

Table 6.19 L_2 error norms for the displacement of m_1 (m_2/m_1=5 case) with β = 0.10 for CASE and η_D= 0.010 for the pressure formulation

Fluid DOF	CASE N=1	Pressure	CASE
244	0.02442	0.02082	0.00894
405	0.01574	0.01330	0.00908
847	0.01079	0.01151	0.00602
1449	0.00844	0.00981	0.00272

For each amount of damping used for the m_1/m_2=5 problem, we have observed a significant increase in oscillations when we compare N=1 CASE and pressure formulation solutions to higher-order CASE solutions. We now present results to examine the possibility of reducing the amount of damping used with a N=1 CASE model to obtain solutions that were similar to a higher order CASE solution. In the following discussion, we focus on comparing only the N=1 CASE and higher-order CASE models, due to the differences observed between the pressure formulation and CASE models. The premise of this comparison for the m_1/m_2=5 problem is that if we accept increased oscillations for the higher-order CASE models because they gives better results, then we should also accept increased oscillations in the N=1 CASE models. These appear as we reduce the amount of damping used in the fluid model to yield solutions closer to the benchmark solution. This is an important determination to make, as a N=1 CASE model that gives results that match higher-order CASE model for a given number of fluid DOF would offer a savings in computational expense. This is due to the larger computational expense of higher-order CASE models when compared to N=1 CASE (or CAFE) models with the same number of fluid DOF [26,46,61].

In Section 5.2, we observed that the reduction of β in a 1D N=1 CASE model gave solutions that visually agreed well with higher order CASE solutions. Furthermore, in some cases the oscillations were less severe for the $N=1$ CASE results with reduced β.

For the 2D problem, we examine this effect by comparing the N=1 CASE model with β=0.10 to the N=4 and N=8 CASE models with β=0.25.

Figure 6.31 compares the velocity response of m_1 for the 405 DOF N=1 CASE model with β =0.10 to the 405 DOF N=4CASE model with β =0.25. Visually, both models give solutions that agree well with each other. To compare the difference in oscillations, we show the velocity response during t=0.02s-0.06s in Fig. 6.31b. In this figure we see both models have nearly identical amounts of oscillations present in the velocity response during this time. However, in Fig. 6.31b the N=1 CASE solution gives a delay in the closure of the first cavitation region. For this reason, the 405 DOF N=4 CASE with β =0.25 solution remains closest to the benchmark solution. This is proved by comparing the N=4 error norm, $L_2 \approx 0.07298$, to the N=1 error norm of $L_2 \approx 0.09404$.

Figure 6.32 shows the plots of dynamic densified condensation at t=0.002s, t=0.015s, t=0.03s, and t=0.04s for the 405 DOF N=1 CASE model with β =0.10 to the 405 DOF N=4CASE model with β =0.25. At t=0.002s, both models give almost identical L_2 error norms, and the two solutions remain close at t=0.015s and t=0.03s. The largest difference in error norm occurs at t=0.04s, where the N=4 CASE models gives the solution closest to the benchmark solution. In terms of capturing the upper cavitation boundary, both models show no noticeable difference for the times observed in Fig. 6.32. This is expected because the velocity response results in Figs. 6.31 did not exhibit a noticeable difference in the velocity magnitudes reached during the response to the first cavitation region.

Instead, the primary difference between the N=1 and N=4 solutions during the response to the first cavitation region is the arrival time of the first cavitation closure pulse. In Fig. 6.32d we see the magnitude of dynamic densified condensation in the N=4 CASE solution is greater than in the N=1 CASE solution. This is evidence that, as the cavitation region continues to collapse, the N=4 CASE model will dissipate less of the dynamic densified condensation in the cavitation region than the reduced β N=1 CASE model. Thus the N=4 CASE model ultimately gives the more accurate closure time for the first cavitation region as seen in the velocity response results (Fig. 6.31).

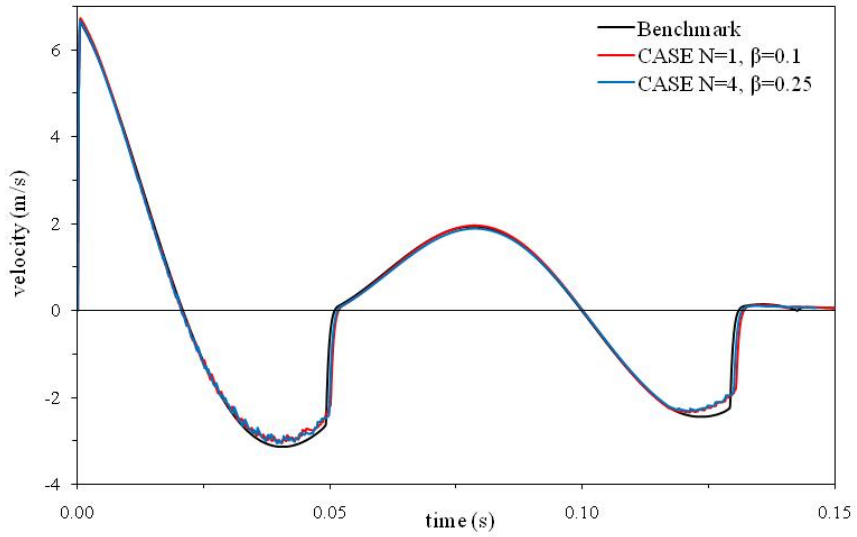

(a)

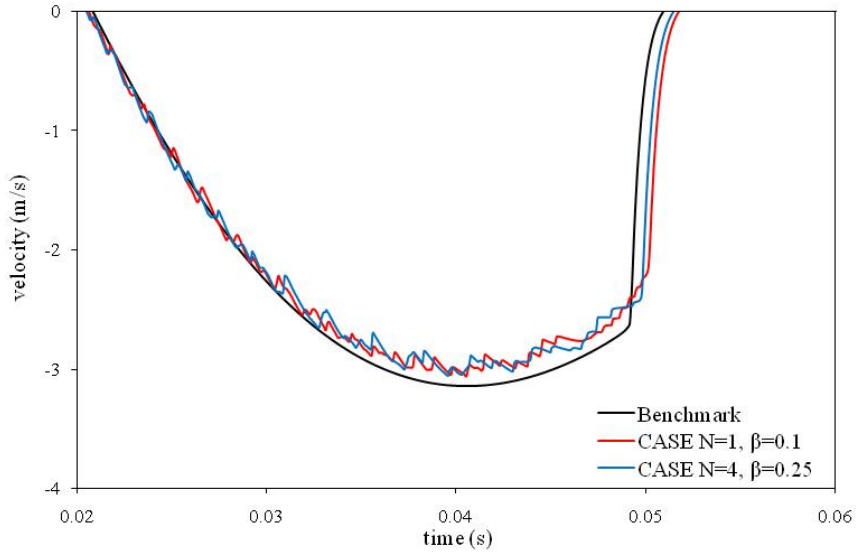

(b)

Figure 6.31 Velocity of m_1 for the m_2/m_1=5 case on two time scales using 405 DOF with β = 0.10 for N=1 CASE and β = 0.25 for N=4 CASE

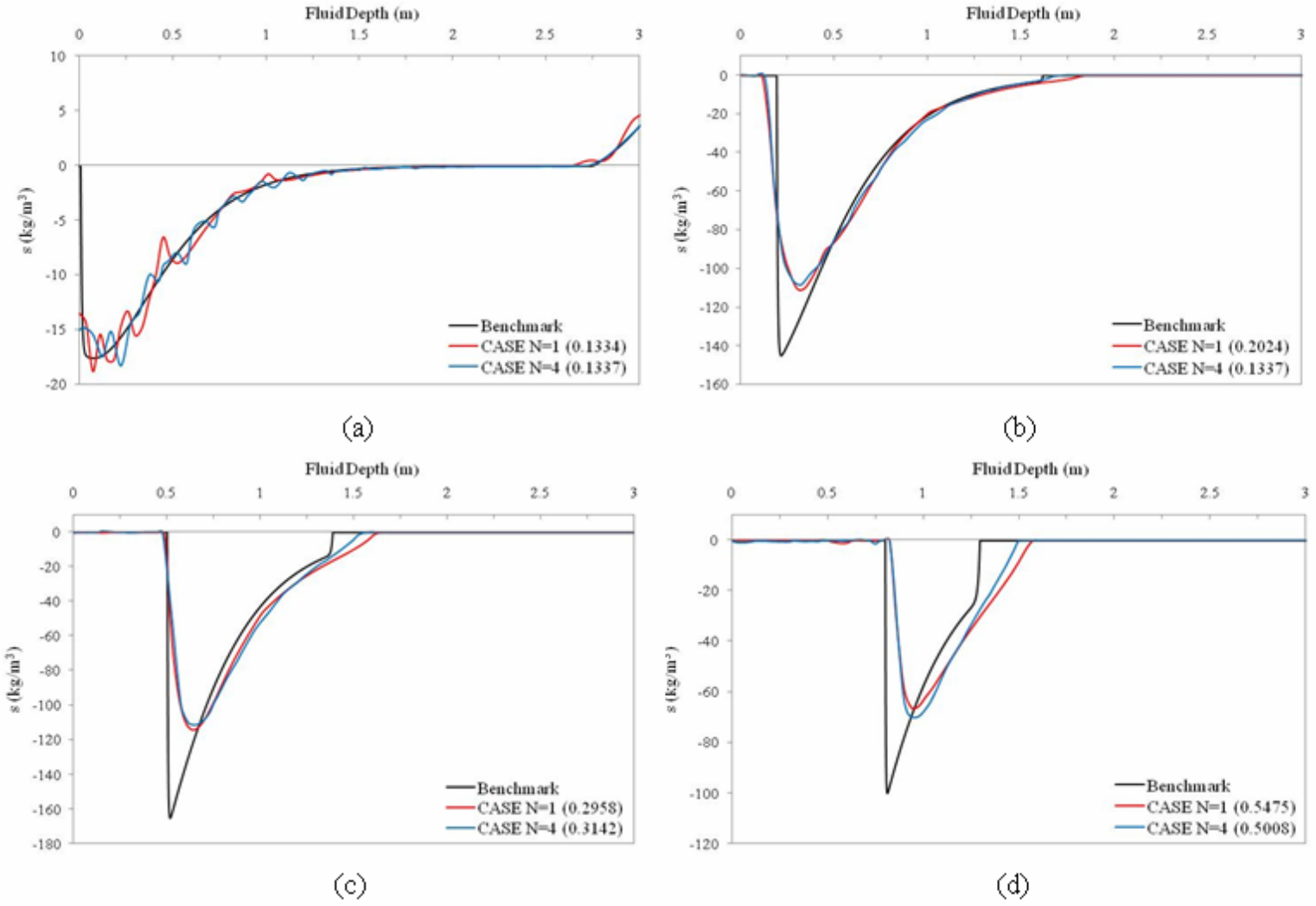

Figure 6.32 Dynamic densified condensation in the fluid at t=0.002 s (a), t=0.015 s (b), t=0.03 s (c), and t=0.04 s (d) for the m_2/m_1=5 case using 405 DOF with β = 0.10 for N=1 CASE and β = 0.25 for N=4 CASE

Similarly, for the 1449 DOF velocity response results shown in Fig. 6.33, we find visually the N=1 CASE model with β=0.10 agrees well with N=8 CASE model with β=0.25. Looking at the oscillations during t=0.02s-0.06s in Fig. 6.33b, we see that initially the two models have similar amounts of oscillations, but between t=0.04s and t=0.06s the N=1 CASE solution with β=0.10 actually has larger oscillations than the N=8 CASE solution with β=0.25. Furthermore, as seen in the 405 DOF model results the N=1 CASE solution again gives a delayed closure time of the first cavitation region. Comparing the L_2 error norm of the 1449 DOF N=8 CASE model with β=0.25, $L_2 \approx 0.03483$, to the error norm of the 1449 DOF N=1 CASE model with β=0.25,

$L_2 \approx 0.05933$, we confirm the higher-order CASE model gives the result closest to the benchmark solution even when compared to the reduced β N=1 CASE model.

This is further explained by comparing the plots of dynamic densified condensation at t=0.002s, t=0.015s, t=0.03s, and t=0.04s for the 1449 DOF N=1 CASE model with β =0.10 to the 1449 DOF N=8 CASE model with β =0.25 in Fig. 6.34. In Fig. 6.34 we see that at each time considered the 1449 DOF N=8 CASE solution with β =0.25 is clearly closest to the benchmark solution. Comparing the location of the upper cavitation boundary at t=0.04s in Fig. 6.34d we see there is a small difference between the N=1 and N=8 solutions. This is in contrast to the 405 DOF solution, where the N=1 CASE solution with β =0.10 and N=4 CASE solution with β=0.25 gave indistinguishable locations for the upper cavitation boundary at t=0.04s. This illustrates the advantage of the higher-order CASE model as higher levels of refinement are used. Furthermore, at t=0.04s in Fig. 6.34d the N=8 CASE model has retained the magnitude of dynamic densified condensation in the cavitation region better than the reduced β N=1 model. Both the improved capture of the upper cavitation boundary and the reduction in dissipation of dynamic densified condensation in the cavitation region lead to the greater accuracy in the velocity response of the N=8 CASE model when compared to the benchmark solution.

Given the results of this section, we find reducing the amount of damping used in a reduced β N=1 CASE model is not able to match the solution of a higher order CASE model for a given number of fluid DOF. This is because the higher order CASE models the development of cavitation in the fluid better, especially for high degrees of refinement. In the structural response this is evident in the delayed closure time of cavitation regions in the N=1 CASE model results. Thus, for the m_2/m_1=5 problem, we find that when compared to the N=1 CASE and pressure formulation models for a given amount of artificial damping/diffusion and a given degree of model refinement, the higher-order CASE model will give superior results. The superiority of the higher-order CASE model is in terms of both cavitation capture in the fluid and correspondingly the structural response.

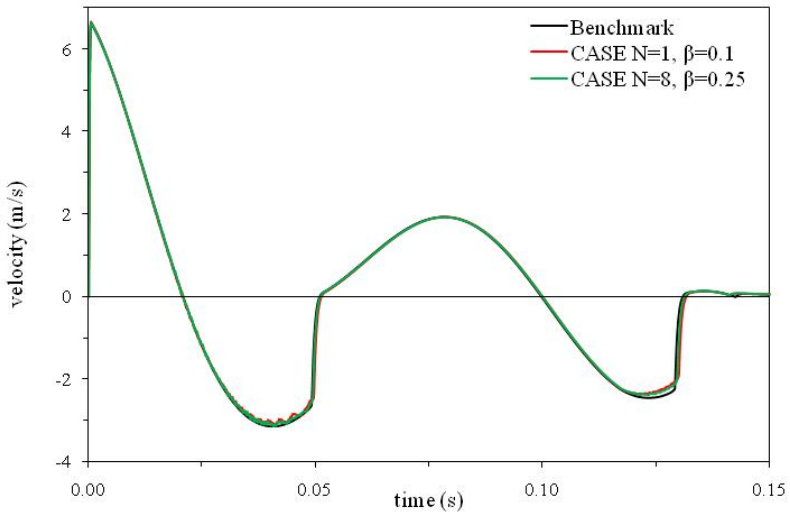

(a)

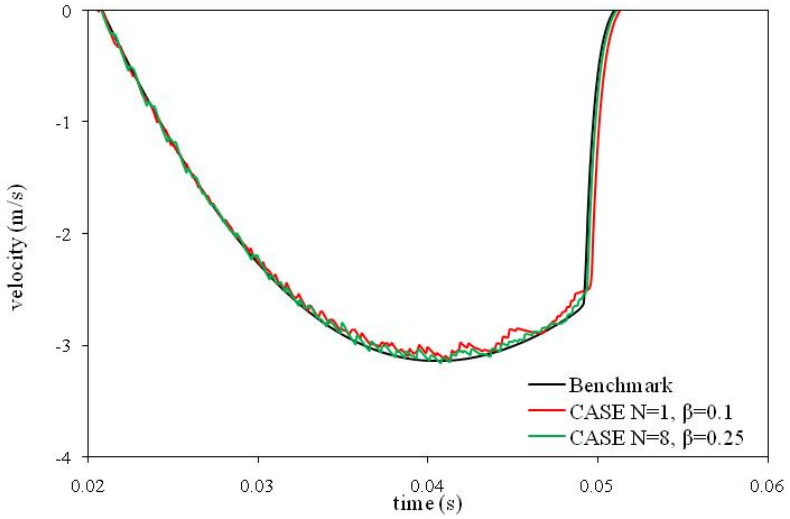

(b)

Figure 6.33 Velocity of m_1 for the m_2/m_1=5 case on two time scales using 1449 DOF with β = 0.10 for N=1 CASE and β = 0.25 for N=8 CASE

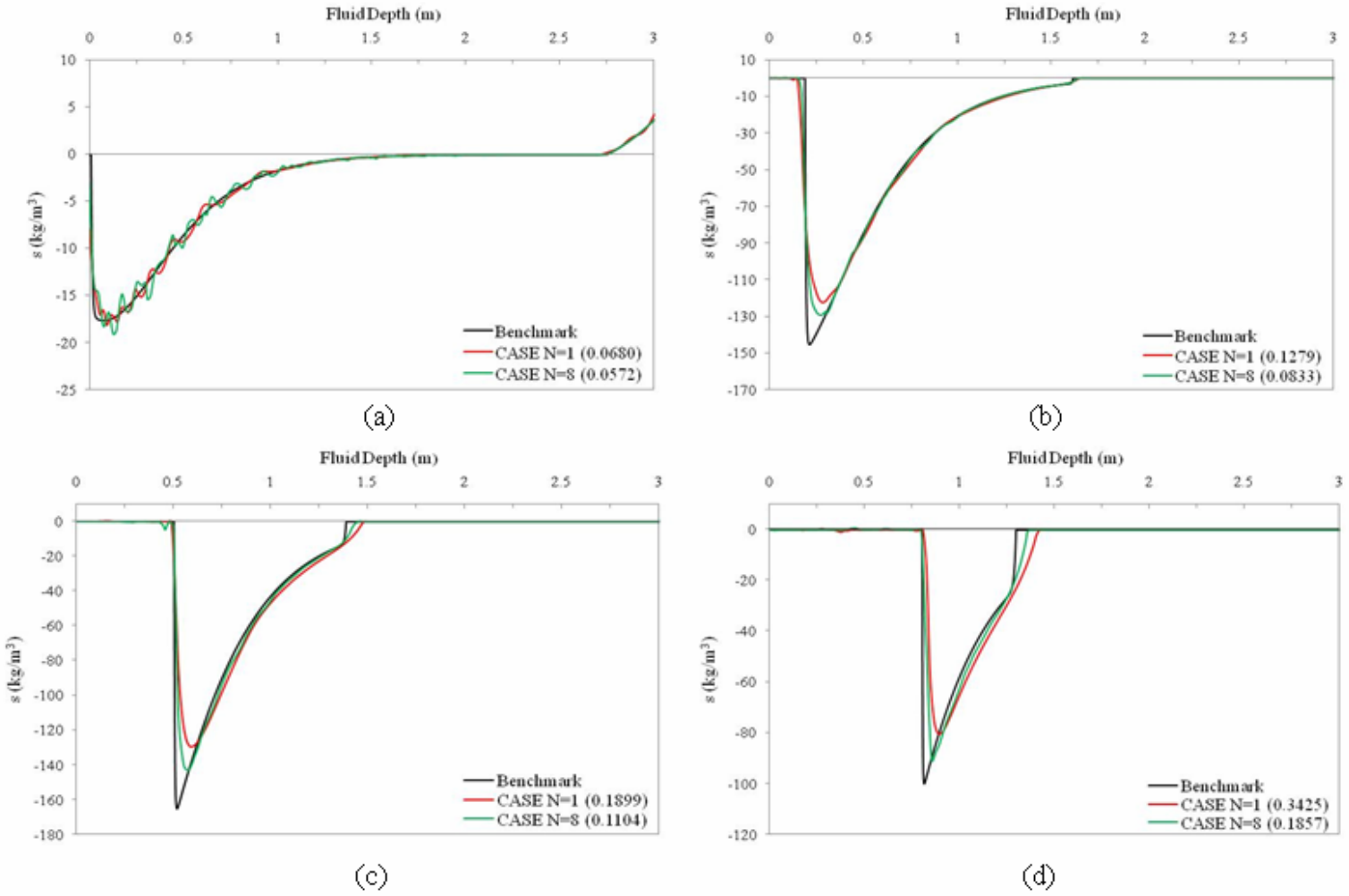

Figure 6.34 Dynamic densified condensation in the fluid at t=0.002 s (a), t=0.015 s (b), t=0.03 s (c), and t=0.04 s (d) for the m_2/m_1=5 case using 1449 DOF with β = 0.10 for N=1 CASE and β = 0.25 for N=8 CASE

6.5 m_2/m_1=25 Results and Discussion

6.5.1 β = 0.25 and η_D= 0.020

In this section we present results for the m_2/m_1=25 problem. This problem is of particular importance because for a ship structure the mass of the hull plating, represented by m_1 in the mass-spring oscillator problem, is typically much lighter than the total mass of the ship [6]. Thus, of the problems considered in this work the m_2/m_1=25 problem may be the most realistic in terms of approximating an actual ship structure.

Figures 6.35a and 6.35b give results for the velocity of m_1 using 405 DOF and 1449 DOF respectively. All fluid models in this section use β = 0.25 for CASE and η_D= 0.020

for the pressure formulation. In the benchmark solution, m_1 reaches a kick-off velocity of ~12.5 m/s at which point the velocity begins to slope downwards as cavitation begins. The cavitation closure pulse re-loads m_1 at t=0.035s causing a sharp increase in positive velocity. The upward motion of m_1 causes a second cavitation region to form. The velocity of m_1 oscillates during this cavitation region until t=0.115s at which point the closure pulse of the second cavitation region re-loads the mass.

Each model in Fig. 6.35a gives smaller velocity magnitudes during the response to the first cavitation region and also shows a small delay in the arrival time of the first cavitation closure pulse. The decreased velocity magnitude and delayed closure pulse is more pronounced in the N=1 CASE and pressure formulation solutions. From t=0.01s-0.035s, Fig. 6.35a shows there are large oscillations present in the response for each 405 DOF fluid model. These oscillations are the most severe that have been observed for the ratios of m_2/m_1 studied in this chapter and are the largest for the N=4 CASE solution. Despite the increase in oscillations, compared to the other models in Fig. 6.35a the N=4 CASE model gives results closest to the benchmark solution. Comparison of the L_2 error norms in Table 6.20 confirms this.

Table 6.20 L_2 error norms for the velocity of m_1 (m_2/m_1=25 case) with β = 0.25 for CASE and η_D= 0.020 for the pressure formulation

Fluid DOF	CASE N=1	Pressure	CASE
244	0.14335	0.14918	0.12070
405	0.13014	0.13720	0.08969
847	0.10568	0.10981	0.05797
1449	0.08754	0.09194	0.04487

As we observed in the m_2/m_1=5 problem, the error norms in Table 6.20 show the increase in the ratio of m_2/m_1 causes an increase in the error norms of the velocity response for each of the models considered. This further illustrates the assertion in [38] that as m_1 is decreased it becomes more sensitive to the fluid model. For example, comparing the solutions to the m_2/m_1=25 problem and m_2/m_1=5 problem the 405 DOF N=1 CASE model gives an increase of 0.0252 in L_2 error norm for the velocity response. Making the same comparison for the pressure formulation and N=4 CASE solutions gives an increase of .0331 and 0.01669, respectively, in the velocity response L_2 error norms.

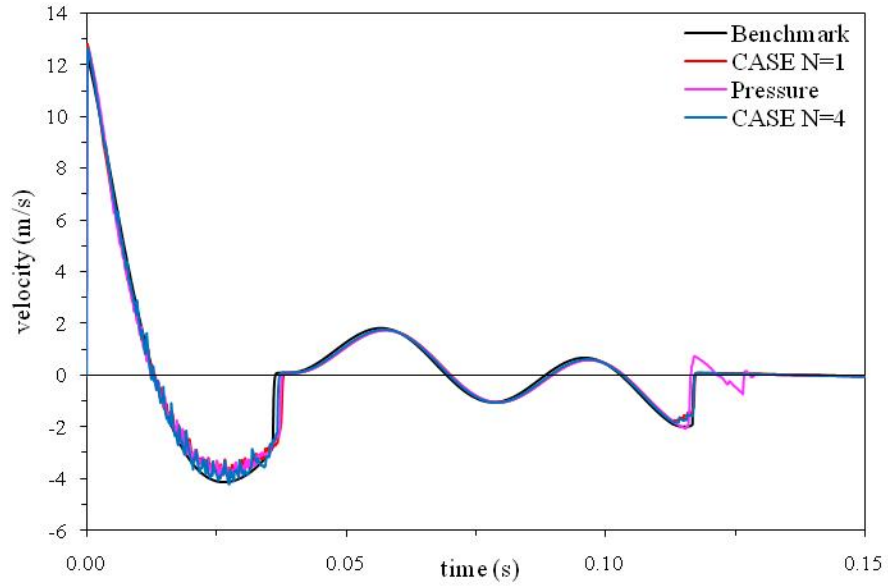

(a)

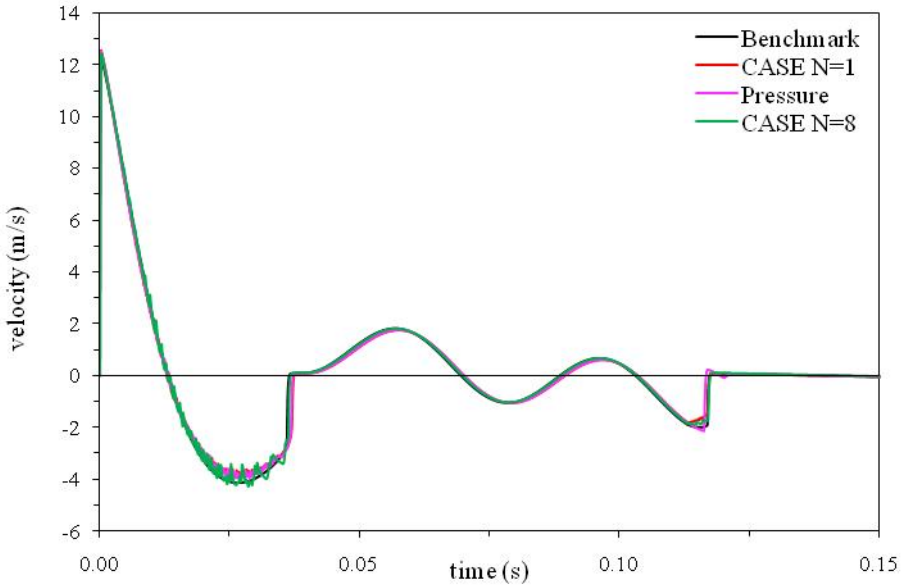

(b)

Figure 6.35 Velocity of m_1 for the m_2/m_1=25 case using 405 DOF (a) and 1449 DOF (b) with β = 0.250 for CASE and η_D= 0.020 for the pressure formulation

In the m_2/m_1=5 problem we also observed a difference between the pressure formulation and N=1 CASE solutions only during the closure of the second cavitation region. Similarly for the m_2/m_1=25 problem, the pressure formulation solution is almost identical to the N=1 CASE solution until the closure of the second cavitation region. At this point, Fig. 6.35a shows the pressure formulation gives a lower velocity magnitude at the closure of the second cavitation region but the arrival time of the closure pulse is almost identical to the N=1 CASE solution. The largest difference in the pressure formulation solution is the prediction of a third cavitation region, visible in the velocity response history as the positive and negative spikes between t=0.115s-0.126s.

Comparing the L_2 error norms for the 405 DOF N=1 CASE ($L_2 \approx 0.13014$) and pressure formulation ($L_2 \approx 0.1372$) solutions in Table 6.20, we see the pressure formulation error norm is very close to the N=1 CASE error norm. Thus, deviation from the benchmark solution between the N=1 CASE and pressure formulation models is relatively unaffected by these discrepancies. Again we attribute this to the fact the pressure formulation solution and the N=1 CASE solution agree well for the majority of the velocity response history.

Figure 6.35b shows the velocity response as the mesh is refined to 1449 DOF. For each model presented in Fig. 6.35b, the refinement of the mesh has improved the solution. Even with the refinement, the N=1 CASE and the pressure formulation solutions give smaller velocity magnitudes during the response to the first cavitation region and also give a delayed arrival time of the first cavitation closure pulse. Refinement of the mesh reduces oscillations in the higher-order CASE solution, although we note the N=8 CASE solution still exhibits large oscillations between t=0.01s-.035s. However, in terms of matching the benchmark solution, Fig. 6.35b shows the 1449 DOF N=8 CASE solution is superior. Comparison of the L_2 error norms in Table 6.20 confirms the N=8 CASE solution to give the closest approximation to the benchmark solution. Thus, the increase in oscillations does cause the N=8 CASE solution to be less accurate when compared to the N=1 CASE and pressure formulation solutions.

Additionally, as each model is refined from 244 DOF to 1449 DOF in Table 6.20, the higher-order CASE model gives a larger reduction in error as the model is refined due to

the superior convergence properties of spectral elements compared when compared to finite elements. This has been observed for each value of m_2/m_1 studied in this chapter.

Comparing the 1449 DOF pressure formulation solution to the 1449 DOF N=1 CASE solution in Fig. 6.35b we observe the difference between the pressure formulation and N=1 CASE solutions during the closure of the second cavitation region has been reduced from the 405 DOF solutions. At the closure of the second cavitation region, Fig. 6.35a shows the pressure formulation again gives a larger velocity magnitude at the closure of the second cavitation region but the arrival time of the closure pulse is almost identical to the N=1 CASE solution. The response due to the occurrence of a third cavitation region (the positive and negative spikes between t=0.115s-0.126s) is also greatly reduced when compared to the 405 DOF pressure formulation solution

The L_2 error norms for the 1449 DOF N=1 CASE ($L_2 \approx 0.08754$) and 1449 DOF pressure formulation ($L_2 \approx 0.09194$) solutions in Table 6.20, again are very close. For the 1449 DOF models we find the total error between the N=1 CASE and pressure formulation models is relatively unaffected by the discrepancies in response to the closure of the second cavitation region. Once again, we attribute this to the fact the 1449 DOF pressure formulation solution and the 1449 DOF N=1 CASE solution agree well during the majority of the velocity response history.

The displacement response of m_1 using 405 DOF and 1449 DOF is given in Figures 6.36a and 6.36b respectively. For the 405 DOF results, the N=4 CASE model gives the closest approximation to the benchmark solution. The difference in response between the pressure formulation and N=1 CASE models due to the closure of the second cavitation region is visible in Fig. 6.36a as the positive displacement bump in the pressure formulation solution during t=0.11s-0.125s. Note that no oscillations are visible at any time in the displacement response history.

Fig. 6.36b shows that refinement of the mesh to 1449 DOF improves the solution of each model and also decreases the difference between the pressure formulation and N=1 CASE models. Clearly, in Fig. 6.36b the 1449 DOF N=8 CASE solution gives the result closest to the benchmark solution. This is confirmed by comparing the L_2 error norms for the displacement of m_1 in Table 6.21.

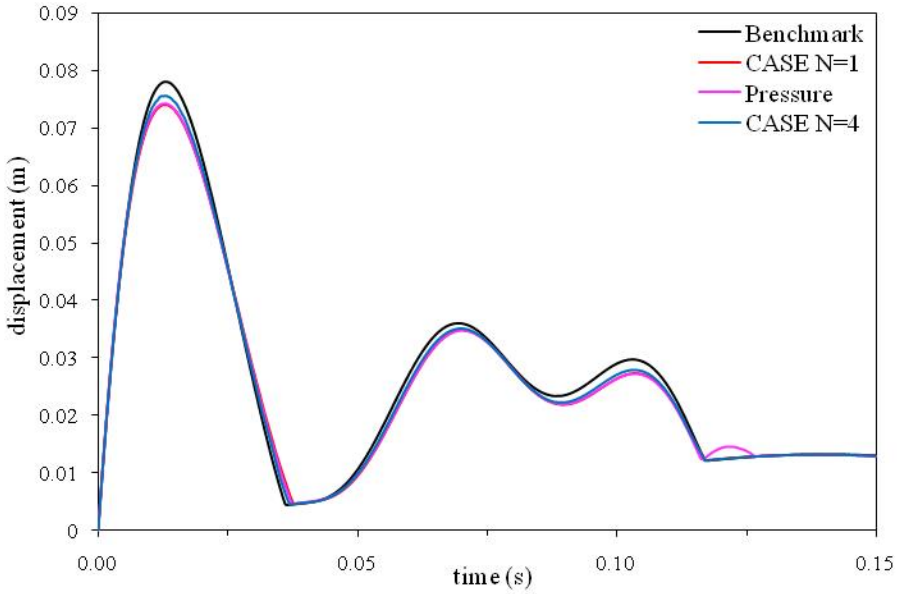

(a)

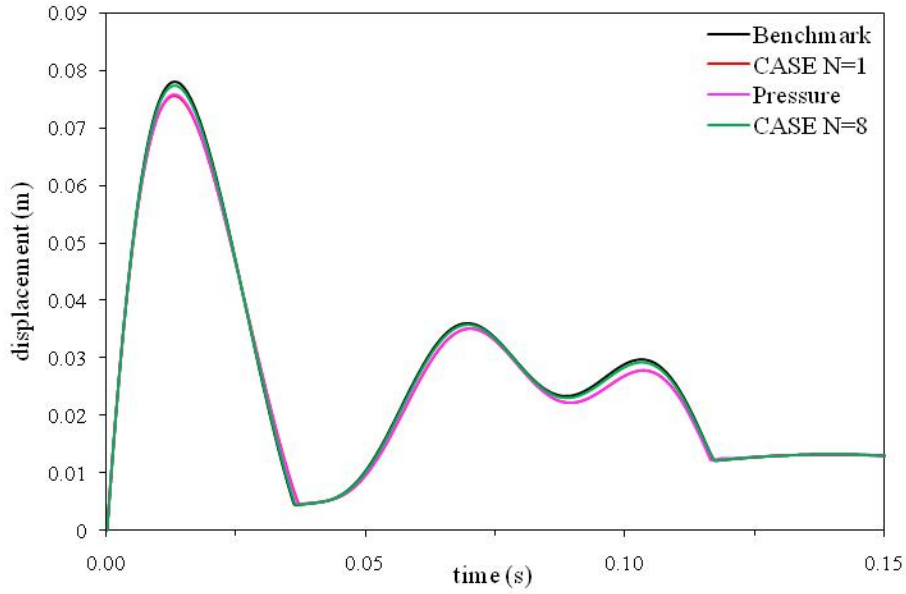

(b)

Figure 6.36 Displacement of m_1 for the m_2/m_1=25 case using 405 DOF (a) and 1449 DOF (b) with β = 0.25 for CASE and η_D= 0.020 for the pressure formulation

Table 6.21 L_2 error norms for the displacement of m_1 (m_2/m_1=25 case) with β = 0.25 for CASE and η_D= 0.020 for the pressure formulation

Fluid DOF	CASE N=1	Pressure	CASE
244	0.05094	0.05657	0.04139
405	0.05270	0.05129	0.03473
847	0.04434	0.04333	0.01629
1449	0.03728	0.03644	0.00955

Furthermore, Table 6.21 shows that for each level of mesh refinement studied, the higher-order CASE models give superior results for the displacement of m_1 when compared to the benchmark solution. Note, that as we observed in the velocity response results, the differences between the pressure formulation and N=1 CASE solutions observed during the displacement response to the second cavitation region do not cause a significant discrepancy in the L_2 error norms of the two solutions. We also note that for each model, the error norms for the displacement response are much lower than those observed for the structural response.

Having examined the structural response of the m_2/m_1=25 problem we now study the effect of cavitation capture on the structural response. To accomplish this we again use the plots of dynamic densified condensation during the duration of the first cavitation region. These are shown in Fig. 6.37 for the 405 DOF fluid meshes and Fig. 6.38 for the 1449 DOF fluid meshes. In both Figs. 6.37 and 6.38, s is plotted at t=0.002s, t=0.015s, t=0.025s, and t=0.02s. At t=0.002s the scattered wave front has just arrived at the NRB. At t=0.015s the upper cavitation boundary in the benchmark solution is located at a depth of 0.375m and the lower cavitation boundary at a depth of 1.75m. At t=0.025s, the upper cavitation boundary in the benchmark solution has propagated to 0.74m and the lower cavitation boundary has contracted to 1.6m. At t=0.03s, both the upper and lower cavitation boundaries have moved closer together in the benchmark solution and the cavitation region is very close to collapsing.

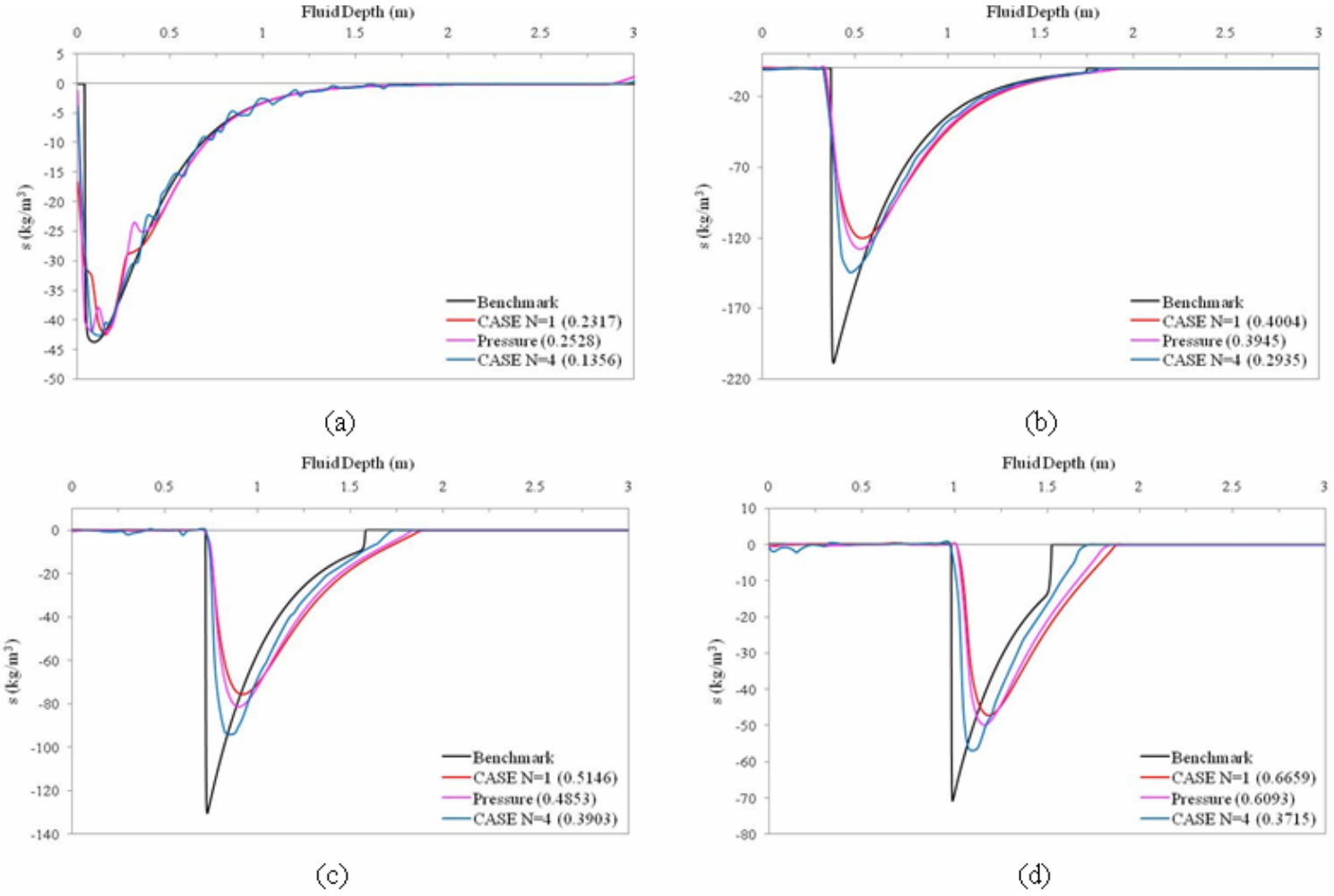

Figure 6.37 Dynamic densified condensation in the fluid at t=0.002 s (a), t=0.015 s (b), t=0.025 s (c), and t=0.03 s (d) for the m_2/m_1=25 case using 405 DOF with β = 0.25 for CASE and η_D= 0.020 for the pressure formulation

For the 405 DOF model results, at t=0.002s in Fig. 6.37a there are oscillations present in each of the solutions. As observed in the velocity response, the greatest number of oscillations in Fig. 6.37a occur for the N=4 CASE solution. Oscillations are also visible as small ripples between the fluid-structure interface and upper cavitation boundary in Figs. 6.37c and 6.37d in the N=4 CASE solution. These oscillations are an example of frothing discussed in Section 1.3.5. Despite the increased oscillations/frothing, comparing the results for the 405 DOF fluid models at all times in Fig. 6.37 the N=4 CASE model gives the solution closest to the benchmark solution at each time. As noted for previous problems in this chapter, the error in each solution increases significantly with time in Fig. 6.37. The advantage of the N=4 CASE model is most apparent at t=0.03s, where the

L_2 error norm, $L_2 \approx 0.3715$, is much smaller than both the N=1 CASE solution, $L_2 \approx 0.6654$, and the pressure formulation solution, $L_2 \approx 0.6093$.

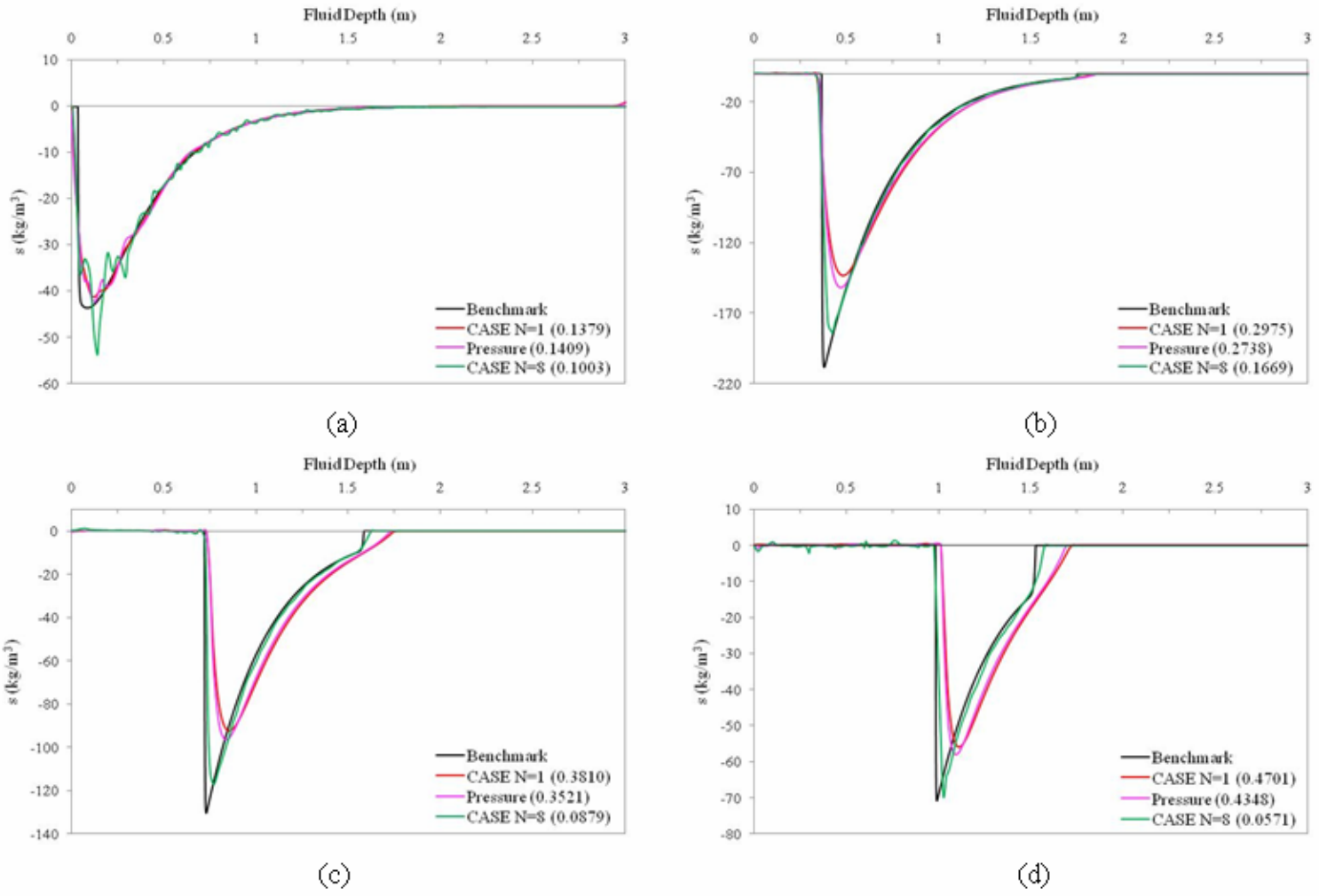

Figure 6.38 Dynamic densified condensation in the fluid at t=0.002 s (a), t=0.015 s (b), t=0.025 s (c), and t=0.03 s (d) for the m_2/m_1=25 case using 1449 DOF with β = 0.25 for CASE and η_D= 0.020 for the pressure formulation

Figure 6.38 shows how refinement of the mesh to 1449 DOF improves the solution at each time for the three models considered. This refinement removes the majority of oscillations observed for the 405 DOF N=1 CASE and pressure formulation models at t=0.002s. However, oscillations remain in the N=8 CASE solution at t=0.002s. Small regions of frothing are also observed between the fluid-structure boundary and upper cavitation boundary in the N=8 CASE solution at t=0.03s.

Despite the oscillations, the N=8 CASE models clearly gives the best solution at each time as evidenced by comparison of the L_2 error norms in each figure. This is especially true at t=0.030s where the L_2 error norm for the N=8 CASE solution, $L_2 \approx 0.0571$, is significantly smaller than both the N=1 CASE solution, $L_2 \approx 0.4701$, and the pressure formulation solution, $L_2 \approx 0.4348$. Additionally, when we compare these error norms to the corresponding errors norms for the 405 DOF fluid model we see that the refinement of the higher-order CASE model to 1449 DOF reduces the L_2 error norm by 0.29339. Which is larger than the 0.1958 reduction observed for the N=1 CASE model and the 0.1745 reduction observed for the pressure formulation model. This increased reduction in error is another demonstration of the superior convergence properties of higher-order CASE models.

In comparing the results at t=0.03s in Fig, 6.38d, it is interesting to observe that in all previous comparisons of error in the capture of densified condensation in the fluid, the error has increased as the simulation time increases. This occurs for both the 1449 N=1 and 1449 DOF pressure formulation models in Fig, 6.38. However, comparison of the error norms in Fig. 6.38c and 6.38d for the 1449 DOF N=8 CASE solution shows a reduction in error from t=0.025s to t=0.030s.

For both the 405 DOF and 1449 DOF results, the errors in capturing cavitation in the fluid are significantly larger than those observed in the structural response. However, compared to the previous problems studied in this chapter, the error seen in the structural response of the m_2/m_1=25 problem is also larger.

As in previous problems, to assess the effect of cavitation capture on the structural response for the m_2/m_1=25 problem we must consider the capture of the upper cavitation boundary and dynamic densified condensation in the cavitation region. As explained in Section 6.3.1, initially the error of predicting the upper cavitation boundary closer to the fluid-structure interface causes a faster decay of the positive velocity magnitude. The best example of this error for the m_2/m_1=25 problem is observed in Figs. 6.37a and 6.37b for the 405 DOF fluid models and Figs. 6.38a and 6.38b for the 1449 DOF fluid models. In these figures both the N=4 and N=8 CASE solutions capture the upper cavitation boundary closest to the benchmark solution. This results in the N=4 and N=8 CASE

models capturing the maximum displacement of m_1 during the response to the first cavitation region closest to the benchmark solution in Fig. 6.36.

As time increases, the dissipation in the magnitude of dynamic densified condensation in the cavitation region causes faster re-pressurization of the cavitation region (see Section 6.3.1). This error in cavitation capture is visible at t=0.025s and t=0.03s in Figs. 6.37 and 6.38 as the upper cavitation boundary being propagated deeper into the fluid. The faster re-pressurization of the cavitation region causes smaller negative velocity magnitudes to be reached during the structural response to the first cavitation region. The error in the propagation of the upper cavitation boundary also causes a delay in the arrival time of the first cavitation closure pulse. Both of these effects are visible in the velocity response results for the 405 DOF and 1449 DOF models in Fig, 6.35.

As time increases both the 405 DOF N=4 and the 1449 DOF N=8 CASE models capture the magnitude of dynamic condensation in the cavitation region and the propagation of the upper cavitation boundary better than the N=1 CASE and pressure formulation models in Figs. 6.37 and 6.38. Correspondingly, the velocity response results for the 405 DOF models (Fig. 6.35a) and 1449 DOF models (Fig. 6.35b) show the N=4 and N=8 CASE models give the closest solutions to the velocity response when compared to the benchmark solution.

It is interesting to note that compared to results in previous sections with smaller values of m_2/m_1. The difference in location of the upper cavitation boundary between the models in Figs. 6.37 and 6.38 is smaller but the error in the structural response is larger. This further shows the increase in sensitivity of the structure to errors in the fluid model and the increased importance of accurate cavitation capture as the value of m_2/m_1 is increased.

6.5.2 β = 0.50 and η_D= 0.035

In this section, we study the effect of increasing the amount of artificial diffusion/damping in the fluid models. This is an important effect to examine for the m_2/m_1=25 problem because of the large oscillations observed in the velocity response results in the previous section. For all models in this section, we take β = 0.50 for CASE models and η_D= 0.035 for the pressure formulation model. Figures 6.39a and 6.39b gives results for the velocity of m_1 using 405 DOF and 1449 DOF respectively.

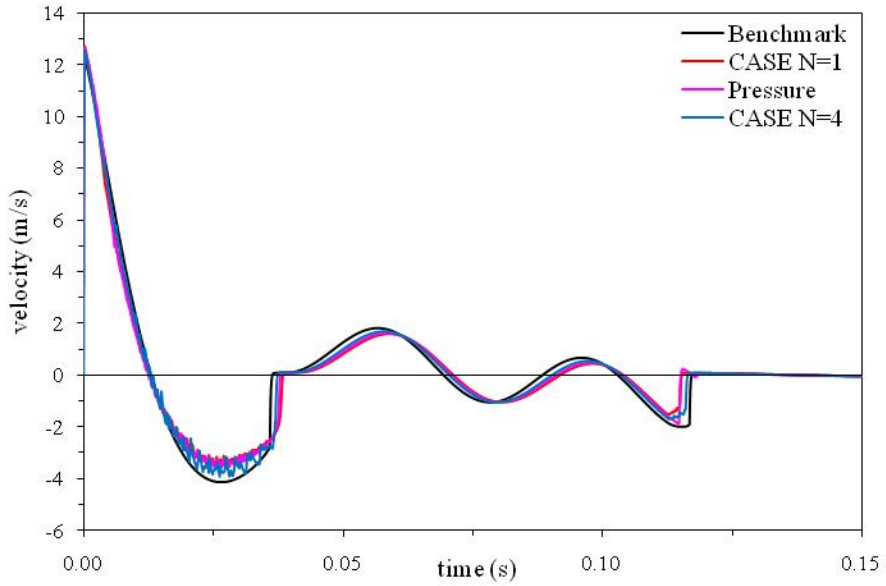

(a)

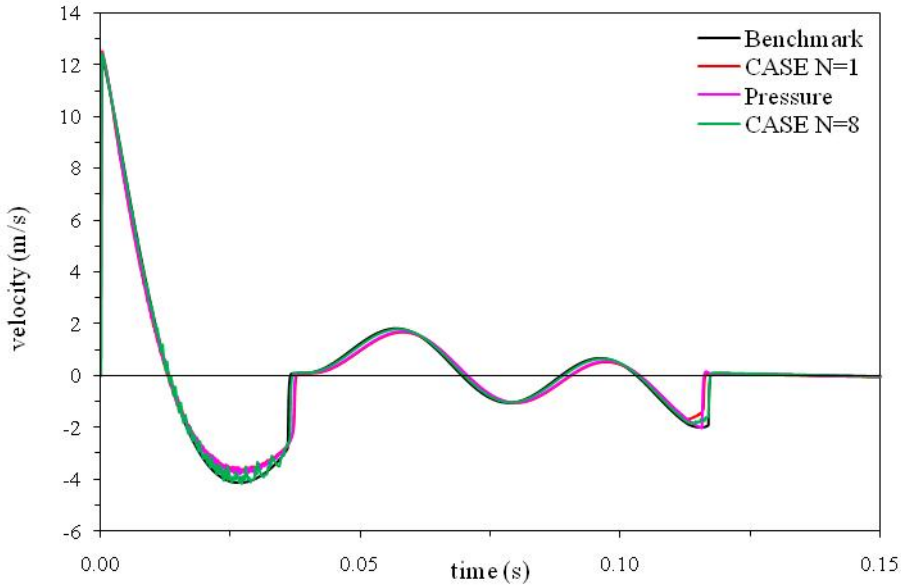

(b)

Figure 6.39 Velocity of m_1 for the m_2/m_1=25 case using 405 DOF (a) and 1449 DOF (b) with β = 0.50 for CASE and η_D= 0.035 for the pressure formulation

When compared to the results using $\beta = 0.25$ for CASE and $\eta_D = 0.020$, the increase in artificial damping/diffusion, the velocity response results for the 405 DOF and 1449 DOF models in Fig. 6.39 show a reduction in oscillations during t=0.01s-.035s. Note even with the increase in β large oscillations are still occur for the N=4 CASE solution. The cost of the reduction in oscillations is further deviation from the benchmark solution.

For the 405 DOF fluid models in Fig. 6.39a this deviation is visible by the smaller velocity magnitudes during the response to the first cavitation region, the delay (especially for the N=1 CASE and pressure formulation solutions) in the arrival of the first cavitation closure pulse, and the difference in velocity response during t=0.04s-0.11s. The N=4 and N=1 CASE models also show a faster arrival of the second cavitation closure pulse during the response to the second cavitation region when compared to the benchmark model. Comparison of the L_2 error norms in Table 6.22 show the N=4 CASE model clearly gives the velocity response closest to the benchmark solution.

When compared to the results with $\beta = 0.25$ and $\eta_D = 0.020$, Table 6.22 confirms the increase in artificial damping/diffusion for the 405 DOF model causes an increase in L_2 error norm of 0.06645 for the N=1 CASE solution, 0.04578 for the pressure formulation solution and 0.040127 for the N=4 solution. Thus, the increase in artificial damping has a significant effect of the velocity response in the m_2/m_1=25 problem.

Returning to Fig. 6.39a, we see, as in the previous section, the pressure formulation solution differs from the N=1 CASE solution as the second cavitation region closes. Although the arrival time of the second closure pulse is almost identical for the two methods, the pressure formulation solution again shows the formation of a third cavitation region. Compared to the results in the previous section, the increase in artificial damping greatly reduces the effect of this third cavitation region on the structure response. Comparison of the error norms in Table 6.22 shows that there is only a small difference in error between the 405 DOF N=1 and pressure formulation solutions. Thus the difference in the response to the closure of the second cavitation region does not cause a significant difference when the total error of the two solutions is considered. This is attributed to the fact the N=1 CASE and pressure formulation solutions agree well throughout the majority of the velocity response history.

Table 6.22 L_2 error norms for the velocity of m_1 (m_2/m_1=25 case) with β = 0.50 for CASE and η_D= 0.035 for the pressure formulation

Fluid DOF	CASE N=1	Pressure	CASE
244	0.22543	0.20720	0.17205
405	0.19659	0.18298	0.12982
847	0.15849	0.14938	0.07657
1449	0.13320	0.12665	0.05271

.

Fig. 6.39b shows that refinement of the mesh improves the solution for each model. The large oscillations observed for the 405 DOF N=4 solution are reduced in the 1449 DOF N=8 CASE solution, however these oscillations remain significantly larger than those observed in the 1449 DOF N=1 CASE and pressure formulation solutions. Comparison of the error norms in Table 6.22 show the N=8 CASE solution to give the superior result. Furthermore, for each level of mesh refinement in Table 6.22 the higher-order CASE model has a significant advantage over the N=1 CASE and pressure formulation models, as shown by the significant decrease in the L_2 error norm for the velocity response. As the mesh is refined the advantage of the higher-order CASE model increases, due to the superior convergence properties of spectral elements.

Figure 6.39b also shows a difference between the N=1 CASE and pressure formulation solutions during the closure of the second cavitation region. This difference is primarily in the magnitudes of velocity reached as the second cavitation region closes. The arrival time of the closure pulse is almost identical for the two methods and the effect of the third cavitation region on the pressure formulation solution is greatly reduced by the refinement of the mesh. Table 6.22 shows the error norm of the pressure formulation is also reduced by the refinement of the mesh. Furthermore, as in the 405 DOF solution, the L_2 error norms for the 1449 DOF N=1 CASE ($L_2 \approx 0.1332$) and pressure formulation ($L_2 \approx 0.1266$) solutions agree well. Again, this shows the difference in the response to the closure of the second cavitation region does not have a large effect on the total error of the pressure formulation solution when compared to the N=1 CASE solution.

The displacement response of m_1 using 405 DOF and 1449 DOF is given in Figures 6.40a and 6.40b respectively. For the 405 DOF results, the N=4 CASE model gives the closest approximation to the benchmark solution. This is confirmed by comparing the L_2

error norms for the displacement of m_1 in Table 6.23. Note the difference in response between the pressure formulation solution and N=1 CASE solution due to the closure of the second cavitation region is not visible in Fig. 6.40a and does not cause a large difference in the L_2 error norms of each solution in Table 6.23.

Table 6.23 L_2 error norms for the displacement of m_1 (m_2/m_1=25 case) with β = 0.50 for CASE and η_D= 0.035 for the pressure formulation

Fluid DOF	CASE N=1	Pressure	CASE
244	0.13767	0.12260	0.09134
405	0.11361	0.10836	0.06321
847	0.08550	0.08590	0.03163
1449	0.06824	0.06945	0.01850

Fig. 6.40b shows refinement of mesh to 1449 DOF improves the solution of each model. The difference between the pressure formulation and N=1 CASE models is indistinguishable for the 1449 DOF case. Clearly, in Fig. 6.36b the 1449 DOF N=8 CASE solution gives the result closest to the benchmark solution. Again, this is confirmed by comparing the L_2 error norms for the displacement of m_1 in Table 6.23. Furthermore, Table 6.23 shows that for each level of mesh refinement studied the higher-order CASE models give superior results for the displacement of m_1 when compared to the benchmark solution. We also note that for each model, the error norms for the displacement response are much lower than those observed for the structural response.

As in the velocity response, the increase in artificial damping/diffusion causes an increase in error in the displacement results. To illustrate this, we compare the displacement error norms for the 405 DOF models with β = 0.25 and η_D= 0.020 to the error norms for the 405 DOF models with β = 0.50 and η_D= 0.035. The increase in artificial damping/diffusion causes an increase in L_2 error norm of 0.06091 for N=1 CASE model, 0.05707 for the pressure formulation model, and 0.02840 for the N=4 CASE model.

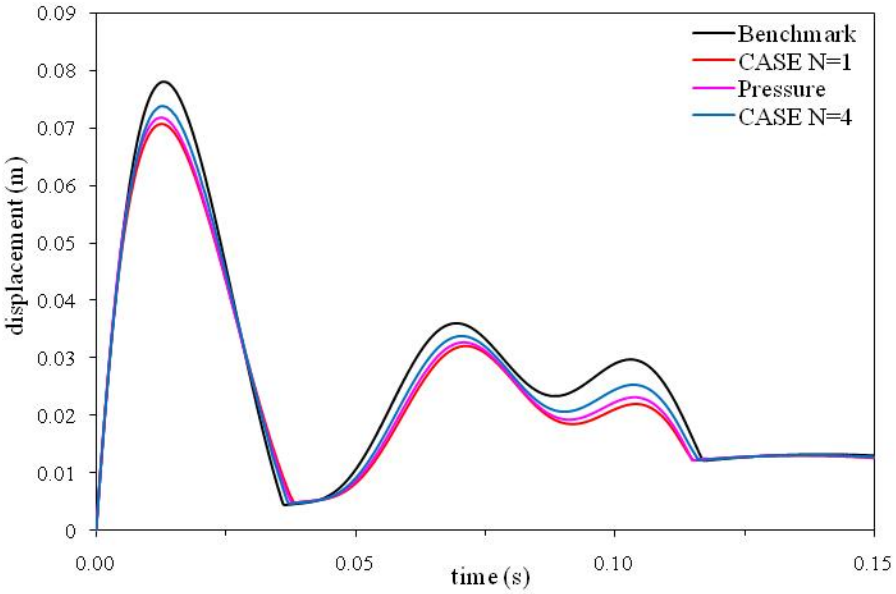

(a)

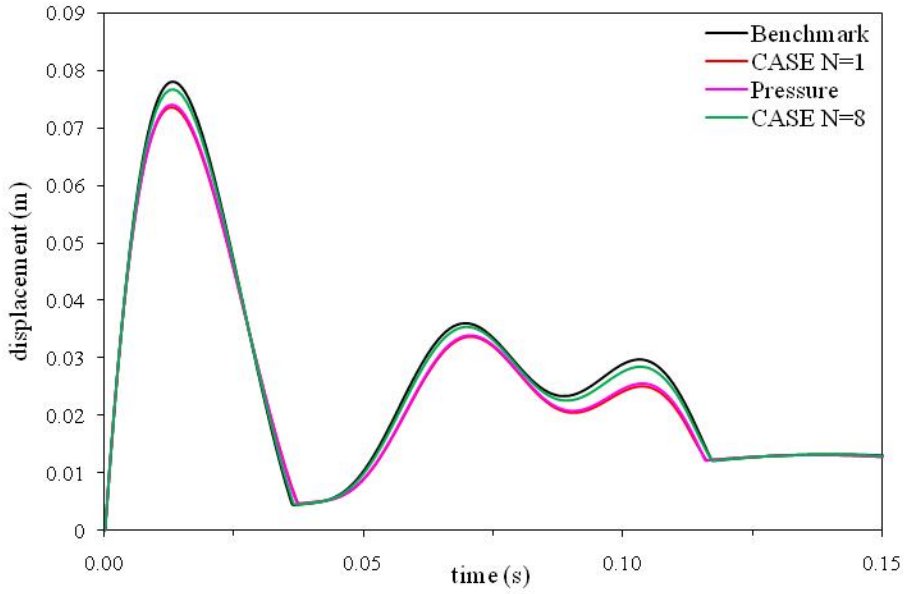

(b)

Figure 6.40 Displacement of m_1 for the m_2/m_1=25 case using 405 DOF (a) and 1449 DOF (b) with β = 0.50 for CASE and η_D= 0.035 for the pressure formulation

Figures 6.41 and 6.42 show the plots of dynamic densified condensation for the 405 DOF and 1449 DOF fluid models, respectively, during the development of the first cavitation region at t=0.002s, t=0.015s, t=0.025s, and t=0.03s. At t=0.002s for the 405 DOF fluid models in Fig. 6.41a we see the increase in artificial damping/diffusion smoothes the oscillations observed in Fig. 6.41a for the all fluid models with β = 0.25 and η_D= 0.020.

Note, while the majority of oscillations are smoothed, small ripples are still observed in 405 DOF N=4 CASE solution at t=0.002s and t=0.03s despite the increase in artificial damping. Figure 6.41 shows that the N=4 CASE model give the solutions closest to the benchmark solution at all times. However, Figs. 6.41b-d show that the increase in artificial damping/diffusion increases the error in capture of the cavitation region when compared to the β = 0.25 and η_D= 0.020 solutions (Fig. 6.23). To illustrate this, consider at t=0.03s the increase in artificial damping/diffusion results in an increase in the L_2 error norm of 0.1934 in the N=1 CASE solution, 0.2015 in the pressure formulation solution, and 0.2399 in the N=4 CASE solution.

Refinement of the mesh to 1449 DOF, shown in Fig. 6.42, gives a decrease in L_2 error norm for each model and time considered. The 1449 DOF N=8 CASE model gives the solutions closest to the benchmark solution at each time in Fig. 6.42. The 1449 DOF N=8 CASE model also gives the largest reduction in error as the mesh is refined at each time considered when compared to the two other models. For example, at t=0.03s the refinement to 1449 DOF reduces the L_2 error norm by 0.2990 for the N=1 CASE solution, by 0.1722 for the pressure formulation solution, and by 0.4847 for the N=8 CASE solution. Note the increase in artificial damping removes the majority of oscillations/frothing observed at t=0.002s in Fig. 6.38a and at t=0.03s in Fig. 6.38d.

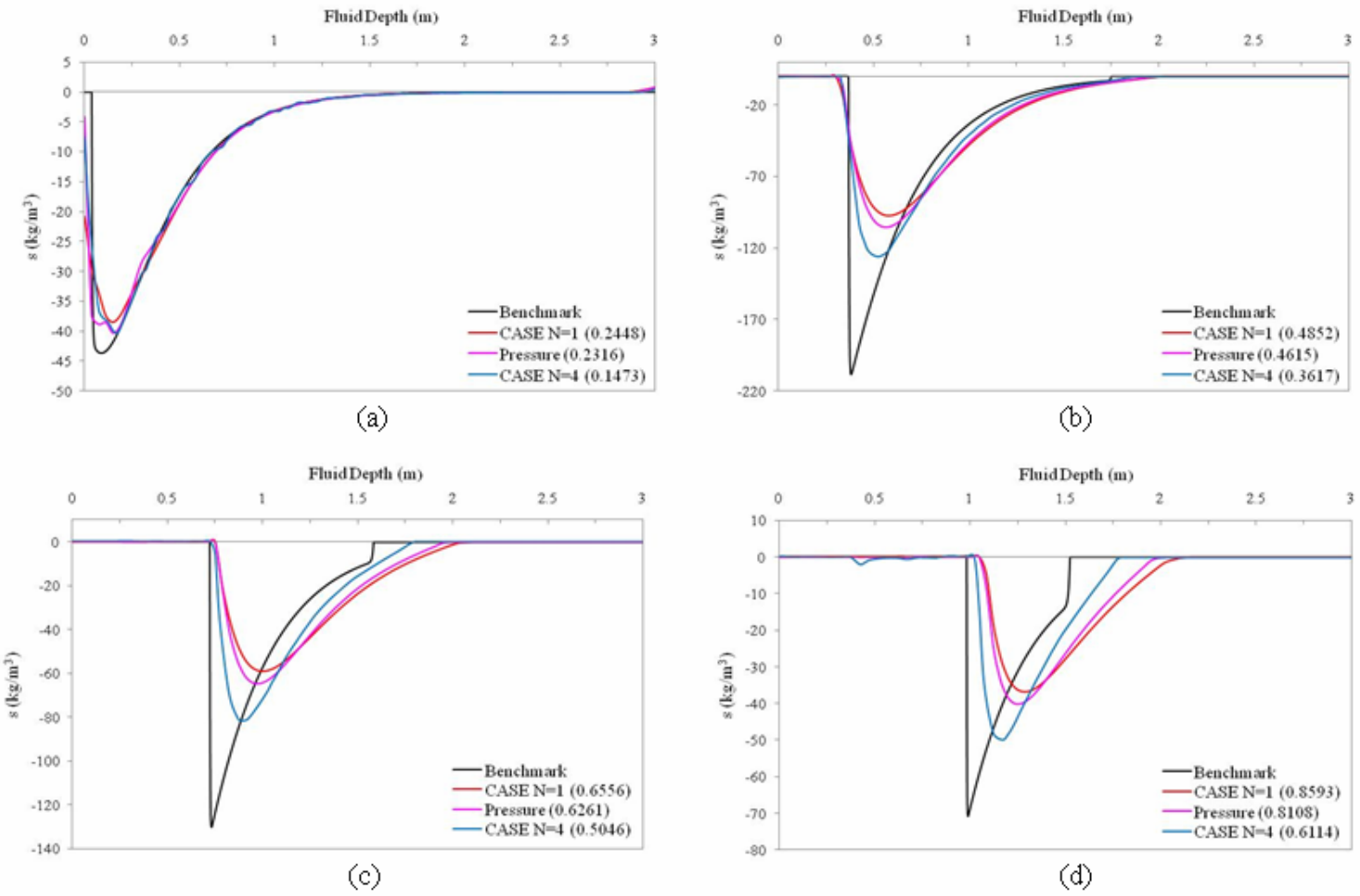

Figure 6.41 Dynamic densified condensation in the fluid at t=0.002 s (a), t=0.015 s (b), t=0.025 s (c), and t=0.03 s (d) for the m_2/m_1=25 case using 405 DOF with β = 0.50 for CASE and η_D= 0.035 for the pressure formulation

As found in the β = 0.25 results, the error in the 1449 DOF N=1 CASE and pressure formulation solutions increases with simulation time but the 1449 DOF N=8 CASE solution actually improves as the simulation time increases. This is observed by comparing the error norm at t=0.025s in Fig. 6.42c (L_2≈0.01574) to the reduced error norm (L_2≈0.01267) at t=0.03s in Fig. 6.42d.

In terms of capturing the magnitude of dynamic densified condensation in the cavitation region and the location of the upper cavitation boundary both the N=4 and N=8 CASE models again give results closest to the benchmark solution, especially as time increases. As described in Section 6.5.1, this results in the superiority of the higher-order CASE models in capturing the structural response. However, compared to the results with β = 0.25 and η_D= 0.020 there is an overall increase in error in both the structure

response results and the capture of the magnitude of dynamic densified condensation in the cavitation region and the location of the upper cavitation boundary.

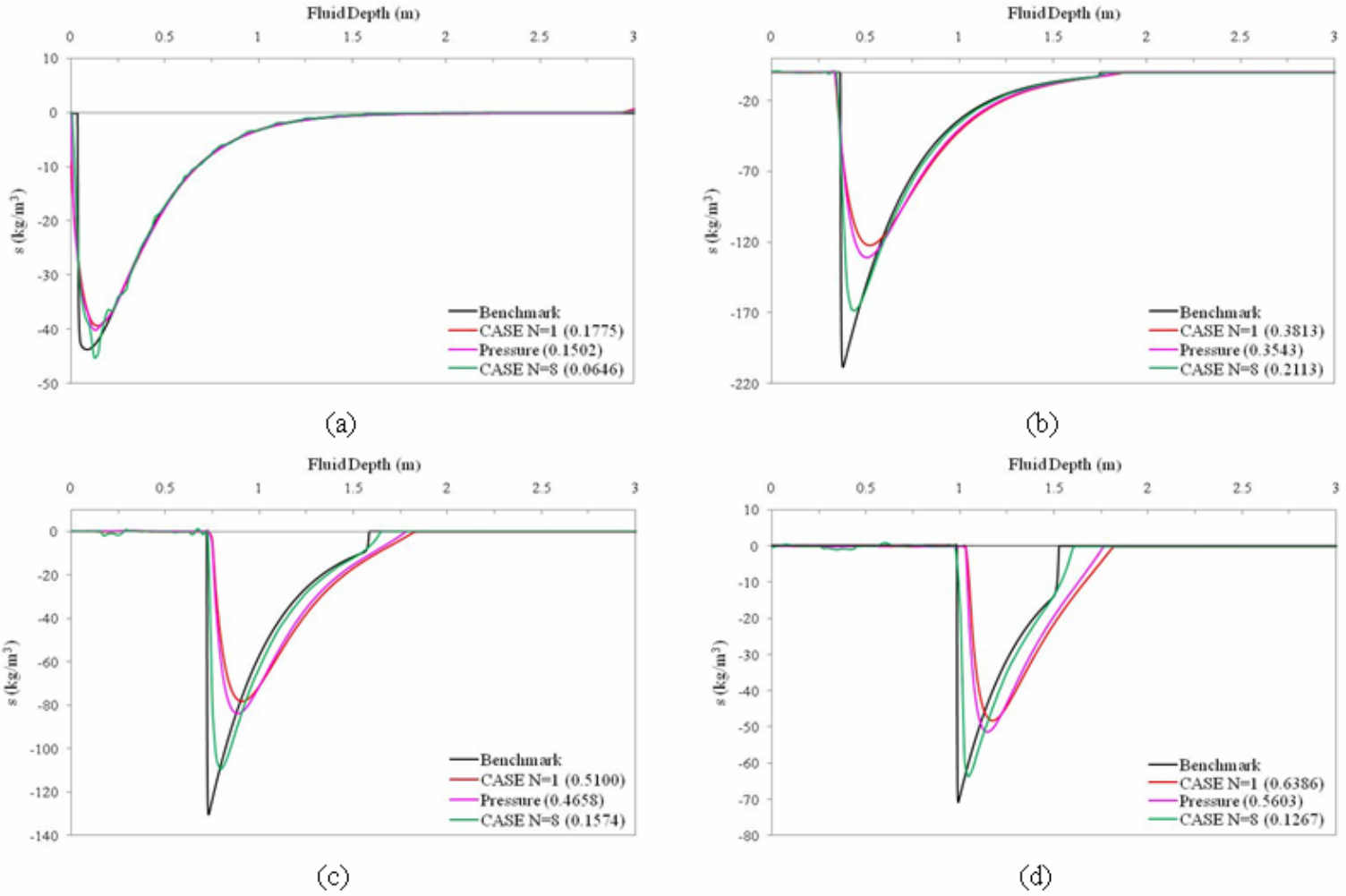

Figure 6.42 Dynamic densified condensation in the fluid at t=0.002 s (a), t=0.015 s (b), t=0.025 s (c), and t=0.03 s (d) for the m_2/m_1=25 case using 1449 DOF with β = 0.50 for CASE and η_D= 0.035 for the pressure formulation

To illustrate the effect of increasing the artificial damping/diffusion on the capture of cavitation we first compare, at t=0.002s and t=0.015s, the 405 DOF results with β = 0.25 and η_D= 0.020 in Fig. 6.37 to the 405 DOF β = 0.50 and η_D= 0.035 in Fig. 6.41. The increased error in cavitation capture due to the increase in artificial damping/diffusion causes the increased difference in the maximum displacement of m_1 for the 405 DOF

results with $\beta = 0.50$ and $\eta_D = 0.035$ in Fig. 3.36a when compared to the 405 DOF results with $\beta = 0.25$ and $\eta_D = 0.020$.

Next we compare, at t=0.025s and t=0.03s, the 405 DOF results with $\beta = 0.25$ and $\eta_D = 0.020$ in Fig. 6.37 to the 405 DOF $\beta = 0.50$ and $\eta_D = 0.035$ in Fig. 6.41. In this comparison, we see that the increased damping/diffusion causes increased dissipation of the dynamic densified condensation magnitude which causes the upper cavitation boundary to be propagated deeper into the fluid. This is the reason the velocity responses with 405 DOF and increased damping/diffusion give smaller negative velocity magnitudes during the response to the first cavitation region and delayed arrival times of the first cavitation closure pulse when compared to the 405 DOF results with $\beta = 0.25$ and $\eta_D = 0.020$.

Thus, for the m_2/m_1=25 problem, increasing artificial damping/diffusion in the fluid model causes an increase in cavitation capture error relative to the benchmark solution. This is responsible for increasing error in the structural response, relative to the benchmark solution, when compared to solution with less artificial damping/diffusion applied to the fluid model.

6.5.3 $\beta = 0.10$ and $\eta_D = 0.010$

In Section 6.4.3, we examined the possibility of reducing the amount of damping used with N=1 CASE models to obtain solutions that were similar to higher order CASE solutions for the m_2/m_1=5 problem. This method of improving N=1 CASE solutions was most effective for the Bleich-Sandler problem in Section 5.3. This is due to the fact the higher-order CASE model gave large oscillations in the velocity response. Because, we have observed largest oscillations of the problems considered in this chapter during the velocity response to the first cavitation region for the m_2/m_1=25 problem, we again examine the possibility using a reduced damping N=1 CASE model.

First we present results for the velocity of m_1 in Fig. 6.43 using $\beta = 0.10$ and $\eta_D = 0.010$ with 405 DOF and 1449 DOF. Figure 6.43a shows that with the decrease in artificial damping/diffusion the N=1 and N=4 CASE models agree well with the benchmark solution. However, each solution still gives a slightly delayed arrival time of the first cavitation closer pulse.

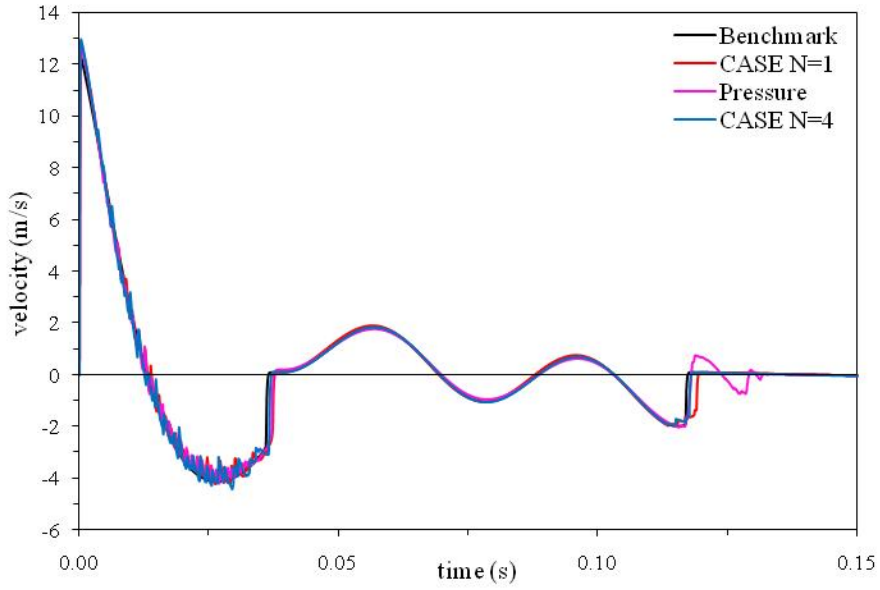

(a)

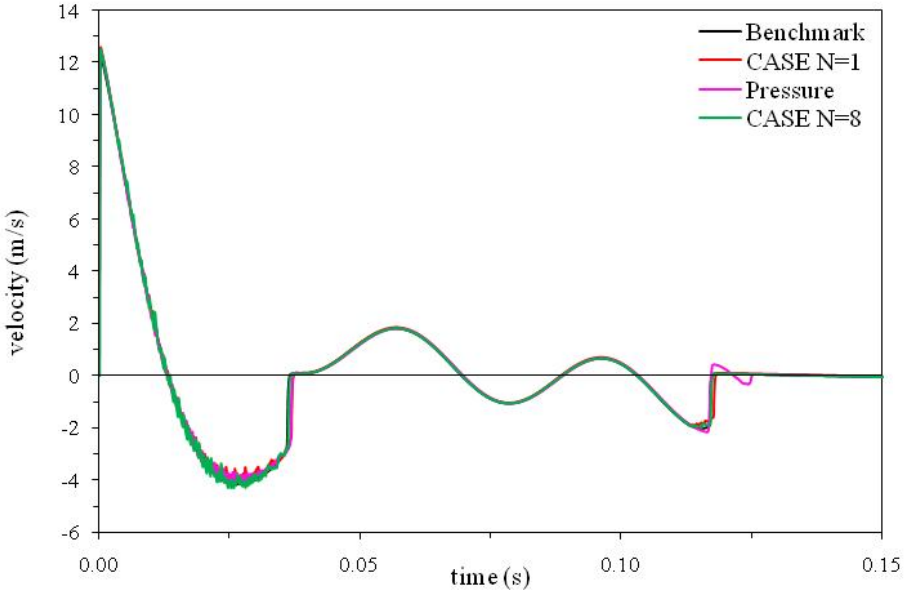

(b)

Figure 6.43 Velocity of m_1 for the m_2/m_1=25 case using 405 DOF (a) and 1449 DOF (b) with β = 0.10 for CASE and η_D= 0.010 for the pressure formulation

We note that compared to the $\beta = 0.25/\eta_D = 0.020$ and $\beta = 0.50/\eta_D = 0.035$ results, this delay in the arrival time of the first cavitation closure pulse is significantly reduced by the reduction in artificial damping/diffusion. There is also a significant increase in oscillations during t=0.0225s-0.035s. The increase in oscillations is most severe in the N=4 CASE solution.

Refinement of the mesh to 1449 DOF improves each of the models shown in Fig. 6.43b. The large oscillations observed in the 405 DOF N=4 CASE are reduced by the refinement of the mesh, but the N=8 CASE solution still shows much larger oscillations than both the N=1 CASE and the pressure formulation solutions. Despite this, the N=8 CASE solution gives the closest approximation to the benchmark solution. This is proved by comparing the L_2 error norms in Table 6.24.

Table 6.24 L_2 error norms for the velocity of m_1 (m_2/m_1=25 case) with $\beta = 0.10$ for CASE and $\eta_D = 0.010$ for the pressure formulation

Fluid DOF	CASE N=1	Pressure	CASE
244	0.14207	0.13659	0.12528
405	0.12786	0.11695	0.09482
847	0.10669	0.09771	0.05969
1449	0.08116	0.07190	0.03785

It is interesting to note the use of $\beta = 0.10$ in 405 DOF models do not give a significant reduction in the L_2 error norm when compared to the models with $\beta = 0.25$. This is especially true for the N=4 CASE model ($L_2 \approx 0.09482$), which actually shows a small increase in error norm when compared to the $\beta = 0.25$ ($L_2 \approx 0.08968$) model. Despite this, Table 6.22 shows with $\beta = 0.10$ and $\eta_D = 0.010$ the higher-order CASE models still gives the results closest to the benchmark solution for all models considered. Thus, despite the small increase in error when compared to the $\beta = 0.25$ model, the higher-order CASE solution still gives superior results compared to the N=1 CASE and pressure formulation solutions.

Returning to Fig. 6.43a, we compare the pressure formulation solution to the N=1 CASE solution. As in the previous two sections the two solutions agree well until the closure of the second cavitation region begins at t=0.115s. At this point in Fig. 6.43a, the

pressure formulation gives a faster arrival time of the second cavitation closure pulse and also predicts the formation of a third cavitation region, which causes the large spikes in the pressure formulation velocity response between t=0.115s-0.126s. We note that compared to the 405 DOF with larger amounts of artificial diffusion, the response to the third cavitation region is much larger for the reduced diffusion case. Furthermore, this is the first example in the m_2/m_1=25 problem where the arrival time of the second cavitation closure pulse in the pressure formulation solution does not closely match that in the N=1 CASE solution. In fact, with β=0.10, the N=1 CASE result gives a significantly delayed arrival time of second cavitation closure pulse when compared to the benchmark solution. Thus, in terms of the arrival time of the second cavitation closure pulse the pressure formulation gives the result closest to the benchmark solution.

Comparison of the L_2 error norms in Table 6.24 shows that despite the large differences observed in the response to the closure of the second cavitation region the error norms of the 405 N=1 CASE ($L_2 \approx 0.12786$) and pressure formulation ($L_2 \approx 0.11695$) solutions agree wel1. Note the pressure formulation gives a slightly smaller error norm. The agreement of the 405 N=1 CASE and pressure formulation solutions L_2 error norms is attributed to the fact that the two methods agree well with each other through the majority of the velocity response history.

When the mesh is refined to 1449 DOF the differences between the N=1 CASE and pressure formulation solution in the response to the second cavitation region are reduced. Most notably, the arrival of the second cavitation closure pulse in each method is closer to the benchmark solution and the influence of the third cavitation region predicted by the pressure formulation on the velocity response is reduced. This is reflected in the L_2 error norms in Table 6.22, as again the error norms of the 1449 DOF pressure and N=1 CASE solutions agree well with each other. In fact, the error norms of the pressure formulation and N=1 CASE solutions agree well with each other for each level of mesh refinement in Table 6.22. Thus, as we have found in the previous sections, in terms of the total error relative to the benchmark solution, the pressure formulation and N=1 CASE models give similar velocity response solutions. This is because the differences in the response to the closure of the second cavitation region only affect a small portion of the response.

Results for the displacement of m_1 for the 405 DOF and 1449 DOF fluid models are given in Fig. 6.44. Both the 405 DOF (Fig. 6.44a) and the 1449 DOF (Fig. 6.44b) the results for the higher-order CASE models are almost indistinguishable from the benchmark solution. This is reflected by comparing the L_2 error norms in Table 6.23 which shows for a given level of refinement the higher-order CASE model gives the solution closest to the benchmark solution. Note for each model in Fig. 6.44, no oscillations are observed in the displacement response.

For the 405 DOF results the pressure formulation and N=1 CASE results show a larger increase in displacement between t=0.50s-0.115s when compared to the benchmark solution. These differences are decreased as the mesh is refined to 1449 DOF as shown in Fig. 6.44b and by observing the reduction in L_2 error norm in Table 6.23. The difference between the N=1 CASE and the pressure formulation models observed in the velocity response appears as the displacement increase after t=0.115s in the pressure formulation solution. This difference in the displacement response is attributed to the formation of the third cavitation region mentioned in the discussion of the velocity response results. Note this increase is visible for both the 405 DOF and 1449 DOF results in Fig. 6.44, but is reduced by the refinement of the mesh. In terms of the error norms, Table 6.25 shows the N=1 CASE and pressure formulation solutions agree well despite the observed difference at t=0.115s in the displacement response.

Table 6.25 L_2 error norms for the displacement of m_1 (m_2/m_1=25 case) with β = 0.10 for CASE and η_D= 0.010 for the pressure formulation

Fluid DOF	CASE N=1	Pressure	CASE
244	0.04586	0.04425	0.02150
405	0.03334	0.03496	0.00616
847	0.01598	0.02480	0.00432
1449	0.00690	0.01486	0.00188

It is interesting to note that for the displacement response the fluid models with β = 0.10 and η_D= 0.010 show a decrease in error when compared to the fluid models with β = 0.25 and η_D= 0.020.

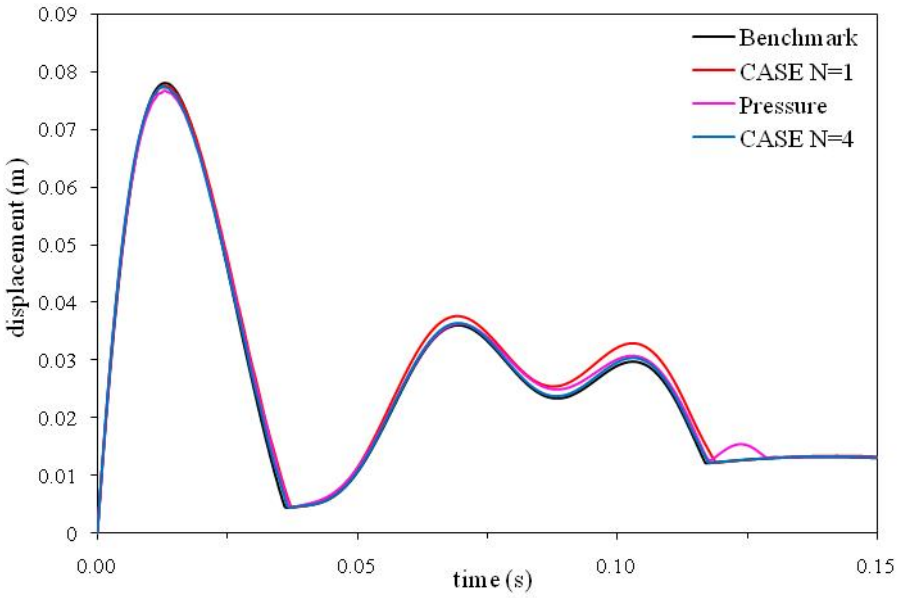

(a)

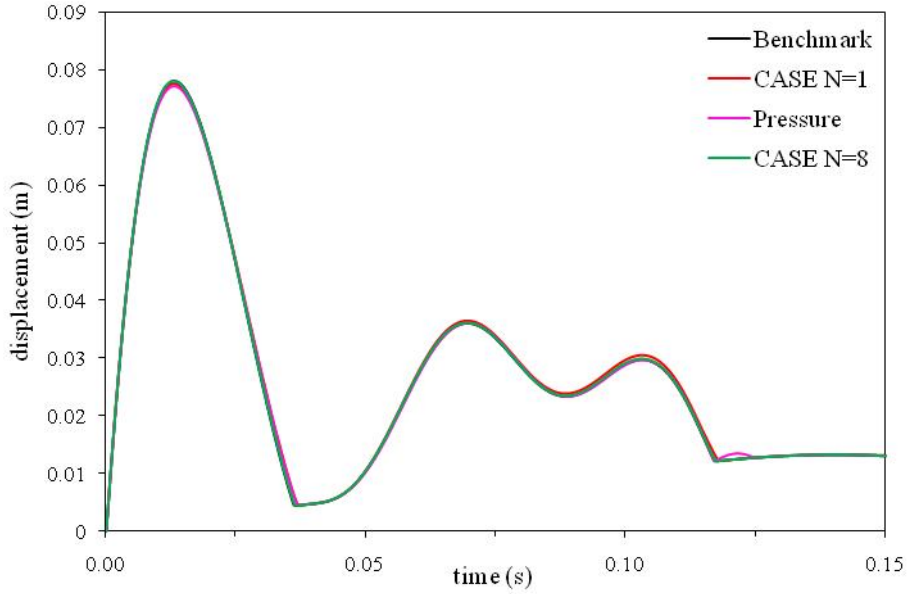

(b)

Figure 6.44 Displacement of m_1 for the m_2/m_1=25 case using 405 DOF (a) and 1449 DOF (b) with β = 0.10 for CASE and η_D= 0.010 for the pressure formulation

For example, for the 405 DOF N=1 CASE fluid models the error norm is decreased from L_2≈0.05270 with β = 0.25 to L_2≈0.03334 with β = 0.10. For the 405 DOF N=4 CASE model the error norm is decreased from L_2≈0.03473 with β = 0.25 to L_2≈0.006161 with β = 0.10. This is in contrast to the velocity response results, where the same reduction in β gave a small decrease in the error norm of the 405 DOF N=1 CASE solution and a small increase in the error norm of the 405 DOF N=4 CASE solution.

With each amount of artificial damping/diffusion used in the fluid model we have observed a significant increase in oscillations when we compare N=1 CASE and pressure formulation solutions to higher-order CASE solutions to m_1/m_2=25 problem. One of the goals in this section was to examine the possibility of using a reduced damping N=1 CASE model to obtain results that matched higher-order CASE models. In Section 6.4.3, we determined this was not possible for the m_1/m_2=5 problem because even with reduced damping, the N=1 CASE model did not give solutions closer to the benchmark solution than the higher-order CASE model. This occurred because the higher-order CASE models retained an advantage in cavitation capture, especially for higher degrees of mesh refinement.

In our discussion of the velocity response results, we noted that for the m_1/m_2=25 problem reducing the amount of artificial damping/diffusion in the fluid model did not result in a significant decrease in the error norm of the velocity response when compared to the benchmark solution. It follows that, like the m_1/m_2=5 problem, for a given number of fluid mesh DOF a reduced damping N=1 CASE model will not be able to match a higher-order CASE solution for the m_1/m_2=25 problem.

We demonstrate this by comparing the 405 DOF N=1 CASE model with β = 0.10 to the 405 DOF N=4 CASE model with β = 0.25 in Fig.6.45. And then by comparing the 1449 DOF N=1 CASE model with β = 0.10 to the 1449 DOF N=8 CASE model with β = 0.25 in Fig.6.46. The results in Fig. 6.45 show that although the two models give similar magnitudes for the velocity response to the first cavitation region, the 405 DOF N=1 CASE gives a delayed arrival time for both the first and second cavitation closure pulses. This results in the L_2 error norm of the 405 DOF N=1 CASE solution (L_2≈0.12786) being larger than the error norm of the 405 DOF N=1 CASE solution (L_2≈0.08968) even though the N=4 uses a larger β.

The same result is visible in Fig. 6.46 for the 1449 DOF models, where a closer view of the response to the first cavitation region in Fig. 6.46b clearly shows the delay in the arrival of the first cavitation closure pulse in the N=1 CASE solution. Again, this results in the L_2 error norm of the N=1 CASE solution ($L_2 \approx 0.08116$) being larger than the error norm of the N=8 CASE solution ($L_2 \approx 0.04497$) with a larger β.

The higher-order CASE model remains superior to the N=1 CASE model because the higher order CASE model gives a more accurate solution to the development of cavitation in the fluid. This is best demonstrated by comparing the densified condensation results for the 1449 DOF N=1 CASE model with $\beta = 0.10$ to the 1449 DOF N=8 CASE model with $\beta = 0.25$. We show this at times, at t=0.002s, t=0.015s, t=0.025s, and t=0.03s, in Fig. 6.47.

Comparison of the solutions and L_2 error norms given in Fig. 6.47 shows the N=8 CASE solution to give superior results for the capture of cavitation in the fluid despite using a larger value of β. Most significantly, when compared to the benchmark the N=8 CASE model captures the magnitude of dynamic densified condensation and the location of the upper cavitation boundary the best as the cavitation region collapses. This is observed in Fig. 6.47d, at t=0.03s. We know from previous discussion (see Sections 6.5.1 and 6.4.1) that capturing these phenomena play an important role in the accuracy of the structural response. Thus, the cavitation capture results show the higher-order CASE models that use a larger β to give more accurate structural responses than reduced damping N=1 CASE models, as seen in Figs. 6.45 and 6.46, because of the increased accuracy in cavitation capture when compared to the benchmark solution.

Given the results of this section, we conclude for the m_2/m_1=25 problem, that when compared to the N=1 CASE and pressure formulation models for a given amount of artificial damping/diffusion and a given degree of model refinement, the higher-order CASE model gives superior results. The superiority of the higher-order CASE model is in terms of both cavitation capture in the fluid and the structural response, whose accuracy is very dependent on the capture of cavitation in the fluid. This superiority is maintained even when the higher-order CASE model is compared to the N=1 CASE model with reduced damping.

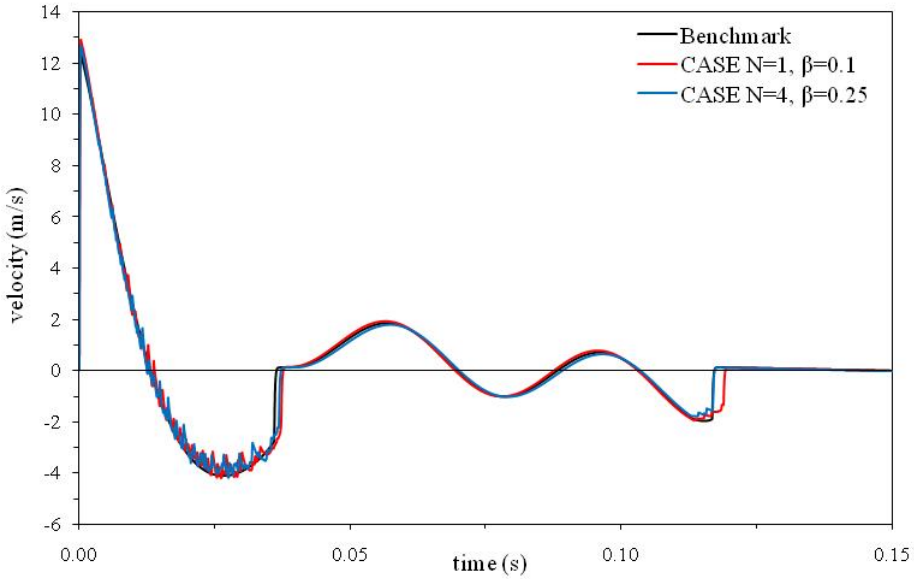

(a)

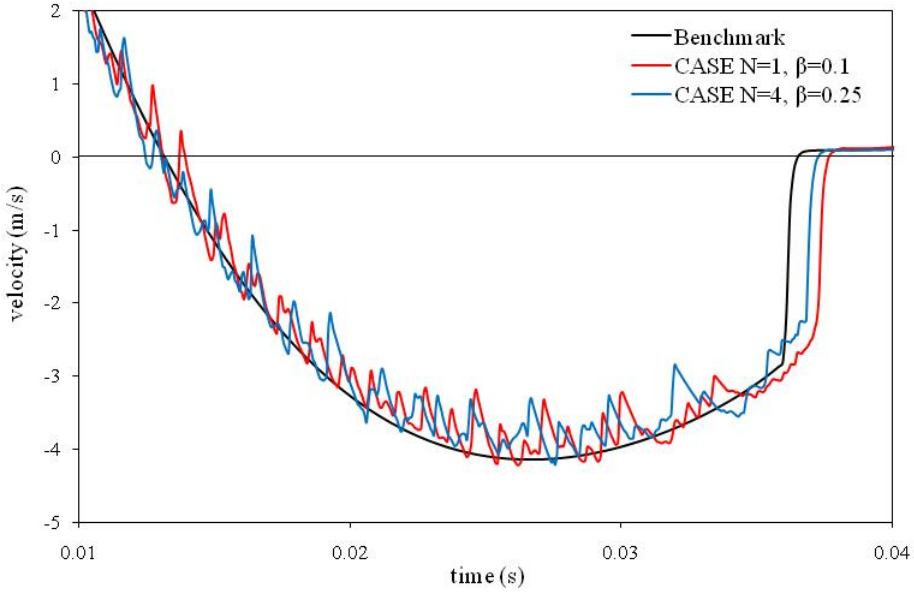

(b)

Figure 6.45 Velocity of m_1 for the m_2/m_1=25 case on two time scales using 405 DOF with β = 0.10 for N=1 CASE and β = 0.25 for N=4 CASE

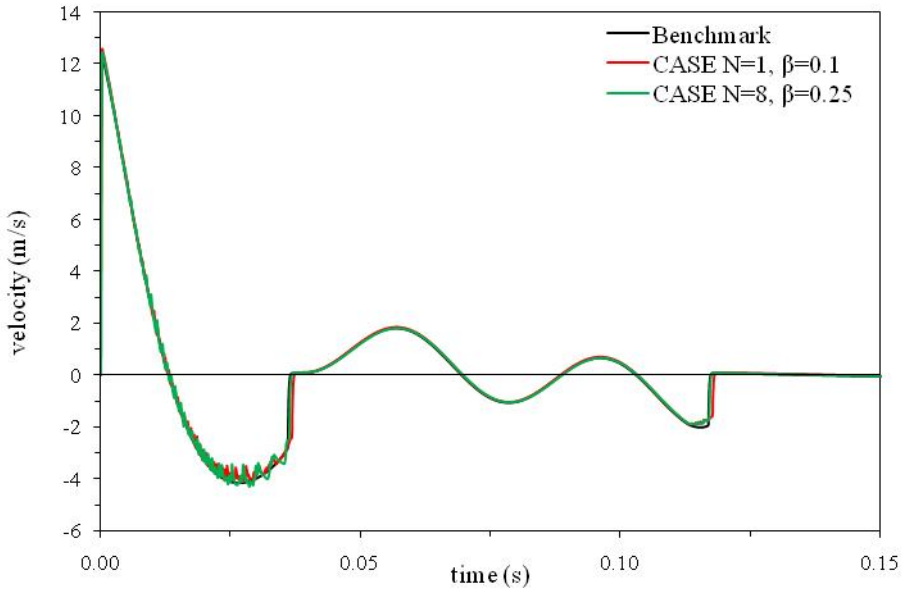

(a)

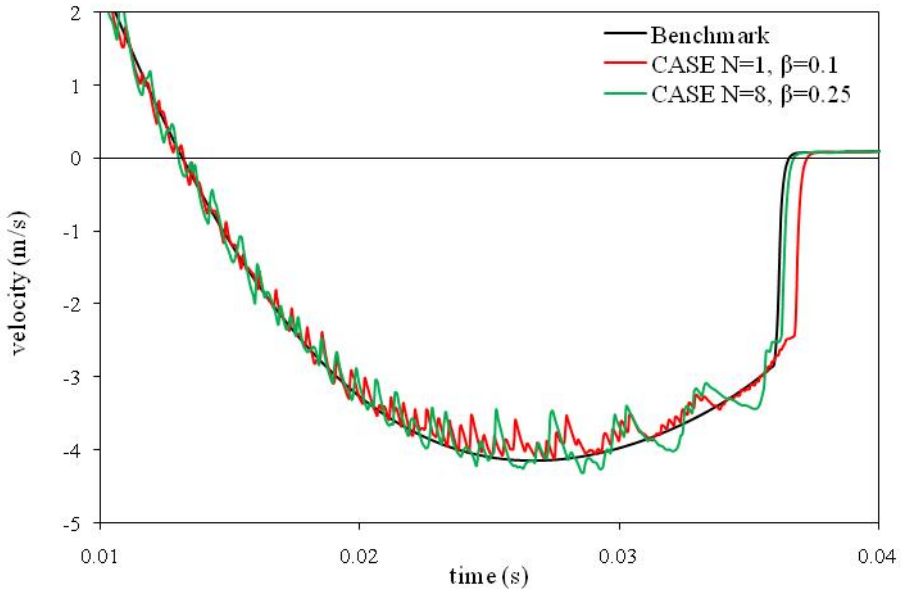

(b)

Figure 6.46 Velocity of m_1 for the m_2/m_1=25 case on two time scales using 1449 DOF with β = 0.10 for N=1 CASE and β = 0.25 for N=4 CASE

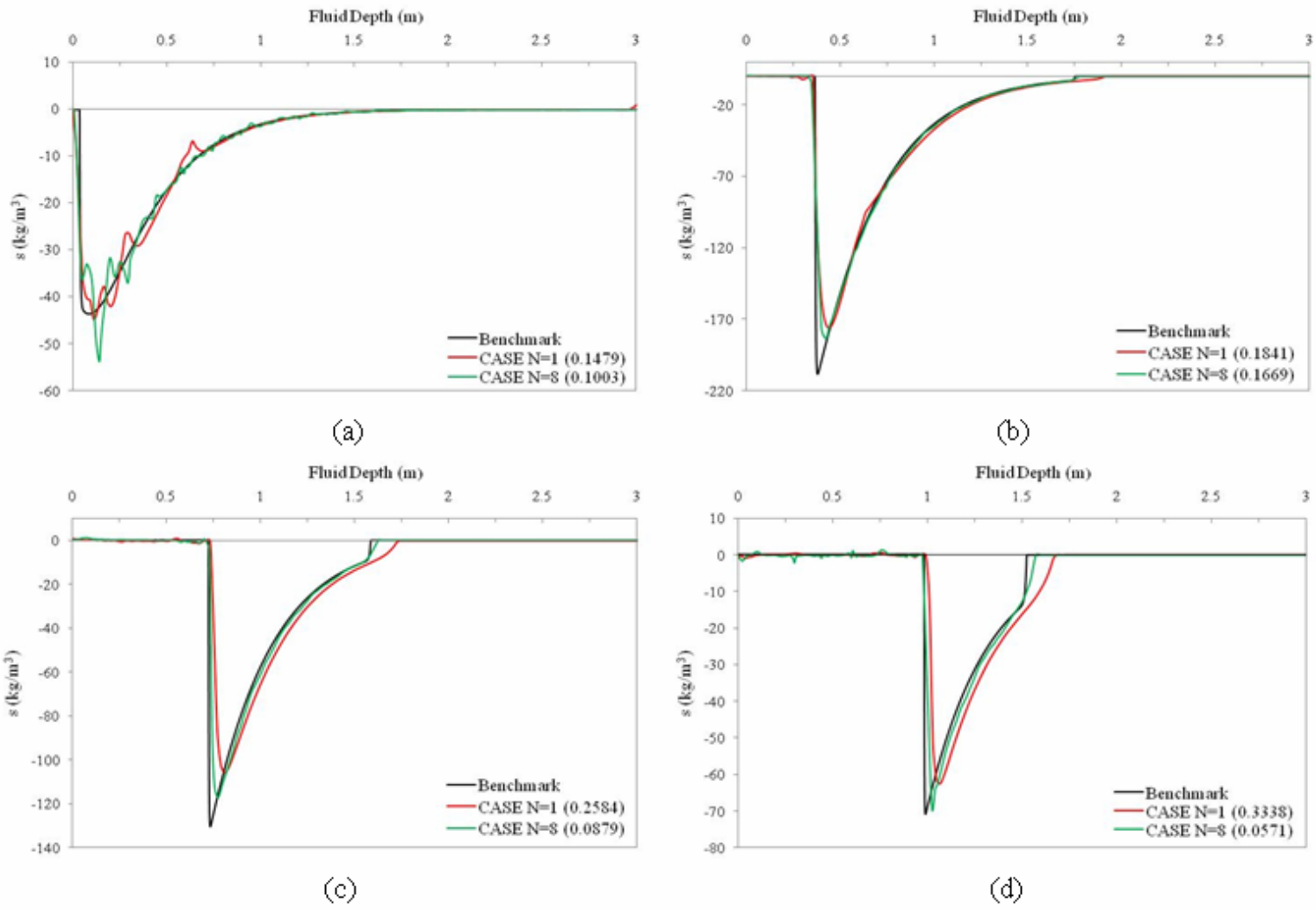

Figure 6.47 Dynamic densified condensation in the fluid at t=0.002 s (a), t=0.015 s (b), t=0.025 s (c), and t=0.03 s (d) for the m_2/m_1=25 case using 1449 DOF with β = 0.10 for N=1 CASE and β = 0.25 for N=8 CASE

6.6 Computational Efficiency

For the problems studied in this chapter we have observed that for a given amount of artificial damping and a given degree of fluid mesh refinement the higher-order CASE models give superior results when compared to both the N=1 CASE and the pressure formulation models. Thus for a desired level of accuracy, a higher-order CASE model requires fewer fluid DOF [26,44]. To examine the smaller DOF requirement of computational efficiency, we plot the L_2 error norms for the velocity response against the CPU time for each of the m_2/m_1 ratios used in this chapter. On each of the plots in the

section, we have included results obtained with a 3133 DOF and a 8421 DOF N=1 CASE model. These results are included to demonstrate the cost associated with highly refined N=1 CASE models that give similar error norms to higher-order CASE models with a much lower degree of mesh refinement.

Figures 6.48, 6.49, 6.50, and 6.51 show the L_2 error norms for the velocity response against the CPU time for the m_2/m_1=0, m_2/m_1=1, m_2/m_1=5, and m_2/m_1=25 problems respectively. Note that in Fig. 6.48a we have included labels to identify the number of fluid model DOF used in the CPU time figures. In each problem the increased refinement of the N=1 CASE model to 3133 DOF and 8421 DOF results in solutions that are closer to the N=6 and N=8 CASE models but the more refined N=1 CASE models significantly increase the CPU time. Thus, in general, we find that for each value of β the higher-order CASE models require less CPU time to achieve a desired error norm due to the reduced refinement requirements. The reduced refinement requirement of the higher-order CASE models can also yield computational savings in terms of required operations and more importantly required memory [26,44,61] details of which are discussed in [44,67] for CASE models.

Note that in Figs. 6.48a, 6.49a, 6.50a, and 6.51a, we have included the CPU times for the pressure formulation using η_D= 0.020 to demonstrate the large increase in CPU time for the method discussed in Section 6.1. These results show that when compared to the N=1 and higher-order CASE models, the application of artificial diffusion through the FE-FCT algorithm in pressure formulation model causes a large increase in computational time when applied to multi-dimensional grids. From a computational efficiency standpoint, this makes the pressure formulation model with the FE-FCT algorithm unsuitable for application to large scale, multi-dimensional, far-field UDNEX models.

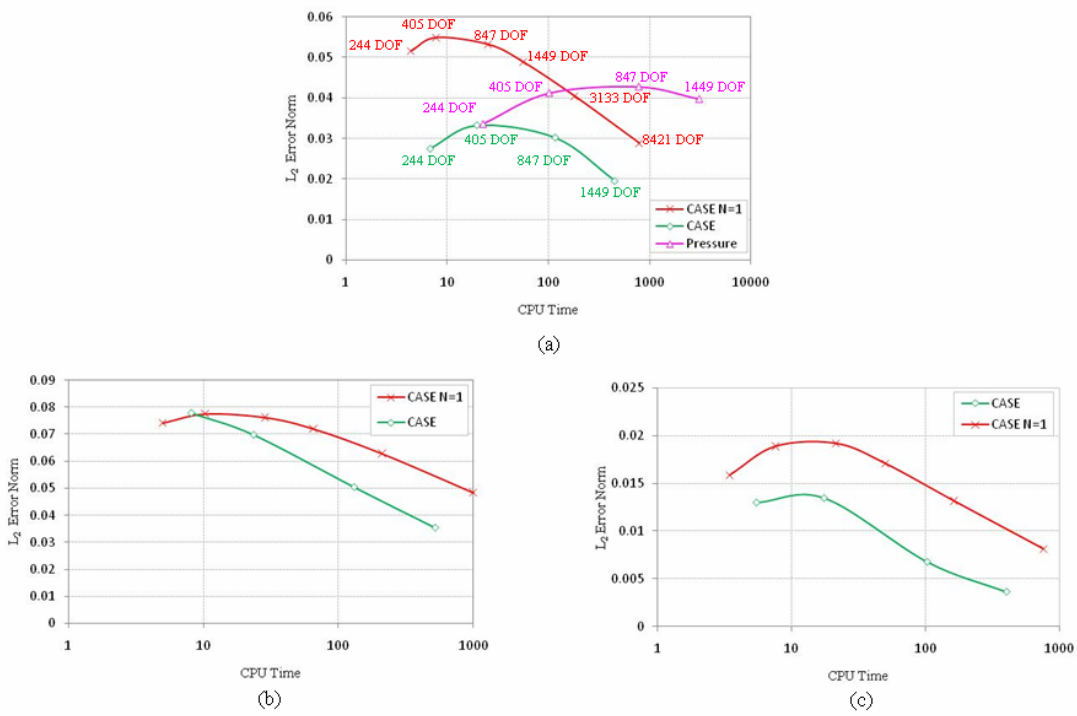

Figure 6.48 L_2 error norm for the velocity of m_1 against CPU time for the m_2/m_1=0 case using $\beta = 0.25$ and $\eta_D = 0.020$ (a), $\beta = 0.50$ (b), and $\beta = 0.10$ (c)

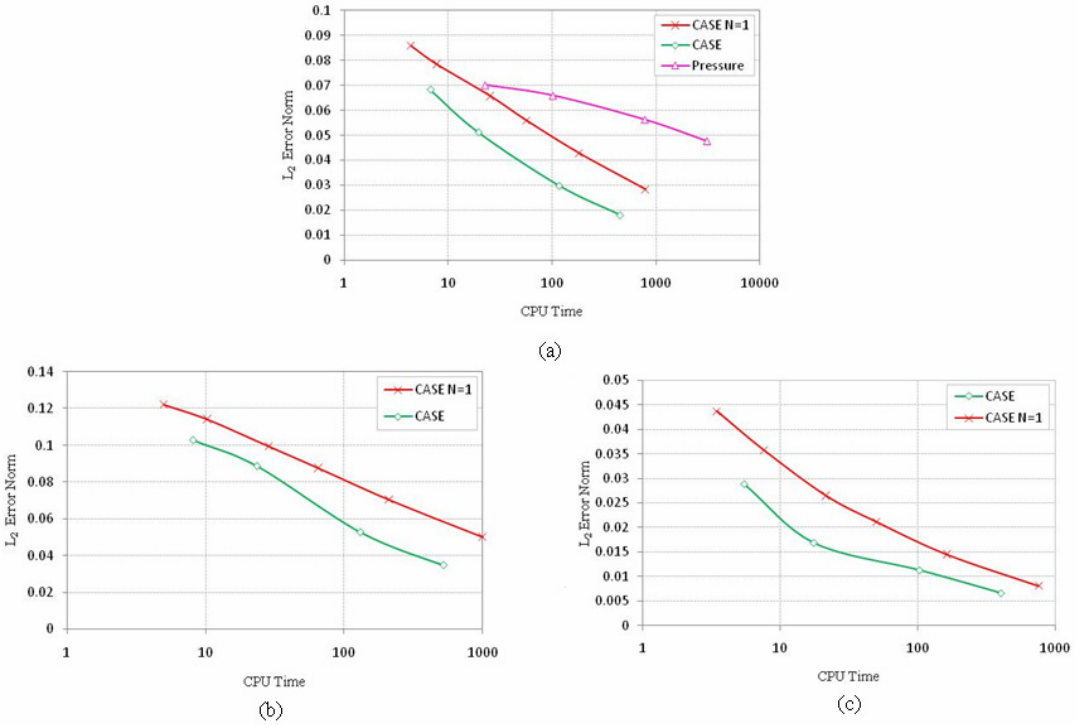

Figure 6.49 L_2 error norm for the velocity of m_1 against CPU time for the m_2/m_1=1 case using $\beta = 0.25$ and $\eta_D = 0.020$ (a), $\beta = 0.50$ (b), and $\beta = 0.10$ (c)

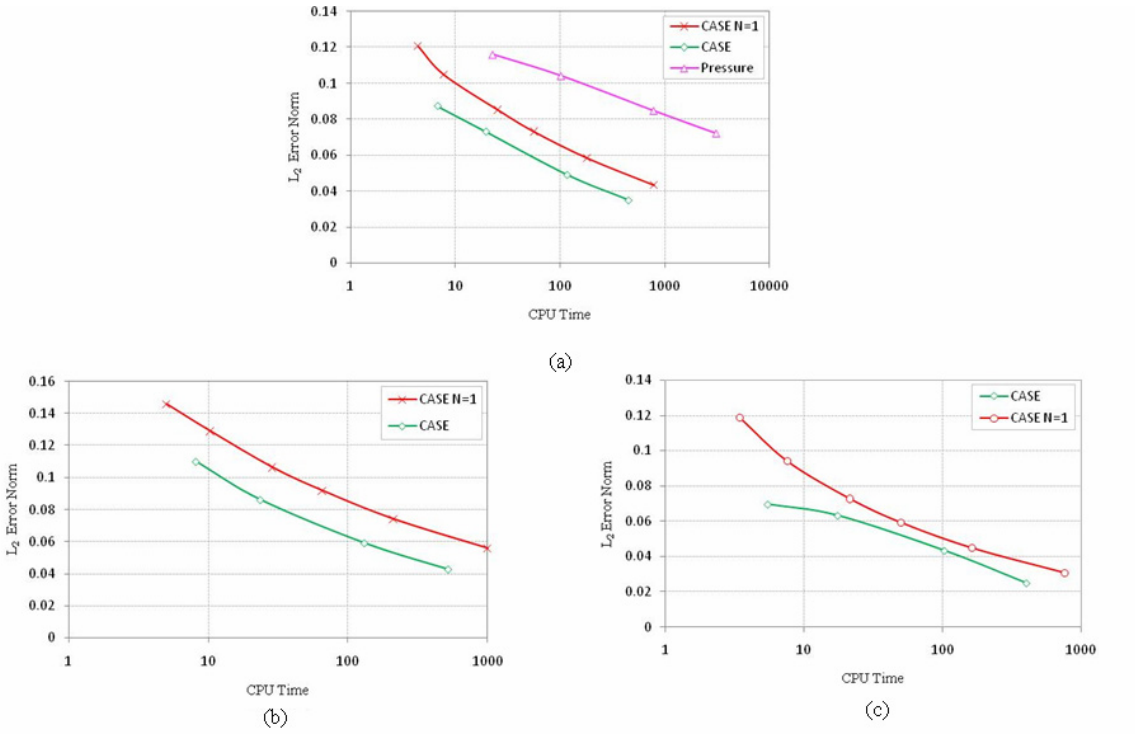

Figure 6.50 L_2 error norm for the velocity of m_1 against CPU time for the m_2/m_1=5 case using β = 0.25 and η_D= 0.020 (a), β = 0.50 (b), and β = 0.10 (c)

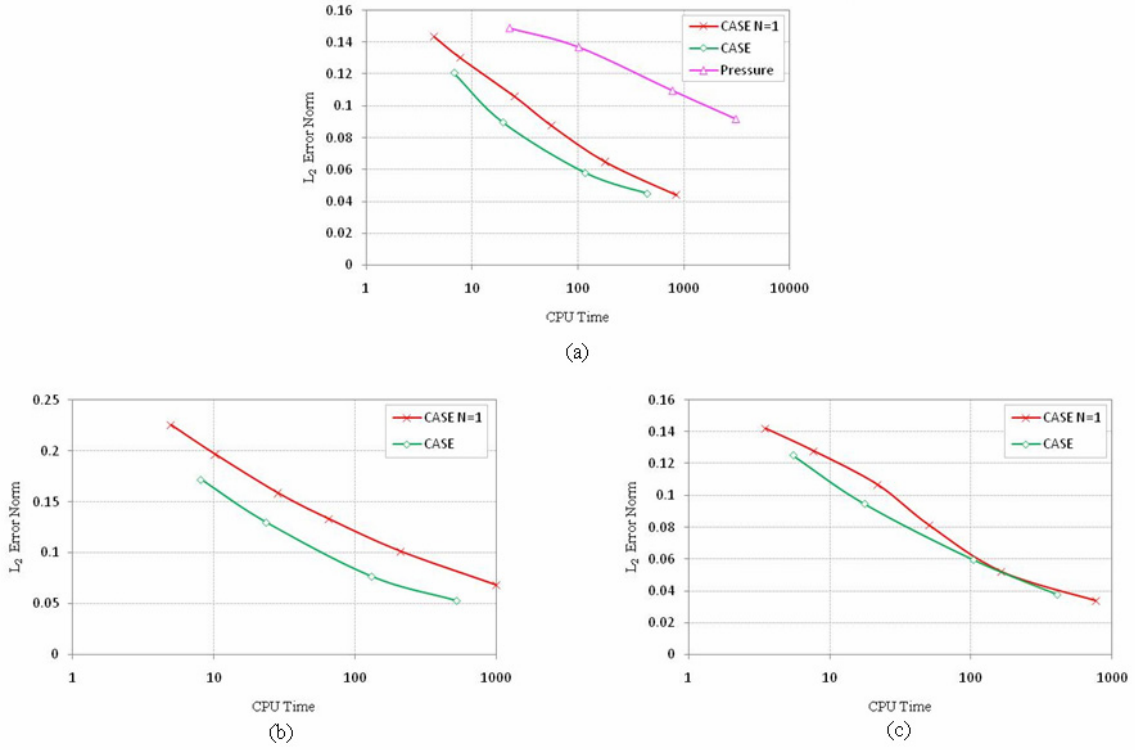

Figure 6.51 L_2 error norm for the velocity of m_1 against CPU time for the m_2/m_1=25 case using β = 0.25 and η_D= 0.020 (a), β = 0.50 (b), and β = 0.10 (c)

Recall from Sections 6.4.3 and 6.5.3 we compared the N=1 CASE models with β=0.10 to the higher-order CASE models with β=0.25 to determine if using less damping in the N=1 CASE models could match the higher-order CASE solutions with a larger amount of damping. From this comparison we found that although the difference between the N=1 and higher-order CASE models is reduced due to the reduction in artificial damping, the higher-order CASE model remains superior. Because of this reduced difference and also because the time step of CASE models is affected by the choice of β we compare CPU times for the N=1 CASE models with β=0.10 to the higher-order CASE models with β=0.25 to determine if the higher-order CASE models maintain a computational advantage. To accomplish this we again plot the L_2 error norm for the velocity response against the CPU time. This is shown in Fig. 6.52 for the m_2/m_1=5 problem and in Fig. 6.53 for the m_2 m_1=25 problem.

For the m_2/m_1=5 problem in Fig. 6.52 the CPU time comparison shows that with the exception of the N=3 CASE model, the N=1 CASE model with reduced damping and the higher-order CASE model require almost identical amounts of CPU time for a desired value of L_2 error norm. However, the higher-order CASE model still requires less fluid DOF for a desired value of the velocity response L_2 error norm. For example the 847 DOF N=1 CASE model with β=0.10 gives $L_2 \approx 0.07272$ which is very close to the 405 DOF N=4 CASE model which gives $L_2 \approx 0.07298$. Compared to the higher-order CASE model, the required DOF for the N=1 CASE model with β=0.10 increases significantly when a lower L_2 error norm is desired. To match the L_2 norm for the 847 DOF N=6 CASE model ($L_2 \approx 0.04894$) the N=1 CASE model with β=0.10 requires approximately 2250 fluid DOF. Thus, although the CPU times and L_2 in Fig. 6.52 for these two models are almost identical, the higher-order CASE model still has a computational advantage due to the lower number of fluid DOF which, as mentioned earlier, reduce the amount of memory required [26,44,61].

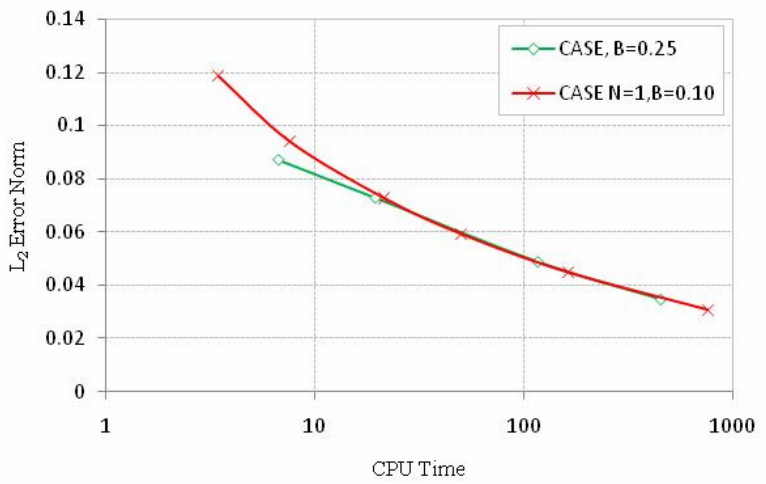

Figure 6.52 L_2 error norm for the velocity of m_1 against CPU time for the m_2/m_1=5 case using β = 0.25 for the higher-order CASE model and β = 0.10 for the N=1 CASE model

We find similar results for the m_2/m_1=25 problem in Fig. 6.53. For this problem the less refined higher-order CASE models with β=0.25 require less CPU time for a desired L_2 error norm when compared to the 244 DOF – 1449 DOF N=1 CASE models with β=0.10. For L_2 error norms lower than 0.060, the N=1 CASE model with β=0.10 actually requires less CPU time. However, as in the previous problem the N=1 CASE model requires significantly more fluid DOF when compared to the higher-order CASE model. This is illustrated in Fig. 6.53 where to match the L_2 error norm and CPU time of the 847 DOF N=6 CASE model the N=1 CASE model requires approximately 2500 DOF. Again the reduced fluid DOF used in the higher-order CASE models offer savings in required memory. Thus even though the CPU time is increased for higher degrees of refinement, the higher-order CASE models still maintain a computational efficiency advantage.

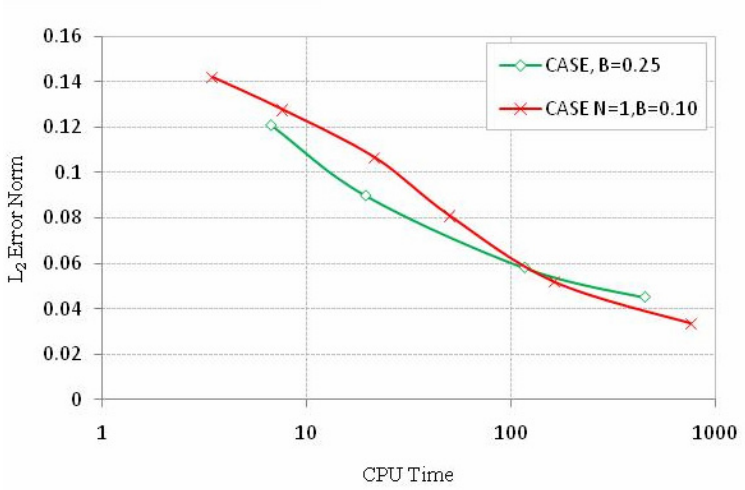

Figure 6.53 L_2 error norm for the velocity of m_1 against CPU time for the m_2/m_1=25 case using β = 0.25 for the higher-order CASE model and β = 0.10 for the N=1 CASE model

6.7 Summary

In this chapter, we have evaluated a N=1 CASE model, a pressure formulation model, and a higher-order CASE model using different ratios of m_2/m_1 for the two degree of freedom mass spring oscillator problem. For each ratio of m_2/m_1 used, the higher-order CASE model gave superior velocity and displacement response results when compared to the benchmark solution. In agreement with [44,67], the improvement of the higher-order CASE model over the N=1 CASE and pressure formulation model was found to be particularly advantageous for large degrees of mesh refinement (i.e. large N CASE elements).

We observed that the reason that the higher-order CASE model gives superior structural response results is due to the fact that it captures cavitation in the fluid more accurately than the N=1 CASE and pressure formulation model. Relative to the benchmark solution, the error norms in the capture of cavitation in the fluid is much greater than the error norms observed in the structural response. However, we observed the capture of the propagation of the upper cavitation boundary [38] and of the magnitude of dynamic densified condensation in the cavitation region has a significant effect on the velocity magnitude of the structure during the response to cavitation, on the re-loading of the structure due to cavitation closure, and on the maximum displacement of the structure during response to cavitation. This is especially true for larger values of m_2/m_1 that

represent more realistic ship structures. These results demonstrate the need to accurately resolve both the shape and magnitude of cavitation regions in the fluid in order to obtain accurate structural responses to cavitation in far-field UNDEX problems [44].

Through comparison of each ratio of m_2/m_1 used, we observed that for all fluid models oscillations in the structural response increase as the ratio of m_2/m_1 is increased. This is especially true for higher-order CASE fluid models, which confirms the findings in [44,67]. However, for each ratio of m_2/m_1 used we observed that the oscillations only occur in the velocity and fluid response. In the velocity response the oscillations only affect the solution for a small portion of the total response history. Thus, when the total error is considered, the increased oscillations in higher-order CASE models do not significantly degrade the accuracy of the solution. We do note that while this conclusion is true for the problem studied in this section, it may not be true for all fluid-structure interaction problems associated with UNDEX. The situation, where this conclusion may not be true, is in problems for which the structure is very sensitive to the fluid and the duration of the first cavitation region, where oscillations are most prevalent, dominates the entire response time (e.g. the Bleich-Sandler problem). However, for the most realistic ship structure studied in this work (i.e. the m_2/m_1=25) we still found the higher-order CASE model to give a significant advantage despite the greater increase in oscillations.

The oscillations in both the structural response and fluid can be reduced for all models by increasing the amount of artificial damping/diffusion and/or mesh refinement in the fluid model. However, for each problem the increase in artificial damping/diffusion resulted in an increase in error in both the structural response and fluid results. Conversely, decreasing the amount of artificial damping/diffusion used in the fluid model generally resulted in a improvement in the structural response results. However, this resulted in an increase in oscillations, thus is only effective for small values of m_2/m_1 that are not affected by increased oscillations in the fluid. Based on this, we confirm taking β=0.25 or 0.50, as is commonly done [2,8,22,26,38,44,45,67,68,77], appears to be the best choice.

We also made a comparison of a reduced damping N=1 CASE model to a higher-order CASE model to determine if, due to the increase in oscillation in higher-order

CASE models, an N=1 CASE model could give similar results. Through this comparison, we found the superiority that the higher-order CASE mode has maintained due to its ability to capture cavitation in the fluid.

We observed that the higher-order CASE model gives a reduction in CPU time required for a desired level of accuracy when compared to the N=1 CASE models. This is due to the lower number of fluid DOF required by higher-order CASE models for a desired level of accuracy [26,44]. When we compared the CPU time of the higher-order CASE models to a reduced damping N=1 CASE model we found the reduction in CPU time given by the higher-order CASE model to be lessened for low degrees of fluid mesh refinement. For higher degrees of mesh refinement in the m_2/m_1=5 problem, the higher-order CASE and reduced damping N=1 CASE models required almost identical CPU times. For higher degrees of mesh refinement in the m_2/m_1=25 problem, the N=1 CASE model actually required less CPU time. However, in these comparisons the higher-order CASE model still maintained the advantage of requiring a lower degree of fluid refinement for a given level of accuracy. Because the total DOF used in the fluid affects not only the CPU time but also required memory [26,44,61], we conclude that the higher-order CASE model gives an overall improvement in computational efficiency when compared to the N=1 CASE model due to the smaller number of fluid DOF required for a desired level of accuracy.

When we compared the pressure formulation model to the N=1 CASE model, we found that for small ratios of m_2/m_1, the two models gave results that show no observable differences. For large ratios of m_2/m_1, we found that the pressure formulation model differed from both the N=1 CASE and the benchmark solution in its prediction of secondary cavitation regions. These differences appear to be largely dependent on the problem and the level of mesh refinement. We also found the application of artificial diffusion in the pressure formulation model causes a large increase in computational expense when applied to multi-dimensional grids. Thus we conclude that the pressure formulation FE-FCT model is not suitable for far-field UNDEX modeling.

Despite this, the problem dependency of the pressure formulation raises an interesting point. Throughout this chapter we noted that as the ratio of m_2/m_1 is increased, the errors observed in the structural response also increased. This result illustrates the assertion in

[38] that the response of a small m_1 is more sensitive to errors in the fluid model. We summarize this point in Figs. 6.48-6.50, which show the velocity response L_2 error norm versus the ratio of m_2/m_1 using 405 DOF and 1449 DOF with $\beta = 0.10/\eta_D = 0.010$, $\beta = 0.25/\eta_D = 0.020$, $\beta = 0.50/\eta_D = 0.035$ respectively. Figs. 6.48-6.50 show for both the 405 DOF and 1449 DOF fluid models and for each amount of damping/diffusion used, the divergence from the benchmark velocity response increases as the ratio of m_2/m_1 is increased. Note Figs. 6.48-6.50 also clearly show advantage of the higher-order CASE model when compared to the N=1 CASE and pressure formulation models for each ratio of m_2/m_1 considered in this chapter. The increase in error is largest for the 405 DOF fluid models, indicating the error in the structural response is less dependent on the m_2/m_1 ratio as the fluid mesh is refined. When we consider the application of both CASE models to a broad range of far-field UNDEX problems we must assume the sensitivity of more complex structures to the fluid model will not be necessarily be known. The results of this chapter show that the only way to guarantee accuracy of the structural response in this situation is to refine the fluid to the point where it will give accurate structural responses no matter how sensitive the structure is to the fluid model. Given the results in Figs. 6.48-6.50, and the fact that the results of the mass-spring oscillator problem demonstrated the superior convergence rate of spectral elements, the use of higher-order CASE models allows the fluid model refinement level at which the structural response will be accurate to be reached for a much lower degree of mesh refinement.

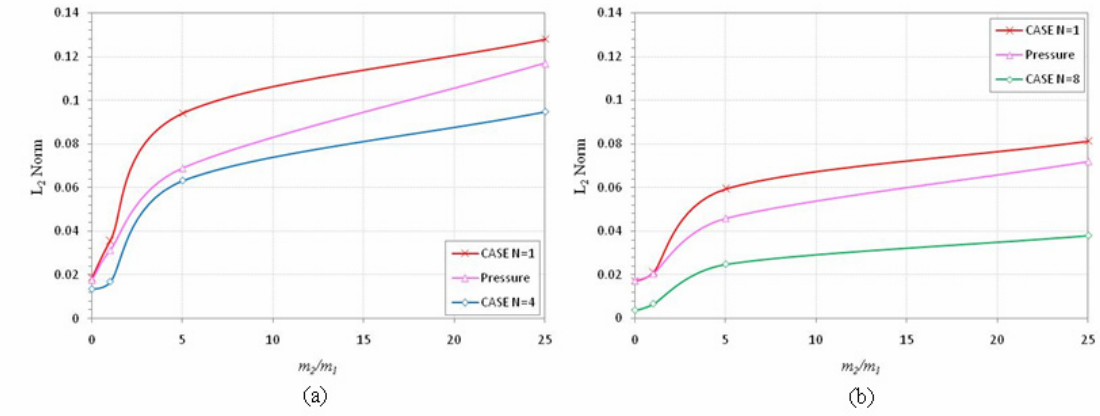

Figure 6.54 L_2 error norm of the velocity response as a function of the ratio m_2/m_1 using a 405 DOF fluid mesh (a) and a 1449 DOF fluid mesh (b) with $\beta = 0.10$ for CASE and $\eta_D = 0.010$ for the pressure formulation

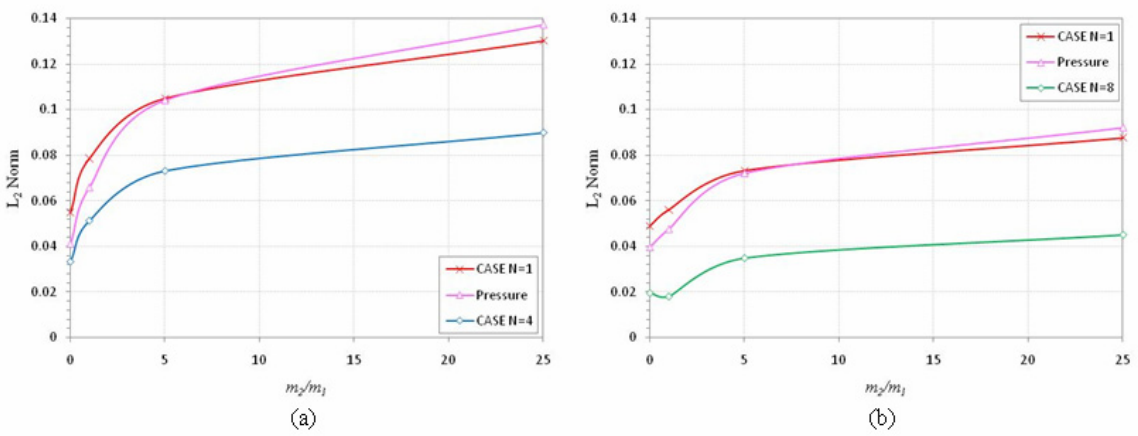

Figure 6.55 L_2 error norm of the velocity response as a function of the ratio m_2/m_1 using a 405 DOF fluid mesh (a) and a 1449 DOF fluid mesh (b) with $\beta = 0.25$ for CASE and $\eta_D = 0.020$ for the pressure formulation

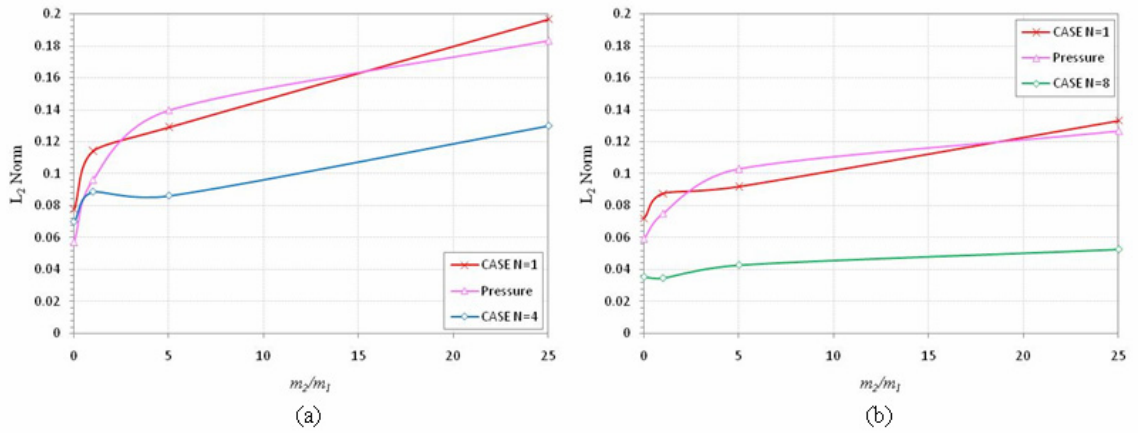

Figure 6.56 L_2 error norm of the velocity response as a function of the ratio m_2/m_1 using a 405 DOF fluid mesh (a) and a 1449 DOF fluid mesh (b) with $\beta = 0.50$ for CASE and $\eta_D = 0.035$ for the pressure formulation

CHAPTER 7 CONCLUSIONS

In this dissertation, we examined three acoustic fluid models that used finite elements (CAFE), spectral elements (CASE), and a finite element flux-corrected transport (FE-FCT) algorithm to model far-field underwater explosion effects on ships. For the fluid-structure interaction problems considered in this work, we applied a scattered field fluid model that was coupled to the structure using a non-conformal coupling algorithm and treated the infinite boundary of the fluid domain using the plane wave non-reflecting boundary condition.

We evaluated each fluid model first by determining ability to capture a step exponential wave propagating through the fluid. These results showed that despite the appearance of large amplitude oscillations along the wave form, the CASE model reduced dispersion error and thus gave the better wave propagation results when compared to CAFE. When artificial damping was added, the oscillations that appeared in both the CAFE and CASE models were smoothed. However, the addition of artificial damping increased error in the results because of wave front smearing and dissipation of the wave magnitude.

When the time step was taken as less than the critical limit the FE-FCT algorithm in the wave propagation problem proved to capture the sharpness of the wave front and removed dispersive oscillations. Compared to the CAFE and CASE results with and without damping, the FE-FCT algorithm gave the most accurate results. Thus, when the time step is taken as less than the critical limit, the FE-FCT algorithm is the superior most method for capturing a step exponential wave propagating in an acoustic fluid.

Next, we examined the ability of each method to capture cavitation in a far-field UNDEX problem. Application of the FE-FCT algorithm to cavitation problems proved to be problematic, as the strong flux limiter was unable to remove large oscillations caused by the formation of the cavitation region. Adding residual diffusion to the FE-FCT algorithm and using a one-sided flux limiter allowed a small reduction in oscillations in the structural response for low degrees of mesh refinement. However, as the fluid model is refined, similar results were observed for CAFE models with the same amount of artificial damping/diffusion. In addition, the FE-FCT algorithm showed a

difference in the prediction of small secondary cavitation regions in some fluid-structure interaction problems. These same differences were also observed when the FE-FCT algorithm was applied to the pressure formulation model using only diffusion and grew in severity as the structure became more sensitive to the fluid model. Because of this, and the computational inefficiency of applying the FE-FCT algorithm to the 2D problems studied, we concluded the FE-FCT algorithm presented in this work to be unsuitable for far-field UNDEX models.

An analysis of a two degree-of-freedom mass spring oscillator problem illustrated the assertion in [38] that as the mass of the structure coupled to the fluid is decreased, its response becomes more sensitive to errors in the fluid model. Comparison of cavitation capture in the fluid showed in particular that the capture of the propagation of the upper cavitation boundary [38] and of the magnitude of dynamic densified condensation had a significant effect on the structural response. This effect became more apparent when the mass of the hull coupled to the fluid was small compared to the mass of the total ship structure. Of all the models considered, this configuration of the hull (small mass) and internal structure/equipment (large total mass) best represents a realistic ship structure. Thus, in support of [44,38], we conclude there is a need to accurately resolve both the shape and magnitude of cavitation regions in the fluid in order to accurately capture the cavitation response of the structure in far-field underwater explosion problems.

In each of the problems considered we found the higher-order CASE model to give the most accurate cavitation capture, which in turn gives superior structural response results with the higher-order CASE model. Furthermore, in both the fluid and structural response solutions, the higher-order CASE model showed faster convergence to the benchmark solutions than the first order fluid models. This proved to be true even when the higher-order CASE model was compared to the N=1 CASE model with reduced artificial damping.

As in [26,44], we observed that the higher-order CASE models require a smaller number of fluid degrees of freedom for a given level of accuracy. In the problems studied, this resulted in the higher-order CASE model requiring less CPU time for a desired level of accuracy when compared to the N=1 CASE models.

The application of higher-order CASE models to cavitation problems does cause an increase in oscillations in both the velocity and fluid response [44,67]. The increase in oscillations was not observed in the displacement response of the structure. The severity of these oscillations grows as the structure becomes more sensitive to the fluid model. However, the increase in oscillations did not cause the higher-order CASE models to be less accurate than the N=1 CASE and pressure formulation results when compared to the benchmark solution. We find that this is due to the fact that the oscillations only affect the velocity response for a small portion of the total response history.

Because of this and the findings that the higher-order CASE model gives superior cavitation capture in the fluid, superior structural response results, and faster convergence to the benchmark solution in each of the problems considered in this work, we conclude that of the fluid models used in this work higher-order CASE modes are best suited for application to far-field UNDEX problems. Although this was the conclusion of other researches [26,44,45,67], these studies of CASE models did not thoroughly assess the superior cavitation capture of higher-order CASE models and the problem dependency of increased oscillations in the higher-order CASE models which are important contributions of this work.

For future work in the area of far-field UNDEX modeling using the CASE methodology, we suggest evaluation of CASE for a large scale 3D problem. The CASE methodology is easily extended to 3D problems, details of which are provided in [26,67]. While a large scale problem was solved in [45] using higher-order CASE a comparison between N=1 CASE and higher-order CASE models, such as the comparisons presented in this work, has yet to be made for a large scale 3D problem.

In an evaluation of a more realistic large scale far-field UNDEX problem, we also suggest a study of how higher-order CASE models capture large regions of bulk cavitation using the same metric (i.e. comparison of dynamic densified condensation in the cavitation region) presented in Chapter 6.

A large scale problem of interest might be the numerical simulation of shock testing preformed on the Navy's floating shock platform (FSP) which is used in the shock testing of shipboard equipment [82]. Details of on the construction of the FSP and FSP shock tests can be found in [83,84,85].

REFRENCES

1) OPNAV Instruction 9070.1, "Shock Hardening of Surface Ships," 12 January 1987.

2) Shin, Y. and Schneider, N. "Ship Shock Trial Simulation of USS Winston S. Churchill (DDG 81): Modeling and Simulation Strategy and Surrounding Fluid Volume Effects," *74th Shock and Vibration Symposium*, San Diego, CA, 2003.

3) Corrado, J., "Overview of Navy Enterprise Full Ship Shock Trials Alternative Program", *79th Shock and Vibration Symposium Abstract Book*, Orlando, FL, 2008.

4) Baron, M.L. and Daddazio, R., "Underwater Explosions," in *Shock and Vibration Computer Programs*, 1995.

5) Misovec, A.P., *Explosion Phenomena*, David W. Taylor Naval Ship Research and Development Center, 1976.

6) Reid, W.D., *The Response of Surface Ships to Underwater Explosions*, Department of Defense, 1994

7) Cole, R.H., *Underwater Explosions*, Princeton University Press, 1948.

8) Wood, S.L., "Cavitation Effects on a Ship-Like Box Structure Subjected to an Underwater Explosion," Thesis, Naval Postgraduate School, Monterey, CA, 1998.

9) Makinen, K., "Cavitation Models for Structures Excited by a Plane Shock Wave," *Journal of Fluids and Structures*, 12:85-101, 1998.

10) Keil, A.H., *The Response of Ships to Underwater Explosions*, Department of the Navy, 1961.

11) Mair, H.U., and Huang, H., "Lagrangian Hydrocode Modeling of Underwater Explosive/Target Interaction". *61th Shock and Vibration Symposium*, 79-89, 1990.

12) Park, J., "A Coupled Runge Kutta Discontinuous Galerkin-Direct Ghost Fluid (RKDG-DGF) Method for Near-field Early-time Underwater Explosion (UNDEX) Simulations," Dissertation, Virginia Polytechnic Institute and State University, Blacksburg, VA., 2008.

13) Arons, A.B., Slifko, J.P., and Carter, A., "Secondary Pressure Pulses Due to Gas Globe Oscillation in Underwater Explosions. I. Experimental Data," *Journal of the Acoustical Society of America* 20:271, 1948.

14) Arons, A.B., "Secondary Pressure Pulses Due to Gas Globe Oscillation in Underwater Explosions. II. Selection of Adiabatic Parameters in the Theory of Oscillation," *Journal of the Acoustical Society of America* 20:277, 1948.

15) Arons, A.B., and Yennie, D.R., "Energy Partition in Underwater Explosion Phenomena," *Reviews of Modern Physics* 20:519, 1948.

16) Swisdak, M., "Explosion Effects and Properties: Part II.– Explosion Effects in Water," NSWC/WOR TR 76-166, 1978.

17) Rogers, P.H., "Weak-shock Solution for Underwater Explosive Shock Waves," *Journal of the Acoustical Society of America*, 62:1412, 1977.

18) Geers, T.L. and Hunter, K.S., "An integrated wave-effects model for an underwater explosion bubble*," Journal of the Acoustical Society of America,* 111:1584-1601, 2002.

19) Hunter, K.S. and Geers, T.L., "Pressure and velocity fields produced by an underwater explosion," *Journal of the Acoustical Society of America*, 115:1483-1496, 2002.

20) DeRuntz, J.A., "The Underwater Shock Analysis Code and its Applications," *60th Shock and Vibration Symposium*, 1:89-107, 1989.

21) DeRuntz, J.A., "The Underwater Shock Analysis (USA) Manual," Unique Software Applications, Colorado Spring, CO, 1996.

22) Felippa, C.A. and DeRuntz, J.A., "Finite Element Analysis of Shock Induced Hull Cavitaiton," *Computational Methods in Applied Mechanical Engineering*, 44:297-337, 1984.

23) Fox, S.L., "Nonlinear Response of Cylindrical Shells to Underwater Explosion: Testing and Numerical Prediction Using USA/DYNA3D," Thesis, Naval Postgraduate School, Monterey, CA, 1992.

24) Beiter, K.A., "The Effect of Stiffener Smearing in a Ship-Like Box Structure Subjected to an Underwater Explosion, in Mechanical Engineering," Thesis, Naval Postgraduate School, Monterey, CA, 1998.

25) Felippa, C.A. and DeRuntz, J.A., "Acoustic Fluid Modeling by the Displacement Potential Formulation, with Emphasis on the Wedge Element," *Computers and Structures*, 41:669-686, 1991.

26) Sprague, M.A., and Geers, T.L., "A Spectral-Element Method for Modeling Cavitation in Transient Fluid-Structure Interaction," *International Journal for Numerical Methods in Engineering*, 60:2467-2499, 2004.

27) Zienkiewicz, O.C. and Bettess, P., "Fluid-Structure Dynamic Interaction and Wave Forces. An Introduction to Numerical Treatment," *International Journal for Numerical Methods in Engineering*, 13:1-16, 1978.

28) Klenow, B., Nisewonger, A., Batra, R.C., and Brown, A., "Reflection and transmission of plane waves at an interface between two fluids," *Computers & Fluids*, 36:1298-1306, 2007.

29) Everstine, G.C., "Finite Element Formulations of Structural Acoustics Problems," *Computers & Structures*, 65:207-321, 1997.

30) Newton, R.E., "Finite Element Analysis of Shock-Induced Cavitation," *ASCE Spring Convention*, 1980.

31) Sandberg, G., "New finite element formulation of shock-induced hull cavitation," *Computer Methods in Applied Mechanics and Engineering*, 120:33-44, 1995.

32) Dassault Systèmes, *ABAQUS v.6.6 Users Manual*, 2007.

33) Newton, R.E., "Effects of Cavitation on Underwater Shock Loading – Part I," Rept. NPS69-78-013, Naval Post Graduate School, Monterey, CA., 1978.

34) Bleich, H.H. and Sandler, I.S., "Interaction Between Structures and Bilinear Fluids," *International Journal of Solids and Structures*, 6:617-639, 1970.

35) Liu, T.G., et.al., "Isentropic one-fluid modeling of unsteady cavitating flow," *Journal of Computational Physics*, 201:80-108, 2004.

36) Xie, W.F., et.al., "Application of a one-fluid model for large scale homogeneous unsteady caviation: The modified Schmidt model," *Computers & Fluids*, 35:1177-1192, 2006.

37) Zienkiewicz, O.C., Paul, D.K., and Hinton, E., "Cavitation in Fluid-Structure Response (With Particular Reference to Dams Under Earthquake Loading)," *Earthquake Engineering and Structural Dynamics*, 11:463-481, 1983.

38) Sprague, M.A., and Geers, T.L., "Computational Treatments of Cavitation Effects in Near-Free-Surface Underwater Shock Analysis," *Shock and Vibration*, 7:105-122, 2001.

39) Hung, C.F., Hsu, P.Y., and Hwang-Fuu, J.J., "Elastic shock response of an air-backed plate to underwater explosion," *International Journal of Impact Engineering*, 35:151-168, 2005.

40) Gong, S.W., and Lam, K.Y., "On attenuation of floating structure response to underwater shock," *International Journal of Impact Engineering*, 32:1857-1877, 2006.

41) Shin, Y.S., and Santiago, L.D., "Surface ship shock modeling and simulation: two-dimensional analysis," *Shock and Vibration*, 5:129-137, 1998.

42) Virtanen, J., and Juntunen, M., "Dynamic Simulation of Fast Attack Craft Subjected to Underwater Explosion (UNDEX)," *77th Shock and Vibration Symposium*, Monterey, CA, 2006.

43) Kannari, P., "Damage analysis of a ship rudder subject to UNDEX loads," *77th Shock and Vibration Symposium*, Monterey, CA, 2006.

44) Sprague, M.A., and Geers, T.L., "A Spectral-Element Method for Modeling Cavitation in Transient Fluid-Structure Interaction," *Journal of Computational Physics*, 184:149-162, 2003.

45) Sprague, M.A., and Geers, T.L., "A Spectral-Element/Finite-Element Analysis of a Ship-Like Structure Subjected to an Underwater Explosion," *Computer Methods in Applies Mechanics and Engineering,* 195:2149-2167, 2006.

46) Mulder, W.A., "Spurious modes in finite-element discretizations of the wave equation may not be all that bad," *Applied Numerical Mathematics*, 30:425-445, 1999.

47) Giannakouros, J., and Karniadakis, G.E.M., "Spectral Element-FCT method for scalar hyperbolic conservation laws," *International Journal for Numerical Methods in Fluids*, 14:707-727, 1992.

48) Yoon, K.T., and Chang, T.J., "Three-dimensional mixed explicit-implicit generalized Galerkin spectral element methods for high-speed turbulent compressible flows," *Computer Methods in Applies Mechanics and Engineering,* 135:343-367, 1998.

49) Boris, J.P. and Book, D.L., "Flux-Corrected Transport I. SHASTA, A fluid transport algorithm that works," *Journal of Computational Physics*, 135:172-186, 1997.

50) Book, D.L., Boris, J.P., and Hain, K., "Flux-Corrected Transport II. Generalizations of the Method," *Journal of Computational Physics*, 18:248-283, 1975.

51) Boris, J.P. and Book, D.L., "Flux-Corrected Transport III. Minimal-Error FCT Algorithms," *Journal of Computational Physics*, 20:397-431, 1976.

52) Zalesak, S.T., "The Design of Flux Corrected Transport (FCT) Algorithms for Structured Grids," in *Flux-Corrected Transport: Principles, Algorithms, and Applications*, D. Kuzmin, Lohner, R., and Turek, S., ed., Springer, pp. 29-78, 2005.

53) Zalesak, S.T., "Fully Multidimensional Flux-Corrected Transport Algorithms for Fluids," *Journal of Computational Physics*, 31:335-362, 1979.

54) Georghiou, G.E., Morrow, R., and Metaxas, A.C., "A two-dimensional, finite-element, flux-corrected transport algorith for the solution of gas discharge problems," *Journal of Physics D*, 33:2453-2466, 2000.

55) Lohner, R., Morgan, K., Peraire, J., and Vahdati, M., "Finite element flux-corrected transport (FEM-FCT) for the Euler and Navier-Stokes equations," *International Journal for Numerical Methods in Fluids*, 7:103-109, 1987.

56) Giannakouros, J., and Karniadakis, G.E.M., "A spectral element-FCT method for the compressible Euler equations," *International Journal for Numerical Methods in Fluids*, 115:65-85, 1994.

57) Xiao, S. "An FE-FCT method with implicit functions for the study of shock wave propagation in solids," *Wave Motion*, 40:263-276, 2004.

58) Kinsler, L.E., et.al., *Fundamentals of Acoustics-Fourth Edition*, Wiley, 2000.

59) Nimmagadda, P.B.R. and Cipolla, J. "A pressure based cavitation model for underwater shock problems," *71st Shock and Vibration Symposium*, Arlington, VA, 2000.

60) Pozrikidis, C. *Introduction to Finite and Spectral Element Methods using MATLAB*, Chapman & Hall/CRC, 2005.

61) Seriani, G., and Priolo, E. "Spectral element method for acoustic wave simulation in heterogeneous media," *Finite Elements in Analysis and Design*, 16:337-348, 1994.

62) Boyd, J.P., *Chebyshev & Fourier Spectral Methods,* Springer-Verlag, 1989.

63) Dauksher, W., and Emery, A. "Accuracy in modeling the acoustic wave equation with Chebyshev spectral finite elements," *Finite Elements in Analysis and Design*, 26:115-128, 1997.

64) Seriani, G., and Oliveira, S.P. "Dispersion analysis of spectral element methods for elastic wave propagation," *Wave Motion*, 45:729-744, 2008.

65) Komatitsch, D., Barnes, C., and Tromp, J. "Wave propagation near a fluid-structure interface: A spectral element approach," *Geophysics*, 65:623-631, 2000.

66) Hughes, T.J.R., *The Finite Element Method: Linear Static and Dynamic Finite Element Analysis*, Dover Publications, 2000.

67) Sprague, M.A., "Advanced Computational Techniques for the Analysis of 3-D Fluid-Structure Interaction," Dissertation, University of Colorado, Boulder, CO., 2002.

68) Klenow, B. and Brown, A., "Assessment of Non-Reflecting Boundary Conditions for Application in Far-Field UNDEX Finite Element Models," *77th Shock and Vibration Symposium*, Monterey, CA, 2006.

69) Farhat, C., Lesoinne, M., and LeTallec, P., "Load and motion transfer algorithms for fluid/structure interaction problems with non-matching discrete interfaces: momentum and energy conservation, optimal discretization, and application to aeroelasticity," *Computer Methods in Applied Mechanics and Engineering*, 157:95-114, 1998.

70) Book, D.L., "The Conception, Gestation, Birth, and Infancy of FCT," in *Flux-Corrected Transport: Principles, Algorithms, and Applications,* D. Kuzmin, Lohner, R., and Turek, S., ed., Springer, pp. 5-28, 2005.

71) Christon, M.A., et.al., "A Mixed Time Intergration Method for Large Scale coustic Fluid-Structure Interaction," *CED-Vol.6, High Performance Computing in Computational Dynamics*, ASME, pp.25-38, 1994.

72) Sommerfeld, A., "Lectures on Theoretical Physics," in the series: *Partial Differential Equations in Physics*, Vol.VI(28), Academic Press, 1964.

73) Givoli, D. *Numerical Method for Problems in Infinite Domains*, Elsevier, 1992.

74) Zienkiewicz, O.C., Taylor, R.L., and Nitharasu, P., *The Finite Element Method for Fluid Dynamics 6th Edition*, Elsevier, 2005.

75) Castellani, A. "Boundary Conditions to Simulate an Infinite Space," *Meccanica*, 9:199-205, 1974.

76) Lax, P.D., "Accuracy and resolution in the computation of solutions of linear and nonlinear equations," in *Recent Advances in Numerical Analysis, Symposium of the Math Research Center,* University of Wisconsin, Academic, NY, 1978.

77) Klenow, B., "Assessment of LS-DYNA and Underwater Shock Analysis (USA) Tools for Modeling Far-Field Underwater Explosion Effects on Ships," M.S. Thesis, Virginia Polytechnic Institute and State University, Blacksburg, VA, 2006.

78) Dassault Systèmes, *ABAQUS v.6.6 Benchmarks Manual*, 2007.

79) Xie, W.F., et.al., "Dynamic response of deformable structures subjected to shock load and cavitation reload," *Computational Mechanics*, 40:667-681, 2007.

80) Galiev, SH. U., "Influence of cavitation upon anomalous behavior of a plate/liquid/underwater explosion system," *International Journal of Impact Engineering*, 19:345-359, 1997.

81) Schwer, L.E., "Validation metrics for response histories: perspectives and case studies," *Engineering with Computers*, 23:295-305, 2007.

82) "The Floating Shock Platform for Shock Testing Equipment up to 30,000 pounds," UERD Report 7-61, Portsmouth, VA, 1961.

83) Sebert, K.A.., "A Mathematical Model of the Transient Motion Response of the US Navy Floating Shock Platform," Thesis, University of Akron, Akron, OH, 1984.

84) Clements, E.W., "Shipboard Shock and Navy Devices for its Simulation," NRL Report 7396, NRL, Washingtion D.C., 1972.

85) Clements, E.W., "Characteristics of the Navy Large Floating Shock Platform," NRL Report 7761, NRL, Washingtion D.C., 1974.